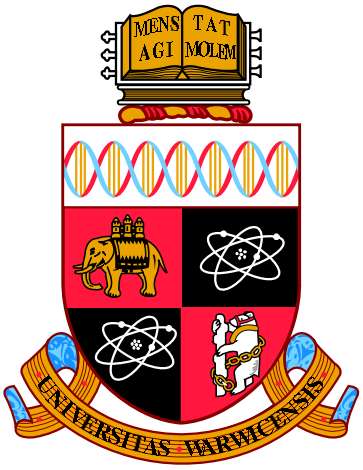

The Use of Solid State NMR to Monitor Reactions and Doping in Inorganic Materials

by

Samuel John Page

Thesis

Submitted to the University of Warwick

for the degree of

Doctor of Philosophy

Department of Physics

November 2017

Contents

List of Tables

List of Figures

Acknowledgments

First and foremost I would like to thank my supervisor Dr John V. Hanna, as without his guidance and insightful discussions this thesis would not have been possible.

I would like to express my gratitude to Johnson Matthey, EPSRC and the University of Warwick for whose financial support is greatly acknowledged. Furthermore, I am grateful to the all of the help, and discussions, provided by collaborators throughout my research projects. In particular those at Johnson Matthey including, Dr James Cookson, and Dr Noelia Cabello, who over not only supported the research but who have provided the expertise to synthesise the LFP systems. To Professor Julian Jones, Dr Shu Chen and Dr Sarah Greasly, for providing insight discussions about biomaterials. And I am grateful to Dr Brant Walkley and Professor John L Provis for providing the high quality geopolymer samples.

I would also like to acknowledge my friends and colleagues in the solid state NMR group, who made this all possible, but in particular: To my fellow doctoral students Joshua Clark, Thomas Hooper, and Maria Vlachou, who joined me throughout this journey and made this whole experience thoroughly enjoyable. To Dr. Gregory Rees for providing his expertise and training in solid state NMR. And to the office Cake Club for providing a midweek treat and chat.

Finally, and by no means least, I would like to thank my family: my mother, father, and sister who have provided support to me during both my academic studies, and throughout my life in general.

Declarations

I hereby declare that **The Use of Solid State NMR to Monitor Reactions and Doping in Inorganic Materials** is an original work and has not been submitted for a degree or diploma or other qualification at any other University.

For Chapter 4, all the samples in Section 4.3.1 & 4.3.2 were synthesised by partners at Johnson Matthey Technology Centre, UK. The exception was in Section 4.3.3 where I produced the samples using facility at Johnson Matthey Technology Centre, UK, under the guidance of Dr. Noelia Cabello. Furthermore, I performed the X-ray diffraction for these at Warwick.

For Chapter 5, all samples were synthesised by Dr. Sarah Greasley and Dr. Shu Chen at the Department of Materials, Imperial College London. The HRTEM was also performed by Dr. Shu Chen.

For Chapter 6, all samples were produced by Dr. Brant Walkley at the Department of Chemical and Biomolecular Engineering, The University of Melbourne.

Abstract

Solid state nuclear magnetic resonance (NMR) is a powerful probe of inorganic materials systems. Through carefully changing materials compositions and synthesis methods, the impact on the local structure can be investigated. These have been applied to three main materials sectors:

Paramagnetic materials in NMR have traditionally suffered from poor resolution due to broadening experienced at the nuclei from localised unpaired electrons. In this work, a fast magic angle spinning (MAS) and low field approach has been applied to these paramagnetic cathode materials to improve this resolution, and elucidate structural information from the investigated materials. The resolution gained from these techniques has been used to highlight differences observed in the ^{7}Li shifts of lithium iron phosphate (LFP) produced by different synthesis techniques. This was found to be related to the cell volume of the $LiFePO_4$ phase. Furthermore, the investigation of V doped LFP by ^{7}Li and ^{31}P MAS NMR has resulted in the observation of many common impurities resulting from synthesis. Additionally, ^{31}P resonances could be identified that were related to V near the phosphorus site, indicating successfully doping in some of the higher Li containing samples.

Through ^{29}Si and ^{17}O MAS NMR, changes in the local structure between Ca and Zn doped Stöber nanoparticles are observed. Similarly to other Ca containing materials, incorporation of Ca into the Stöber network has been shown to disrupt Si bridging bonds promoting the formation of non-bridging bonds in the silica network. However, addition of Zn tells a different story. This is first observed in the static measurements, where incorporation of high amounts of Zn leads to no evidence of hydroxyls observed in the Stöber network. Whereas, high resolution transmission

electron microscopy (HRTEM) and density functional theory (DFT) calculations confirm the presence of crystalline Zn_2SiO_4 – II in the nanoparticles.

Finally, activation of two series of synthetic sodium- and aluminium substituted calcium silicate hydrate (C-(N)-(A)-S-H) geopolymers are investigated. Increasing the CaO has been shown to increase the disorder of the silica network, and also to promote the increase of crystallinity of the systems through observation of calcium aluminate phases. Additionally, increasing the amount of aluminium relative to the silicon in the system, promotes more of these crystalline phases to form.

Abbreviations

3Q	Triple Quantum
BO	Bridging Oxygens
BMS	Bulk Magnetic Susceptibility
CS	Chemical Shift
CSA	Chemical Shift Anisotropy
C-(N)-(A)-S-H	Sodium- and Aluminium substituted Calcium Silicate Hydrate
DFT	Density Functional Theory
EFG	Electric Field Gradient
FID	Free Induction Decay
FSP	Flame Spray Pyrolysis
FWHM	Full Width Half Maximum
HRTEM	High Resolution Transmission Electron Microscopy
LAB	Lab Reference Frame
LFP	Lithium Iron Phosphate - $LiFePO_4$
LMP	Lithium Manganese Phosphate - $LiMnPO_4$
MAS	Magic Angle Spinning

M(H)	Magnetisation as a Function of Field
MQMAS	multiple quantum magic angle spinning
M(T)	Magnetisation as a Function of Temperature
T_N	Néel Temperature
NBO	Non Bridging Oxygens
NC	Network Connectivity
NMR	Nuclear Magnetic Resonance
OPC	Ordinary Portland Cement
PAS	Principle Axis System
ppm	Parts Per Million
Q_{is}	Quadrupolar Induced Shift
ROT	Rotating Frame
rf	Radio Frequency
S/N	Signal-to-Noise
SQ	Single Quantum
SQUID	Superconducting Quantum Interference Device
ST	Solvothermal
TM	Transition metal
T_1	Spin-lattice relaxation time
T_1	Spin-spin relaxation time
XRD	X-Ray Diffraction

Chapter 1

Introduction

1.1 A Brief History of Solid State NMR

Nuclear magnetic resonance (NMR) is now an effective analytical tool for a wide range of applications. However, it took a long road of building on previous studies for NMR to become the widely useful technique it is today. Full accounts of the discovery of the magnetic resonance phenomenon and the history of NMR are described elsewhere [1–3], however a few key discoveries relating to solid state NMR on materials are outlined here.

The first demonstration of NMR on liquids and solids was performed almost simultaneously by two different laboratories. Published in December 1945, Purcell, Torrey and Pound detected a weak radio frequency signal from almost a kilogram of paraffin wax in a magnetic field that would be considered fairly weak today (0.71 T) [4]. Only a month later, Bloch, Hansen, and Packard published their findings where a resonance was observed for this same phenomenon, however this time detecting the ^{1}H in water [5]. For these experiments both Bloch and Purcell were awarded the 1952 Nobel Prize in physics:

> *'for their development of new methods for nuclear magnetic precision measurements and discoveries in connection therewith'*

Since then, NMR continued under the realm of physicists where it was hoped to be a non-destructive way to measure the strength of the magnetic moments of nuclei. However, this relied upon the assumption that the resonant frequency was only dependent on the strength of the applied magnetic field. This was later proved not to be true, with discoveries of both the Knight shift and the chemical shift interaction (CSA) which turned NMR from simply an interesting physical phenomenon to the powerful analytical tool it is today [6, 7].

This early research into NMR consisted of having a continuous static radio frequency wave and slowly sweeping the magnetic field, leading to slow and inefficient acquisition of spectra. However, in 1949 Erwin Hahn demonstrated an alternative method. Through changing the frequency of applied *rf* pules and thus keeping the external magnetic field static, more complicated experiments such as the echo sequence were allowed [8]. This resulted in the ability to directly measure the transverse relaxation (T_2, Section 3.1.4) of nuclear spins.

For many years after the initial discovery of NMR the majority of development was focused on liquid samples, as the observed resonances were often much narrower than solid materials. This is due to the orientation dependence of many interactions, as the rapid tumbling of molecules in liquids removes these anisotropies, resulting in the much narrower observed resonances. To resolve this issue in solid materials, a technique called magic angle spinning (MAS) was proposed by Andrew, Bradbury and Eades, who reported that the dipolar Hamiltonian could be reduced by spinning at the angle (54.74 °) [9]. Later termed the 'magic angle' this averages the orientation dependence resulting from the second rank Legendre polynomial ($\frac{1}{2}(3\cos^2\theta - 1)$) present in many Hamiltonians. While, this successfully removed the anisotropies of many interactions, for quadrupolar nuclei, some orientation dependence still existed. This resulted from the second order quadrupolar interaction which has a fourth rank Legendre polynomial component ($\frac{1}{8}35\cos^4\theta - 30\cos^2\theta + 3$). It was later shown to be possible to rotate at a 2nd angle (30.56 °, or 70.12 °) in addition to the magic angle using techniques such as double rotation (DOR) and later dynamic angle spinning (DAS), which resolved both anisotropic components of the quadrupolar interaction [10, 11].

Even with pulsed NMR, and MAS NMR in solids, signal-to-noise was still an issue due to the inherent poor sensitivity of NMR. However, developments in both averaging of many acquired spectra, and Fourier transforming of the signal from pulsed experiments, high resolution NMR was now conceivable [12,13]. Furthermore, the improvement of signal-to-noise and the introduction of pulsed NMR lead to the possibility of 2D NMR. The idea was first proposed as a possibility by Jean Jeener in 1971 at the AMPERE Summer School [14]. This concept was experimentally confirmed in 1976, where Aue, Bartholdi, and Ernst not only proposed the basic theory but demonstrated some of the early 2D experiments [15]. This lead to many developments in 2D pulse sequences, including the possibility of detecting multiple quantum spin states [14, 16]. Pulsed NMR and 2D NMR eventually lead to the 1991 Nobel prize for chemistry being awarded to Richard Ernst:

'for his contributions to the development of the methodology of high resolution nuclear magnetic resonance (NMR) spectroscopy'

These advances in 2D NMR lead to the development of the multiple quantum magic angle spinning (MQMAS) experiment, arguably one of the most important experiments for quadrupolar solid state NMR [17]. Through successfully separating the 2nd order quadrupolar broadening into the 2nd dimension of the experiment high resolution quadrupolar NMR was achieved without using the technically advanced methods of DOR and DAS.

All these separate developments paved the way to the materials solid state NMR field today, where some or all of these techniques are employed as a powerful probe to the local structure of materials.

1.2 Motivations

There are three underlying motivations of this thesis; First, to develop a greater understanding of how changes in the manufacturing process can affect the final product produced. Second, to investigate what effect compositional changes have on the local structure of materials. Finally, to study the effects a small amount of doping has on the resulting material. Some or all of these motivations are applied to three distinct areas, all of current importance in inorganic materials systems; The paramagnetic lithium iron phosphate and its derivatives, the disordered Stöber nanoparticles, and the disordered C-(N)-(A)-S-H geopolymer system. As solid state NMR has been proven as a powerful tool to detect subtle changes in the local structure of both paramagnetic and disordered materials, use of this technique is a great choice for characterising changes in these three systems [18].

1.3 Thesis Overview

To understand some concepts in this thesis the background theory of NMR is given in Chapter 2. It covers the main NMR interactions present in the systems under investigation in this thesis.

In Chapter 3, the main methods used in this thesis are detailed. This covers most of the solid state NMR techniques, as well as the magnetic measurements used in this thesis.

Chapter 4 details the study on different methods to produce the paramagnetic cathode material LFP, and it's derivatives $LiMn_xFe_{1-x}PO_4$ and V doped LFP. Through the use of low magnetic fields and fast MAS NMR ($\nu_r = 60\,\text{kHz}$)

differences observed between different manufacturing methods are investigated. In addition, x-ray diffraction and the magnetic properties of the materials also highlight the differences observed in the systems.

The focus of Chapter 5 is a ^{29}Si and ^{17}O investigation into the incorporation of Ca and Zn into Stöber nanoparticles. Through isotropic enrichment of ^{17}O, changes in the oxygen structure are observed. Furthermore, the use of high-resolution transmission electron microscopy (HRTEM) and density functional theory (DFT) calculations the reaction products can be confirmed.

In Chapter 6, a multinuclear solid state NMR approach is applied to a synthetic C-(N)-(A)-S-H system. Through ^{29}Si 1D MAS and ^{27}Al MQMAS experiments, changes in the Ca/(Si+Al) and Al/Si ratios of synthetic precursors are investigated. A consequence of understanding of these synthetic precursors should impact how subtle changes in real world fly ash composition will be affected. Activation of the synthetic precursors has further brought an opportunity to investigate how these changes affect the final geopolymer composition, where introduction of both Na_2SiO_3 and enriched $H_2{}^{17}O$ enabled ^{23}Na and ^{17}O MQMAS NMR experiments to be conducted in addition to the ^{29}Si 1D MAS and ^{27}Al MQMAS experiments.

Chapter 2

Theory of Solid State NMR

The theory in this chapter has been based on a number of sources to provide the best well rounded background into NMR theory for each section. The following sources have been used: [19–28]

2.1 Background to Solid State NMR

2.1.1 Angular Momentum

Spin is one of the four important physical properties of nuclei, with the others being mass, electric charge, and magnetism. While nuclear magnetism and nuclear spin have almost no effect on the physical or chemical properties of materials, nuclear magnetic resonance (NMR) utilises these properties to provide an important structural tool for examining these nuclei.

Spin (I) results from an inequality of protons and neutrons at the nucleus and is quantised as discrete units of $\hbar$, where

$$I = 0, \frac{1}{2}, 1, \frac{3}{2}, 2, ... \tag{2.1}$$

Nuclear magnetism is heavily linked to this property of spin and all nuclei, where $I > 0$, have a magnetic moment (μ) which is proportional to their angular momentum

$$\hat{\boldsymbol{\mu}} = \gamma \hat{\boldsymbol{I}} \tag{2.2}$$

where γ is the gyromagnetic ratio, an intrinsic frequency for each nuclear isotope. The gyromagnetic ratio may be positive or negative, and is normally specified in units of rad $s^{-1}T^{-1}$. The difference in sign relates to whether the nuclear magnetic moment is aligned either parallel (positive) or anti-parallel (negative) to the angular

momentum, however the consequences of this are usually ignored. This magnetic moment is what interacts with an external applied magnetic field and is the basis of the NMR experiment.

2.1.2 Bulk Magnetisation

While it is useful for understanding to only think of a single isolated spin in a magnetic field, most experiments contain bulk amounts of spins in a system together. The net magnetisation of nuclei in a sample ($\boldsymbol{M}$) can be considered as a sum of all the vectors of the individual magnetic moments

$$\boldsymbol{M} = \sum_i \mu_i \tag{2.3}$$

where the magnetic moment associated with the ith nucleus is μ_i. When no magnetic field is applied, all magnetic moments are aligned randomly in space, effectively cancelling each other out leading to ($\boldsymbol{m} = 0$, Figure 2.1(a)). However, when a static and uniform external magnetic field (B) is applied to this group of magnetic moments, a net alignment is observed along the B axis (Figure 2.1(b)). However, this alignment along $\boldsymbol{B}$ is generally small and can be given as

$$\boldsymbol{M} = \frac{N\gamma^2 \boldsymbol{B} I(I+1)\hbar^2}{3kT} \tag{2.4}$$

where N is the number of spins, k is the Boltzmann constant, and T is the temperature. This results in nuclei where $I = 0$ being NMR silent, as there is net no alignment along the magnetic field. Fortunately, almost every element has at least one isotope with $I > 0$. It can also clearly be observed that to obtain the strongest signal an experiment will need to have the following conditions: low temperature, high applied magnetic field, large amount of spins, and a spin with a high gyromagnetic ratio.

Equation 2.4 also explains the inherent insensitivity in the technique. For a relatively high γ nucleus such as ^{1}H only 3.2×10^{-3}% of the nuclei are aligned with the magnetic field. Whereas, for a low γ nucleus such as ^{89}Y, even less are aligned at only 1.6×10^{-4}%. Additionally, investigations into isotopes with low natural abundance, the relative proportion of contributing nuclei is diminished further. However, this can be improved through the enrichment of said nuclei.

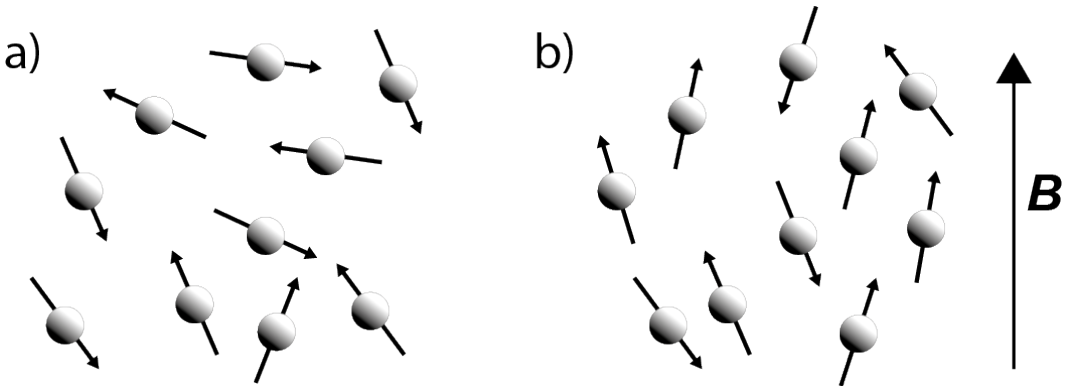

Figure 2.1: Net magnetisation for a series of spins where (a) no $\boldsymbol{B}$ is applied and no net magnetisation is observed, (b) where net magnetisation is observed along the applied $\boldsymbol{B}$ vector.

2.2 Solid State NMR Interactions

The total energy experienced by the nucleus is the sum of all the separate interaction Hamiltonians. These are summed by the total Hamiltonian ($\hat{\mathscr{H}}_{tot}$) for the system

$$\hat{\mathscr{H}}_{tot} = \hat{\mathscr{H}}_{ext} + \hat{\mathscr{H}}_{int} \tag{2.5}$$

$$= (\hat{\mathscr{H}}_Z + \hat{\mathscr{H}}_{RF}) + (\hat{\mathscr{H}}_{CS} + \hat{\mathscr{H}}_d + \hat{\mathscr{H}}_J + \hat{\mathscr{H}}_q + \hat{\mathscr{H}}_p) \tag{2.6}$$

Where $\hat{\mathscr{H}}_Z$ and $\hat{\mathscr{H}}_{RF}$ are results of the interactions derived from external factors such as the main magnetic field and with a radio frequency field, respectively. The remainder of these individual Hamiltonians are related to the system under study, therefore are called the internal interactions. When the applied magnetic field is altered by electrons surrounding the nucleus, the effect is called the chemical shift interaction ($\hat{\mathscr{H}}_{CS}$). Any direct dipole-dipole coupling between nuclei is described as $\hat{\mathscr{H}}_d$. The indirect dipole-dipole interaction ($\hat{\mathscr{H}}_J$), indicates the through bond interaction from the electron spins. The Quadrupolar interaction ($\hat{\mathscr{H}}_q$), is the description of how an electric field gradient (EFG) interacts with the nuclear quadrupole moment. With the Paramagnetic interaction ($\hat{\mathscr{H}}_p$) describing the magnetic perturbation caused by any isolated unpaired electrons in the system. For the purposes of this thesis, the Knight shift, which describes how conduction electrons introduce an extra effective magnetic field, will be disregarded, as it is not observed in any of the systems presented in this thesis.

2.3 External Interactions

2.3.1 Zeeman Interaction

When a single, isolated atomic nucleus with $I > 0$ is placed in an externally applied magnetic field ($\boldsymbol{B}$), the Zeeman Hamiltonian is given by

$$\hat{\mathscr{H}}_Z = -\hat{\boldsymbol{\mu}} \cdot \boldsymbol{B}. \tag{2.7}$$

However, convention states that the external magnetic field $\boldsymbol{B}$ is defined as the z axis. Applying this convention, the Hamiltonian can be written as:

$$\hat{\mathscr{H}}_Z = -\gamma \begin{pmatrix} \hat{I}_x \\ \hat{I}_y \\ \hat{I}_z \end{pmatrix} \cdot \begin{pmatrix} 0 \\ 0 \\ B_0 \end{pmatrix} = -\gamma B_0 \hat{I}_z \tag{2.8}$$

or

$$\hat{\mathscr{H}}_Z = \omega_0 \hat{I}_z \tag{2.9}$$

where the Larmor frequency (ω_0), which corresponds to the energy difference between nuclear spin states is given as

$$\omega_0 = -\gamma B_0. \tag{2.10}$$

If the static magnetic field is given in Tesla (T), we can give the Larmor frequency in terms of rad^{-1}. As the gyromagnetic ratio is an intrinsic property of the nucleus and is different for each nuclear isotope, the energy of the Zeeman Hamiltonian changes for the nuclear isotope under investigation. This Zeeman Hamiltonian can be used to calculate energy differences between nuclear spin states. Nuclei with spin I have $2I+1$ differing orientations, and Zeeman splitting is observed with this many levels separated by ω_0 (Figure 2.2), with the 1/2 to -1/2 transition being the central transition and others being the satellite transitions.

2.3.2 Frame Rotations

Visualisation of the motion of each interactions relative to the nuclear spin in solid state NMR can be complex. To aid explanation of how each interaction is related to the nucleus in three-dimensional space, the concept of frame rotation needs to be introduced. First the idea of the principle axis system (PAS) is introduced, where the spatial information of the interaction ($\boldsymbol{A}$) is diagonalised along the PAS axis

such as,

$$\boldsymbol{A}^{PAS} = \begin{pmatrix} A_{xx} & 0 & 0 \\ 0 & A_{yy} & 0 \\ 0 & 0 & A_{zz} \end{pmatrix}. \tag{2.11}$$

However, as the PAS frame is different for each interaction it can be best to rotate them into a common frame usually defined as the lab frame. In most cases the Zeeman interaction, and thus the applied magnetic field, is defined as the lab frame as it is generally the largest interaction present in a system. For this rotation between frames, the spatial information of a Hamiltonian needs to be represented. One method to obtain this is when the Hamiltonian is described in spherical tensor form:

$$\hat{\mathscr{H}} = C \sum_{l=0,2} \sum_{m=-l}^{l} A_{lm} \hat{\boldsymbol{T}}_{l-m}, \tag{2.12}$$

where C is a constant based on the interaction. [29] The spatial component (A) and the spin tensor ($\boldsymbol{T}$) are represented with the limit l being the rank and m being the order of the tensors. Under rotations, only the spacial term is affected.

The Euler angles ($\alpha,\ \beta,\ \gamma$) describe the rotations between these different frames. This is represented diagrammaticality by Figure 2.3 but is given by the rotation operator

$$\hat{R}(\alpha, \beta, \gamma) = \hat{R}_z(\alpha)\hat{R}_y(\beta)\hat{R}_z(\gamma), \tag{2.13}$$

which represents the three rotations applied, transforming the original frame ($x,\ y,\ z$) to the final frame ($x''',\ y''',\ z'''$). First a rotation is applied parallel to the z axis by the angle α, followed by a rotation along the y axis by β, and finally a rotation

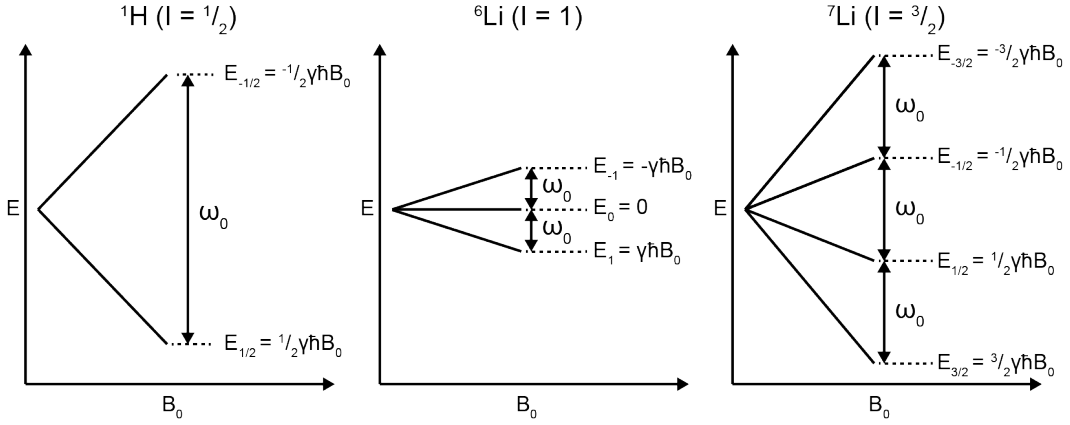

Figure 2.2: Nuclear Zeeman splitting for $I = \frac{1}{2}, 1, \frac{3}{2}$ nuclei (^{1}H, ^{6}Li and ^{7}Li).

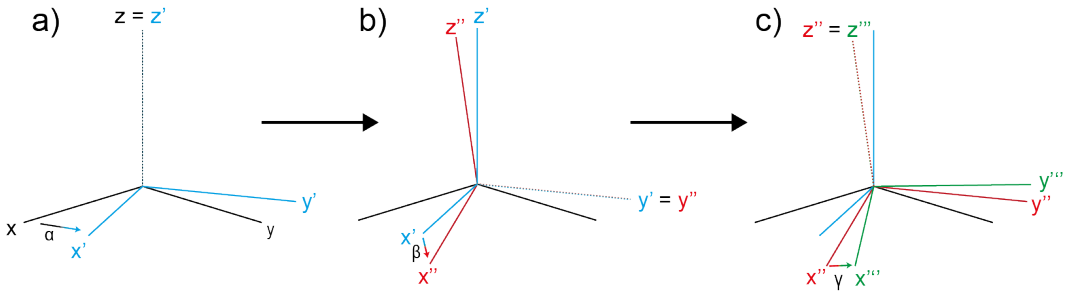

Figure 2.3: Representation of frame rotations using Euler angles (α, β, γ). The original frame (x, y, z) rotated to the final frame (x''', y''', z''') over three steps.

about the z axis by γ. The rotation operator in Equation 2.13 can be represented by a rotation matrix instead.

$$\hat{R}(\alpha,\beta,\gamma) = \begin{pmatrix} \cos\alpha & -\sin\alpha & 0 \\ \sin\alpha & \cos\alpha & 0 \\ 0 & 0 & 0 \end{pmatrix} \begin{pmatrix} \cos\beta & 0 & \sin\beta \\ 0 & 1 & 0 \\ -\sin\beta & 0 & \cos\beta \end{pmatrix} \begin{pmatrix} \cos\gamma & -\sin\gamma & 0 \\ \sin\gamma & \cos\gamma & 0 \\ 0 & 0 & 1 \end{pmatrix} \tag{2.14}$$

$$= \begin{pmatrix} \cos\alpha\cos\beta\cos\gamma - \sin\alpha\sin\gamma & -\cos\alpha\beta\sin\gamma - \sin\alpha\cos\gamma & \cos\alpha\sin\beta \\ \sin\alpha\cos\beta\cos\gamma + \cos\alpha\cos\gamma & -\sin\alpha\cos\beta\sin\gamma + \cos\alpha\cos\gamma & \sin\alpha\sin\beta \\ -\sin\beta\cos\gamma & \sin\beta\sin\gamma & \cos\beta \end{pmatrix} \tag{2.15}$$

This rotation operator can be applied to the spatial information in a tensor to transform the original orientation ($\boldsymbol{A}(x,y,z)$) to the new orientation ($\boldsymbol{A}(X,Y,Z)$) so that:

$$\boldsymbol{A}(X,Y,Z) = \boldsymbol{R}^{-1}(\alpha,\beta,\gamma)\cdot\boldsymbol{A}(x,y,z)\cdot\boldsymbol{R}(\alpha,\beta,\gamma) \tag{2.16}$$

2.3.3 The Radio Frequency Pulse

Observation of an NMR signal requires perturbation of equilibrium created by the application of the external magnetic field. This can be achieved through the application of a second applied magnetic field (B_1), that is smaller than the external magnetic field (B_0). The application of a B_1 field is achieved using an oscillating radio frequency (rf) pulse at frequency ω_{rf}. If the applied rf pulse is close to the Larmor frequency ($\omega_{rf} \approx \omega_0$), then a strong effect on the nuclear magnetisation is observed. The oscillation of the rf field adds a time dependence to the applied magnetic field so that

$$\boldsymbol{B}(t) = 2\boldsymbol{B}_1\cos(\omega_{rf}t + \phi) \tag{2.17}$$

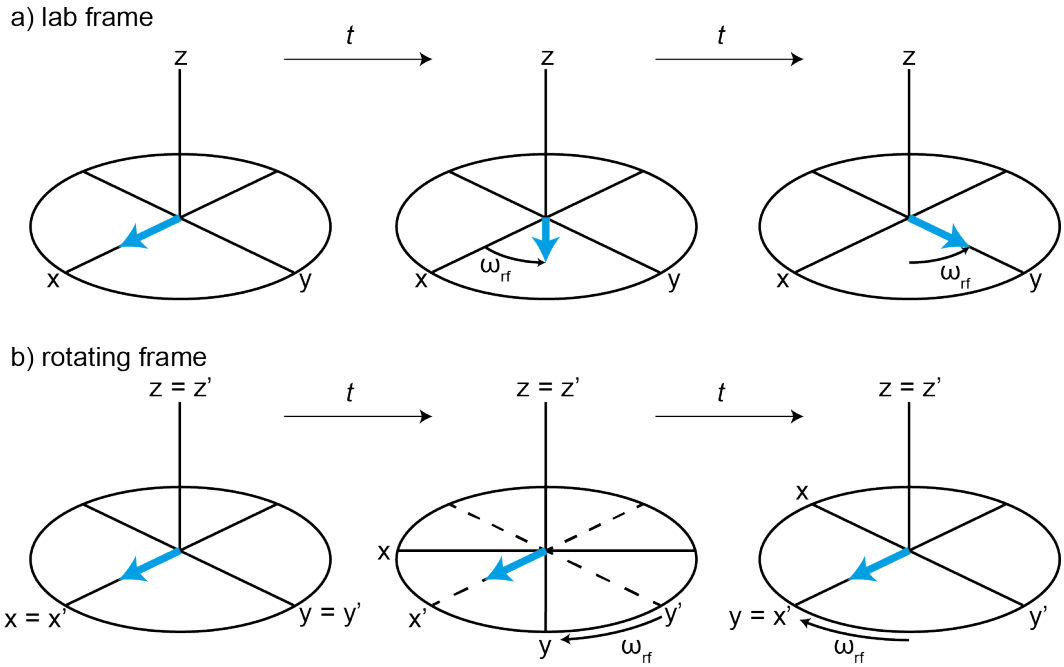

Figure 2.4: Diagrammatic representation of the applied *rf* magnetisation (blue arrow) over time in the (a) the lab frame. (b) rotating frame.

where ϕ is the phase of the *rf* pulse.

The *rf* interaction can be considered as simply another Zeeman interaction applied at a different vector. This results in a *rf* Hamiltonian being analogous to the Zeeman Hamiltonian so that

$$\hat{\mathscr{H}}_{rf} = -\gamma \hat{\boldsymbol{I}} \boldsymbol{B}(t) \tag{2.18}$$

$$= -2\gamma \hat{\boldsymbol{I}} \boldsymbol{B}_1 \cos(\omega_{rf} t + \phi) \tag{2.19}$$

While this represents the applied magnetic field as a vector, in practice the *rf* pulse is generally applied along the x-axis so that:

$$\hat{\mathscr{H}}_{rf} = -2\gamma \hat{I}_x B_1 \cos(\omega_{rf} t + \phi). \tag{2.20}$$

With the Zeeman Hamiltonian (Equation 2.9), the sum of the external interactions is then

$$\hat{\mathscr{H}}_{ext} = \omega_0 \hat{I}_z + 2\hat{I}_x \omega_1 \cos(\omega_{rf} t + \phi) \tag{2.21}$$

where ω_1 is the nutation frequency of the applied *rf* pulse i.e. the frequncy at which the pulse rotates the magnetisation around the x-axis (in this case).

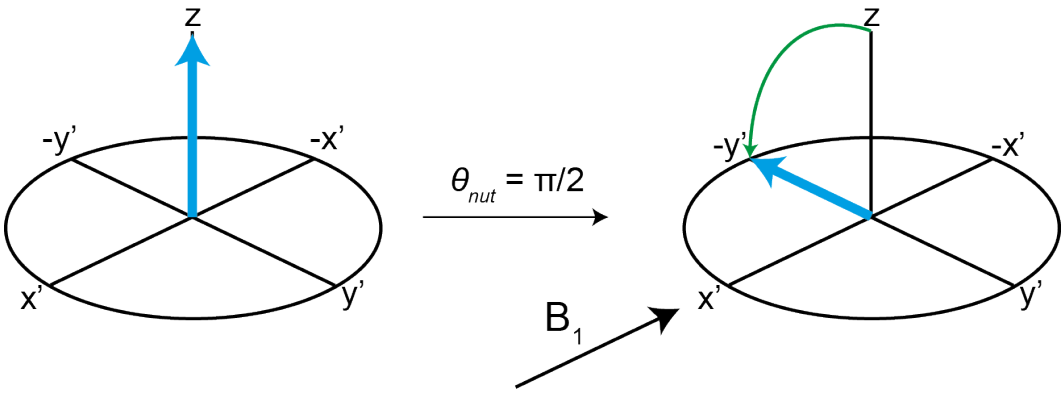

Figure 2.5: A representation of the bulk magnetisation (blue arrow) in the ROT frame when a B_1 field is applied where $\theta_{nut} = \pi/2$.

While representing the effect that the applied *rf* pulse has in this manner is useful, it can be useful to transform this interaction into the rotating frame (ROT). The rotating frame is often used to visualise the changes in magnetisation by offering a classical viewpoint into the system. Before transformation into the rotating frame, the resonant part of the *rf* field is rotating at ω_{rf} with respect to the lab frame (Figure 2.4(a)). However, by viewing the magnetisation from the rotating frame that rotates with ω_{rf} around B_0, it is possible to make the *rf* field (B_1) appear static while the x-y plane rotates around it (Figure 2.4(b)).

This removes the time dependence of $\hat{\mathscr{H}}_{ext}$ so that the Hamiltonian becomes:

$$\hat{\mathscr{H}}_{ext}^{rot} = -((\omega_0 - \omega_{rf})\hat{I}_z + 2\omega_1\hat{I}_x) \tag{2.22}$$

However, considering the case when $\omega_{rf} \approx \omega_0$ so that the $(\omega_0 - \omega_{rf})$ term approaches zero, the Hamiltonian becomes:

$$\hat{\mathscr{H}}_{ext}^{rot} = -2\omega_1\hat{I}_x \tag{2.23}$$

The application of B_1 now means that any spins aligned along the static magnetic field $\hat{I}_z$ now experience a rotation in the $y' - z'$ plane towards $-\hat{I}_y$. The amount that the *rf* pulse 'tips' or nutates the magnetisation is dependent on the duration of the pulse, τ_1 where the tipping angle θ_{nut} is determined as:

$$\theta_{nut} = \omega_1\tau_1 \tag{2.24}$$

A tipping angle of 90° ($\pi/2$) transfers the magnetisation so that it is aligned entirely in the $-\hat{I}_y$ direction (Figure 2.5). If the B_1 field is turned off, the magnetisation

will not remain fixed at this vector, however instead it will return to equilibrium in a finite time (see Sections 3.1.3 & 3.1.4). This rotating moment induces a current in an appropriately placed coil, and is the basis of the NMR experiment and called the free induction decay (FID).

2.4 Internal Interactions

2.4.1 Chemical Shielding Interaction

The observation that the exact frequency of the resonance, observed by NMR, is dependent on the chemical environment, transformed the technique from a simply interesting physical phenomenon, to a widely useful analytical technique [7,30]. This observation, termed the chemical shielding interaction, describes the local magnetic field around a nucleus due to changes in the electron orbitals around the investigated nucleus. The introduction of $\boldsymbol{B}_0$ on the system causes the electrons in these orbitals to orbit the nucleus generating a secondary induced magnetic field. Due to Lenz's law which states:

'The direction of current induced in a conductor by a changing magnetic field due to Faraday's law of induction will be such that it will create a magnetic field that opposes the change that produced it.' [31]

the induced magnetic field, from the electron orbitals, is applied opposite and acts in a way that opposes or 'shields' the applied magnetic field at the nucleus.

The Hamiltonian describing chemical shielding for a nuclear spin I is best described by:

$$\hat{\mathscr{H}}_{CS} = \gamma \hat{\boldsymbol{I}} \cdot \boldsymbol{\sigma} \cdot \boldsymbol{B} \tag{2.25}$$

where $\boldsymbol{\sigma}$ is the chemical shielding tensor. As stated in Section 2.3.2, all interactions can initially be defined in their PAS frame, so that the chemical shielding tensor is represented as,

$$\boldsymbol{\sigma}^{PAS} = \begin{pmatrix} \sigma_{xx} & 0 & 0 \\ 0 & \sigma_{yy} & 0 \\ 0 & 0 & \sigma_{zz} \end{pmatrix}. \tag{2.26}$$

However, to accurately describe this interaction in relation to the rest of the system it needs to be rotated into the LAB frame. This rotation is described by

Equation 2.16, where the tensor is transformed to

$$\boldsymbol{\sigma}^{LAB} = \begin{pmatrix} \sigma_{XX} & \sigma_{XY} & \sigma_{XZ} \\ \sigma_{YX} & \sigma_{YY} & \sigma_{YZ} \\ \sigma_{ZX} & \sigma_{ZY} & \sigma_{ZZ} \end{pmatrix} \tag{2.27}$$

where capital subscripts represent the tensor components now in the LAB frame. So now, the induced field observed at the nucleus and represented in the lab frame, includes both the main field and the shielding. This induced magnetic field ($\boldsymbol{B}^{ind}$) is represented by

$$\boldsymbol{B}^{ind} = (\mathbf{1} - \boldsymbol{\sigma}) \cdot \boldsymbol{B}_0 = \begin{pmatrix} 1 - \sigma_{XX} & -\sigma_{XY} & -\sigma_{XZ} \\ -\sigma_{YX} & 1 - \sigma_{YY} & -\sigma_{YZ} \\ -\sigma_{ZX} & -\sigma_{ZY} & 1 - \sigma_{ZZ} \end{pmatrix} \begin{pmatrix} 0 \\ 0 \\ B_0 \end{pmatrix} = \begin{pmatrix} -\sigma_{XZ} B_0 \\ -\sigma_{YZ} B_0 \\ (1 - \sigma_{ZZ}) B_0 \end{pmatrix} \tag{2.28}$$

where only the terms aligned along the magnetic field are of interest, and as the σ_{XZ} and σ_{YZ} components are second order terms they can be neglected. Therefore, only σ_{ZZ}, which is aligned along B_0, is of interest. This results in the chemical shielding Hamiltonian now given in the form

$$\hat{\mathscr{H}}_{CS} = \gamma \hat{I}_z \cdot \sigma_{ZZ} \cdot B_0 \tag{2.29}$$

To obtain the shielding tensor component σ_{ZZ}, the appropriate rotations from the PAS to the LAB frame needs to be performed. So σ_{ZZ} is then,

$$\sigma_{ZZ} = \sigma_{iso} + \frac{\Delta\sigma}{2} + \left[(3\cos^2\theta - 1) + \eta(\sin^2\theta \cos 2\phi) \right] \tag{2.30}$$

where the polar coordinates, θ and ϕ, are of the LAB frame represented in the PAS form of the tensor. The symmetry of the chemical shielding at the nucleus can now be expressed as these three terms:

$$\text{Isotropic Shielding Value} \qquad \sigma_{iso} = \frac{1}{3}(\sigma_{xx} + \sigma_{yy} + \sigma_{zz}) \tag{2.31}$$

$$\text{Shielding Anisotropy} \qquad \Delta\sigma = \sigma_{zz} - \sigma_{iso} \tag{2.32}$$

$$\text{Asymmetry} \qquad \eta = \frac{\sigma_{yy} - \sigma_{xx}}{\Delta\sigma} \tag{2.33}$$

It is common for combinations of σ_{iso}, $\Delta\sigma$, and η to be given instead of the three principle axis terms. For a single crystal of a compound placed in a magnetic field, all chemically identical nuclei would have the same orientation with respect to

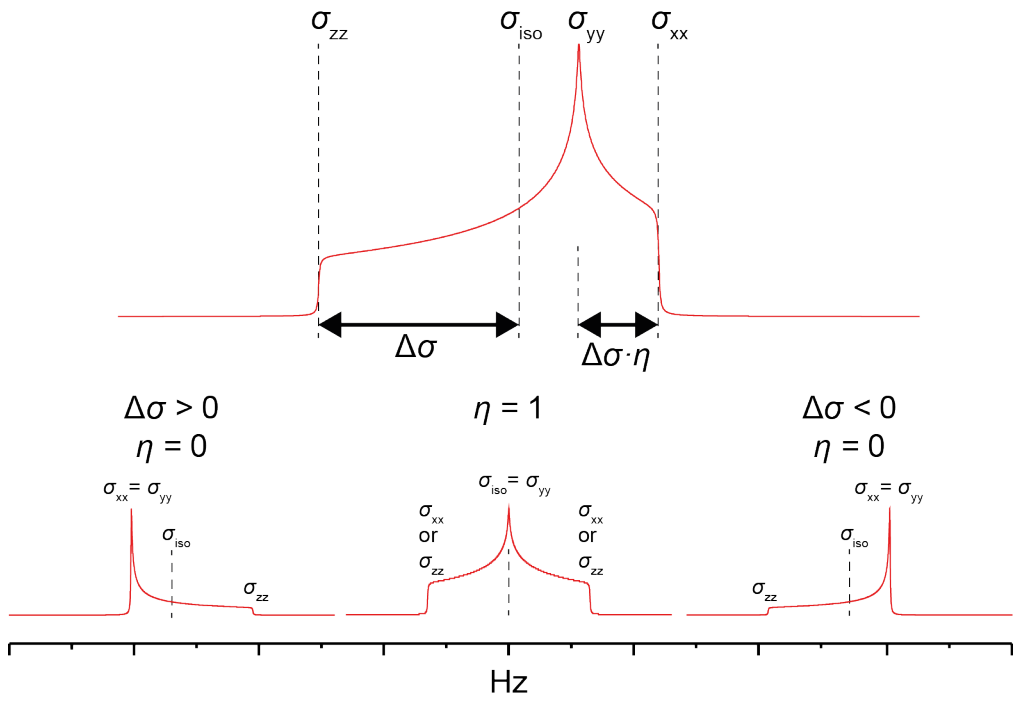

Figure 2.6: A summary of the CSA shielding parameters in a powdered static sample, where the resulting lineshapes are due to different values of $\Delta\sigma$ and η. By convention, the y-axis (intensity) is given in arbitrary units and not labelled. All spectra in this thesis will follow this convention.

B_0. This would result in a single peak appearing in the NMR spectrum, with the shift dependent on the θ and ϕ relative to B_0. However, a sufficiently fine powder with all possible orientations of crystallites, all possible orientations of θ and ϕ are observed. The result is a broad line formed by the overlapping of all the different crystallite orientations, with the lineshape dependent on $\Delta\sigma$ and η. This lineshape is represented diagrammaticality in Figure 2.6.

Throughout this thesis rather than using σ_{iso}, the isotropic chemical shift (δ_{iso}) will be used as an experimental measure of the shift. Experientially δ_{iso} is used as it normalises shielding of a sample (σ_{sample}) against a known shielding of reference sample (σ_{ref}) so that:

$$\delta_{iso} = \frac{\nu_{sample} - \nu_{ref}}{\nu_{ref}} \times 10^6 = \frac{\sigma_{ref} - \sigma_{sample}}{1 - \sigma_{ref}} \tag{2.34}$$

where ν_{sample} and ν_{ref} are the measured experimental frequency of σ_{sample} and σ_{ref} respectively at any given magnetic field. This results in δ_{iso}, which is given in parts per million (ppm), being field independent and therefore an ideal comparison for

NMR spectroscopists.

2.4.2 Dipolar Interaction

The dipolar interaction or the direct dipole-dipole interaction, describes the energy relationship between two magnetic nuclear spins in a system. As each nuclear spin generates its own magnetic field, each interacts with the other's generated magnetic field. The classical representation of the energy of two interacting dipoles, μ_j and μ_k is given by,

$$E^{dipolar} = \frac{\mu_0}{4\pi}\frac{1}{r^3}\left[\hat{\boldsymbol{\mu}}_j \cdot \hat{\boldsymbol{\mu}}_k - \frac{3(\hat{\boldsymbol{\mu}}_j \cdot \boldsymbol{r}_{jk})(\hat{\boldsymbol{\mu}}_k \cdot \boldsymbol{r}_{jk})}{r^2}\right] \tag{2.35}$$

which depends on the r the distance, and $\boldsymbol{r}_{jk}$ the vector between the centre of these two dipoles. The vacuum permeability is given by μ_0, which is otherwise known as the magnetic constant. Using Equation 2.2, the dipolar Hamiltonian can be given:

$$\hat{\mathscr{H}}_d = \frac{\mu_0}{4\pi}\frac{\gamma_j\gamma_k\hbar^2}{r^3}\left[\hat{\boldsymbol{I}}_j \cdot \hat{\boldsymbol{I}}_k - \frac{3(\hat{\boldsymbol{I}}_j \cdot \boldsymbol{r})(\hat{\boldsymbol{I}}_k \cdot \boldsymbol{r})}{r^2}\right] \tag{2.36}$$

however, it is common to express $\hat{\mathscr{H}}_d$ in Cartesian polar coordinates leading to the 'alphabet' expression,

$$\hat{\mathscr{H}}_d = \frac{\mu_0}{4\pi}\frac{\gamma_j\gamma_k\hbar^2}{r^3}\left(A + B + C + D + E + F\right) \tag{2.37}$$

where the A to F terms are represented by:

$$A = \hat{I}_{jz}\hat{I}_{kz}(3\cos^2\theta - 1) \tag{2.38}$$

$$B = -\frac{1}{4}\left[\hat{I}_{j+}\hat{I}_{k-} + \hat{I}_{j-}\hat{I}_{k+}\right](3\cos^2\theta - 1) \tag{2.39}$$

$$C = \frac{3}{2}\left[\hat{I}_{jz}\hat{I}_{k+} + \hat{I}_{j+}\hat{I}_{kz}\right]\sin\theta\cos\theta e^{-i\phi} \tag{2.40}$$

$$D = \frac{3}{2}\left[\hat{I}_{jz}\hat{I}_{k-} + \hat{I}_{ji}\hat{I}_{kz}\right]\sin\theta\cos\theta e^{+i\phi} \tag{2.41}$$

$$E = \frac{3}{4}\left[\hat{I}_{j+}\hat{I}_{k+}\right]\sin^2\theta e^{-2i\phi} \tag{2.42}$$

$$F = \frac{3}{4}\left[\hat{I}_{j-}\hat{I}_{k-}\right]\sin^2\theta e^{+2i\phi} \tag{2.43}$$

Where θ is the angle between the vector $\boldsymbol{r}_{jk}$ and the magnetic field aligned along the z-axis, and ϕ is the corresponding angle between $\boldsymbol{r}_{jk}$ and the y-axis (Figure 2.7) Additionally, $\hat{I}_+$ and $\hat{I}_-$ represent the raising and lowering operators ($\hat{I}_+ = I_x + iI_y$,

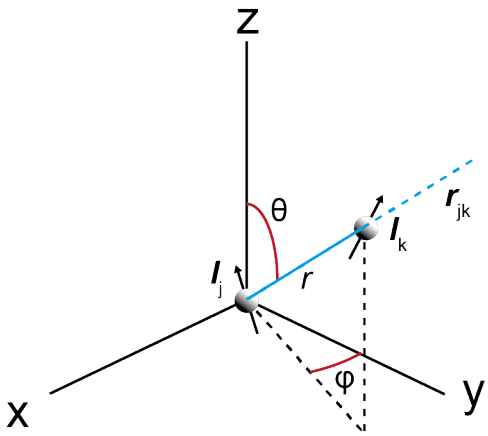

Figure 2.7: A representation of the distance (r) and angles (θ, ϕ) of two magnetic dipoles with respect to the axis which is represented in the LAB frame.

$\hat{I}_- = I_x - iI_y$), acting on both j and k.

To fully understand the dipolar effect on two coupled spins in terms of an NMR experiment, the interaction needs to be rotated into the ROT frame where the experiment is traditionally observed. This can be described using the rotation operator (Equation 2.16). However, application of this rotation on homonuclear dipolar coupling results in slight differences in physical effects when compared to heteronuclear dipolar coupling.

The application of this rotation operator to a homonuclear system results in,

$$\hat{\mathscr{H}}_d^{homo} = \frac{\mu_0}{4\pi}\frac{\gamma_j\gamma_k\hbar^2}{r^3}\left[(A+B) + R_z^{-1}(\phi)(C+D+E+F)R_z(\phi)\right] \tag{2.44}$$

The A and B terms commute with B_0 and are therefore unaffected by the frame transformation. However, the non-secular terms C, D, E, and F are transformed into the rotating frame and become time dependent (at frequency ω_0). Since the frequency dependence of the non-secular part of the Hamiltonian is much greater than the secular component, the non-secular terms can effectively be ignored giving a reduced form of $\hat{\mathscr{H}}_d^{homo}$:

$$\hat{\mathscr{H}}_d^{homo} = \frac{\mu_0}{4\pi}\frac{\gamma_j\gamma_k\hbar^2}{r^3}\left[\hat{I}_{jz}\hat{I}_{kz} - \frac{1}{4}\left(\hat{I}_{jx}\hat{I}_{kx} + \hat{I}_{jy}\hat{I}_{ky}\right)\right](3\cos^2\theta - 1) \tag{2.45}$$

For a heteronuclear case, we follow the same frame transformation procedure as applied for homonuclear systems. However, heteronuclear dipolar coupling has a key difference. Term B represents the transverse components of the local field due to I_k. While in a homonuclear case, I_k precesses at the same resonant frequency as term

I_j, where it can cause additional transitions and disturb the local magnetic field. However, it is unlikely for heteronuclear nuclei to posses similar enough resonant frequencies, therefore this term can also gains a time dependence in the rotating frame. The overall result from this is that the frame rotation only acts on the nuclear spin under observation, I_j so that the Hamiltonian becomes:

$$\hat{\mathscr{H}}_d^{hetero} = \frac{\mu_0}{4\pi}\frac{\gamma_j\gamma_k\hbar^2}{r^3}\left[(A) + R_z^{-1}(\phi)(B+C+D+E+F)R_z(\phi)\right] \tag{2.46}$$

Where the B term becomes non-secular. Substitution of the secular terms into the reduced Hamiltonian results in the heteronuclear dipolar coupling being:

$$\hat{\mathscr{H}}_d^{hetero} = \frac{\mu_0}{4\pi}\frac{\gamma_j\gamma_k\hbar^2}{r^3}\left[\hat{I}_{jz}\hat{I}_{kz}\right](3\cos^2\theta - 1) \tag{2.47}$$

Dipolar coupling is important for magnetisation transfer experiments. This includes the cross polarisation experiment described in Section 3.1.7.

2.4.3 Indirect Dipole-Dipole Interaction

The indirect dipole-dipole interaction, which is sometimes referred to as spin-spin, J-coupling, or scalar coupling, expresses the effect of bonding electrons between two or more nuclei directly bonded to each other. This through bond effect is observed when perturbations to the electrons in the bond exhibit a further magnetic field at the nucleus. The indirect dipole-dipole Hamiltonian which describes the coupling between two spins, $\hat{\boldsymbol{I}}_j$ and $\hat{\boldsymbol{I}}_k$, is given by:

$$\hat{\mathscr{H}}_j = 2\pi\boldsymbol{J}_{jk}\hat{\boldsymbol{I}}_j \cdot \hat{\boldsymbol{I}}_k \tag{2.48}$$

The second rank j-coupling tensor ($\boldsymbol{J}_{jk}$) is one of the few interactions given in Hz and is why the factor of 2π exists in $\hat{\mathscr{H}}_j$. As Equation 2.48 displays, no dependence on B_0 is observed. In liquids where the interaction is isotropic $\boldsymbol{J}_{jk}$ is equal to the average of the diagonal elements of the tensor:

$$J_{jk} = \frac{1}{3}\left(J_{xx}^{jk} + J_{yy}^{jk} + J_{zz}^{jk}\right) \tag{2.49}$$

However, unlike in solution, for solids, the source of this interaction is not isotropic and arises from three main sources; spin-orbital, spin-dipolar, and Fermi contact interactions. Where the main contribution is from the Fermi contact interaction, however in diamagnetic solids the size of the interaction is usually very small and obscured by other, larger interactions. For paramagnetic materials the

contribution from the Fermi contact interaction can be much larger, however this will be discussed below in Section 2.4.5.

2.4.4 Quadrupolar Interaction

Nuclei where the spin quantum number is greater than $\frac{1}{2}$ are considered quadrupolar nuclei. For the 88 out of 120 NMR active nuclear isotopes that have $I > \frac{1}{2}$, a non spherical charge distribution is observed around the nucleus, giving rise to the electric quadrupole moment (eQ). Along with nuclear spin, eQ is an intrinsic fundamental property of each quadrupolar nuclei. The quadrupolar interaction describes the coupling of this electric quadrupole moment with the electric field gradient (EFG) around the nucleus.

The EFG is dependent on the environment around the nuclei, resulting in the strength of the quadrupolar interaction being proportional to the size of this interaction. A consequence of this is that the observable size of the quadrupolar interaction can vary from effectively zero up to several MHz in size, depending on the environment around the nucleus. In many cases, due to the size of the electric quadrupole moment, the quadrupolar interaction tends to dominate most other internal interactions resulting in it being the dominant interaction observed. In a liquid NMR experiment this is not so much of an issue, as the anisotropic components are averaged out due to motional averaging. However, for solid state NMR where no significant motion is observed, the quadrupolar interaction results in a large anisotropic components of the interaction.

The basic form of the quadrupolar Hamiltonian can be expressed as:

$$\hat{\mathscr{H}}_q = \frac{eQ}{2I(2I-1)\hbar}\hat{\boldsymbol{I}} \cdot \boldsymbol{V} \cdot \hat{\boldsymbol{I}} \tag{2.50}$$

Where $\hat{\boldsymbol{V}}$ is a tensor for the EFG at the nuclear site. Again, this is generally displayed in the PAS where the vector along V is diagonal:

$$\boldsymbol{V} = \begin{pmatrix} V_{xx} & 0 & 0 \\ 0 & V_{yy} & 0 \\ 0 & 0 & V_{zz} \end{pmatrix} \tag{2.51}$$

By convention these are chosen such that

$$|V_{zz}| \geq |V_{yy}| \geq |V_{xx}| \tag{2.52}$$

is true. For the PAS vector, the Laplace equation ($V_{xx} + V_{yy} + V_{zz} = 0$) holds true,

so that only two of the vector components need to be known. It is customary to combine these components so that the principle field gradient is

$$eq = V_{zz} \tag{2.53}$$

and the asymmetry parameter

$$\eta_Q = \frac{V_{xx} - V_{yy}}{V_{zz}} \tag{2.54}$$

where $1 \geq \eta_Q \geq 0$.

When expressed in the PAS system Equation 2.50 now becomes

$$\hat{\mathscr{H}}_q = \frac{C_Q}{4I(2I-1)} \left[3I_z^2 - I(I+1)\frac{1}{2}\eta_Q \left(I_x^2 + I_y^2 \right) \right] \tag{2.55}$$

where C_Q, the quadrupolar coupling constant, results as a 'tidy up' of some of the terms, can be defined as

$$C_Q = \frac{e^2 qQ}{h} \tag{2.56}$$

and is used as a measure of the strength of the interaction, in Hz. Along with asymmetry η_Q, the spin I, and the isotropic shift δ_{iso} of the nucleus, the main factors which describe the size and position of the quadrupolar lineshape are defined. How these individually affect the static lineshape is represented diagrammaticality in Figure 2.8. It can be observed that in a perfectly symmetric environment such that the C_Q is small, the resulting quadrupolar Hamiltonian will be small and thus dwarfed by other interactions. Furthermore, from Equation 2.55 it is clearly shown that $\hat{\mathscr{H}}_q = 0$ when $I = 1/2$.

Before understanding the interaction of the quadrupolar Hamiltonian with other internal and external interactions it needs to be transformed into the rotating frame. However, it is more convenient for this transformation if $\hat{\mathscr{H}}_q$ is represented as a second rank irreducible spherical tensor:

$$\hat{\mathscr{H}}_q = \frac{C_Q}{2I(2I-1)} \sum_{q=-2}^{2} (-1)^q V^{(2,-q)} T^{(2,q)} \tag{2.57}$$

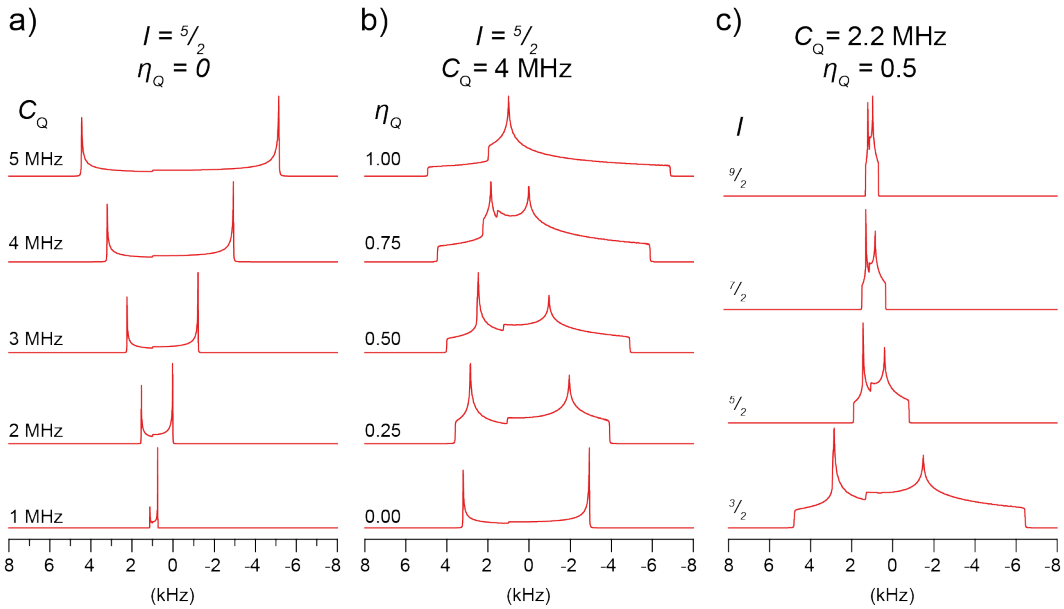

Figure 2.8: A representation of the quadrupolar lineshape when the following parameters are varied (a) C_Q, (b) η_Q and (c) I. For all parameters δ_{iso} is equivalent to 1 kHz.

Where the spherical tensor of $V^{(2,-q)}$ are represented in the Cartesian frame Σ by,

$$V^{(2,0)} = 3\sqrt{\frac{1}{6}}V_{zz} \tag{2.58}$$

$$V^{(2,1)} = -V_{xz} - iV_{yz} \tag{2.59}$$

$$V^{(2,-1)} = V_{xz} - iV_{yz} \tag{2.60}$$

$$V^{(2,2)} = \frac{1}{2}\left(V_{xx} - V_{yy}\right) + iV_{xy} \tag{2.61}$$

$$V^{(2,-2)} = \frac{1}{2}\left(V_{xx} - V_{yy}\right) - iV_{xy} \tag{2.62}$$

and for the spin tensor ($T^{(2,q)}$) as:

$$T^{(2,0)} = \frac{1}{6}\sqrt{6}[3\hat{I}_z^2 - I(I+1)] \tag{2.63}$$

$$T^{(2,1)} = -\frac{1}{2}\left(\hat{I}_z\hat{I}_+ + \hat{I}_+\hat{I}_z\right) \tag{2.64}$$

$$T^{(2,-1)} = \frac{1}{2}\left(\hat{I}_z\hat{I}_- + \hat{I}_-\hat{I}_z\right) \tag{2.65}$$

$$T^{(2,2)} = \frac{1}{2}\hat{I}_+\hat{I}_+ \tag{2.66}$$

$$T^{(2,-2)} = \frac{1}{2}\hat{I}_-\hat{I}_- \tag{2.67}$$

Using this notation the full representation of the spherical tensor in the Cartesian coordinate frame becomes

$$\hat{\mathscr{H}_q} = \frac{C_Q}{2I(2I-1)} \begin{Bmatrix} \frac{1}{3}\sqrt{6}\left[3\hat{I}_z^2 - I(I-1)\right] V^{(2,0)} + \left(\hat{I}_z\hat{I}_+ + \hat{I}_+\hat{I}_z\right) V^{(2,-1)} \\ -\left(\hat{I}_z\hat{I}_- + \hat{I}_-\hat{I}_z\right) V^{(2,1)} + \hat{I}_+^2 V^{(2,-2)} + \hat{I}_-^2 V^{(2,2)} \end{Bmatrix} \tag{2.68}$$

and since the EFG tensor is expressed in the PAS frame it can be seen that:

$$V_{PAS}^{(2,0)} = \sqrt{\frac{3}{2}}eq \tag{2.69}$$

$$V_{PAS}^{(2,\pm1)} = 0 \tag{2.70}$$

$$V_{PAS}^{(2,\pm2)} = \frac{1}{2}eq\eta_Q \tag{2.71}$$

While the quadrupolar interaction is large, it is still smaller than the Zeeman interaction, so it can be considered a perturbation of the Zeeman states. Frame rotation from the PAS frame to the rotating frame is applied with the rotation operator (Equation 2.16). Similarity to the dipolar interaction (Section 2.4.2), some terms are secular, and others are non-secular. The secular terms, known as the first order quadrupolar interaction, remain time independent and are given as:

$$\hat{\mathscr{H}_q^{(1)}} = \frac{eQ}{4I(2I-1)\hbar}\frac{\sqrt{6}}{3}\left(3\hat{I}_z^2 - I(I+1)\right) V^{(2,0)} \tag{2.72}$$

And the non-secular terms, known as the second order quadrupolar interaction, express a time dependence of the Larmor frequency (ω_0) of the investigated nucleus. Which can be given as:

$$\hat{\mathscr{H}_q^{(2)}} = -\frac{1}{\omega_0}\left[\frac{eQ}{4I(2I-1)\hbar}\right]^2 \begin{Bmatrix} 2V^{(2,-1)}V^{(2,1)}\hat{I}_z\left[4I(I+1) - 8\hat{I}_z^2 - 1\right] \\ +2V^{(2,-2)}V^{(2,-2)}\hat{I}_z\left[2I(I+1) - 2\hat{I}_z^2 - 1\right] \end{Bmatrix} \tag{2.73}$$

Which results in the total quadrupolar Hamiltonian for this perturbation as the sum of these two terms:

$$\hat{\mathscr{H}_q} = \hat{\mathscr{H}_q^{(1)}} + \hat{\mathscr{H}_q^{(2)}} \tag{2.74}$$

For C_q and η_Q to be displayed, so that an equation representative of the quadrupolar static NMR spectrum is represented, the $V^{(2,0)}$, $V^{(2,1)}$, $V^{(2,-1)}$, $V^{(2,2)}$ and $V^{(2,-2)}$ terms need to be described as Wigner rotations from the PAS to the ROT frame.

For this the following relationship is used,

$$V^{(2,i)} = \sum_{j=-2}^{2} D^{(2)}_{j,i}(\alpha, \beta, \gamma) V^{(2,j)}_{PAS} \tag{2.75}$$

Where the rotations of the three Euler angles α, β, γ are represented in Figure 2.3. In this case, it is worth noting that γ is not represented as B_0 is a symmetric axis for the spins. With the Wigner rotations listed by P. Man [32], $V^{(2,0)}$ can be given as

$$V^{(2,0)} = \sqrt{\frac{3}{2}} eq \left[\frac{1}{2}(3\cos^2\beta - 1) + \frac{1}{2}\eta_Q \sin\beta \cos 2\alpha \right] \tag{2.76}$$

so that the first order quadrupolar interaction can be given as

$$\hat{\mathscr{H}}^{(1)}_q = \frac{1}{3}\omega_Q \left[3\hat{I}^2_z - I(I+1) \right] \tag{2.77}$$

with:

$$\omega_Q = \frac{3C_Q}{4I(I-1)} \left[\frac{1}{2}(3\cos^2\beta - 1) + \frac{1}{2}\eta_Q \sin\beta \cos 2\alpha \right] \tag{2.78}$$

Likewise for the second order quadrupolar interaction,

$$V^{(2,1)}V^{(2,-1)} = -\frac{3}{2}e^2q^2 \left\{ \begin{array}{r} (-\frac{1}{3}\eta^2_Q \cos^2 2\alpha + 2\eta_Q \cos 2\alpha - 3)\cos^4\beta \\ +(\frac{2}{3}\eta^2_Q \cos^2 2\alpha - 2\eta_Q \cos 2\alpha - \frac{1}{3}\eta^2_Q + 3)\cos^2\beta \\ +\frac{1}{3}\eta^2_Q(1 - \cos^2 2\alpha) \end{array} \right\} \tag{2.79}$$

$$V^{(2,2)}V^{(2,-2)} = -\frac{3}{2}e^2q^2 \left\{ \begin{array}{r} (\frac{1}{24}\eta^2_Q \cos^2 2\alpha - \frac{1}{4}\eta_Q \cos 2\alpha + \frac{3}{8})\cos^4\beta \\ +(-\frac{1}{12}\eta^2_Q \cos^2 2\alpha + \frac{1}{6}\eta_Q - \frac{3}{3}\eta^2_Q + 3)\cos^2\beta \\ +\frac{1}{24}\cos^2 2\alpha + \frac{1}{4}\eta_Q \cos 2\alpha + \frac{3}{8} \end{array} \right\} \tag{2.80}$$

Since the quadrupolar interaction weakly perturbs the Zeeman interaction, a description of how $\hat{\mathscr{H}}^{(1)}_q$ and $\hat{\mathscr{H}}^{(2)}_q$ affects the Zeeman states can be formulated through standard perturbation theory. As noted in Section 2.3.1, when a nucleus of spin I is located in a static magnetic field, it splits into $2I+1$ energy levels ($|m\rangle$). Where the energy of the splitting of the Zeeman states can be defined as,

$$\langle m| \hat{\mathscr{H}}_Z |m\rangle = -m\omega_0 \tag{2.81}$$

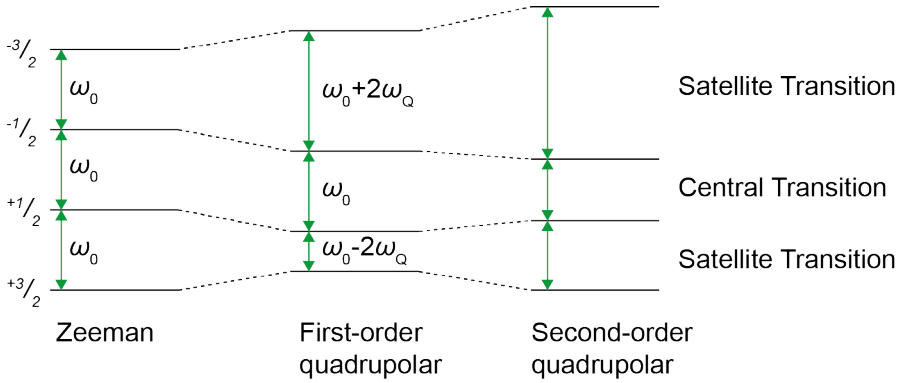

Figure 2.9: Energy level diagram for a spin $\frac{3}{2}$ nucleus

where the difference between two neighbouring energy states, m and $m-1$, expressed in terms of angular velocity is:

$$\omega^{(z)}_{m-1,m} = \langle m-1|\,\hat{\mathscr{H}}_Z\,|m-1\rangle - \langle m|\,\hat{\mathscr{H}}_Z\,|m\rangle = \omega_0 \tag{2.82}$$

In a similar fashion, the first order quadrupolar interaction shifts energy levels $|m\rangle$ by an amount

$$\langle m|\,\hat{\mathscr{H}}^{(1)}_q\,|m\rangle = \frac{1}{3}\omega_Q[3m^2 - I(I+1)] \tag{2.83}$$

where the difference in energy levels caused by the first order quadrupolar shift ($\omega^{(1)}_{m-1,m}$), when associated with the transition $(m-1, m)$ is:

$$\begin{aligned}\omega^{(1)}_{m-1,m} =& \langle m-1|\,\hat{\mathscr{H}}^{(1)}_q\,|m-1\rangle - \langle m|\,\hat{\mathscr{H}}^{(1)}_q\,|m\rangle \\ =& \omega_Q(1-2m)\end{aligned} \tag{2.84}$$

This results in a first order perturbation of the energy transitions which is dependent on ω_Q. It is worth noting that the transition between the $-1/2$, and $1/2$ spin states remains at the same energy difference as the Zeeman interaction and is called the central transition. The other transitions that do exhibit this perturbation with ω_Q are called the satellite transitions. This first order perturbation on the Zeeman levels is shown in Figure 2.9 for a spin 3/2 nucleus.

Before addressing $\hat{\mathscr{H}}^{(2)}_q$ as a perturbation of the Zeeman interaction, it can be noted from Equation 2.73 that the second order quadrupolar Hamiltonian has an inverse dependence on ω_0. Therefore, upon increasing the magnetic field the

strength of $\hat{\mathscr{H}}_q^{(2)}$ is reduced. The description of this shift is

$$\langle m|\,\hat{\mathscr{H}}_q^{(2)}\,|m\rangle = -\frac{1}{\omega_0}\left[\frac{eQ}{4I(2I-1)\hbar}\right]^2 \left\{\begin{array}{l} 2V^{(2,-1)}V^{(2,1)}m\left[4I(I+1)-8m^2-1\right] \\ +\,2V^{(2,-2)}V^{(2,-2)}m\left[2I(I+1)-2m^2-1\right]\end{array}\right\} \tag{2.85}$$

and the second order quadrupolar shift contribution ($\omega^{(2)}_{m-1,m}$), is:

$$\begin{aligned}\omega^{(2)}_{m-1,m} &= \langle m-1|\,\hat{\mathscr{H}}_Z\,|m-1\rangle - \langle m|\,\hat{\mathscr{H}}_Z\,|m\rangle \\ &= -\frac{1}{\omega_0}\left[\frac{eQ}{4I(2I-1)\hbar}\right]^2 \left\{\begin{array}{l} V^{(2,-1)}V^{(2,1)}\left[24m(m-1)-4I(I+1)+9\right] \\ +\,\frac{1}{2}V^{(2,-2)}V^{(2,-2)}\left[12m(m-1)-4I(I+1)+6\right]\end{array}\right\}\end{aligned} \tag{2.86}$$

Therefore, for any given transition $(m-1,m)$, the combined contribution of the Zeeman, first and second order quadrupolar interactions is:

$$\omega_{m-1,m} = \omega_0 + \omega^{(1)}_{m-1,m} + \omega^{(2)}_{m-1,m} \tag{2.87}$$

Where substitutions of $V^{(2,1)}V^{(2,-1)}$ and $V^{(2,2)}V^{(2,-2)}$ give the shift of the central line

$$\begin{aligned}\omega^{(2)Static}_{-1/2,1/2} = -\frac{1}{6\omega_0}\left[\frac{3C_Q}{2I(2I-1)}\right]^2 [I(I+1)-\frac{3}{4}] \\ \times[A(\alpha,\eta_Q)\cos^4\beta + B(\alpha,\eta_Q)\cos^2\beta + C(\alpha,\eta_Q)]\end{aligned} \tag{2.88}$$

Here:

$$A(\alpha,\eta_Q) = -\frac{27}{8} + \frac{9}{4}\eta_Q\cos 2\alpha - \frac{3}{8}(\eta_Q\cos 2\alpha)^2 \tag{2.89}$$

$$B(\alpha,\eta_Q) = \frac{30}{8} - \frac{1}{2}\eta_Q^2 - 2\eta_Q\cos 2\alpha + \frac{3}{4}(\eta_Q\cos 2\alpha)^2 \tag{2.90}$$

$$C(\alpha,\eta_Q) = -\frac{3}{8} + \frac{1}{3}\eta_Q^2 - \frac{1}{4}\eta_Q\cos 2\alpha - \frac{3}{8}(\eta_Q\cos 2\alpha)^2 \tag{2.91}$$

An assumption was made in Section 2.3.3 that the *rf* pulse is larger than the internal interactions present in the system. This is not always the case for the quadrupolar Hamiltonian, where it can be roughly the same size or bigger than the *rf* pulse. When the quadrupolar interaction is larger than the *rf* frequency (ω_1), interferences can can occur between the interactions. The result of this is that for a small quadrupolar interaction, such as a perfectly octahedral environment around the nucleus, the nutation is unaffected and is what would be called a selective pulse.

However, when $\omega_Q > \omega_1$ the quadrupolar interaction dominates the *rf* pulse leading to faster excitation (by a factor of $I + 1/2$), where this would now be referred to as a non selective pulse. When $\omega_Q >> \omega_1$, a discrepancy in the excitation of sites is still observed. Therefore experimentally, in most quadrupolar systems a 30° non-selective pulse is generally used as it can be shown to give almost quantitative results.

2.4.5 Paramagnetic Interaction

Investigations into paramagnetic materials present an interesting challenge compared to diamagnetic compounds. A material is deemed paramagnetic when the magnetic susceptibility (χ) is positive. If χ is negative, then the material is dominated by diamagnetism. Positive χ is a result of the presence of a localised unpaired electron which upon interaction with B_0 forms an internal induced magnetic field parallel to this applied magnetic field.

The paramagnetic Hamiltonian $\hat{\mathscr{H}_p}$ can generally be described as the sum of two distinct interactions:

$$\hat{\mathscr{H}_p} = \hat{\mathscr{H}^C} + \hat{\mathscr{H}^D} \tag{2.92}$$

where $\hat{\mathscr{H}^C}$ is the through bond or Fermi contact interaction and $\hat{\mathscr{H}^D}$ is the through space or electron-nuclear dipolar interaction. These interactions contain contributions to the isotropic shift and thus it can be considered that these contributions are added to the diamagnetic shift $\delta^{diamagnetic}$ i.e. the shift that would be measured if the material contained no unpaired electrons

$$\delta^{measured} = \delta^{diamagnetic} + \delta^{hyperfine} \tag{2.93}$$

where

$$\delta^{hyperfine} = \delta^{contact} + \delta^{dipolar} \tag{2.94}$$

with $\delta^{contact}$and $\delta^{dipolar}$ being the contribution from both the Fermi contact and the electron-nuclear dipolar interactions respectively.

To understand how the interaction between the nucleus (I) and the electron (S) forms this paramagnetic Hamiltonian $\hat{\mathscr{H}_p}$, contributions to $\delta^{hyperfine}$ from the magnetic susceptibility needs to be understood. For a given group of spins placed in an external magnetic field the induced magnetic field per unit volume, the magnetisation per unit volume M can be described as

$$M = \frac{\mu_{ind}}{V} = \frac{1}{\mu_0}\chi_V B_0 \tag{2.95}$$

where the applied magnetic field is proportional to the magnetic susceptibility per unit volume χ_V and the inverse of the magnetic constant μ_0. Therefore, its possible to calculate the magnetic susceptibility per mole χ_M by

$$\chi_M = V_M \chi_V = V_M \frac{\mu_0 M}{B_0} \tag{2.96}$$

where V_M is the molar volume. This can be further defined as the magnetic susceptibility per molecule χ being divided by Avogadro's constant N_A:

$$\chi = \frac{\chi_M}{N_A}. \tag{2.97}$$

From Equation 2.95 and from $\mu_{ind} = N_A \langle \mu \rangle V / V_M$, χ can be expressed as:

$$\chi = \frac{\mu_0 \langle \mu \rangle}{B_0} \tag{2.98}$$

where $\langle \mu \rangle$ is the average induced magnetic moment per particle.

The relaxation and precession dynamics of the electron spin S are several orders of magnitude faster than the NMR timescale. This causes the electron spin S to be averaged over several Zeeman states giving rise to the Curie spin $\langle S_z \rangle$

$$\langle S_z \rangle = \frac{\sum\limits_{M_s} M_S \left\{ \frac{-g_e \mu_B M_s B_0}{k_B T} \right\}}{\sum\limits_{M_s} \left\{ \frac{-g_e \mu_B M_s B_0}{k_B T} \right\}} \tag{2.99}$$

$$\langle S_\pm \rangle = 0 \tag{2.100}$$

With the high temperature approximation this simplifies to

$$\langle S_z \rangle = -\frac{g_e \mu_B B_0}{3 k_B T} S(S+1). \tag{2.101}$$

As the induced magnetic moment per particle is proportional to the curie spin $\langle \mu \rangle = -\mu g_e \langle S_z \rangle$ [33] therefore the Curie moment can be determined

$$\langle \mu_s \rangle = \frac{g_e^2 \mu_B^2 S(S+1)}{3 k_B T} B_0. \tag{2.102}$$

Using Equation 2.98, the Curie moment can be expressed in terms of the

isotropic molecular magnetic susceptibility (Equation 2.102)

$$\chi_{iso} = \mu_0 \frac{g_e^2 \mu_B^2 S(S+1)}{3k_B T}, \tag{2.103}$$

and in terms of the Curie spin (Equation 2.101)

$$\langle S \rangle = \langle S_z \rangle = -\frac{\chi_{iso}}{\mu_0 \mu_B g_e} B_0. \tag{2.104}$$

The Hamiltonian of the through bond coupling between the nucleus I and the electron S is proportional to the s orbital for the atom containing the spin I

$$\hat{\mathscr{H}}^C = A\chi \cdot \hat{I} \tag{2.105}$$

where the through bond coupling of the nucleus to the average electron spin is described by the hyperfine Fermi constant A is

$$A = \frac{\mu_0}{3S} \hbar g_e \mu_B \gamma_I \rho_s \tag{2.106}$$

where the γ_I is the nuclear gyromagnetic ratio. The gyromagnetic ratio and magnetic moment of the electron (g-value) is represented by g_e and the spin density at the nucleus, ρ_s which is described by the sum i of the spin density for the ith nuclear orbitals

$$\rho_s = \sum_i [|\Psi_i^-(0)|^2 - |\Psi_i^+(0)|^2] \tag{2.107}$$

with the positive $|\Psi_i^-(0)|^2$ and $|\Psi_i^+(0)|^2$ negative spin densities respectively.

To determine the shift contribution of the Fermi contact $\delta^{contact}$ towards the hyperfine shift $\delta^{hyperfine}$ the energy of the contact interaction needs to be related to the size and strength of the magnetic field

$$\delta^{contact} = \frac{E_{contact}}{\gamma_I \hbar I_z B_0}, \tag{2.108}$$

where $E_{contact}$ is the energy for this isotropic hyperfine coupling

$$E_{contact} = A I_z \langle S_z \rangle . \tag{2.109}$$

Thus, when the Curie spin (Equation 2.104) and the isotropic magnetic susceptibility (Equation 2.103) are substituted in, the Fermi contact interaction is:

$$\delta^{contact} = A \frac{g_e \mu_B S(S+1)}{3\gamma_I \hbar k_B T} \tag{2.110}$$

From this it is clear where the inverse reliance on temperature for this interaction originates. If the electronic field at the paramagnetic nucleus is anisotropic, the g factor should be replaced by the term $\frac{1}{3}(g_{\parallel} + 2g_{\perp})$ which represents the parallel $g_{\parallel}$ and perpendicular $g_{\perp}$ components, thus representing an axially symmetric tensor. In this case the magnetic susceptibility has an orientation dependence relative to the external magnetic field. Therefore, the average induced magnetic field represented in Equation 2.98 instead becomes

$$\langle \hat{\mu} \rangle = \frac{\hat{\chi}\hat{B}_0}{\mu_0} \tag{2.111}$$

The second part of the paramagnetic Hamiltonian, the electron nuclear interaction ($\hat{\mathscr{H}}^D$), can be described as analogous to the dipolar interaction discussed in Section 2.4.2. The determination of the interaction energy is fundamentally the same as Equation 2.35 in Section 2.4.2. However, this change from a nuclear-nuclear to an electron nuclear interaction produces a few key differences. Firstly the distance between the electron and the nucleus r can be approximated by the distance from the nucleus to the metal centre. This approximation allows us to ignore any fractional electron density covered by the Fermi contact shift. By displaying the dipolar Hamiltonian $\hat{\mathscr{H}}_d$ from Equation 2.36 in terms of the nucleus and the electron by the taking magnetic moment of the nucleus as described in Section 2.1.1

$$\hat{\boldsymbol{\mu}} = \gamma \hat{\boldsymbol{I}} \tag{2.2}$$

and describing the magnetic moment of the electron $\hat{\mu}$ as the averaged induced electron magnetic moment $\langle \hat{\mu} \rangle$ in the magnetic field. This Hamiltonian now represents the electron nuclear interaction

$$\hat{\mathscr{H}}^D = -\frac{\mu_0}{4\pi}\left[\frac{3(\hbar\gamma_I \hat{\boldsymbol{I}} \cdot \boldsymbol{r})(\langle \hat{\boldsymbol{\mu}} \rangle \cdot \boldsymbol{r})}{r^5} - \frac{\hbar\gamma_I \hat{\boldsymbol{I}} \langle \hat{\boldsymbol{\mu}} \rangle}{r^3}\right]. \tag{2.112}$$

Therefore, by using Equations 2.97 & 2.111 and describing $\hat{\boldsymbol{I}} = \hat{I}_{\kappa}\kappa$ since the nucleus is quantized along the direction of the external magnetic field κ. The Hamiltonian can be rewritten as

$$\hat{\mathscr{H}}^D = -\frac{\hbar\gamma_I B_0}{4\pi r^5}\hat{I}_k\kappa \cdot \left[3\boldsymbol{r}(\boldsymbol{r} \cdot \boldsymbol{\chi}) - r^2\boldsymbol{\chi}\right] \cdot \kappa. \tag{2.113}$$

A second rank magnetic susceptibility tensor $\boldsymbol{\sigma}_p$ can then be defined as

$$\boldsymbol{\sigma}_p = 3\boldsymbol{r}(\boldsymbol{r} \cdot \boldsymbol{\chi}) - r^2\boldsymbol{\chi} \tag{2.114}$$

which results in the electron nuclear Hamiltonian having the form

$$\hat{\mathscr{H}}^D = -\frac{\hbar\gamma_I}{4\pi r^5}\hat{\boldsymbol{I}}\cdot\boldsymbol{\sigma}_p\cdot\boldsymbol{B}. \tag{2.115}$$

resulting in a remarkable similarity to the chemical shielding Hamiltonian

$$\hat{\mathscr{H}}_{CS} = \gamma\hat{\boldsymbol{I}}\cdot\boldsymbol{\sigma}\cdot\boldsymbol{B}. \tag{2.25}$$

And as with CSA (Section 2.4.1), the paramagnetic interaction is observed to scale linearly with magnetic field.

To transform this interaction in the LAB frame, it can be easier for $\hat{\mathscr{H}}^D$ to be expressed as PAS frame in spherical tensor form:

$$\hat{\mathscr{H}}^D = \sum_{m=-1,0,1} D_{2,0}d^2_{0m}(\beta)T_{2,m} \tag{2.116}$$

Where $d^2_{0m}(\beta)$ is the reduced Wigner matrix element, with β being the angle between the PAS and the magnetic field. $D_{2,0}$ is the only non-zero component of the dipolar tensor $\boldsymbol{D}$:

$$D_{2,0} = \sqrt{6}\frac{\hbar\gamma_I\mu_B g_e}{4\pi r^3} \tag{2.117}$$

and the spin operator terms ($T_{2,m}$), in a large applied magnetic field are:

$$T_{2,0} = \frac{2}{3}I_zB_0 - \frac{\sqrt{2}}{3}\chi_{0,0}I_zB_0 \tag{2.118}$$

$$T_{2,\pm1} = \mp\frac{1}{2}\langle S_\pm\rangle I_z = 0 \tag{2.119}$$

$$T_{2,\pm2} = 0 \tag{2.120}$$

Where only the terms that commute with I_z are retained. The dipolar Hamiltonian then becomes

$$\hat{\mathscr{H}}^D = \left\{\frac{2}{3}D_{2,0}\chi_{2,0} - \frac{1}{2}\left(D_{2,1}\chi_{2,-1} + D_{2,-1}\chi_{2,1}\right) - \frac{\sqrt{2}}{3}D_{2,0}\chi_{0,0}\right\}I_zB_0 \tag{2.121}$$

where $\chi_{2,n}$ are represented by:

$$\chi_{0,0} = -\sqrt{3}\chi_{iso} \tag{2.122}$$

$$\chi_{0,\pm1} = \sqrt{\frac{2}{3}}\Delta\chi_{ax} \tag{2.123}$$

$$\chi_{0,\pm2} = \frac{3}{4}\frac{\Delta\chi_{rh}}{\Delta\chi_{ax}} \tag{2.124}$$

where the axial and rhombic components of the tensor $\boldsymbol{\chi}$, in the PAS frame, are:

$$\chi_{ax} = \chi_{zz} - \frac{\chi_{xx} + \chi_{yy}}{2} \tag{2.125}$$

$$\chi_{rh} = \chi_{xx} - \chi_{yy} \tag{2.126}$$

Equation 2.121 can then be simplified to: [27]

$$\hat{\mathscr{H}}^D = \left\{ \delta^{dipolar} + \sqrt{\frac{1}{6}}\Delta\sigma_p(3cos^2\beta - 1) \right\} I_z B_0 \tag{2.127}$$

where the shift anisotropy is expressed as

$$\Delta\sigma_p = \frac{\chi_{iso}}{\hbar\gamma_I r^3} \tag{2.128}$$

and the dipolar shift term is:

$$\delta^{dipolar}\frac{1}{12\pi r^3}\left\{ \Delta\chi_{ax}(3\cos^2\theta - 1) + \frac{3}{2}\Delta\chi_{rh}\sin^2\theta\cos 2\varphi \right\} \tag{2.129}$$

where the angles θ and φ describe the orientation of the nuclear spin relative to the PAS of $\boldsymbol{\chi}$, as this component solely relies on the spins relative to each other in the molecule.

2.5 Magic Angle Spinning

In liquid state NMR the rapid tumbling of molecules over a short time-scale, averages out all the anisotropic components of the internal interactions. This results in the anisotropic components of many interactions rarely being observed in the liquid state. However, in solids there is not enough molecular motion present for the anisotropic components to be averaged out. Furthermore, in many cases, samples are polycrystalline in nature, representing all possible orientations, resulting in broadening of the spectral lines. While it is possible to successfully analyse these

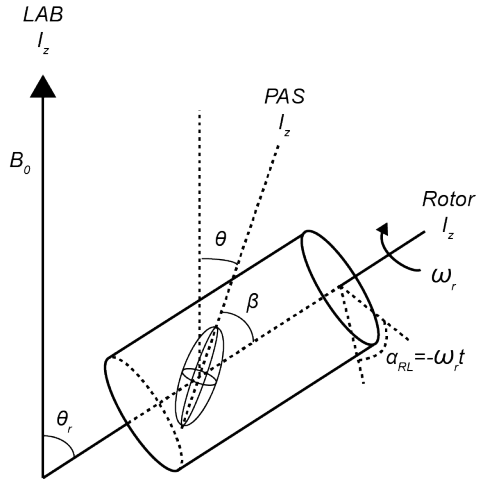

Figure 2.10: A representation of the rotation of a sample relative to the B_0 field in a MAS experiment. Where θ is the original rotation between the PAS and LAB frames, θ_r is the rotation between the LAB and MAS frames, β is the rotation from the PAS to the MAS, and α_{RL} is the physical rotation of the sample at frequency ω_r.

spectra in some simple cases, many systems investigated consist of many chemically inequivalent sites where it may be difficult, if not impossible, to distinguish spectral features and gain any meaningful information from the spectrum.

Faced with this, Andrew, Bradbury and Eades [9, 34] demonstrated that rotating a solid sample at the so called 'magic angle' removed part of the dipolar broadening observed in the spectrum. The remaining dipolar broadening appeared at multiples of the applied rotation speed (in Hz), and is termed the spinning sidebands. Since then, this technique has been employed as a technique coined 'Magic Angle Spinning' (MAS).

For many interactions in solids the orientation dependence has been shown to have a $3\cos^2\theta - 1$ term, where θ is the angle between the PAS system and the Lab frame (Figure 2.10). In a sufficiently powdered sample, θ consists of all possible orientations relative to the LAB frame, resulting in the large anisotropic lineshapes observed. However, if a sample is physically rotated about an axis, the average orientation of its anisotropic interactions will now become the same as the rotation axis. For MAS the angle applied is θ_r, and the average of the orientation dependence can now be shown to be,

$$\left\langle 3\cos^2\theta - 1 \right\rangle = \frac{1}{2}\left(3\cos^2\theta_r - 1\right)\left(3\cos^2\beta - 1\right) \tag{2.130}$$

where β is the angle between the PAS and MAS frames. These angles are represented

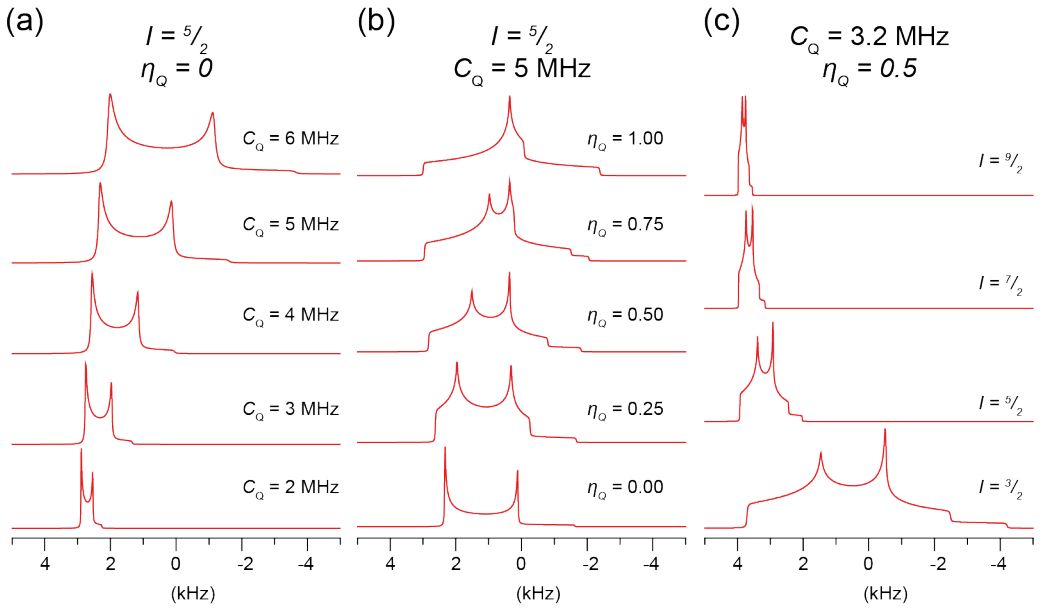

Figure 2.11: A representation of the quadrupolar lineshape under MAS when $\theta_r = 54.74°$ when the following parameters are varied (a) C_Q, (b) η_Q and (c) I. For all parameters δ_{iso} is equivalent to 1 kHz.

in Figure 2.10, with a α_{RL} being the axis around which the sample physically rotates at frequency ω_r.

This $3\cos^2\theta - 1$ term is called the Legendre polynomial and can be solved so that $3\cos^2\theta - 1 = 0$. This condition is met when the angle is set at 54.74 ° Therefore, physical rotation of a sample at an angle of θ_r which now solves this Legendre polynomial, and reduces the anisotropic first order components to zero. However, this is only true when the MAS speed much greater than the size of the anisotropy in Hz($\Delta\omega$). In most cases, the anisotropy is equal or much larger than the achievable ω_r, resulting in residual broadening remaining in the spectral lines and generating additional resonances at multiples of ω_r distance apart from δ_{iso} refereed to as the spinning side-bands. For the dipole-dipole interaction, some of this residual broadening can be removed through decoupling (Section 3.1.6), however for the paramagnetic interaction this is not possible. One solution to this can be deduced from Equation 2.127, where it can be observed that through a reduction of the magnetic field strength the impact of this interaction can be minimised.

However, through spinning at the magic angle it is only possible to fully remove the first order components of the interactions. Higher order anisotropic components, such as the second order quadrupolar interaction are only partially reduced by MAS, resulting in the observation of the lineshapes in Figure 2.11. However, this

higher order effect can be shown to have a dependence on the fourth order Legendre polynomial ($P_4(\cos\theta) = 35\cos^4\theta - 30\cos^\theta + 3$). This has two solutions so that $P_4(\cos\theta) = 0$, $30.6\,^\circ$ and $70.1\,^\circ$. Therefore, by spinning at a one of these angles a large proportion of the second order quadrupolar interaction would be removed. However, only spinning at this angle would not solve the 2nd order Legendre polynomial ($3\cos^2\theta - 1$), resulting in the first order lineshapes from interactions being observed. To combat this, techniques such as double rotation (DOR) and dynamic angle spinning (DAS) exist, simultaneously rotating at both the magic angle and one of the second order quadrupolar angles, reducing both the first and second order terms to zero. However, this is difficult to implement experimentally and will not be covered in this work.

Chapter 3

Experimental Methods

3.1 NMR Spectroscopy

The theory of solid state NMR has been explained in the previous chapter. To conduct NMR experiments this needs to be explained in the context of the techniques used. This section has primarily been sourced from the following literature: [19–21, 32, 35]

3.1.1 The NMR Spectrometer

In principle the basic components of a NMR spectrometer do not vary much between instruments. A simple overview of the NMR components are discussed below, however more detailed descriptions can be found in the following sources [19, 20, 36].

To provide the high static fields required for the Zeeman transitions in NMR, most modern spectrometers utilise a superconducting magnet. Employing a wound superconducting wire which is immersed in a liquid helium bath ensures the material is below the critical temperature, so that once charged with current it will run indefinitely as long as the cryogenic temperatures are maintained. Superconducting magnets are chosen for their capabilities to not only produce a high field but the high magnetic field homogeneity and high stability required for NMR. Other methods to produce magnetic fields such as electromagnets, or permanent iron core magnets, either cannot produce magnetic fields stable enough, require a large continuous power draw, or do not have the field homogeneity required for high resolution NMR.

While the magnetic field homogeneity produced by superconducting magnets is already high, to reach requirements for high resolution NMR (typically 2×10^{-9} T over a volume of $1\,\mathrm{cm}^3$), small adjustments to the magnetic field need to be made. This adjustment of the magnetic field is referred to as shimming, and typically is

achieved through two means; a cryogenic shim set and a room temperature shim set. Both cryogenic and room temperature shims are sets of coils with different geometries, and application of currents through these coils tweak the magnetic field in either the x, y or z axis or by a function of these (e.g. $x^2-y^2, z^2-(x^2+y^2)$). The cryogenic shims are also superconducting, and are generally set after the system is first installed and not changed thereafter. These are supplemented with the room temperature shims, which are effectively a series of electromagnets. Rather than the semi-permanent nature of the cryogenic shims the room temperature shims are effectively a fine-tuning of the magnetic field. In liquid NMR these are generally changed sample to sample, while in solid state NMR are generally only modified as a consequence of changing the probe, due to inhomogeneities arising from different probe geometries. Shimming has been described as an art form, as modern spectrometers tend to have at least $12-18$ room temperature shims which need to be modified sequentially and iteratively to produce the narrowest lineshapes [37].

The NMR probe can be considered to be the one of the most important parts of the NMR experiment. The main feature of the probe is the coil used to excite and detect the nuclear spins. Located at the centre of the homogeneous field generated by the shims, the coil is wound around the sample chamber and connected to a resonant circuit which ensures that the coil has the lowest possible resistance at the frequency used in the NMR experiment. This resonance is able to be adjusted to higher or lower frequencies using the tuning capacitor and changing the output impedance using the matching capacitor. Experiments requiring two or more nuclei, such as the cross polarisation experiment (Section 3.1.7), can have the resonant circuits designed in such a way that multiple resonant frequencies are possible. In addition to the aforementioned capabilities, the NMR probe may also contain additional equipment for the application of MAS, variable temperature, or other experimental features desired.

To simplify the NMR console it can be considered as two basic parts, the transmitter and the receiver. The transmitter is responsible for generating the *rf* pulse at the frequency, amplitude, phase and time required by the spectroscopist. While, the receiver, is responsible for the amplification of the low power NMR signal, and then mixing down to lower frequencies suitable for the analogue to digital converter (ADC) so it can then be read into the computer for analysis by the spectroscopist. Furthermore, the console is responsible for the timing of this so that all pulses are applied at the correct time needed for the experiment, and controlling the duplexer, which ensures the detector is not open to the high power *rf* pulse from the transmitter, which would likely irreparably damage the sensitive

electronic components.

3.1.2 One Pulse Experiment

One of the simplest NMR experiments is the one pulse experiment. It is the application of a single *rf* pulse to bring magnetisation into the transverse plane and then measuring the response of this transverse magnetisation (Section 3.1.4). The maximum signal (S) generated, from a single pulse, is when θ_{nut} is equal to 90 °, so that the resulting magnetisation is entirely aligned in the transverse plane (Figure 2.5).

The induced signal of the interaction is:

$$S = V_c \gamma B_0 M \tag{3.1}$$

Where V_c is the volume of the samples. Substituting the net magnetisation of a sample the total signal induced is now given by:

$$S = \frac{N V_c \gamma^3 B_o^2 \hbar^2 I(I+1)}{3kT} \tag{3.2}$$

As observed, this makes the signal dependent on many factors, and as discussed in Section 2.1.2, results in the inherent insensitivity of the technique.

In addition to this inherent insensitivity, NMR spectroscopy has to contend with additional uncontrolled random signals called 'noise'. Noise can arise from many sources, but by far the largest source is from thermal motion of electrons in the receiver coil. To combat this, the experiment can be repeated multiple times, ensuring that after each pulse the magnetisation has returned to equilibrium (Section 3.1.3) before the next experiment begins. As noise is inherently random, each repetition of the experiment reduces the amount of noise observable and therefore increase the signal-to-noise (S/N) ratio. The S/N ratio increases with $\sqrt{n}$ where n is the number of transients (or number of experiments) acquired. It is immediately apparent that from this, that to double the S/N the experiment needs to be increased by a factor of four. This can be problematic in cases when signal is inherently low relative to the noise. As increasing the number of the transients acquired gets diminishing returns, and quickly leads to unrealistic experimental times. In such cases to increase the signal observed, other factors would need to be considered including, increasing B_0, V_c, or through isotopic enrichment of nuclei.

3.1.3 Longitudinal Relaxation Time - T_1

After the *rf* pulse (Section 2.3.3), bulk magnetisation returns to thermodynamic equilibrium through a process called relaxation. This is described by two separate mechanisms, the longitudinal relaxation time (T_1), and the transverse relaxation time (T_2). The first of these, T_1 is the time required for the bulk magnetisation to return to thermal equilibrium along the z-axis after the system is perturbed. Returning to equilibrium does lead to a slight energy loss at the nuclear spins in the form of heat, however the amount is small and no notable temperature changes are observed in the bulk sample. The classical description of the time dependence of the z magnetisation (M_z) can be given by the Bloch equation,

$$\frac{dM_z}{dt} = \frac{M_0 - M_z}{T_1} \tag{3.3}$$

where M_0 is the magnetisation at thermal equilibrium. The description of the build up from no magnetisation, such as after a 90° pulse, until the bulk magnetisation is along the B_0 field is described by the exponential relationship,

$$M_z = M_0(1 - e^{-\frac{t}{T_1}}) \tag{3.4}$$

where T_1 is given as the rate constant.

The length of T_1 varies for both the nuclei, and the system under study, as a result of differences in the strength of local interactions around the investigated nuclei. Fluctuations in the strength of these interactions (caused by time variations) cause transitions between the Zeeman energy levels and thus a change in the bulk magnetisation. Furthermore, the frequency of these energy transitions is dependent on the strength of the interactions present, and the amount of fluctuations at ω_0 in the system. A result of this, in quadrupolar nuclei, where the quadrupolar interaction is usually the most dominant interaction, its relative size tends to reduce the T_1 observed. Whereas, for non-quadrupolar systems or when the interaction is small, the predominant relaxation mechanism is due to the dipolar interaction. Since the paramagnetic interaction is analogous to the dipolar interaction, although with an unpaired electron rather than a nucleus, the presence of a paramagnetic species also has significant contributions towards relaxation [38]. This contribution is due to rapid electron spin flipping, resulting in a significant decrease in T_1 is observed for paramagnetic materials, thus enabling rapid repetition of experiments.

3.1.4 Transverse Relaxation Time - T_2

In the rotating frame, after the magnetisation is transferred to the $x-y$ plane due to an applied *rf* pulse you would expect that all nuclei would remain aligned together. However, differing magnetic fields, due to the varying strength of interactions experienced at each nucleus, result in a slightly different precession relative to the rotating frame. Nuclei that experience a lower relative local magnetic field lag behind with respect to the rotating frame, whereas higher fields appear to be precessing faster than the rotating frame. The sum of all the magnetisation over time, forms a dispersion of the magnetisation in the $x-y$ plane. After a sufficient period of time, this magnetisation becomes fully dispersed. The transverse relaxation (T_2) describes this dispersion of magnetisation in the x-y plane. Similarly to T_1, T_2 can be described by the Bloch equations, in both the x

$$\frac{dM_x}{dt} = \frac{-M_x}{T_2} \tag{3.5}$$

and y dimensions,

$$\frac{dM_y}{dt} = \frac{-M_y}{T_2} \tag{3.6}$$

and where the solution for the transverse magnetisation in the rotating frame is given by,

$$M_x(T) = M_x(0)e^{\frac{-t}{T_2}} \tag{3.7}$$

and

$$M_y(T) = M_y(0)e^{\frac{-t}{T_2}} \tag{3.8}$$

However, this value for T_2 is the ideal transverse relaxation. Magnetic field inhomogeneities in the static magnetic field, arising due to poor shimming, sum with the ideal magnetic field so that

$$\frac{1}{T_2^*} = \frac{1}{T_2} + \frac{1}{T_{2(\Delta B_0)}} \tag{3.9}$$

where $T_{2(\Delta B_0)} = 1/R_{inhom}$ where R_{inhom} is the size of the magnetic field inhomogeneities on the lineshape, and T_2^* is the total transverse magnetisation. The free induction decay observed in NMR experiments is due to this T_2^* as the receiver coil is aligned along this plane. It can also be shown that T_2^* is proportional to line width so that:

$$\Delta\nu_{\frac{1}{2}} = \frac{1}{\pi T_2^*} \tag{3.10}$$

So that a larger interaction results in a smaller T_2^* and thus a larger linewidth.

This fact can be exploited to determine the homogeneity of the magnetic field, as the magnetic field can be adjusted so that R_{inhom} is reduced resulting in as narrow a line as possible. This process is called shimming and is best performed with a sample with inherently long T_2.

3.1.5 The Hahn Echo Experiment

The first spin echo experiment in NMR was performed by Erwin Hahn who discovered that using successive $\pi/2$ pulses separated by a short time period (τ), an echo like appearance evolved in the observed signal [8]. This $\pi/2 - \tau - \pi/2$ sequence, later termed the solid echo or the quadrupolar-echo, is useful for refocusing the quadrupolar interaction in integer spin quadrupoles.

However, later modification to the original sequence by Carr and Purcell, changed the second $\pi/2$ pulse to a π pulse to promote coherence refocusing [35]. Later termed the Hahn echo, the π pulse effectively rotates the spins completely about the pulse axis. As the spins are flipped they effectively start to undo the dephasing, as the faster precessing spins are now effectively behind the slower spins. At a time period τ after the π pulse, all coherences become refocused, allowing for the FID to be collected from this point.

This technique is partially useful in systems with broad resonances where T_2^* is low. As during the small dead time after any final pulse, the first few points of a FID are not collected. This is problematic as in broad resonances crucial information can be lost from removing these points resulting in spectral lines that are now not representative of the system. Whereas, collecting the FID from the top of the echo ensures all coherences are fully refocused, and no information is lost. Furthermore, if both sides of the echo are fully collected doubling the effective signal collected from this experiment, although in many cases this is not possible.

Generally, when used in conjunction with MAS (Section 2.5), the pulses are timed so that $\tau = n\omega_r$, where n is a integer, and ω_r represents a full rotor cycle.

3.1.6 Heteronuclear Decoupling

While MAS is successful at removing most of the heteronuclear dipolar coupling, some anisotropic components sometimes still remain. This typically occurs in situations where low abundance nuclei X (such as ^{29}Si with 4.7 %) are contained in a network with a large amount of high abundant spins nearby (such as ^{1}H at 99.98 %). Through the use of decoupling sequences any broadening remaining from this interaction can be removed. These sequences are typically applied on the ^{1}H nucleus

during the acquisition of the FID of the nucleus under observation X.

The simplest case involves a continuous high powered *rf* pulse on ^{1}H. However, when applied with a typical nutation frequency (ω_1) of 100 kHz for the length of the FID, it can cause undesired sample heating or exceed what would be considered safe for the equipment involved. This has caused other, more efficient sequences to be developed, including but not limited to, two pulse phase modulated (TPPM) and SPINAL-64 [39, 40].

3.1.7 Cross Polarisation

Spectra from nuclei with low sensitivity or a long T_1 can be difficult to acquire by conventional techniques. As described in Section 3.1.2, if the signal-to-noise obtained in a reasonable length of time is not sufficient, quadrupling the acquisition time further will only result in a doubling of the S/N. However to combat this, cross polarisation magic angle spinning (CPMAS) can be employed to improve the sensitivity of experiments. Through exploitation of dipolar coupling, spin polarisation from a high abundant and sensitive nucleus such as ^{1}H can be transferred to spatially close lower abundance X nuclei (such as ^{29}Si). Enabling the T_1 of the ^{1}H to be used, which can have a lower T_1 value due to strong homonuclear coupling. Furthermore, CPMAS can result in an enhancement of signal up to a factor of the gyromagnetic ratios (γ_H/γ_X) of the nuclei.

To perform this experiment first ^{1}H magnetisation is transferred into the $x-y$ plane using a pulse applied at the Larmor frequency of the ^{1}H nucleus. Directly after this, a spin lock pulse on the ^{1}H channel is matched to a contact pulse on the X channel. This requires the Hartmann-Hahn matching condition,

$$\gamma_H B_1(^1\mathrm{H}) = \gamma_X B_1(X) \tag{3.11}$$

where the amplitudes of both pulses are the same. Simplistically, this sets the energy gaps between the two sets of spins to be equal, thus allowing the redistribution of spin states, with a net gain in the X spins in the $x-y$ axis. Finally after this contact pulse has ended, decoupling on the ^{1}H channel is usually applied, to remove dipolar coupling during the acquisition of the FID on the X channel.

In practice the amplitude of either the contact pulse or the spin lock pulse, are varied over the contact time, as this allows for small imperfections in the setting of the Hartmann-Hahn matching. While Equation 3.11 is true for low MAS speed ($<\sim$12 kHz), upon increasing MAS frequencies where the rotor period is a fraction of the contact time, the net cross polarisation term averages to zero or at least

a small value reducing the effectiveness of the Hartman-Hahn matching condition. However, an aditional matching condition can be found where

$$(\gamma_H B_1(^1\mathrm{H}) - \gamma_X B_1(X)) = \pm n\omega_r \qquad n = 1, 2, ... \tag{3.12}$$

is true, resulting in the sideband match condition. However, in this thesis CP has only been performed at $\omega_r = 5\,\mathrm{kHz}$, where the Hartmann-Hahn condition still holds true, so this is not a concern.

3.1.8 Multiple Quantum Magic Angle Spinning (MQMAS)

While it is possible to remove the second order quadrupolar interaction from the solid state NMR spectrum through rotating at an additional magic angle (Section 2.5), implementation of these techniques is difficult and requires expensive dedicated probes. The 2D-MQMAS experiment first proposed in 1995 by Frydman *et al.* [41] sought to resolve this issue by achieving high resolution by spinning the sample at just one angle. Through correlation of the phase evolutions of multiple quantum (MQ) and single quantum (1Q) coherences, the fourth rank component of the second order quadrupolar broadening can be removed, resulting in the formation of a purely isotropic echo.

The simplest MQMAS experiment utilises 2 pulses for the MQ transition, however this results in 'phase-twist' lineshapes observed in the 2D spectrum, leading to lower resolution and obscuring analysis. However, since the discovery of this original experiment, researchers have modified the pulse sequence to ensure pure absorption lineshapes can be obtained. While this can be achieved by ether a phase modulation, or an amplitude modulation with respect to t_1, in this thesis the latter will be used exclusively. Additionally, the experiment performed is the 3QMAS pulse sequence (Figure 3.1), where a 3Q transition (e.g. for a 3/2 nucleus, between the $+3/2$ and $-3/2$ spin states) is utilised in the MQ transition.

The 3QMAS experiment first has a high power *rf* pulse to excite the MQ coherences. Then the 3Q transition is allowed to evolve under the internal Hamiltonian over a time period t_1. These evolving quantum coherences are then reconverted back into the 1Q state. A short delay τ, which acts to remove any unwanted coherences and align the remaining along B_0 is applied before the selective $\pi/2$ Z-filter pulse which brings everything into the observable 1Q coherence.

For this 3Q transition to evolve without any extra resonances being observed in the final spectrum, the $0 \rightarrow \pm 3 \rightarrow 0 \rightarrow -1$ coherence pathway has to be adopted. This coherence pathway is selected by phase cycling, where the phase (ϕ, Equation

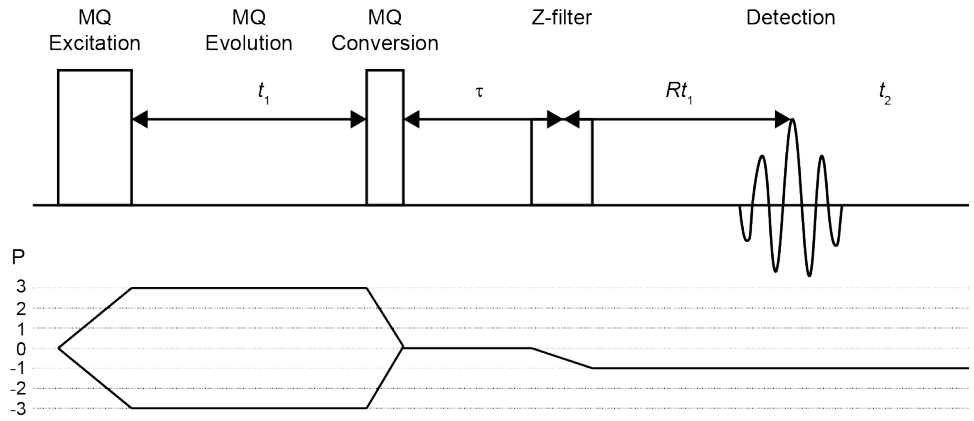

Figure 3.1: The pulse sequence for the z-filter 3QMAS experiment, with the coherence pathway shown below.

2.17) is cycled in $|p|$ steps of $360/|p|$ stages. By choosing the $0 \rightarrow \pm 3 \rightarrow 0 \rightarrow -1$ coherence pathways displayed in Figure 3.1, both the echo and antiecho contributions are equal for all crystallites in the system, where the isotropic echo (T_{2e}) is observable at $Rt1$ away from the z-filter pulse:

$$t_{2e} = -\left[\frac{C_4(I,p)}{C_4(S,-1)}\right] t_1 = R(I,p)t_1 \tag{3.13}$$

Where R is equal to,

$$R(I,p) = \frac{p\left[36I(I+1) - 17p^2 - 10\right]}{36I(I+1) - 27} \tag{3.14}$$

where the sign of $C_4(I,p)$ is always reversed when changing that of p, so that it is always possible to obtain a positive ratio for $R(I,p)$. Application of a 2D Fourier transform on the time domain signal, provides a correlation spectrum consisting of two narrow bands of resonances with features extended along the direction where,

$$F_1 = R(I,p)F_2 \tag{3.15}$$

where F_2 and F_1 represent the frequencies in the single quantum and multi quantum dimensions respectively. While this is useful, by convention the data is usually 'sheared' so that the features are aligned with the F_2 axis (δ_{MAS}), transforming F_1 into a new isotropic dimension δ_{iso} [42].

It is usual to add two extra axes to the MQMAS spectrum. The first is the chemical shift (CS) axis, where if the quadrupolar interaction is small the line will be located on this line. Observation of any broadening in the resonance parallel to

this line represents disorder present in the chemical shift of the site. The second axis, called the quadrupolar induced shift (Q_{is}) represents the shift induced by a sufficiently large quadrupolar interaction away from the CS axis. Furthermore, any disorder in the C_Q of a resonance is observed parallel to the Q_{is} line.

3.2 MPMS Measurements

Fundamentally, the magnetic property measurement system (MPMS) is a way to measure the magnetic properties of a sample by monitoring a change in the current of a set of superconducting coils as a sample is steadily moved through them. The theory for this section has primarily come from two main sources 'Magnetism in Condensed Matter' [23] and 'Fundamentals of Magnetism and Magnetic Measurements' [43].

The superconducting detection coils in the MPMS are linked to further detection coils of a superconducting quantum interference device (SQUID), which measures any change in current of the superconducting wire outputting a voltage which is proportional to the SQUID detection coils. This is due to the extreme sensitivity to changes in magnetic fields for the SQUID detector, and as a consequence it needs to be shielded from direct exposure to both the ambient magnetic fields in the laboratory and from those produced by the superconducting magnet in the MPMS device.

By convention, some definitions of the different magnetic fields used in SQUID magnetometry are slightly different to those used in NMR. While, M is still magnetisation, the applied magnetic field is given as H, and the magnetic flux at the SQUID detector is B. Furthermore, there is a great deal of resistance by the magnetics community to adopt SI units, and still magnetic measurements are given in the Gaussian cgs system. As a result of this, for the MPMS measurements throughout this thesis, M is given in electromagnetic units (emu) in terms of either the volume, mass or number of moles in a sample, where one emu is equal to 10 amperes. The units for H are given in oersted (Oe), where 1 Oe = 1 G (Gauss), and the units for B are also given in G. In this cgs system the three magnetic fields are related by the equation:

$$B = H + 4\pi M \tag{3.16}$$

By definition the applied magnetic field (H) does not change when the sample is placed in the system, so B can be seen the net local field and M is the field which changes the local field from H to B.

As this is a relatively easy conversion, and experimentally the magnetisation

from the sample is generally given in terms of M. This dependence can be given as the magnetic susceptibility

$$\chi = \frac{M}{H} \tag{3.17}$$

For this thesis, M will be given in terms of mass, so the mass magnetic susceptibility (χ_g) is given in units of emu/g. The first of two principle MPMS measurements utilised in this thesis is M(H), where M is given as a function of changing applied field, is evident from Equation 3.17. As the measurements in this thesis are primarily done on paramagnetic materials, there is a linear dependence in most M(H) measurements resulting in determination of the magnetic mass susceptibility (χ_m).

The Curie-Weiss susceptibility χ_{CW} describes the temperature relationship that paramagnetic materials have with magnetic susceptibility:

$$\chi_{CW} = \frac{C}{T - \theta} \tag{3.18}$$

Where θ is the Curie Weiss temperature and related to the strength of the interaction between magnetic moments, and C is the curie constant given as,

$$C = \frac{1}{k_b} P_{eff}^2 N \tag{3.19}$$

Where N is the number of spins and P_{eff} is the effective magnetic moment. This temperature dependence is the basis of the second primary MPMS measurement, M(T) where the magnetisation is measured as a function of the change in temperature. The magnetisation of M(T) is usually given as $1/\chi$ so that the approximate location of θ can be given as the curie temperature. However, as is the case with many materials, an anti-ferromagnetic transition occurs near θ, known as a Néel temperature (T_N), which is given instead.

The two principle MPMS experiments in this thesis are then given as M(H) and M(T), where the dependence of magnetisation is given as a function of field and temperature respectively. These measurements are used to determine the magnetic behaviour of materials, such as if its paramagnetic, diamagnetic, or contains any magnetic impurities.

Chapter 4

Low Field and Fast MAS Studies on Paramagnetic Cathode Battery Materials

4.1 Introduction

4.1.1 Background

The application of lithium iron phosphate ($LiFePO_4$, LFP) as a replacement for current lithium-ion cathode materials has become more desirable recently, due to its advantages which include a low production cost, environmental safety, good storage capacity, thermal stability and reproducibility during charge/recharge cycles [44,45]. The electrochemical potential of LFP at $\sim$3.5 V *vs.* Li/Li^+ is well below the electrolyte oxidation voltage regions, contributing towards the observed reliability and safety of the electrochemical cell [46]. Work is ongoing to develop a green process to recycle recovered LFP, further decreasing the environmental impact of the cathode material [47]. These factors all contribute to its desirability as a cathode material, and its use in many devices, has given rise to a global LFP use of 49,500 tons in 2015, which is projected to increase to 309,500 tons by 2020 [48–50].

Occupying an orthorhombic olivine structure, LFP has a one dimensional channel along the *b*-axis which Li^+ forms chains of edge sharing octahedra [51]. Each Li octahedra edge shares with two Fe octahera, which form zig-zag corner sharing planes parallel to this channel. Additionally, each Li^+ shares two edges and two corners with a four different P tetrahedra. These four P tetrahedra strongly attract oxygen forming highly symmetric $PO_4{}^-$ units and create small distortions in the Fe octahedra. [52] The Li channel created by the Fe octahedra and P tetra-

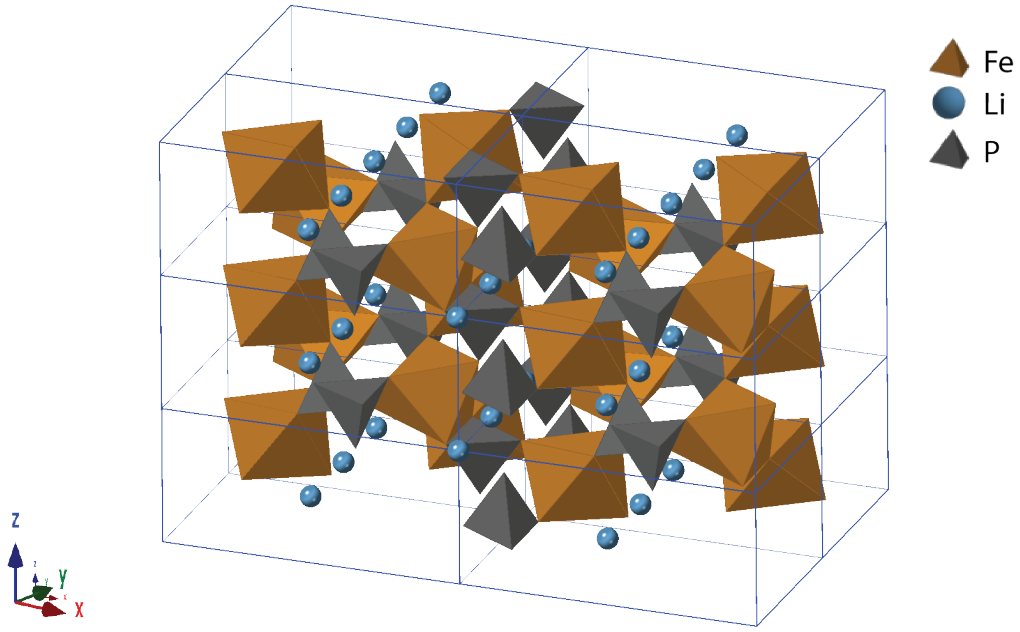

Figure 4.1: The olivine crystal structure of $LiFePO_4$ with FeO_6 octahedra in orange, PO_4 tetrahedra in grey, and the blue Li sitting in channels forming an LiO_6 octahedra.

hedra is shown in Figure 4.1 and can become blocked by various factors such as disorder, foreign phases, or by stacking faults [53–55]. As Li^+ diffusion is limited to along the channels and not between them, any defects which block the channels is detrimental to the performance of the cathode material [51, 54]. However, methods exist to mitigate this effect, these including producing plate-like crystals with the Li^+ channel along the shortest plane [53, 56, 57].

In transition metal (TM) oxides the ordering of the d electrons, and thus the materials properties, heavily depends on the environment that the TM occupies. As Fe occupies a octahedral environment, in LFP, the 5 d-block electron orbitals split into the triply degenerate t_{2g} and doubly degenerate e_g energy states. Figure 4.2(a) shows the electron orbitals that make up these energy states. It is known that the $3d^6$ electrons from $Fe_2{}^+$ are in the high spin configuration (Figure 4.2(b)), thus five electrons occupy all of the up-spin $3d$ states, with the remaining electron per iron occupying a down-spin t_{2g} band. [58, 59] It is known that LFP is in this high spin configuration as the crystal field splitting energy, U_{CF} ~1.64 eV, is smaller than the exchange splitting, U_X ~3.41 eV. [59] The high spin state can also be determined experimentally though measuring the magnetic properties of LFP. [60] It is known that LFP is paramagnetic, indicating the existence of unpaired electrons and thus

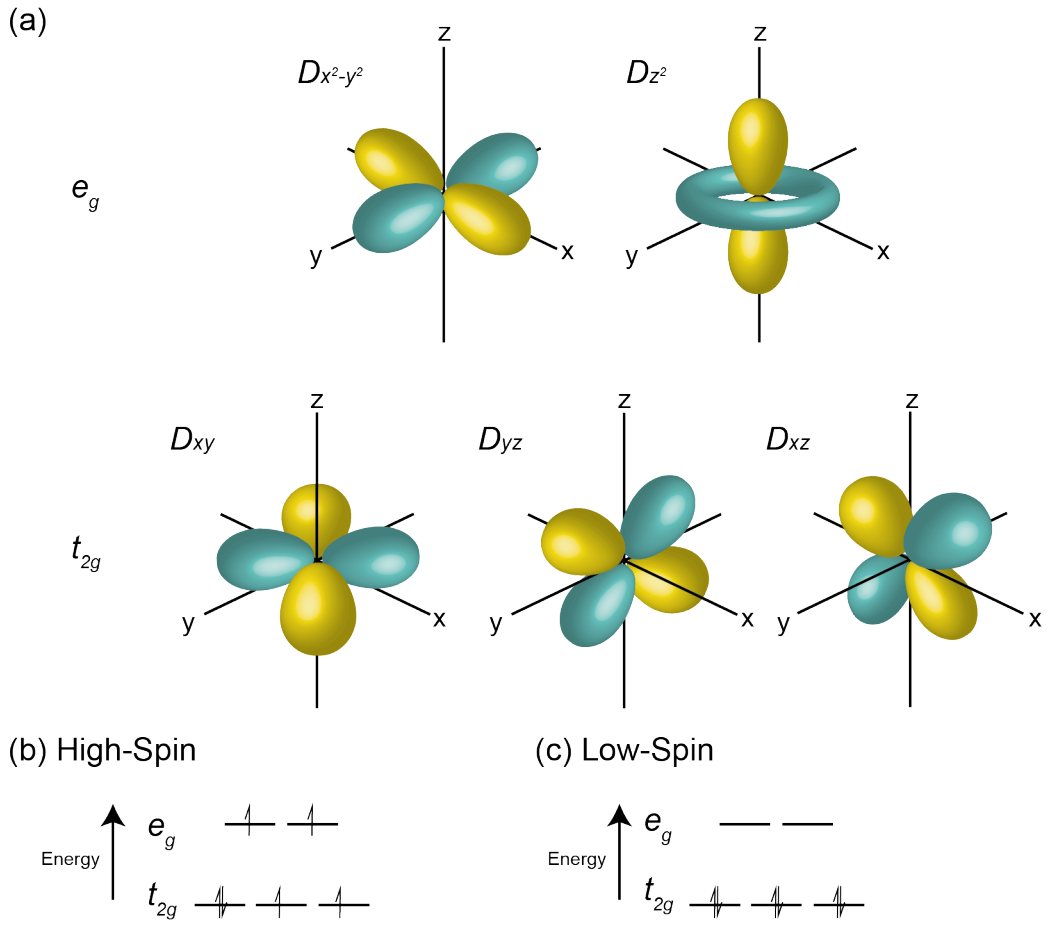

Figure 4.2: (a) The shapes of the five 3d orbitals. The crystal field splitting for a octahedral complex with $3d^6$ electrons in (b) high-spin and (c) low-spin arrangements.

confirming the high spin configuration (Figure 4.2(b)). If the $3d^6$ electrons were in low-spin configuration (Figure 4.2(c)), due to the octahedral nature of the site, the t_{2g} orbitals would be fully occupied leaving no unpaired electrons and resulting in a diamagnetic material. [60]

The orthorhombic phase of LFP was first identified in the mineral Triphylite in 1932 [61]. In 1997, Padhi *et al.* [44], utilised LFP as a potential cathode material. From their initial tests, LFP achieved favourable electrochemical properties, including a fully reversible specific capacity of 110 mA h/g with a voltage plateau of 3.5 V. However, a limit for the intercalation potential of 0.6 Li per unit cell was reached. This was initially determined as the potential limit for LFP, as chemical lithiation of the analogue $FePO_4$ resulted in no increase in the intercalation potential [44]. Lithium's low diffusion rate at the phase-boundary and the low inherent conductivity of particles of LFP, have been thought to be the cause of these conductivity issues [53, 62].

Early investigations tried several methods to improve this low intercalation capacity. Researchers identified the specific capacity to be strongly temperature dependent, although the theoretical capacity of 170 mA h/g could not be reached, even up to 80°C [45, 63]. Others focused on doping LFP with electronically conductive materials, such as copper or silver, in an attempt to improve the kinetics and availability of the Li in the material [64]. However, the largest improvement in specific capacity came from carbon coating LFP to achieve an electronically conductive material. This carbon coating enabled researchers to almost reach the theoretical capacity of LFP [65, 66]. Following this initial research, the synthesis and problems associated with the carbon coating of LFP have become an active area of research [67–69].

4.1.2 Production Methods of Lithium Iron Phosphate

Electrochemical performance of LFP has been shown to be strongly dependent on the synthesis method utilised, and the quality of the carbon coating [55, 57, 70]. Factors including the particle size, morphology, and cation ordering can critically affect the performance of the material [71, 72]. It is also important to be aware of the mechanism by which lithium moves through the lattice, as any method that introduces deformities into the channels will reduce the material's performance [51, 54]. Synthesis methods of LFP generally fall into two main categories: solid state synthesis and solution chemistry. Generally, both methods contain a stoichiometric amount of an iron salt, a lithium salt, and a phosphate source as precursor materials [55].

In general, the aim is to produce LFP with a small particle size and a large surface area. Achieving this will enable the following benefits, firstly as diffusion is proportional to the square of distance, the rate capability is improved for smaller particles. Secondly, the high surface area of the small particles provides proportionally greater surface sites, increasing the gravimetric capacity of the electrode. Thirdly, an improvement in the reaction kinetics is achieved due to an increase in electron transport [73].

Solid state methods are currently utilised in industry for the production of LFP, which generally involve a long sintering process at a high temperature in an inert atmosphere [74]. Thus ensuring that the starting material has decomposed and produced a pure olivine phase of LFP. However, sintering LFP at a high temperature can cause unintended effects, including the risk of creating impurities (Fe_2O_3 or $Li_3Fe_2(PO_4)_3$) or causing the agglomeration of particles [75]. To reduce the temperature and synthesis time, many researchers employ mechanical methods such as ball milling [76, 77] or high energy milling [78], as this reduces the risk of impurities. In addition, the use of these mechanochemical methods can produce LFP with a greater electrochemical performance due to the small particle size created, and a high surface area [77–80].

In the solid state method it is common to use an Fe(II) precursor, however some of these materials are either unstable, expensive, or both. Therefore, some researchers have looked into synthesis procedures involving Fe(III) precursors. These materials are generally more stable and cheaper than their Fe(II) counterparts, however care needs to be taken during synthesis to ensure that the Fe(III) is fully reduced to Fe(II). This reduction of Fe(III) can be achieved by a variety of methods, including adding a reducing gas such as H_2 into the Ar atmosphere during the sintering process [81, 82]. Through the use of this method, an increase of Fe_2P in the system is observed, although the use of low calcination temperatures will reduce the amount of this impurity generated [83]. While Fe_2P is an impurity, small amounts can increase the conductivity of LFP by several orders of magnitude, by forming a grain boundary between the carbon coating and the LFP particles [84].

Carbothermal reduction during the sintering process has been shown to aid reduction of Fe(III) into Fe(II) [85, 86]. However, precise details of this method have been debated and it is thought to only be efficient at sintering temperatures exceeding 1000 °C, and is an effect of $H_{2(g)}$ being evolved as the carbon source decays [81]. As aforementioned, the sintering of LFP, approaching temperatures up to 1000 °C, can cause undesired effects including impurities or large particle formation giving low surface area [75].

The solution methods used to produce LFP include many varied techniques such as solvothermal, flame spray pyrolysis, sol-gel, and co-precipitation [55]. This chapter focusses on solvothermal and flame spray pyrolysis solution methods for LFP synthesis. One of the reasons that solution methods have not been scaled up, to use in industry, is the difficulty in finding precursors that are not only stable in your solvent of choice at the desired oxidation level, but are also cheap enough to offset the use of solvents at an industrial scale. However, solid state synthesis methods generally involve high temperatures, multiple steps and long heat treatments, therefore solution methods can reduce this complexity and thus, the cost of the manufacturing process [74].

The solvothermal method involves the chemical reaction of precursors in a closed vessel, in the presence of non aqueous solvent, at a higher temperature than the boiling point of the solvent utilised. This method is analogous to the hydrothermal technique and is often used interchangeably, however they differ through the solvent choice, as the solvothermal method uses a non-aqueous solvent, whilst hydrothermal methods use an aqueous solvent [87].

Solvothermal synthesis has a significant amount of control over the size, shape distribution, and crystallinity of the particles by optimising the reaction parameters [72, 88–94]. High purity LFP was first solvothermally synthesised in 2001, however the capacity produced, 100 Ah/kg, only reaches 58 % of the theoretical maximum [88]. The same group, later demonstrated that care was needed to form LFP without forming unwanted electrochemically inactive trigonal $FePO_4$ units [54].

Research groups have shown that by altering the pH conditions during the solvothermal synthesis, the morphology of the resulting LFP particles can be controlled [56]. The production of needle-like and plate-like morphologies could be created at low and mid pH respectively, at higher pH levels the particles had random structures. The solvothermal method also has the ability to form more unique structures such as dumbbell like shapes [72], nano plates [92], or nanorods [95], all with impressive electrochemical performance. These small or obscure morphologies of LFP particles can give large surface areas and allow the enhancement of the electrochemical performance [73, 96, 97]. If mechanical mixing is employed during this process careful optimization of this agitation can also improve the performance of LFP [98].

As with the other methods, carbon coating of solvothermally produced LFP can easily be achieved to further increase the performance of the material. Carbon coating of solvothermal LFP can be completed by in-situ methods during the synthesis or conducted after the particles are made [92, 99–101].

Flame spray pyrolysis (FSP) is a popular method for the production of LFP, due to its ability to create nm sized particles [73, 102, 103]. FSP disperses a combustible solution of precursors through a nozzle with the use of gases, such as O_2, this dispersed solution is then ignited and the resulting nano particles are collected [104]. Generally, this is aided with the addition of a fuel gas such as acetylene or methane, enabling rapid combustion of the solvent mixture and giving rise to gaseous metal ions that grow in clusters forming metal oxides. These clusters rapidly grow to form stable particles which are then collected on a filter at the flame exhaust.

To ensure pure LFP is produced, the combustible solution must contain a Li, Fe and P in a ratio of 1:1:1. These can be a mixture of inorganic and organic precursors, but care is needed that they will not precipitate out into separate phases, at ambient temperatures. Like other methods, FSP can produce LFP with high capacities and in situ carbon coating [102, 103]. Although for FSP, in-situ carbon coating of the LFP requires a specialised set-up to enable particle formation, acetylene carbon black (ACB) coating, and then particle quenching after combustion but before final collection is also required [102].

4.1.3 Doping and Analogues of Lithium Iron Phosphate

Doping LFP is of interest to increase its inherent low conductivity. One of the first investigations into improving LFP's conductivity explored doping Mg^{2+}, Al^{3+}, Ti^{4+}, Zr^{4+}, Nb^{5+}, and W^{6+} into the Li^+ site to form $Li_{1-x}M_xFePO_4$ [105]. This resulted in an increase in conductivity by 8 orders of magnitude, when compared to un-doped LFP. However, subsequent studies have pointed towards this increase being related to the generation of a highly conductive layer of Fe_2P on the surface of LFP [84].

Other dopants investigated seek to replace the transition metal site in small amounts. It has been shown that doping small amounts of V into LFP can improve the reversible capacity, rate capability, and its performance at higher temperatures [106, 107]. However, the stoichiometry of the precursors has to be carefully controlled, during the synthesis of V doped LFP, otherwise an unintended replacement of Li or P can occur [108–110].

Although, not all impurities formed by the addition of V are negative. Optimal performance, as a cathode, has been observed when $Li_3V_2(PO_4)_3$ and VO_2 can be detected in the material. The existence of small amounts of $Li_3V_2(PO_4)_3$ on the surface of V doped LFP can promote Li and electron mobility subsequently improving the performance [110]. While VO_2, on the surface of LFP, increases the electrochemical performance when compared to base LFP, however interstitial V

doing also could not be ruled out as a contributing factor [111].

By substituting Fe^{2+} with other transition metals, phospho-olivine analogues of LFP can be produced. These substitutions are made with an aim to operate in niches that LFP cannot sufficiently fulfil, including applications needing a high energy density [112]. Replacement of the Fe^{2+}, site with Mn^{2+}, Co^{2+} or Ni^{2+}, theoretically increases the operating voltage from LFP's 3.4 V to 4.1 V, 4.8 V, and 5.0 V, respectively [44, 112, 113]. However, some of these increases come at the expense of reducing the desirable material's properties. For example, with $LiMnPO_4$ (LMP) the intrinsic ionic and electronic conductivity are lower than LFP [44, 114]. However, this has spurred investigations into the $LiFe_xMn_{(1-x)}PO_4$ cathode series to see if a suitable trade-off between electronic conductivity and an increase in operating voltage can be achieved.

4.1.4 NMR on Paramagnetic Cathode Materials

Systems containing paramagnetic species are usually seen as unfavourable for the acquisition of high quality solid state NMR data. Paramagnetic species can introduce broadening to the spectra, caused by the electron-nuclear dipolar interaction and large shifts from the Fermi-contact interaction. This means using solid state NMR to investigate cathode materials is problematic as many contain paramagnetic environments. These affects can be mitigated by the use of fast MAS, low B_0 fields, and the use of advanced pulse sequences to increase the resolution of paramagnetic anisotropies.

Developments in fast MAS have driven more research into the area with commercial solid state MAS probes now achieving MAS rates of 111 kHz. It was first shown that an increase in MAS speed can increase resolution and sensitivity of ^1H and ^{13}C in paramagnetic compounds [115, 116]. As mentioned in Section 2.4.5, the electron-nuclear dipolar interaction has similar terms to the CSA interaction resulting in large anisotropies, that can be averaged by reducing the angular dependence term $(3\cos^2\theta - 1)$. Upon rotation of the sample at the magic angle (54.74°) at a speed faster than the size of the interaction, these terms can be completely averaged out. However, the size of the electron-nuclear dipolar interaction is generally significantly larger than the MAS frequencies achievable, resulting in the observation of spinning side-bands.

Fortunately the electron-nuclear dipolar interaction also has an inverse relationship with the static magnetic field (B_0). Therefore, decreasing B_0 reduces the size of the interaction making the observed paramagnetic broadening more manageable. An example of increasing resolution by decreasing B_0 is shown in Figure

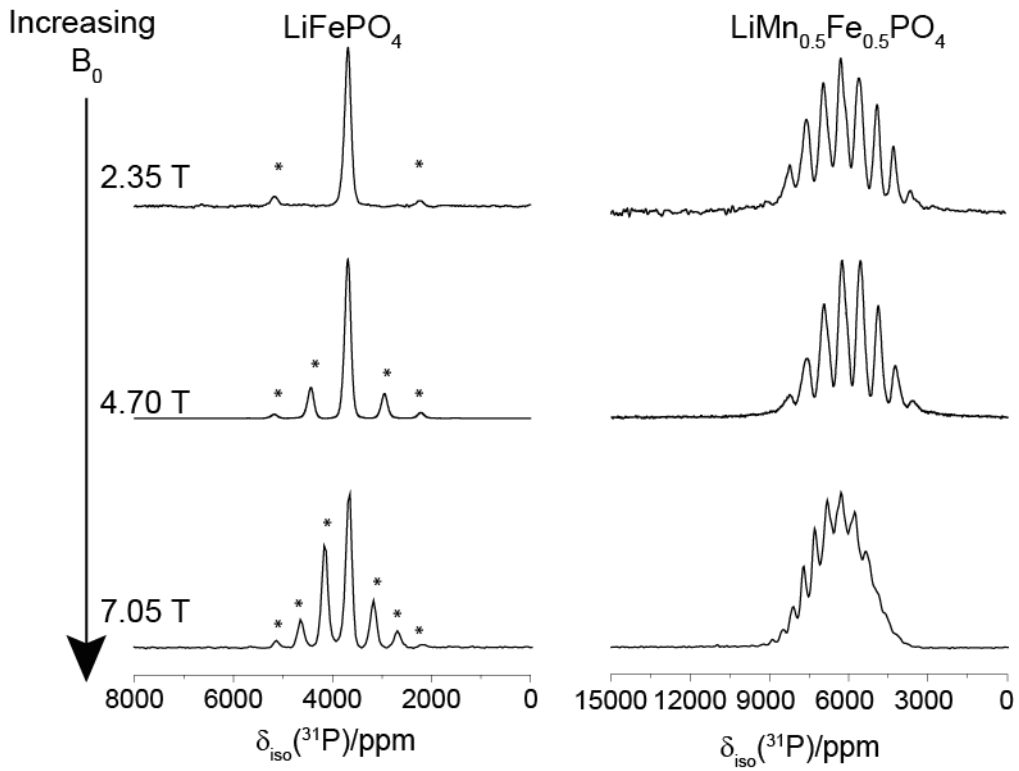

Figure 4.3: ^{31}P MAS NMR spectra of $LiFePO_4$ and $LiMn_{0.5}Fe_{0.5}PO_4$ at increasing magnetic fields where (*) denotes the spinning side-bands for $LiFePO_4$. These are not shown for $LiMn_{0.5}Fe_{0.5}PO_4$ as the overlaping nature prohibits side-band identification. All spectra were aquired with $\omega_r = 60\,\text{kHz}$

4.3, where the increase in broadening caused by the electron-nuclear paramagnetic interaction at higher magnetic fields for LFP and $LiMn_{0.5}Fe_{0.5}PO_4$ cathode materials is observed. Whilst this is not such an issue for single phase LFP, even for B_0 up to 7.05 T, a single ^{31}P resonance is still clearly visible amongst the side-bands. However, for materials with multiple ^{31}P resonances, as demonstrated for $LiMn_{0.5}Fe_{0.5}PO_4$ in Figure 4.3, dipolar broadening obscures identification of the individual sites resulting in a broad unresolved resonance. Figure 4.3 also illustrates the extreme shift seen in paramagnetic species, as the resonances are far from the typical diamagnetic chemical shift range of 250 to -250 ppm.

Low field paramagnetic NMR is an area of research that has been relativity unexplored. One possible reason for this is the reduction of the signal achieved, as illustrated in Equation 3.2, as B_0 has an exponential relationship with the amount of signal produced. However, this reduction in signal-to-noise can be partly overcome for paramagnetic materials. As explained in Section 2.4.5, the electron-nuclear inter-

action leads to a reduction in T_1 enabling shorter recycle delays, when compared to diamagnetic systems, meaning more transients acquired over the same time period and, hence, overcoming the signal-to-noise issues.

The other main component of the paramagnetic interaction is the through bond component of the paramagnetic shift, the Fermi contact shift. As noted in Section 2.4.5, there is a dependence on B_0, and an inverse reliance on temperature. The resulting shift along with contributions from the pseudo contact shift form the resulting paramagnetic shift. As both of these interactions have dependencies on temperature and B_0, it is impossible to differentiate the shift contributions by NMR experiments alone.

To understand the paramagnetic shift, a focus of research has been on cataloguing the different shifts seen in paramagnetic minerals. Grey and Lee have catalogued various ^{6}Li shifts for a variety of Mn rocksalts, spinels, and layered materials to gain insight into the paramagnetic shift of these systems [117].

Another method to aid the characterization of paramagnetic materials is through the use of calculation techniques such as DFT. Using DFT to determine the effect that each TM-O-P bond pathway has on the ^{31}P nucleus, the paramagnetic shifts can be estimated [118]. Using this procedure it has been possible to determine the 32 different P environments for $LiM_xFe_{1-x}PO_4$ where M is Co^{2+} or Mn^{2+} and compared the DFT results to NMR observations [118–120].

As mentioned in Section 4.1.3, doping LFP has been a major focus for investigations into improving its capabilities as a cathode material. While substituted LFP has been investigated by NMR, to the best of our knowledge no investigations into solid state NMR of these doped materials has been conducted. Investigations of other doped materials have demonstrated the power of solid state NMR to provide information on the local structure [121–123]. As described in Section 4.3.3, V doped LFP is a promising area for improving the electrochemical performance of LFP, therefore analysis of into V doped materials will be the primary focus in this work.

Significant research has gone into solid state NMR investigations of Li^+ position during the charging cycle. Both in-situ and ex-situ analysis of charging cycles have been completed, these both have advantages and disadvantages.

In-situ techniques have involved developing methods to charge and discharge the electrochemical cell whilst inside the NMR instrumentation. This generally involves modifying existing NMR probes to contain the cell. Techniques that use existing equipment have been developed, one such example is through preparation of an electrochemical cell in a typical 5 mm liquid NMR tube [124].

The main drawback to this type of method is that currently its not possible to introduce MAS alongside the charging cycle [125]. This results as a build up of eddy currents from the metallic sections of the electrochemical cell, making MAS of the in-situ cells currently unachievable. The resulting lack of MAS can obscure identification of the different sites in the cathode under study, generating a broad featureless line [126]. In addition, metallic components have to be limited due to there shielding effect of the applied *rf* fields [127].

However, alongside these drawbacks, there are benefits to investigating battery materials by in-situ NMR. It has been shown to be possible to identify all the lithium products through the charging cycle process [128]. In addition the use of in-situ NMR has quantified the generation of dendrite formation during the discharge/recharge cycle [129].

Whilst in-situ NMR is limited by the lack of MAS, ex-situ does not have this limitation. However, while the use of MAS NMR to gain higher resolution is a great benefit to investigations of Li during the charging cycle, some complications arise. While the cathode material can be collected from the electrochemical cell at different states of charge for subsequent MAS NMR analysis, care needs to be taken to prevent exposure to atmospheric conditions [130]. Despite this, ex-situ NMR has been used in combination with other techniques to propose models for lithiation and delithiation of cathode materials [131,132]. The resulting work will focus on ex-situ solid state NMR analysis to investigate the changes visible by different synthesis methods of LFP, the $LiFe_{(x)}Mn_{(1-x)}PO_4$ systems, and V doped LFPs.

4.2 Experimental

4.2.1 Synthesis

All LFP samples were prepared by Johnson Matthey at the Johnson Matthey Technology Centre, Sonning Common. For Section 4.3.1, apart from Fe_2P (99.5%) which was purchased from Sigma-Aldrich, the samples in were prepared by methods as described in literature; for ball milled, [133] solvothermal, [134] and FSP [135]. Materials produced in Section 4.3.2 were produced in the same manner as above however replacing stoichiometric amounts of the Fe precursor with a Mn precursor.

The LFP samples doped with V were produced using a high energy ball milling method containing Li_2CO_3, $FeC_2O_4 \cdot 2H_2O$, $NH_4H_2PO_4$, and NH_4VO_3 as precursors. The compositions in Table 4.1 for the $Li_{1-3x}Fe_{1-x}V_xPO_4$ (x= 0.01, 0.03, 0.05) series were prepared and mixed together. The amount of Li precursor introduced was varied from the stoichiometric ratios, as each sample produced a

Li_2CO_3 excess or deficiency shown in Table 4.1. Using a 3 mm ZrO_2 milling media in a ratio of 10:1 milling media to precursors, the samples were ground in a planetary mill in five 10 minute repetitions. The resulting material was then dried at 100 °C in an oven overnight. Calcination of the resulting material was performed at 600 °C for 10 h under argon, with an initial ramp rate of 5 °C min^{-1}.

4.2.2 XRD Measurements

The XRD measurements were performed using a Panalytical Empyrean XRD instrument equipped with a Co target and a Fe filter to suppress the Co K_β wavelength. Measurements were performed from 15° to 120° (2θ) using a 0.012° step size, collecting counts for 58.4 s at each step. The samples were spun on an Al disk throughout the measurement. Rietveld refinement of the phases present was conducted using the Topas program [136].

4.2.3 Solid State NMR

All low-field ^{7}Li MAS NMR measurements were performed at 2.35 T using a Bruker Avance III HD spectrometer operating at a Larmor frequency of 38.91 MHz. These experiments were performed using a Bruker 1.3 mm HX probe which enabled a MAS frequency of 60 kHz to be implemented. All ^{7}Li spectra were acquired with a rotor synchronised echo ($\theta - \tau - 2\theta$) sequence, using a selective (solid) $\pi/2$ pulse time of 1 µs along with a recycle delay of 0.04 s. The pulse length calibration was performed on $LiCl_{(s)}$ from which a $\pi/2$ pulse time of 1 µs was measured. The ^{7}Li T_1 experiments were conducted using an inversion recovery method, where first a 4 µs π pulse was applied with a varible delay τ before the subsequent $\pi/2$ pulse. The τ delay was increased from zero until a maximum intensity of the signal was reached. This signal build up was then plotted against the exponential relation for the magnetisation of T_1 (Equation 3.4). All ^{7}Li centre of gravity (apparent) shifts were reported against the IUPAC recommended primary reference of $LiCl_{(aq)}$ (9.7 mol, $\delta_{iso} = 0.0$ ppm), via a $LiCl_{(s)}$ secondary which has a known shift of -0.77 ppm. [137]

All low-field ^{31}P MAS NMR measurements were performed at 2.35 T using a Bruker Avance III HD spectrometer operating at a Larmor frequency of 40.70 MHz. These experiments were performed using a Bruker 1.3 mm HX probe which enabled a MAS frequency of 60 kHz to be implemented. All ^{31}P spectra were acquired with a rotor synchronised echo ($\theta - \tau - 2\theta$) sequence, using a $\pi/2$ pulse time of 1 µs along with a recycle delay of 0.001 s. The pulse length calibration was performed on $NH_4H_2PO_{4(s)}$ (ADP) from which a $\pi/2$ pulse time of 1 µs was measured. All ^{31}P

Table 4.1: Compositions of $Li_{1-3x}Fe_{1-x}V_xPO_4$, with the Li ratio increased or decreased from stoichiometric amounts (highlighted by the grey rows).

	Mass (g)				mmol				Molar Ratios			
Sample Name	Li_2CO_3	$FeC_2O_4 \cdot 2H_2O$	NH_4VO_3	$NH_4H_2PO_4$	Li	Fe	V	P	Li	Fe	V	P
LFVP1-N	0.97	4.86	0.03	3.17	13.1	27.0	0.27	27.6	0.95	0.98	0.01	1.00
LFVP1-3E	1.00	4.86	0.03	3.17	13.5	27.0	0.27	27.6	0.98	0.98	0.01	1.00
LFVP3-6D	0.86	4.66	0.10	3.17	11.6	25.9	0.81	27.6	0.84	0.94	0.03	1.00
LFVP3-N	0.92	4.76	0.10	3.17	12.4	26.4	0.81	27.6	0.90	0.96	0.03	1.00
LFVP3-3E	0.95	4.76	0.10	3.17	12.9	26.5	0.81	27.6	0.93	0.96	0.03	1.00
LFVP3-8E	1.00	4.76	0.10	3.17	13.5	26.5	0.81	27.6	0.98	0.96	0.03	1.00
LFVP5-5D	0.80	4.66	0.16	3.17	10.8	25.9	1.35	27.5	0.79	0.94	0.05	1.00
LFVP5-3D	0.83	4.66	0.16	3.17	11.2	25.9	1.35	27.5	0.81	0.94	0.05	1.00
LFVP5-N	0.86	4.66	0.16	3.17	11.6	25.9	1.35	27.5	0.84	0.94	0.05	1.00
LFVP5-5E	0.91	4.66	0.16	3.17	12.3	25.9	1.35	27.5	0.89	0.94	0.05	1.00
LFVP5-10E	0.96	4.66	0.16	3.17	13.0	25.9	1.35	27.5	0.94	0.94	0.05	1.00
LFVP5-14E	1.00	4.66	0.16	3.17	13.5	25.9	1.35	27.5	0.98	0.94	0.05	1.00

centre of gravity (apparent) shifts were reported against the IUPAC recommended primary reference of H_3PO_4 (85 percent, $\delta_{iso} = 0.0$ ppm), via a $NH_4H_2PO_{4(s)}$ secondary which has a known shift of 0.99 ppm. [137, 138]

To calibrate the temperature of the NMR measurements, the following procedure was used. $Sm_2SnO_{7(s)}$ was used as a temperature standard, as the isotropic shift of ^{119}Sn resonance has a known $1/T$ relation. [139] The ^{119}Sn measurements were conducted with a 0.01 s acquisition delay and a selective (solid) $\pi/2$ pulse width of 1.75 µs. To calibrate the temperature due to MAS frictional heating, a static measurement was completed. Through simulating the static lineshape at a known temperature the difference is temperature from MAS is known. Measurements were then conducted at MAS and the temperatures required for the experiment. The shift was then plotted against temperature and then adjusted against the true temperature (minus the frictional heating) found from the static measurement.

4.2.4 SQUID Magnetometry

All superconducting quantum interference device (SQUID) measurements were performed using a Quantum Design MPMS 5S SQUID Magnetometer. Magnetisation as a function of field (M(H)) measurements were performed at multiple temperatures (10, 50, 100, 200, and 300 K) by measuring the response in magnetic flux density, as the sample passes through the superconducting wire of the SQUID device at increasing magnetic fields, H. The response was measured as magnetic field (H) was increased in stages from 0 Oe to 1200 Oe in steps of 400 Oe, then from 2000 Oe to 8000 Oe in 2000 Oe steps, and then finally from 10,000 Oe to 50,000 Oe in 5000 Oe steps.

Magnetisation as a function of temperature (M(T)) measurements were performed by keeping the magnetic field (H) static at 1000 Oe and then increasing and decreasing the temperature, whilst measuring the response from the SQUID device. The response was measured as the temperature was first increased in stages from 10 K to 49 K in 1 K steps, then from 50 K to 300 K in 2 K steps. Once 300 K was reached the measurements were performed in reverse until the initial temperature of 10 K was achieved.

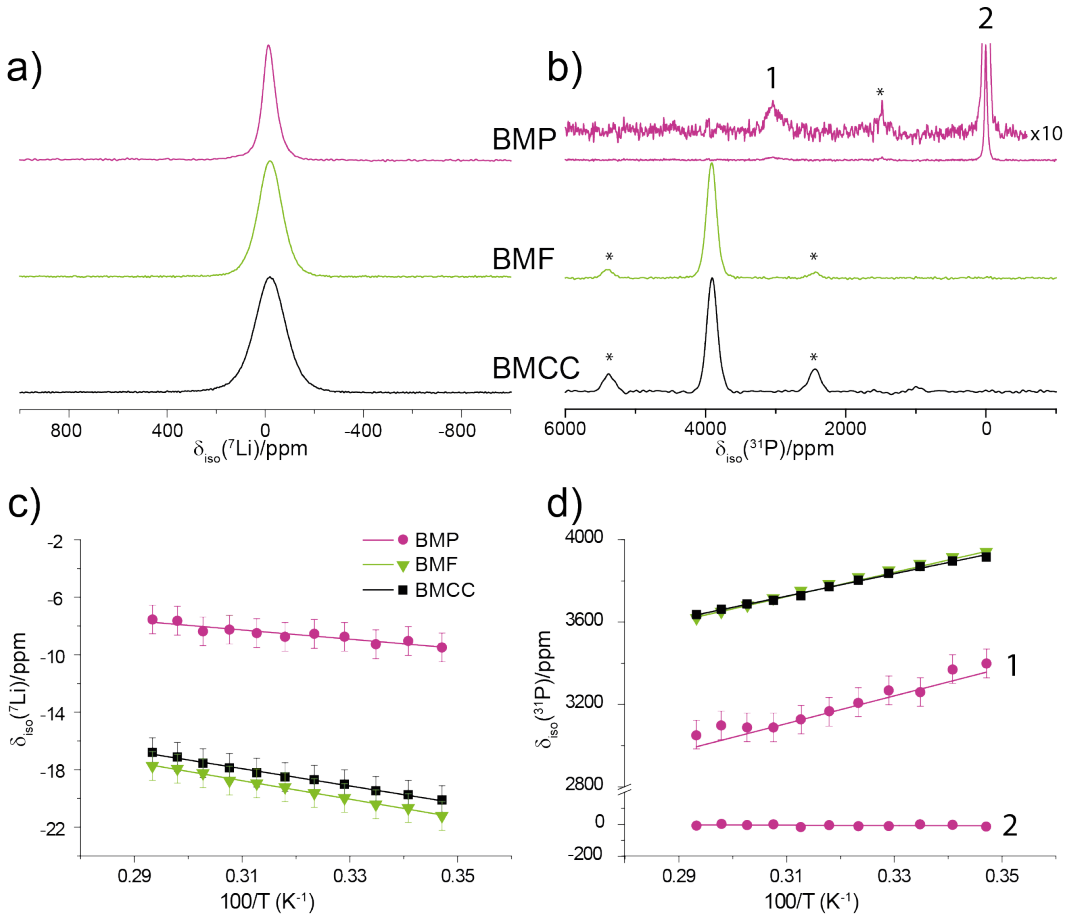

Figure 4.4: The 1D MAS (60 kHz) spectra of the ball milled samples BMP, BMF and BMCC measured at 298 K for (a) ^{7}Li and (b) ^{31}P, with * representing the spinning side-bands. The inverse temperature relationships for the same samples are shown in (c) ^{7}Li and (d) ^{31}P. The error bars for the temperature and for most ^{31}P sites are too small to be observed. For the ^{31}P data of BMP, two sites are observed. Site 1 signifies the broad paramagnetic resonance observed between 3000 and 3300 ppm. Site 2 is noted as residual ammonia hydrogen phosphate($(NH_4)_2H{\cdot}PO_4$) and can be observed at 0 ppm. Additionally due to minimal differences in the ^{31}P resonance attributed to LFP, the BMF and BMCC samples are observed at the same shift and therefore overlap in the inverse temperature plot (d).

4.3 Results and Discussion

4.3.1 ^{7}Li and ^{31}P MAS NMR investigations of different production methods of $LiFePO_4$

Initial investigations focused on monitoring the ball milled samples throughout the reaction stages. Firstly a sample (BMP) was taken after the ball milling treatment,

but before the sintering stage, and therefore should primarily contain the precursor materials lithium carbonate(Li_2CO_3), iron oxalate dehydrate ($FeC_2O_4{\cdot}2\,H_2O$), and ammonia hydrogen phosphate($(NH_4)_2H{\cdot}PO_4$). As seen in Figure 4.4(a), the ^{7}Li data shows a single broad resonance centred at 7 ppm. The shift of this Li resonance has a $1/T$ relationship (Figure 4.4(c)) indicating sites close proximity to a paramagnetic centre.

The ^{31}P data for BMP (Figure 4.4(b&d)) gives two resonances. A sharp peak occurring at 0 ppm and an additional broad resonance with a $1/T$ relationship appearing at 3000 ppm at 341 K. Whilst the first resonance (0 ppm) appears to have no large shift or a temperature dependence we can safely say it is the remaining $(NH_4)_2H{\cdot}PO_4$ precursor. However, the second resonance has a large temperature dependent shift from the normal ^{31}P range of 200 to -150 ppm. This large shift likely arises from the Fermi contact interaction, indicating that ^{31}P is close to a paramagnetic centre. This observation suggests that a preliminary reaction has occurred to form a paramagnetic ^{31}P containing product.

Upon sintering BMP, the material undergoes a rapid change to form LFP ($LiFePO_4$) and burns off any remaining starting material. The resulting material (BMF) is single phase $LiFePO_4$, with no measurable impurities by XRD. In Figure 4.4(a)&(c), we see a single ^{7}Li resonance at $\delta_{iso} = 18$ ppm with a small $1/T$ dependency. For the ^{31}P MAS NMR (Figure 4.4(b)&(d)), we observe a single resonance with a large temperature dependent shift away from the normal ^{31}P range [140]. This indicates that the P site is close to a paramagnetic centre. The result agrees with what has previously been observed [140].

The final sample in the ball milled sample series is BMCC, which is the product of taking BMF and carbon coating the material. The resulting ^{7}Li and ^{31}P data for BMCC, in Figure 4.4, is similar to what is seen in the BMF. There are no measurable differences for the ^{31}P shifts indicating both BMF and BMCC are experiencing the same chemical environments. Slight differences ($\sim$1 ppm) for ^{7}Li shifts are seen, however due to full width half maximum (FWHM) of the resonance the differences are within error of fitting. From this we can determine that the carbon coating procedure gives no noticeable modifications to the bulk LFP structure.

A series of flame spray pyrolysis (FSP) produced products were next analysed by solid state NMR methodology. The sample FS is directly after the FSP process but before annealing and carbon coating. It can be observed in the XRD pattern of FS (Figure 4.8(a)), from the absence of sharp reflections, it is amorphous. This amorphous nature is also observed in the ^{7}Li and ^{31}P MAS NMR spectra. As shown in Figure 4.5(a)&(c), the ^{7}Li spectrum of FS has a two broad overlapping

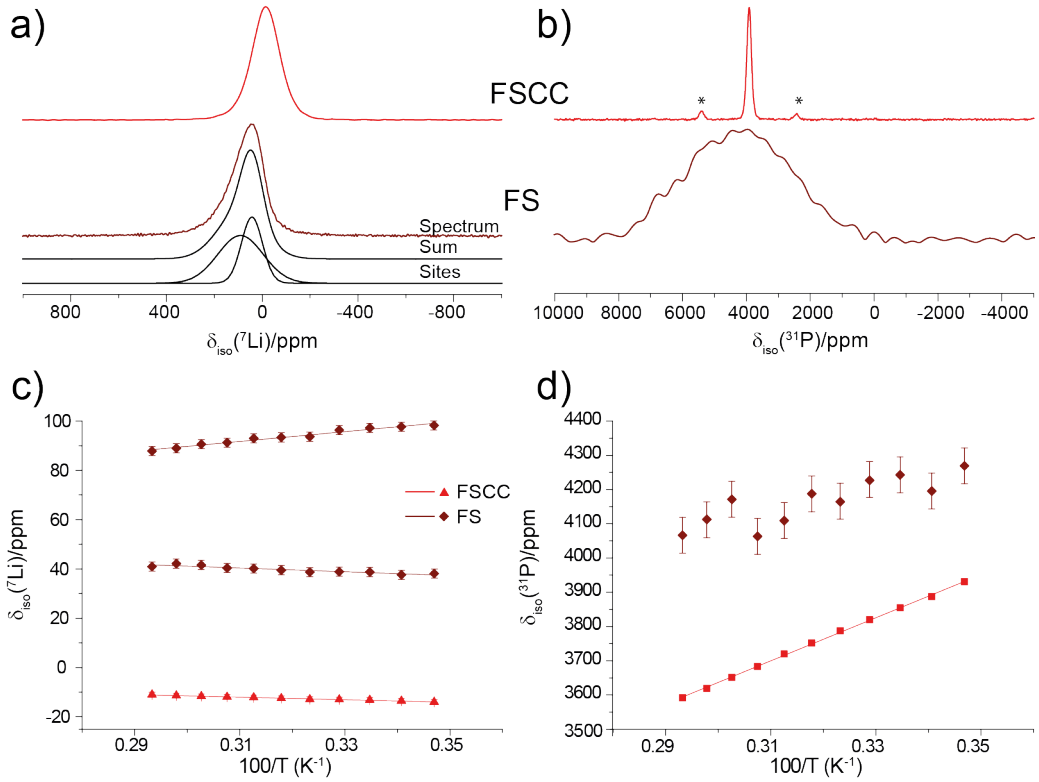

Figure 4.5: The 1D MAS (60 kHz) spectra of the products from the flame spray pyrolysis method. The FS and FSCC samples were measured at 298 K for (a) ^{7}Li and (b) ^{31}P, with * representing the spinning side-bands. The inverse temperature relationships for the same samples are shown in (c) ^{7}Li and (d) ^{31}P. The error bars for the temperature and for most ^{31}P sites are too small to be observed.

^{7}Li resonances. In addition, when we look at the resonance for the ^{31}P data (Figure 4.5(b)&(d)), a similar effect is observed. A large amorphous resonance spanning from 0 to 8000 ppm with a small temperature dependence is seen. However, with the inherent errors fitting such a large resonance this weak $1/T$ relation could be due to errors in identifying the peak centre.

To complete the synthesis of the FSP material crystallisation and carbon coating treatment were undertaken to produce FSCC. For FSCC, the ^{7}Li MAS NMR data (Figure 4.5(a)&(c)), a single resonance with a $1/T$ dependence is observed, resulting in similar results to BMF and BMCC. Additionally, for the ^{31}P MAS NMR data of FSCC (Figure 4.5(b)), a single temperature dependent resonance is observed, mirroring the ball milled LFP materials.

The final method to produce LFP investigated was via solvothermal synthesis. This final material was carbon coated to produce STCC. In Figure 4.6, it can

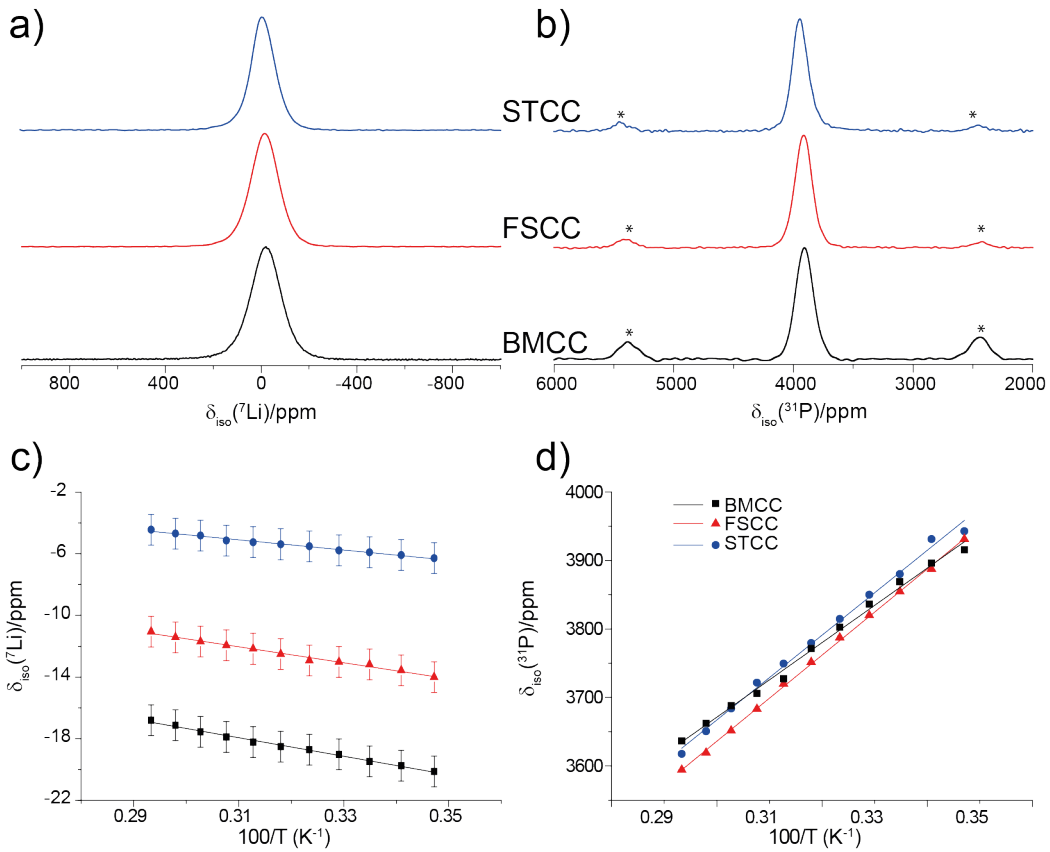

Figure 4.6: The 1D MAS (60 kHz) spectra of fully carbon coated materials BMCC, FSCC, and STCC. The samples were measured at 298 K for (a) ^{7}Li (b) ^{31}P. The VT reliance for the same samples for (c) ^{7}Li and (d) ^{31}P. The * represents the spinning side-bands. The error bars for the temperature and for ^{31}P sites are too small to be observed.

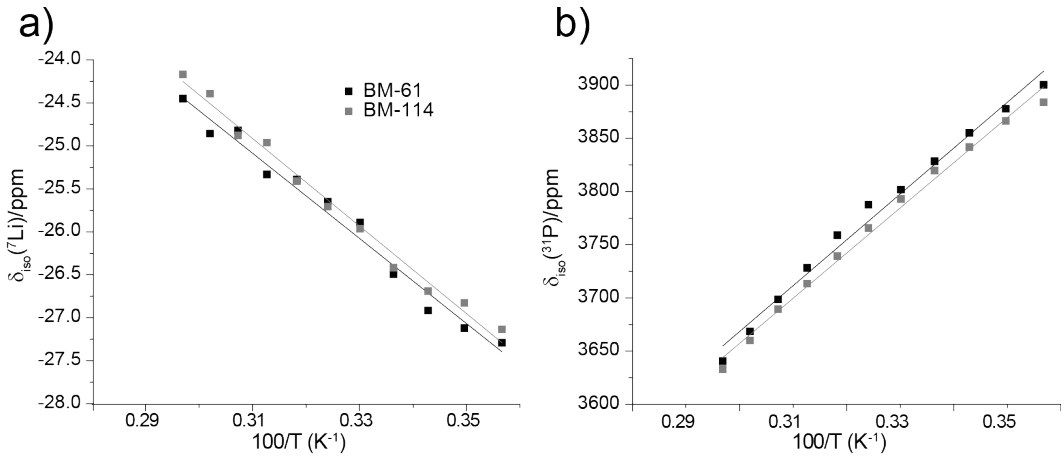

Figure 4.7: The inverse temperature dependence of BM-61 and BM-114 against (a) ^{7}Li and (b) ^{31}P isotropic shifts.

be observed that the resulting ^{7}Li and ^{31}P data for STCC are similar to the other final products with no significant differences in peak shape.

Initially the NMR spectra of the three final products look similar, indicating that the different synthesis methods used generate the same final material, enabling some initial conclusions to be drawn at this point. As observed in the ball milled samples, there are no major differences between the final two stages, thus we can conclude that carbon coating has no major effect on the structure observed in the NMR data. It can also be concluded that it is possible to observe amorphous LFP as opposed to crystalline LFP from just the NMR spectra.

Significant differences are also observed, where closer inspection of Figure 4.6(c), reveals subtle differences in the ^{7}Li isotropic shifts. These resulting divergences in isotropic shift indicate that for each method the environment around each ^{7}Li is slightly different. Initially it was thought that these differences were a particle size effect, therefore two new samples with different crystallite sizes were produced to test this hypothesis. To achieve this, the ball milling procedure was followed as given in the method section, except with a change in the sintering temperature to give different crystallite sizes. Sintering at 600 (BM-61) and 800 (BM-114) °C average crystallite sizes of 64 and 114 nm could be achieved. However, as seen in Figure 4.7, this results in a minimal effect on the ^{7}Li isotropic shifts between BM-61 and BM-114. Furthermore, the BM-61 and BM-114 show a larger deviation in ^{7}Li shifts from the BMF and BMCC samples previously prepared indicating a different underlying cause. Therefore, although the crystallite size may have some effect on the ^{7}Li and ^{31}P shifts, it is not significant enough to be the cause of the differences

Table 4.2: The cell parameters and cell volumes determined by Rietveld refinement for $LiFePO_4$ in STCC, FSCC, BMCC, BM-61, and BM-114.

Sample	a (Å) ±0.0005	b (Å) ±0.0005	c (Å) ±0.0005	Volume Amount ($Å^3$) ±0.04
STCC	10.3240	6.0026	4.6905	290.67
FSCC	10.3271	6.0063	4.6915	291.00
BMCC	10.3291	6.0071	4.6924	291.15
BM-61	10.3240	6.0076	4.6963	291.27
BM-114	10.3258	6.0095	4.6967	291.44

between BM, FSP and ST methods, and other avenues need to be explored.

Through Rietveld refinement of the obtained XRD patterns (Figure 4.8), a single olivine phase is observed for STCC, FSCC and BMCC. The cell parameters and volumes for $LiFePO_4$ are listed in Table 4.2. Additionally, the $LiFePO_4$ phase is also observed in BM-61 and BM-114, with the XRD patterns given in the Appendix (Figure A.1) and the cell values given in Table 4.2.

It can be observed that an increase in the $LiFePO_4$ cell volume correlates with the decrease in ^{7}Li shift seen in Figure 4.6. This suggests that the ^{7}Li shift is highly related to the cell volume in the olivine system. While directly detecting the Li through XRD is not accurate, as Li is a poor x-ray scatterer, the cell volume of $LiFePO_4$ is known to contract upon removal of Li^+ from the cathode [44]. This unit cell contraction suggests that while the synthesis of FSCC and STCC results in the generation of a large proportion of the intended $LiFePO_4$ phase, the olivine phase is not fully populated with Li^+ ions, resulting in a slight contraction of the unit cell. This trend is also present in the BM-61 and BM-114 samples which have a significantly lower ^{7}Li shift of $\sim$8 ppm when compared to the BMCC analogue, and a greater cell volume supporting this conclusion.

As the conductive iron phosphide (Fe_2P) can be produced during manufacture of LFP or from the carbon coating process, it seemed prudent to investigate where we might observe this coating if its in sufficient quantities. As seen in Figure 4.9, the resulting ^{31}P spectrum of Fe_2P shows a broad signal spanning 20,000 ppm. This is not observed in any of the samples measured, therefore it can be concluded that we do not have an observable amount of Fe_2P in these systems. However, due to the size of the observed resonance, this could be hard to detect and may be mistaken for background noise or probe ringing. Additionally, no reflections of Fe_2P were observed in the XRD patterns (Figure 4.8). This does not exclude the

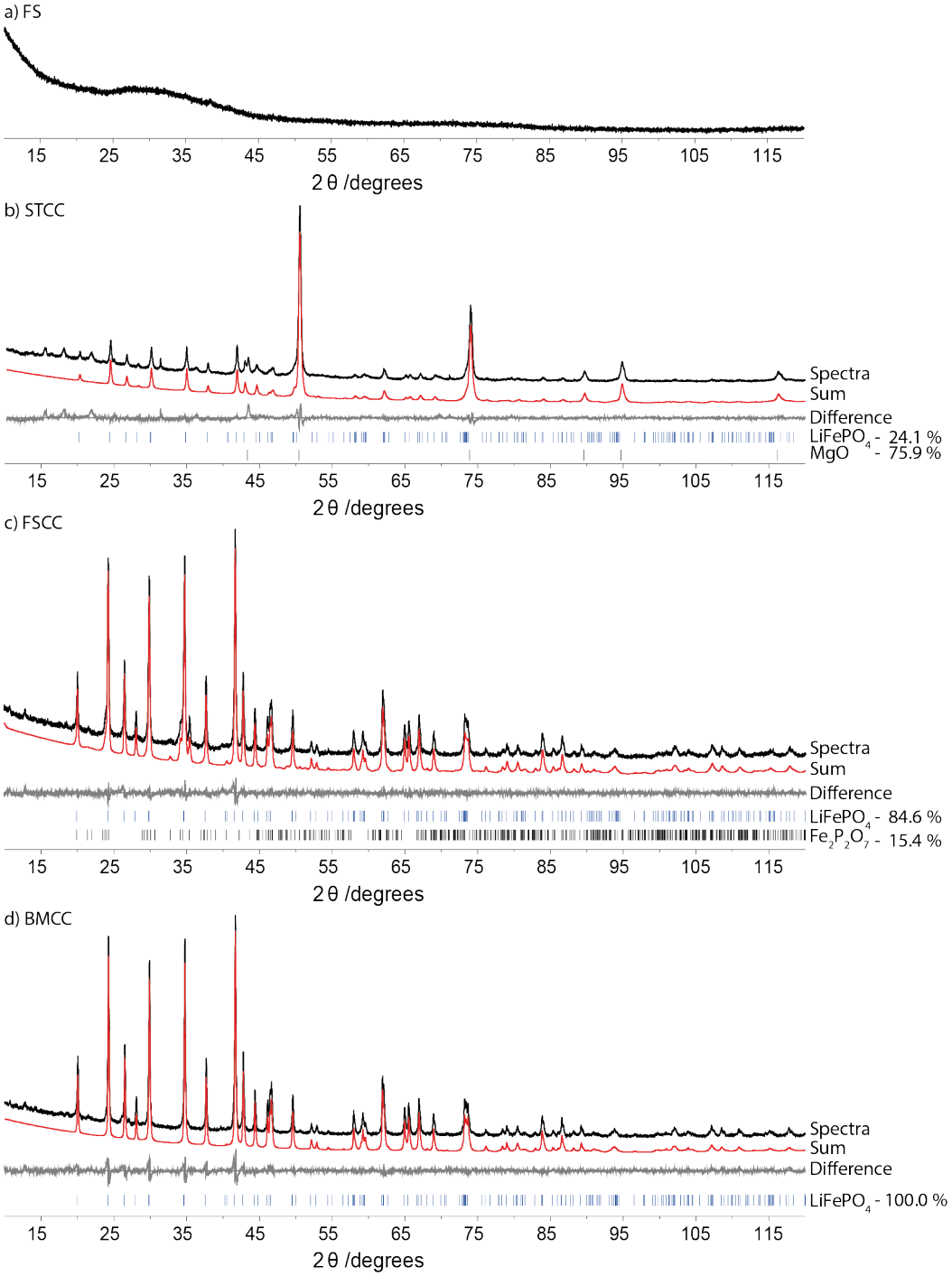

Figure 4.8: The XRD patterns for (a)FS, (b)STCC, (c)FSCC, and (d) BMCC. In the STCC pattern (b) a major MgO contamination is present, this was added as an inert material to dilute the $LiFePO_4$ for unsuccessful pulsed field gradient measurements. This was conducted post NMR measurements but before later XRD patterns were collected.

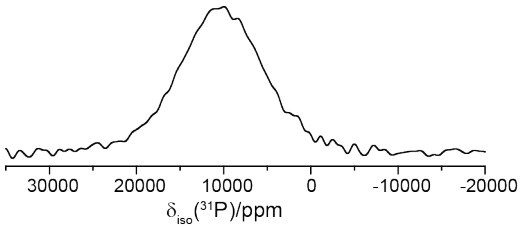

Figure 4.9: The 1D ^{31}P MAS (60 kHz) spectra of the Fe_2P

possibility of this occurring on the produced particles, just that the amount is too low for detection by the XRD in the final products (Figure 4.8), and that it was not discernible from the baseline noise from NMR.

As shown in Section 2.4.5, the magnetic susceptibility for paramagnetic materials can significantly affect both the Fermi contact shift and the electron-nuclear dipole interaction. Thus, using a SQUID magnetometer, the observation of any major differences in magnetic susceptibility can be deduced, and any other contributions to differences in the ^{7}Li shift can be characterised.

In the (M(T)) SQUID data in (Figure 4.10(a), (c) & (e)), we observe the characteristic change in magnetic ordering for LFP at 50 K (known as the Néel temperature T_N). The T_N corresponds to a change from the antiferromagnetic ordering (<50 K) to a paramagnetic Curie-Weiss behaviour above this value (>50 K) [141]. It is worth noting that Fe_2P gives a characteristic magnetic dampening at 230 K [142, 143], and from the SQUID data there is further evidence that no Fe_2P is observed in the investigated materials.

One major difference between the three samples is observed in the M(T) data, as BMCC (Figure 4.10(a)) exhibits a hysteresis behaviour, which is not observed in the FSCC and STCC samples. This hysteresis is observed through collection of the M(T) measurements in a zero-field-cooled/field-cooled (ZFC/FC) manner. To collect ZFC/FC measurements, the sample is initially cooled to the lowest measurement temperature desired with no applied field. Once stabilised, the magnetic field is applied (H= 1 T) and the response is recorded up to the highest required temperature, concluding the ZFC part. This measurement is then conducted in reverse, with the same applied magnetic field, until the lowest required temperature is reached. This concludes the FC part, and thus the measurement [43].

Ferromagnetic materials are known to retain some magnetisation from the ZFC part, and exhibit a hysteresis upon FC [43]. This ferromagnetic behaviour is mirrored the M(H) collected, where a ferromagnetic impurity is observed in the build up of magnetisation up to 1 T. This has been determined to be a contaminant

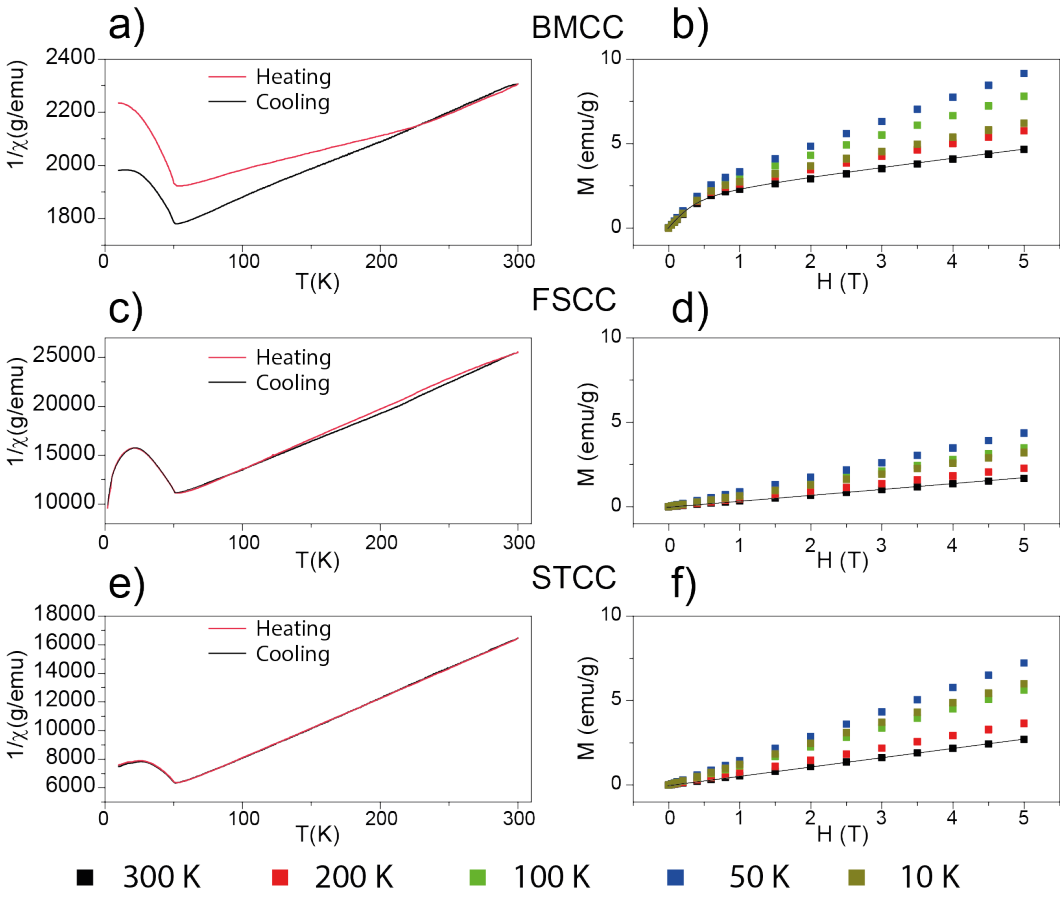

Figure 4.10: The magnetic properties of BMCC (a) & (b), FSCC (c) & (d) and STCC (e) & (f) measured by SQUID magnetometer. The M(T) curves are shown in (a), (c) & (e) while the M(H) plots are shown in (b), (d) & (f). The magnetisation of the variable temperature M(H) plots follows a similar pattern to the M(T) collected. Where the recorded magnetisation increases from the initial measurement recorded at 10 K to reach its maximum at the Neél temperature (∼50 K). Further increases in temperature follow the expected paramagnetic behaviour and thus a reduction in recorded magnetisation.

within the LFP sample, and is attributed to γ-Fe_2O_3 [83]. No build up is observed for the FSCC and STCC samples (Figure 4.10(d)&(f)) where a paramagnetic M(H) relationship behaviour is observed. This linear behaviour is typical for LFP [83], indicating the γ-Fe_2O_3 contaminate is solely limited to the BM method.

Additionally, from the M(H) data, a value for magnetic mass susceptibility (χ_{mass}) can be determined. As seen in Equation 3.17, we know that χ can be determined from the magnetisation (M) and the magnetic field strength (H). Therefore, if we know the magnetisation in terms of mass (M_{mass}) then:

$$\chi_{mass} = \frac{M_{mass}}{H} \tag{4.1}$$

and we can use this to determine χ_{mass}. This value for each of these samples at 300 K is 5.87×10^{-5} emu/g for BMCC, 3.35×10^{-5} emu/g for FSCC and 5.39×10^{-5} emu/g for STCC. However, this only equates when a linear relationship is observed between M and H, making the value determined for BMCC inaccurate. When ferromagnetic impurities are present, as in BMCC, the magnetic build up needs to be taken into consideration. This has shown to be determined by using a formula to calculate the amount and size of the magnetic impurities from the M(H) data [83, 86]. For these small nanoparticles, where the superparamagnetic configuration applies, the magnetisation of the material and the impurities is given by:

$$M = \chi_{mass}H + Nn\mu L\left(\frac{n\mu H}{k_B T}\right), \tag{4.2}$$

where the $\chi_{mass}H$ is determined as the paramagnetic contributions in the material and the $Nn\mu L\,(x)$ is the contribution arising from the size and amount of the magnetic impurities, as described by the Langevin function

$$L(x) = coth(x) - \frac{1}{x}. \tag{4.3}$$

For this equation, N is the number of magnetic clusters present, n is the amount of magnetic moments, of strength μ, present. The result of this for BMCC is a new value of 5.12×10^{-5} emu/g, with 14.64 ppm of magnetic particles, with an average of 780 magnetic moments each. This still results in no correlation between χ_{mass} and ^{7}Li δ_{iso} (Figure 4.6). As crystallite size has no significant effect (Figure 4.7), it should be noted that the unit cell volume of $LiFePo_4$ has the biggest influence on ^{7}Li shift.

Table 4.3: The compositions of the $LiMn_xFe_{1-x}PO_4$ investigated and the notation used for both the ball milled and the flame spray pyrolysis methods.

	Sample Code	
Composition	Ball milled	Flame spray
$LiFePO_4$	BMFe	FSFe
$LiMn_{0.1}Fe_{0.9}PO_4$	BMMn1	FSMn1
$LiMn_{0.3}Fe_{0.7}PO_4$	BMMn3	FSMn3
$LiMn_{0.5}Fe_{0.5}PO_4$	BMMn5	FSMn5
$LiMn_{0.7}Fe_{0.3}PO_4$	BMMn7	FSMn7
$LiMn_{0.9}Fe_{0.1}PO_4$	BMMn9	FSMn9
$LiMnPO_4$	BMMn	FSMn

4.3.2 Studies into Mn Substituted Lithium Iron Phosphate

As noted in the Section 4.1.3, a variety of methods are capable of producing the Mn substituted LFP ($LiMn_xFe_{1-x}PO_4$, $0 \leq x \leq 1$). A decision was made in this section to focus on the two main methods for the production; ball milled and flame spray pyrolysis procedures. This reduced complexity of the data, allows for more direct comparisons. Both a BM and FSP series were synthesised using stoichiometric amounts of each composition, and the synthesised materials are displayed in Table 4.3.

The ^{31}P MAS NMR spectra of these samples are shown in Figure 4.11. As expected, the ^{31}P spectra of BMFe and FSFe show a single resonance similar to that obtained for the previous series in Figure 4.6. For the Mn analogues of LFP, (LMP, $LiMnPO_4$) a single ^{31}P resonance is observed at 8100 ppm for both the BMMn and FSMn.

Upon investigation, compositions between these two end members show a distribution of ^{31}P shifts between the observed LFP and LMP resonances. From this low field (2.35 T) approach the resulting spectrum mirrors what has been previously observed in the literature at relatively high field (11.75 T), through the observation of the indirect dimension of the adiabatic magic angle turning (aMAT) experiments [118]. This relative complexity of the $LiMn_{0.5}Fe_{0.5}PO_4$ system is due to 32 different P sites being present [118]. Using calculations of the Fermi contact shift by Clément *et al.* [118] the NMR shifts for these sites can be estimated. Using the known resonances of LFP and LMP, the ^{31}P isotropic shifts of each site can be adjusted to calculate the relative strength of the Fermi contact interaction observed by each P nucleus [118]. However, to aid the comparison between the BM and FSP series these sites can be grouped into 8 different regions based on the estimated shifts, as shown in Figure 4.12(b).

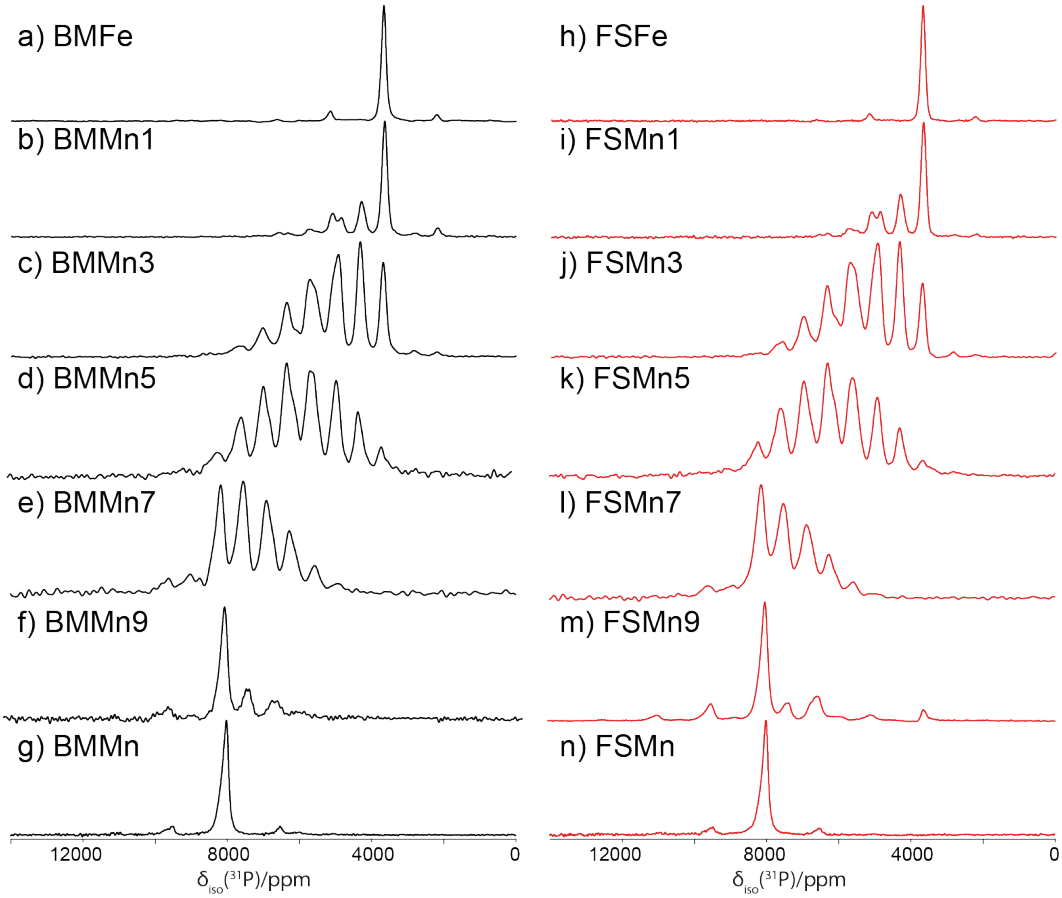

Figure 4.11: The ^{31}P Hahn-echo spectra for (a)-(g) ball milled and (h)-(n) flame spray pyrolysis synthesis methods. All experiments were performed at 60 kHz.

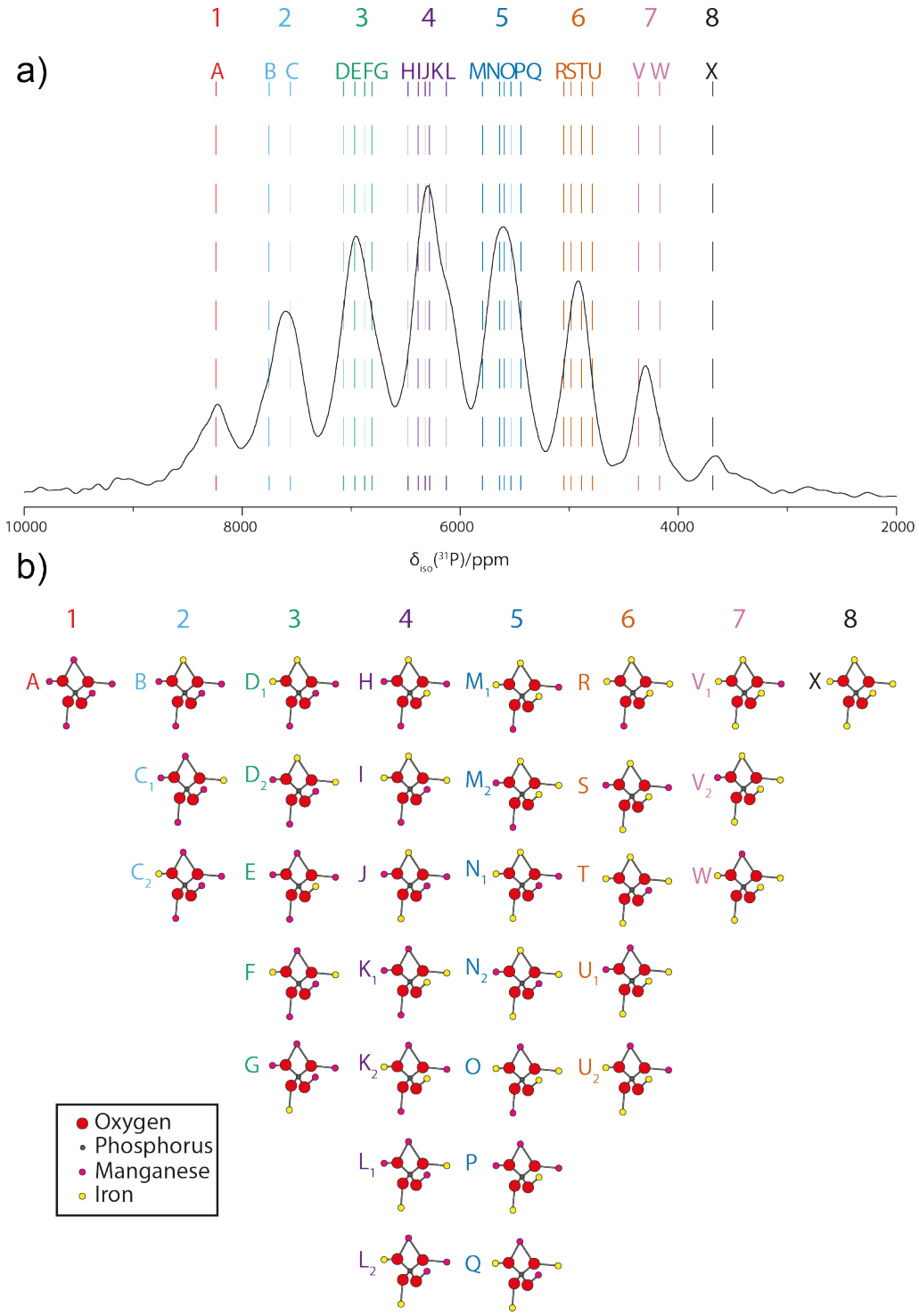

Figure 4.12: (a) The ^{31}P MAS NMR spectra of FSMn5, the letters denote the shifts of the phosphorus sites determined by Clément *et al.* [118]. (b) A structural representation of all the 32 possible arrangements of Fe^{2+} and Mn^{2+} around the ^{31}P site in $LiMn_xFe_{1-x}PO_4$.

These 32 P environments are due to the total contributions of the 5 distinct transition metal sites surrounding each ^{31}P nucleus. The combined contribution from each corresponds to a different ^{31}P resonance, with the structure and resonance marked by a corresponding letter (Figure 4.12). However, as many of these resonances significantly overlap, it is unrealistic to individually simulate each resonance to provide a quantification of each site, even at the relatively low magnetic fields (2.35 T) utilised here. Nevertheless, as several resonances cluster relatively close together, they can be separated into 8 groups of relatively similar shifts. These 8 different groups are displayed in Figure 4.12(b), with group 1 representing LMP, 8 representing LFP, and each in-between having differing amounts of Fe and Mn contributions.

For the majority of the compositions in the Mn substituted systems, comparisons between the BM and FSP series results in negligible differences in each of the 8 different regions. For these samples Mn appears to be randomly distributed among the different sites [118]. However, the $LiMn_{0.9}Fe_{0.1}PO_4$ system contains significant discrepancies between the BM and FSP methods. For BMMn9, the primarily resonance is $LiMnPO_4$ with decreasing amounts of the 2nd and 3rd groups also being observed. In the FSP analogue, FSMn9, while the primary resonance is still $LiMnPO_4$, differing amounts of group 2 and 3 are observed. This results in FSMn9 containing a reduction in the second group of shifts, while a large increase in the group 3 is observed. However, the increase in the third group of resonances appears to be a result of larger contributions from the spinning sideband manifold, of group 1, which also overlaps this resonance. In addition, FSMn9 also appears to contain resonance 8 (Figure 4.12) which is attributed to $LiFePO_4$. This suggests that instead of a mixed phase generated during synthesis, clustering of the Fe precursor into LFP particles has occurred.

Another difference is in the distribution of ^{31}P resonances observed for the $LiMn_{0.7}Fe_{0.3}PO_4$ composition. The FSMn7 sample would appear to have a greater distribution towards the $LiMnPO_4$ end member, compared to the corresponding BM material (BMMn7), which appears to have a more central distribution. As care was taken during acquisition to fully excite the resonance, its unlikely that inefficient pulse excitation is a cause of this difference.

As clustering is present for the final two FS materials, there is a possibility that the FSP systems with Mn substitution greater than 70 mol% are producing materials with some clustering of LFP. However, this is difficult to verify with absolute certainty without producing these samples by the same method.

The ^{7}Li data for Mn substituted series are given in Figure 4.13. A couple of

trends in the data become immediately apparent. Firstly, it is clearly observed that the increase in Mn content reduces the line width of the ^{7}Li resonances. A good method to quantify this is to take the full width half maximum (FWHM) of each peak. A fairly drastic FWHM change is measured, from FWHM values of 600 Hz and 500 Hz for BMMn and FSMn, up to 3800 Hz and 4600 Hz for the BMFe and FSFe end members. This trend can be plotted against the Mn content, as shown in Figure 4.14(a). In the literature it has been determined that for an increase in Mn for $LiMn_xFe_{1-x}PO_4$, an increase in cell volume is observed [142]. This gives a greater mobility of the Li^+ ions in the channels, resulting in narrower lineshapes.

For most concentrations of Mn, the differences in the FWHM between BM and FSP samples are minimal. However, as observed with the ^{31}P spectra in (Figure 4.11) there are greater discrepancies between BMMn9 and FSMn9 than the rest of the series.

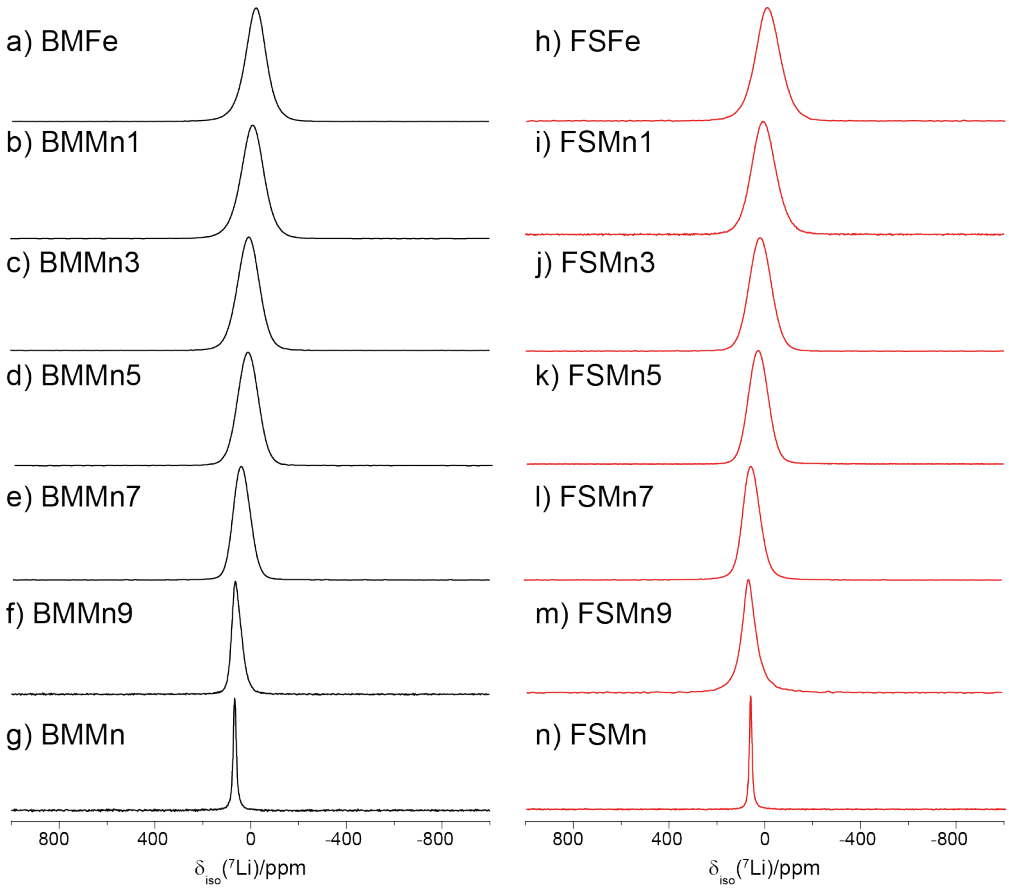

Figure 4.13: The ^{7}Li Hahn-echo spectra for the (a)-(g) ball milled and (h)-(n) flame spray pyrolysis synthesis methods.

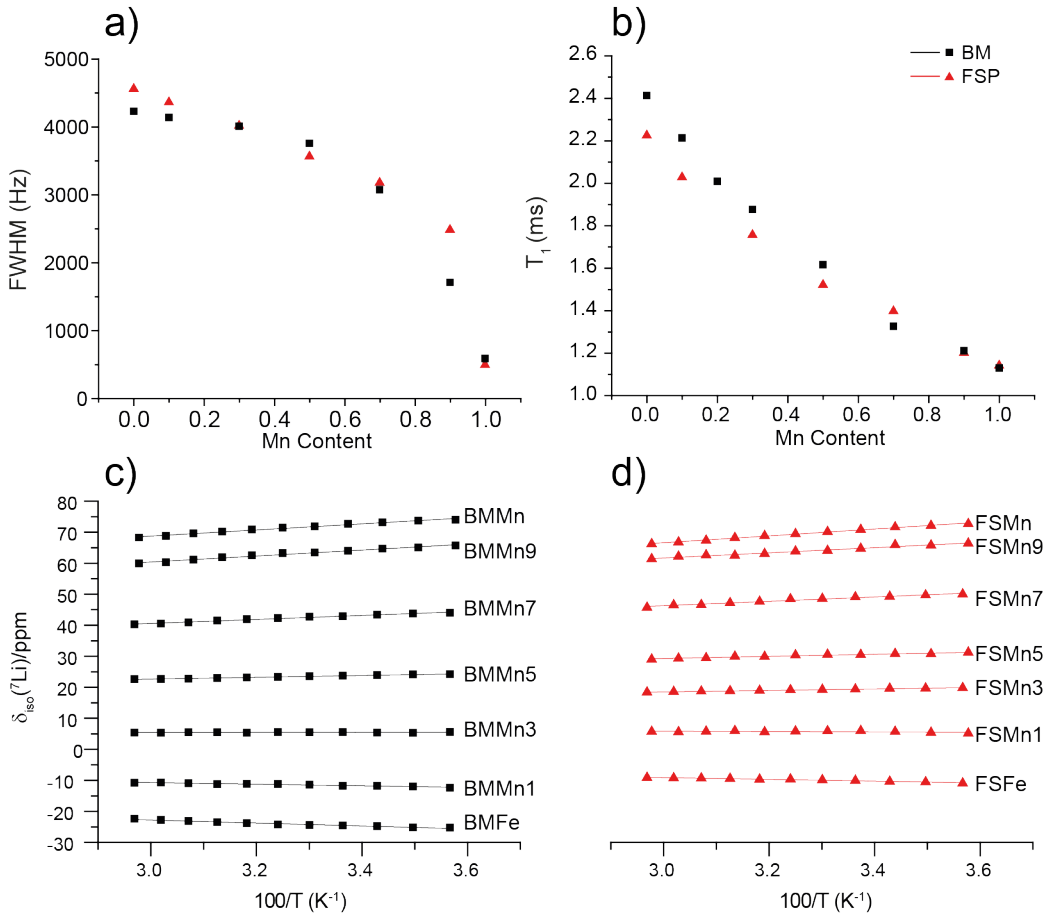

Figure 4.14: The variation in Mn content against the experientially determined ^{7}Li parameters where (a) demonstrates the change in FWHM, (b) the change in T_1 and the effect on δ_{iso} of ^{7}Li for (c) ball milled and (d) flame spray series.

As seen in Figure 4.14(b), the increase in Mn content gives a decrease in the ^{7}Li T_1 observed. As evident in Section 3.1.3, the source of paramagnetic relaxation enhancement is determined by the proximity between the nuclear and electron spin, and the paramagnetic centre density. It is known that the Fe^{2+} paramagnetic centre has a lower electron density than Mn^{2+} [118], and this is the primary reason for the reduction of T_1 in the high Mn materials. However, there are some subtle differences in the T_1 of the BM and FSP materials, as high Fe content the BM material has slightly higher T_1 values. This is due to the contraction of $LiFePO_4$ unit cell in the FSP materials, as determined from XRD (*vide infra*, Figure 4.15).

A change in the δ_{iso} of the ^{7}Li resonances is also observed when the Mn content is varied. As highlighted in Figure 4.14(c) & (d), the δ_{iso} shift varies from, 75 ppm in the LMP system to -22 ppm in the LFP material. It is observed that the

Table 4.4: The unit cell parameters and unit cell volumes determined by Rietveld refinement for the $LiMn_xFe_{1-x}PO_4$ ($0 \leq x \leq 1$) phase in both the BM and FSP materials.

Sample	a (Å) ±0.0005	b (Å) ±0.0005	c (Å) ±0.0005	Volume Amount (Å^3) ±0.04
BMMn3	10.3755	6.0404	4.7113	295.27
BMMn5	10.4034	6.0661	4.7357	298.86
BMMn7	10.4317	6.0857	4.7396	300.89
FSMn3	10.3670	6.0353	4.7094	294.66
FSMn5	10.3859	6.0524	4.7207	296.74
FSMn7	10.4115	6.0726	4.7304	299.08

LFP samples BMFe and FSFe have comparable isotropic shifts to their equivalent final products (Section 4.3.1).

Upon substitution of Fe with 10 % Mn into the olivine structure, a change in isotopic shift is observed with the resonance moving towards pure LMP. The increased substitution results in a continuation of this effect with the resonance shifting closer to the δ_{iso} of LMP. This increase in ^{7}Li isotropic shifts, is due to an increase in spin density observed at the Mn^{2+} nucleus, when compared to the Fe^{2+} nucleus [118]. This substitution effect is the same in the BM and FSP series. However, a narrower range of shifts is observed for the FSP series. This is most significant towards the Fe doped materials with BMFe and FSFe having similar shifts to their analogous materials in Section 4.3.1, indicating a similar difference in the $LiFePO_4/FePO_4$ content. Rather than the difference of ∼10 ppm for pure $LiFePO_4$, for $LiMnPO_4$ materials (BMMn and FSMn) only a 2 ppm difference is observed, suggesting a smaller difference in $LiMnPO_4/MnPO_4$ content.

The XRD patterns given (Figure 4.15(a)-(f)) for three of the BM and FSP analogues contain no measurable impurities. Each contain an olivine $LiMn_xFe_{1-x}PO_4$ phase with the unit cell volume and unit cell parameters, determined from Rietveld refinement, given in Table 4.4. The cell parameters for the olivine phase can be observed to expand upon increasing Mn dopant (Figure 4.15(g)), this is consistent with literature [142]. However, as in Section 4.3.1, the FSP materials have a lower cell volume than their BM analogues. This is attributed to less Li^+ in the unit cell of the FSP materials resulting in the difference in ^{7}Li shifts between BM and FSP analogues. As noted above, substitution of Fe^{2+} for Mn^{2+} results in the ^{7}Li isotropic shifts increase with Mn substitution, due to changes in the spin density of

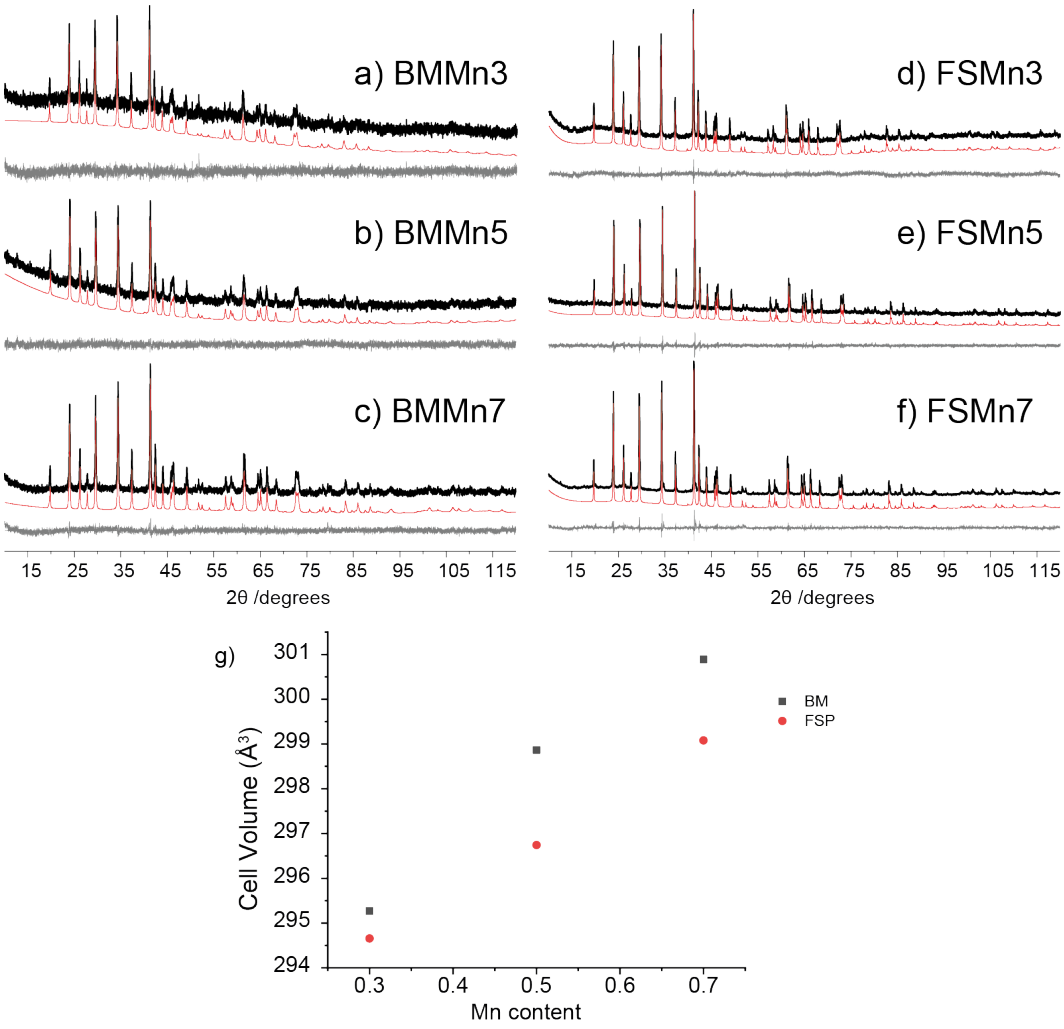

Figure 4.15: The XRD patterns for (a)BMMn3, (b)BMMn5, (c)BMMn7, (d) FSMn3, (e) FSMn5, (f) FSMn7. The unit cell volumes of the $LiMn_xFe_{1-x}PO_4$ $(0 \leq x \leq 1)$ phase shown with increasing Mn content is given in (g).

Table 4.5: The magnetic susceptibility (χ_{mass}) measurements of the $LiMn_xFe_{1-x}PO_4$ BM and FS series with the amount of particles N, made up of n amount of magnetic moments of γ-Fe_2O_3.

Sample	χ_{mass} m emu/g	N ppm	n	T_N K
BMFe	12.74	11.63	1465	51
BMMn1	5.99	0.63	4445	50
BMMn3	6.50	0.21	2875	47
BMMn5	6.77	0.32	1597	44
BMMn7	6.98	1.10	1626	40
BMMn9	7.40	0.19	1704	36
BMMn	7.17	-	-	35
FSFe	3.35	-	-	51
FSMn1	5.89	-	-	49
FSMn3	5.97	0.05	2703	47
FSMn5	6.29	0.14	3653	43
FSMn7	8.14	0.66	1322	39
FSMn9	7.56	8.65	934	38
FSMn	7.56	-	-	35

Mn^{2+} vs Fe^{2+} [118].

It is observed (Figure 4.16), that the majority of samples appear to have characteristic evidence of ferromagnetic impurities. To aid observation of this ferromagnetic impurity the M(H) data displayed (Figure 4.16) was restricted from 0 to 1 T, with the full data collected (up to 5 T) available in the Appendices (Figure A.2). For the BM materials, this is strongly exhibited in the BMFe and BMMn1 spectra. However, every sample in this series, excluding BMMn, exhibits some ferromagnetic character. Since all the BM samples containing Fe exhibits this ferromagnetic impurity for this series, we can confirm that we are observing the same γ-Fe_2O_3 particles discussed in Section 4.3.1.

As noted in Section 4.3.1, where BMCC also exhibits the magnetic build up of M(H) due to the γ-Fe_2O_3 impurity, the use of Equation 4.2 allows the determination of χ_{mass}, meaning the size and amount of magnetic particles can be calculated. Figure 4.16 contains the fits of the M(H) plots and the resulting magnetic properties are shown in Table 4.5. In cases where there was no evidence of impurities, a linear fit was used to determine the χ_{mass} (Equation 4.1).

In the BM series, as Mn is substituted for Fe, a general reduction in the magnetic particles is observed (Table 4.5). This would identify it as an Fe related issue, and due to either contaminants in the Fe precursor, or created as a result

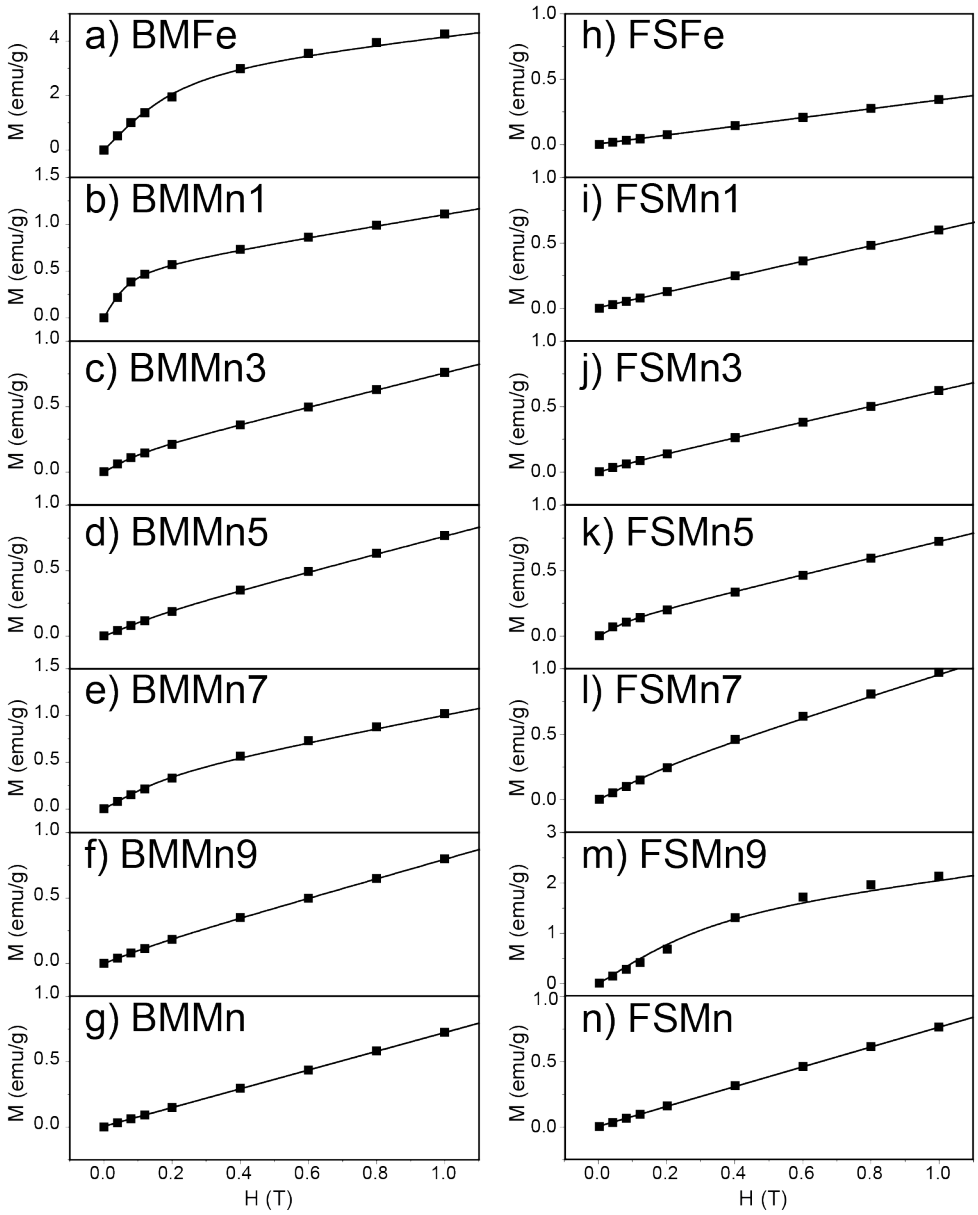

Figure 4.16: The M(H) data for increasing Mn content where (a)-(g) is the ball milled (BM) series and (h)-(f) is the flame spray pyrolysis (FSP) series. Data was collected at 300 K and up to 5 T. For (g), (h), (i) and (n) no ferromagnetic particles were observes so a linear relationship was used to determine χ_{mass} (Equation 4.1). However, evidence for ferromagnetic impurities were observed in (a)-(f), and (j)-(m), so Equation 4.2 was used to determine χ_{mass}. The plot is restricted to 1 T to highlight evidence of ferromagnetic impurities in the sample. The full 5 T data recorded is available in the appendices (Figure A.2)

of the synthesis reaction. Further investigations into LFP produced with varying reaction parameters, or different Fe sources, of the BM method would clarify this.

As in Section 4.3.1, no definitive trend relates the χ_{mass} to the δ_{iso} of ^{7}Li for either the BM or FSP series. In the BM series, excluding BMFe and BMMn, increasing the Mn ratio results in a corresponding increase in the χ_{mass} and ^{7}Li isotropic shifts. However, as neither end members of the series support this observation this can be determined as not a significant factor relating to changes in ^{7}Li isotropic shifts.

The M(H) FS samples exhibit similar magnetic properties to what is observed with the BM samples. For greater Mn content, a corresponding increase in χ_{mass} and δ_{iso} (^{7}Li) is generally observed. However, as seen in the BM series, some samples do not agree with this trend, namely FSMn9 and FSMn. Ferromagnetic impurities are also observed in several samples, with FSMn3 and FSMn5 exhibiting a minimal amount of impurities and FSMn7 and FSMn9 showing quantities comparable to the pure Fe samples (Section 4.3.1). A key difference from the BM series, is that as the Fe content decreases, the impurities increase. This gives further credence that for high Mn ratios (during the FS synthesis), improper synthesis occurs causing formation of $LiFePO_4$ and generation of a small γ-Fe_2O_3 impurity.

The M(T) data for this series are displayed in Figure 4.17. Both the BMFe and FSFe samples exhibit characteristic anti-ferromagnetic ordering, with an agreement with the T_N of 50 K observed previously (Figure 4.10) and in literature [86,141]. The hysteresis observed is similar to the M(T) data presented in Section 4.3.1 for the BMCC sample (Figure 4.10). As discussed earlier, this hysteresis is further evidence of a γ-Fe_2O_3 impurity (Figure 4.16) [83]. As noted in Section 4.3.1, this is not evident in the FSFe sample (Figure 4.3), due to the different synthesis mechanisms and the differing starting materials used.

For the end member of the series, LMP, most of the literature shows similar M(T) results as observed in Figure 4.17 [144–146]. This results in similar magnetic properties to those seen for LFP, but with a decrease of T_N to 36 K. For both the BM and FS series, the change in T_N is reported in Table 4.5 and this linearly changes between the Fe and BM end members.

A sudden drop in the field cooling measurement for FSMn is observed (Figure 4.17) at the T_N. This has been observed before by Xiao *et al.* [145], who determined it was caused by a large increase in carbon coating coverage. As this effect is only seen in the FSMn sample, this indicates that the carbon coating procedure for this sample coated the material produced an abnormally high amount of particle coverage.

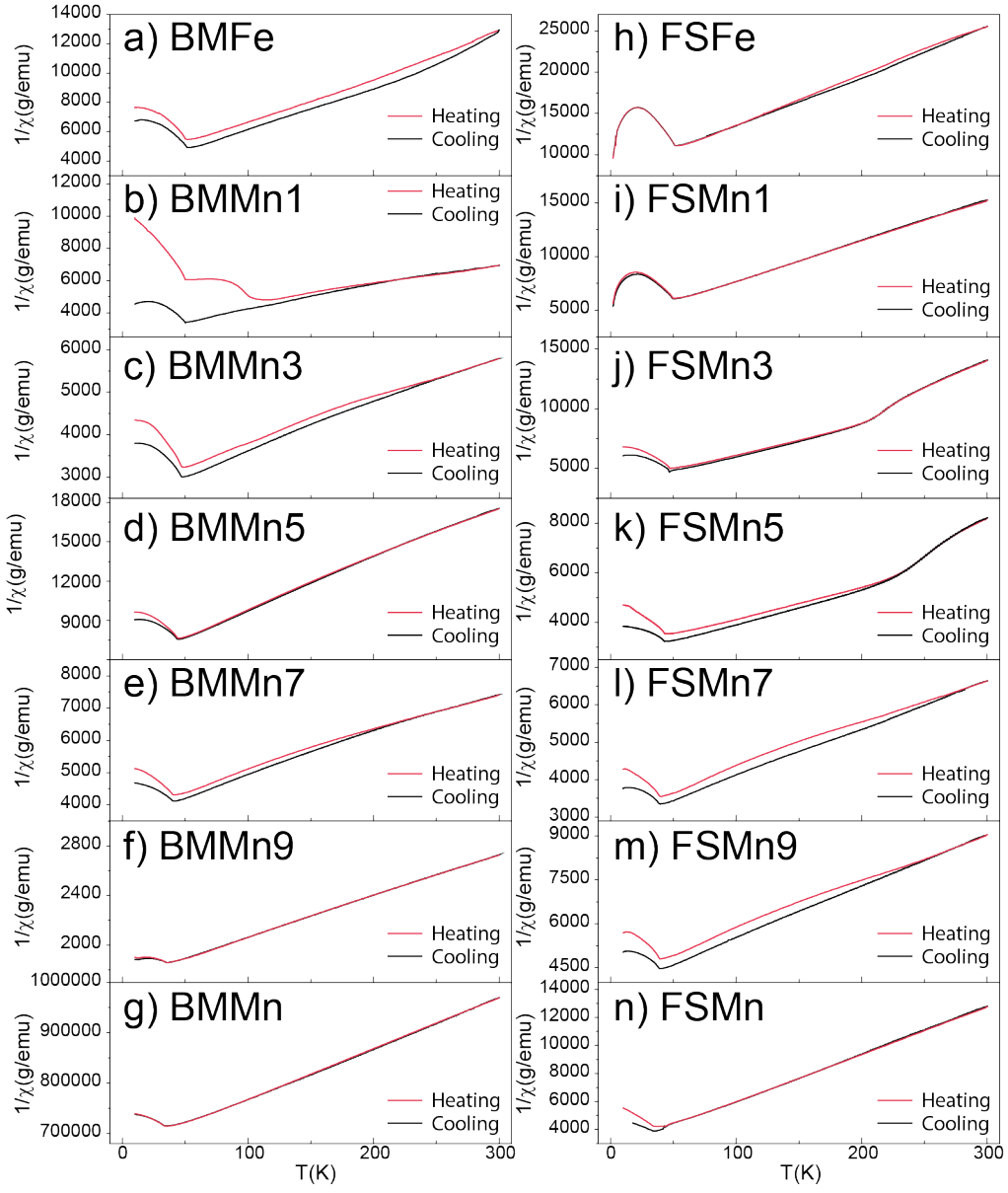

Figure 4.17: The M(T) data for increasing Mn content where (a)-(g) is the ball milled series and (h)-(f) is the flame spray pyrolysis series.

For the majority of the BM series hysteresis is observed in the M(T) data (Figure 4.17). Although BMMn5 and BMMn9 barely exhibit any hysteresis, which is a confirmed by the M(H) data (Figure 4.16 and Table 4.5). The LMP end member of this series, BMMn, contains no Fe and no hysteresis is observed, confirming the M(H) results (Figure 4.5), indicating no γ-Fe_2O_3 is present.

Some hysteresis is also observed in the four FS samples, largely in FSMn9 and FSMn7 and seen in lesser amounts for the FSMn5 and FSMn3 (Figure 4.17), mirroring the M(H) data (Figure 4.16). This is further evidence that synthesis of $LiMn_xFe_{1-x}PO_4$ with high amounts of Mn to Fe ratios, by the FSP method results in formation of some γ-Fe_2O_3.

Two samples in the FSP series, FSMn3 and FSMn5, exhibit a magnetic dampening of their M(T) beginning at relatively high temperatures (Figure 4.17). This magnetic dampening indicates a phase change in the material. This behaviour has been observed in solvothermally produced versions of $LiMn_{0.5}Fe_{0.5}PO_4$, where it has been attributed to Fe_2P and FeP impurities [142,143]. Small amounts of Fe_2P (3 wt %) have been shown to aid conductivity of LFP, however increasing quantities up to 5 wt % or above decreases the capacity of the cathode material [97]. As no measurable impurities were detected in the XRD patterns (Figure 4.15), we can assume that the amount of Fe_2P present is significantly below this level.

From all these results it is clear that the two differing methods, BM and FSP, generate materials with varying environments. For the FS materials, several factors point towards high Mn levels disrupting the formation of $LiMn_xFe_{1-x}PO_4$. In the BM series, every sample containing Fe has a nominal amount of γ-Fe_2O_3 present, but with a general reduction in quantity as the Mn contribution increases in the series. However, with the FS series these magnetic impurities are observed prominently in FSMn9, but reduce to minimal amounts with the reduction in Mn content. For FSMn9 (Figure 4.11) the distribution of the ^{31}P sites shows the formation of some LFP and LMP with a small amount of site 2 and 3, whereas BMMn9 has a ^{31}P resonances closer to the random distribution observed by Clément *et al.* [118] for $LiFe_{0.25}Mn_{0.75}PO_4$. This indicates that FSMn9 does not contain an average distribution of sites. This is also observed in another FSP sample, FSMn7, which also exhibits a change in distribution of the ^{31}P sites when compared to the BMMn7 sample. Although there is no evidence of a $LiFePO_4$ resonance (Group 8, Figure 4.12) present in the spectrum of FSMn7. However, FSMn7 does contain a significant amount of magnetic γ-Fe_2O_3 particles, explaining the resulting change in ^{31}P group distribution.

4.3.3 Vanadium Doped Lithium Iron Phosphates

As discussed in Section 4.1.3, doping LFP to change its properties has been attempted before by doping the V^{3+} ion in aliovalent and isovalent sites [74, 109, 110]. This investigation focuses on the promising results seen from the V doping in the transition metal rich $Li_{1-3x}[V_xFe]PO_4$ material [109]. However, as the resulting material contains some Fe occupying the Li site, efforts have been made to reduce this effect with a modified $Li_{1-3x}[V_xFe_{1-x}]PO_4$ composition.

To investigate the increasing effect of the dopant has on the resulting material compositions, LFP containing 1, 3 and 5 mol% V levels were produced, corresponding to x values of 1, 3 and 5 (LFVP1-N, LFVP3-N and LFVP5-N) in the $Li_{1-3x}[V_xFe_{1-x}]PO_4$ system. For each of these dopant levels, the amount of the Li precursor Li_2CO_3 was varied with composition as given in Table 4.1. The subsequent increase and decrease of Li_2CO_3 from stoichiometric amounts is to investigate any impurities that are created due to improper Li levels. As noted in the literature, calcination of the particles was limited to 600 °C, to limit the production of the unwanted $Li_3V_2(PO_4)_3$ or Fe_2P phases. [110]

The XRD results (Figure 4.18) show that every sample synthesised contains an olivine LFP-type phase (LFVP). This phase, indicated by •, is even prominent in materials with stoichiometry matching the desired material, $Li_{1-3x}[V_xFe_{1-x}]PO_4$. This is the only phase observed in the XRD for three samples which contain the largest increase in Li from stoichiometric amounts (LFVP3-8E, LFVP5-10E and LFVP5-14E), indicating formation of non olivine phases resulting from low Li levels during the synthesis.

Apart from the three highest amounts of Li stoichiometry (LFVP3-8E, LFVP5-10E and LFVP5-14E), a triclinic $Fe_2P_2O_7$ phase (‡) has been identified in the XRD pattern. This has been used as a synthesis route for producing LFP, with $Fe_2C_2O_4$ and $NH_4H_2PO_4$ used in a solid state procedure forming the intermediate $Fe_2P_2O_7$ phase [147]. The solid state synthesis then uses $Fe_2P_2O_7$ and a stoichiometric amount of Li_2CO_3, to produce single phase LFP. Interestingly, these are the same Fe, P, and Li precursors used in this work to produce the V doped LFP phase. Therefore, an excess Li_2CO_3 is used to create the single phase V doped LFP, it is reasonable to believe that $Fe_2P_2O_7$ is generated as a result of the lack of Li precursor.

One sample, LFVP5-3D, contains numerous extra reflections in the XRD pattern, many of which cannot be suitably assigned to known compounds using pattern matching. However, one impurity, a monoclinic form of $Li_3V_2(PO_4)_3$ can be identified and is represented with † in Figure (4.18). As noted in the literature,

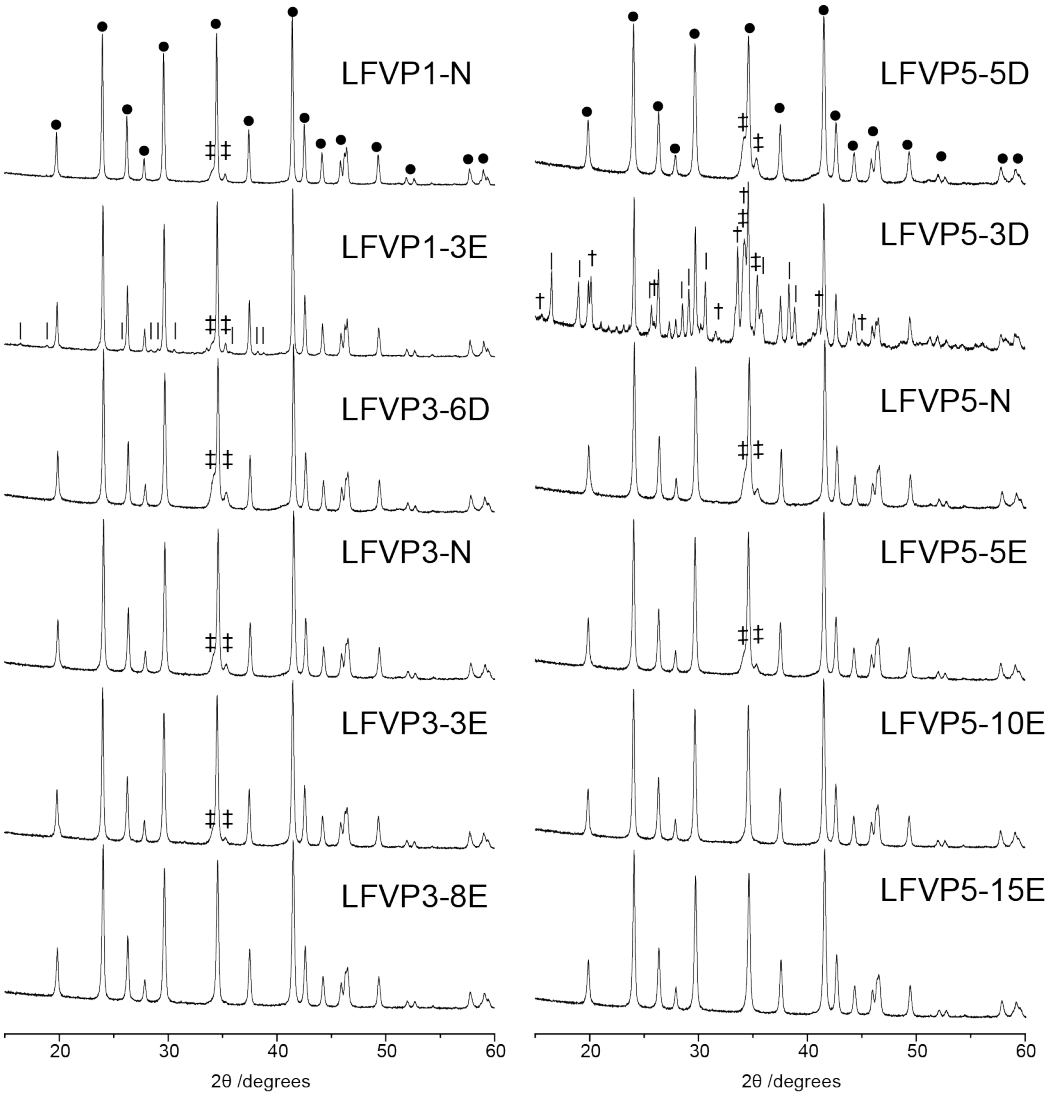

Figure 4.18: The X-ray diffraction patterns of V doped LFP. The • symbol represents an olivine LFP-type phase (LFVP). The ‡ symbol represents $Fe_2P_2O_7$. The † symbol marks the diffraction pattern of the $Li_3V_2(PO_4)_3$ impurity. The | symbol represents an unattributed reflections.

formation of $Li_3V_2(PO_4)_3$ is the result of calcination temperatures greater than 700 °C [110]. While, $Li_3V_2(PO_4)_3$ has been noted as a potential cathode material, it is still an unintended phase [85]. As these impurities are not present in the sample with lower Li deficiencies than LFVP5-3D it is likely during one step, synthesis was incomplete, resulting in extra products.

An unidentified phase (|) is present in LFVP1-3E and LFVP5-3D. However, for LFVP1-3E, the observed reflections are barely above baseline noise, indicating the amount is minimal. For LFVP5-3D the reflections are significantly larger, indicating a greater amount of this phase is formed. This was checked against other common impurities observed in the literature, such as Fe_2P, FeP, Li_3PO_4, Fe_3O_4, and these are not observed in any of the samples [108, 110, 148]. The absence of any erroneous reflections in LFVP3-8E, LFVP5-10E and LFVP5-14E, suggests that doping of V into LFP was successful for these three samples.

The ^{31}P data (Figure 4.19) show, 4 distinct resonances across the series. However, only two resonances are observed for all compositions. The first of these resonances, (marked by • and observed at 3630 ppm) has the same isotropic shift observed in pure LFP (Section 4.3.1). As the dominant resonance observed, this indicates that most of the ^{31}P environments observed in the series do not get any additional shift contributions from nearby V. This is expected as at most only 5 mol% V was doped into the olivine structure, therefore most of the ^{31}P is not experiencing perturbations from V.

The other ^{31}P resonance observed in the whole series is at 4200 ppm (Figure 4.19). This resonance (▪) can be assigned to a ^{31}P close to a paramagnetic V^{2+} species, causing an additional paramagnetic shift for the nearby ^{31}P. This could be similar to group 7, observed in the $LiFe_{(x)}Mn_{(1-x)}PO_4$ series (Figure 4.12), which would confirm that V is being doped into the LFP lattice in this series. If this were true, then it is expected that a small amount similar to group 6, which corresponds to the R and T environments (Figure 4.12), would also be observed. A shoulder on a side-band visible at ∼5000 ppm, hints at the existence of this resonance. This is visible for every sample except LFVP5-3D where its presence is obscured by other features present. To confirm this, V dopant levels could be increased to higher mol%, which would result in this resonance gaining intensity. Another method would be to increase MAS speed to greater than the 60 kHz so that any possible spinning sidebands were separated from the main resonance.

The third ^{31}P resonance (†, δ_{iso} = 10,500 ppm) is only seen in samples that had the $Fe_2P_2O_7$ phase detected by XRD (Figure 4.18). We can then attribute this ^{31}P resonance to $Fe_2P_2O_7$. Again, as this is not observed for the highest Li

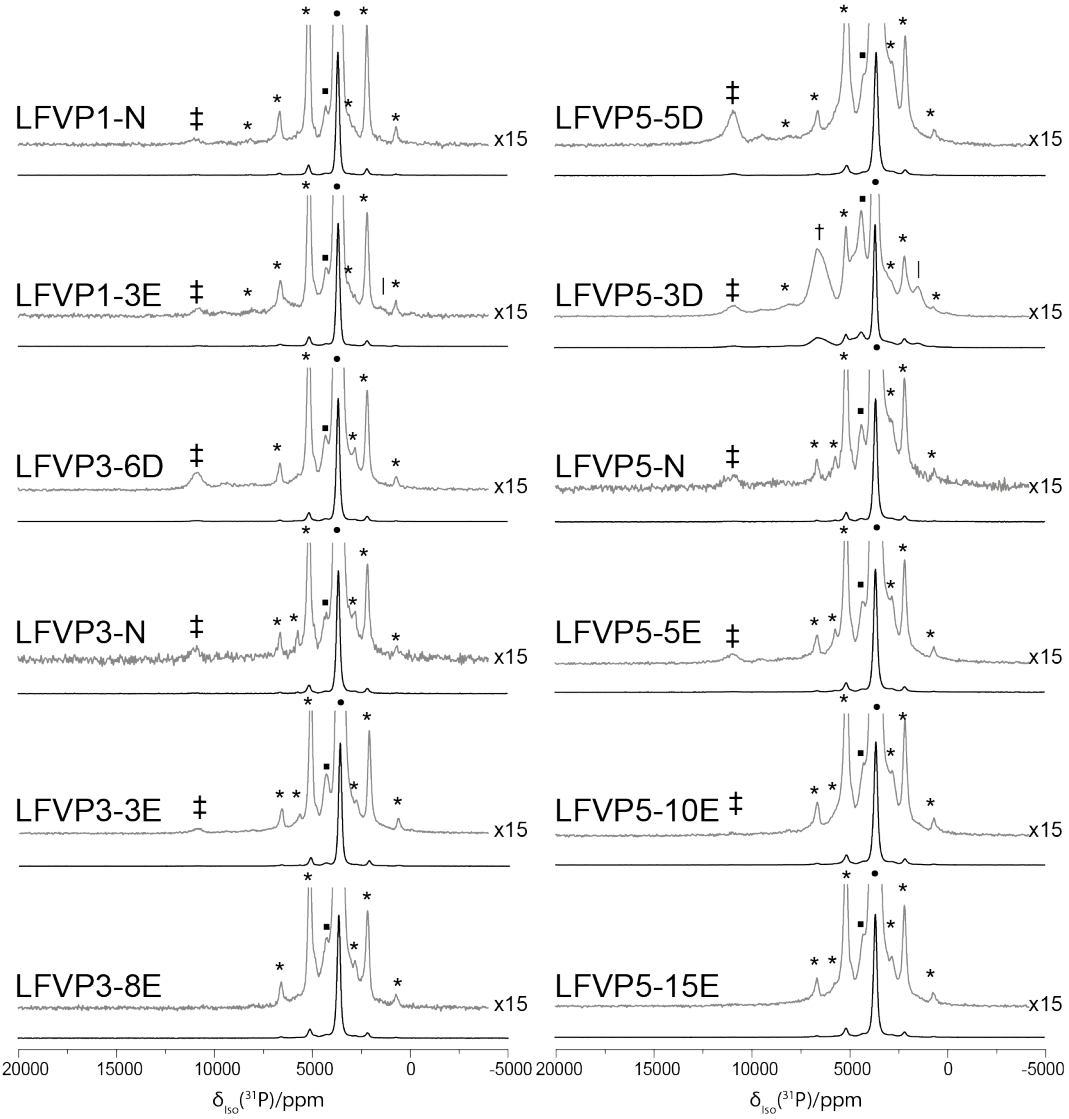

Figure 4.19: The ^{31}P Hahn-echo data collected at 60 kHz for the V doped series. The varible MAS determined resonances are indicated by the ‡, ▪, †, |, and • symbols, whilst spinning side-bands are given with an *.

stoichiometry (LFVP3-8E, LFVP5-10E and LFVP5-14E), this can rationalised by the low levels of Li.

A resonance |, is observable in the ^{31}P MAS NMR for both the LFVP1-3E and LFVP5-3D samples. Additionally, for LFVP1-3E the amount is significantly smaller indicating less of the impurity. This is similar to observation of unattributed reflections for these samples in the XRD (Figure 4.18). The occurrence of this resonance in only these two spectra would indicate the unknown phase consists of some phosphorus. However, the isotropic shift of the resonance ($\delta_{iso} = 1450$ ppm), indicates there are lesser paramagnetic shift contributions to the ^{31}P nucleus than other phases.

The final distinct ^{31}P resonance (†, 6500 ppm), is observed in a single sample, LFVP5-3D. This sample has evidence of monoclinic $Li_3V_2(PO_4)_3$ in the XRD data (Figure 4.18), suggesting that this peak could be be attributed to this resonance. However, ^{31}P MAS NMR data in the literature does not support this, giving 3 resonances observed at ∼4500, 2650, and 2000 ppm (4.7 T, unknown temperature) [149]. While, LFVP5-3D does have a large resonance at ∼4370 ppm previously assigned as V doped in the LFP structure (▪), the relative amount observed is larger than in other samples in the 5 mol% doped series. The larger amount of this resonance could be attributed to the first ^{31}P site of $Li_3V_2(PO_4)_3$, however, none of the other peaks from the literature are clearly observed in the spectrum [149]. The ^{7}Li measurements of the monoclinic $Li_3V_2(PO_4)_3$ have been shown to heavily depend on temperature, in turn resulting in a single peak when performed at 364 K, but 3 distinct peaks at 276 K. [150] While the experimental temperatures of the ^{31}P measurement by Cahill *et al.* [149] were not stated, other experiments in this work were performed between 167-199 K. Therefore, it is possible that the ^{31}P measurements were performed significantly colder than the 340 K experiments performed here. This would affect the structure, causing a phase transformation and hence a change in the shift of the ^{31}P resonances. Therefore, the phase marked by † is a high temperature phase of monoclinic $Li_3V_2(PO_4)_3$.

The ^{7}Li Hahn-echo spectra (Figure 4.20(a)), give a single resonance for the majority of samples in the series. This resonance does not exhibit any major differences in δ_{iso} or peak shape compared to results seen in the previous Sections (4.3.1) & (4.3.2). However, the ^{7}Li resonance observed for LFVP5-3D exhibits a slight tailing towards higher ppm values, indicating that a distribution of sites is being observed, offering further support that the sample has not been synthesised correctly. This tailing could indicate the ^{7}Li in $Li_3V_2(PO_4)_3$ which has been previously observed at this temperature [150].

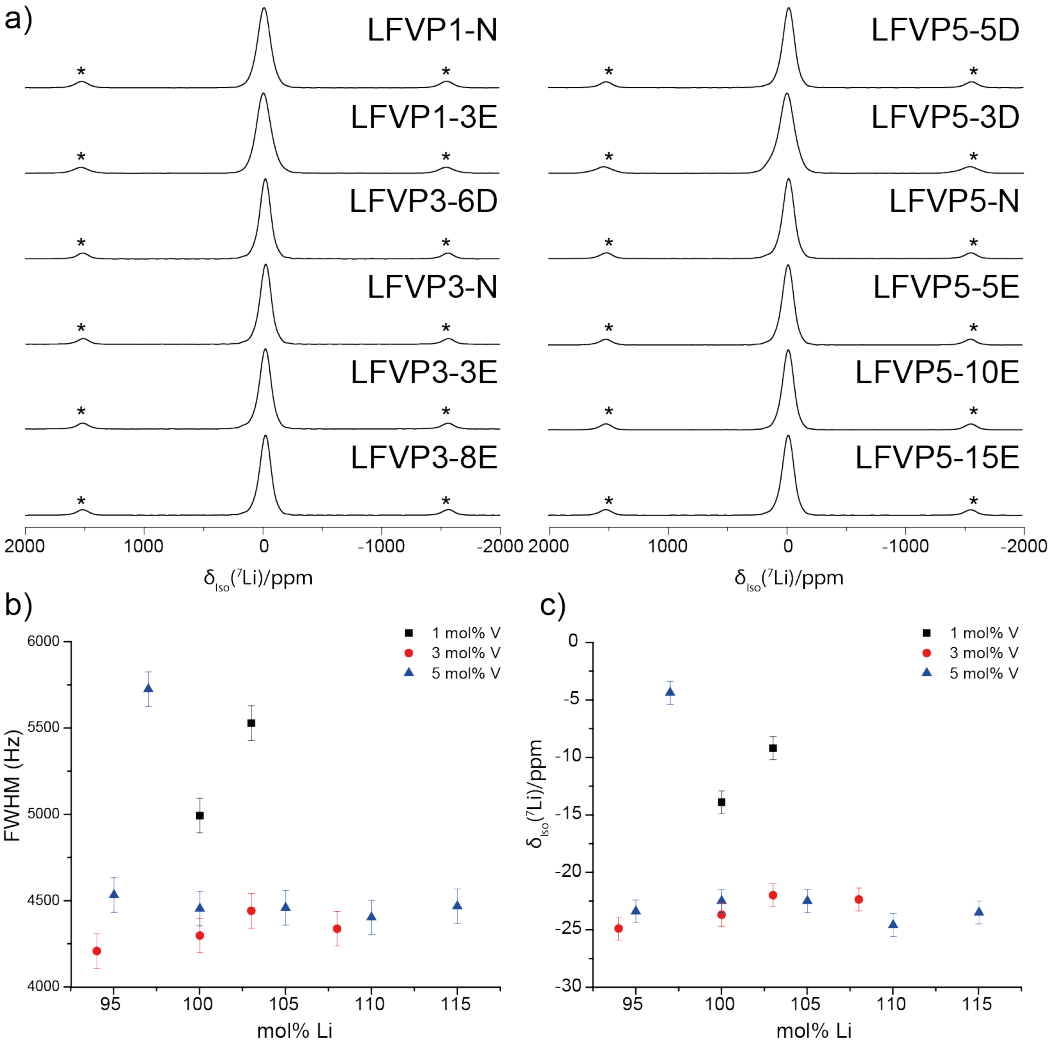

Figure 4.20: (a) The ^{7}Li Hahn-echo data collected at 60 kHz for the V doped series. The spinning side-bands are indicated with (*). The plots of (b) FWHM and (c) ^{7}Li δ_{iso} against Li stoichiometry is shown. All data included is obtained at 340 K to normalise the temperature dependence of the paramagnetic interaction.

Apart from LFVP5-3D which contains significant impurities, the 3 and 5 mol% V samples results in no major differences in FWHM (Figure 4.20(b)), with values falling in the 4400 ± 100 Hz range. This is repeated for the δ_{iso} shifts (Figure 4.20(c)), where no significant trends or changes occur for all 3 and 5 mol% samples excluding LFVP5-3D. This suggests that the ^{7}Li environment is not significantly different for these two series. However, as noted, LFVP5-3D does have significantly larger FWHM values than the rest of the series. The differences noted for LFVP5-3D is likely due to the impurities present arising in a larger distribution of ^{7}Li, which is clearly observed from observation of the spectra (Figure 4.20(a)).

However, for 1 mol% V, large differences are observed in the ^{7}Li results between the two samples and for the higher V doped materials. The FWHM results show not only significant differences between the 100 and 104 mol% Li stoichiometries, but an increase in width from the 3 and 5 mol% V samples. This change is also mirrored with the δ_{iso} of the resonances, as these significantly differ between the samples. This is evidence of an extra phase, as seen in the XRD results (Figure 4.18) of the LFVP1-3E sample.

4.4 Conclusions

This work has clearly shown the strength of a multi technique approach for investigating the differences arising in LFP produced from different synthesis routes. Each of the analytical techniques used provides different structural information about the changes arising between samples when synthesised from solvothermal, ball milled and flame spray pyrolysis routes.

Through ^{7}Li solid state NMR measurements, clear differences are apparent between the samples. This ^{7}Li shift difference is apparent between BM, FSP and ST samples (Section 4.3.1) and relates to contracting of the $LiFePO_4$ unit cell volume. A large change in δ_{iso} is also observed upon increasing Mn substitution in both the BM and FSP series. The substitution of Fe^{2+} with Mn^{2+} corresponds to a subsequent increase in ^{7}Li δ_{iso}, due to greater spin density of the Mn^{2+} nucleus. However, there are still significant differences arising between individual BM and FSP methods relating to change in unit cell volume.

As χ_{mass}, determined by M(H) measurements, has no direct correlation with δ_{iso} of ^{7}Li NMR shifts, we can attribute the difference observed to other contributions. We have shown that carbon coating and crystallite size are not factors contributing towards this change, therefore this difference in δ_{iso} is attributed to changes LFP cell volume, as contributions towards the paramagnetic shift (Section

2.4.5) depend on distance and position relative to the paramagnetic nucleus.

This ^{7}Li effect is less apparent in the V doped series (Section 4.3.3), where no significant differences exist between the ^{7}Li spectra for the 3 and 5 mol% doped series. While a change in shift is observed from the 1 mol% samples, thus further samples are needed to be produced at this level to confirm these differences. However, in samples that contain high amount of impurities, such as LFVP5-3D, a greater deviation in ^{7}Li δ_{iso} and FWHM from the rest of the series is clearly observed. This clearly demonstrates the sensitivity of the ^{7}Li to subtle changes in the local environment.

While the ^{31}P resonance does not demonstrate the same sensitivity to subtle structural changes observed between the FS, BM and ST synthesis methods, any changes to the nearby Fe^{2+} site are clearly observed as a change in δ_{iso}. This is clearly apparent in both the Mn substituted LFP (Section 4.3.2) and the V doped series (Section 4.3.3) with even small changes of Fe through the dopant influencing the observed shift. Furthermore, common phosphorus containing impurities, such as $Fe_2P_2O_7$ and $Li_3V_2(PO_4)_3$, can also clearly be observed. While Fe_2P is not observed by ^{31}P MAS NMR it is clearly seen as a magnetic dampening influencing the M(T) results. The use of M(T) and M(H) measurements can substantiate small quantities of Fe_2P and also identify any ferromagnetic particles present, such as γ-Fe_2O_3, not observed by other methods.

Resulting from this we can determine several things about each synthesis method. The FSP method generally produces LFP with no detectable impurities compared to the majority of BM samples that contain γ-Fe_2O_3 particles. However, replacing Fe^{2+} in LFP with Mn^{2+}, this effect changes. In BM materials, decreasing Fe reduces the amount of γ-Fe_2O_3 observed. This is just an extension of Fe reduction in the system. While, FSP exhibits the opposite effect, when the Fe amount is reduced some magnetic particles form. For the FSMn9 material, some clustering of LFP is observed, while this could indicate erroneous synthesis, the increase of γ-Fe_2O_3 in the FSP series does indicate issues at the largest Mn concentrations.

In the V-doped series, the initial $Li_{1-3x}Fe_{1-x}V_xPO_4$ synthesis did not produce V-doped LFP without impurities. However, three samples LFVP3-8E, LFVP5-10E and LFVP5-14E did produce single phase doped LFP, indicating that excess Li is needed. As no single phase was observed for the 1 mol% Li samples, the excess was too limited in these samples. It would be interesting in the future to see if increasing the excess up to 8 % (Like LFVP3-8E), would give a single phase.

The multitude of techniques clearly demonstrate an ability to accurately determine a series of common impurities present in doped, substituted and single

phase LFP.

Chapter 5

Using ^{17}O NMR to Monitor the Incorporation of Ca^{2+} and Zn^{2+} in Stöber Nanoparticles

5.1 Introduction

Biodegradable, bioactive nanoparticle's have been shown to have great potential for intracellular delivery of ions [151]. Using beneficial cations, this intracellular delivery of ions can have therapeutic benefits, including the stimulation of osteogenesis and angiogenesis [152, 153]. Other cations have also been introduced into these nanoparticles that incorporate antibacterial properties [154]. A popular method to produce bioactive nanoparticles is through sol-gel based methods [153, 155, 156].

Bioactive nanoparticles have developed as an offshoot of the original bioglass system developed by Hench in 1971 [153, 157]. Implantation of this eutectic mix of SiO_2, CaO, Na_2O, and P_2O_5 into bones, resulted in the formation of a bond so strong that it could not be removed without breaking the bone [153, 158].

These sol-gel based bioactive nanoparticle glasses differ from the original bioglass and other melt quench glasses in there overall structure and purpose. Whilst, melt quench glasses tend to be dense, sol-gel materials have an inherent nanoporosity [159]. This increased nanoporosity results in a higher specific surface area, exhibiting greater cellular responses upon uptake [160]. In addition, sol-gel form nanoparticles at room temperature bypassing the need for Na_2O, which is used to lower the melting point in melt quench glasses, making their composition much simpler. By lowering the melting point using Na_2O, the intracellular ability of the glass improves. However, this is not required for sol-gel based systems as the high surface

area results in greater dissolution rates [153].

Synthesising these particles by a subset of the sol-gel methods, the Stöber process, the size, and morphology of the particles can be carefully controlled [161]. The Stöber method was originally developed by Stöber *et al.* in 1968 [162] to produce monodispersed particles of silica. Although this rugged process is related to sol-gel methods, it has one key difference. Using an alkaline catalysed reaction, the presence of OH^- ions result in repulsive forces which produce monodisperse silica spheres [162]. This process can then be controlled to produce spheres with a desired size by adjusting this alkali concentration [161].

The insertion of ions is a non-trivial process, as many methods produce irregular morphology or agglomeration of these originally spherical particles [163, 164]. However, it has been shown, with sufficient control over the reaction parameters, that it is possible to create particles with calcium monodispersed through the particle [161].

Solid state NMR studies on of melt-quench glasses and sol-gel nanoparticles has been an active research area for a while. Solid state NMR's strength to investigate local structural changes make it a powerful technique probing disorder in a wide range of materials [18, 20]. The first investigations into the original bioglass system, utilised ^{23}Na, ^{29}Si and ^{31}P MAS NMR to determine the preferred arrangement of the cationic species [165]. Along with ^{1}H MAS NMR, these are some of the most commonly studied nuclei for these systems [156]. The use of ^{29}Si MAS NMR can give information about the various Q^x species present in the glass (where x is equal to the amount of other O-Si species attached to the silicon unit under study) [166]. While the initial formation of Stöber particles has been investigated using ^{13}C and ^{29}Si liquid state NMR, no direct probes have monitored the introduction of ions this way [167].

While ^{17}O solid state NMR has been performed on bioactive glasses and sol-gel glasses, relatively little has been performed on Stöber nanoparticles [168]. Previous studies have mainly focused on determining the Q speciation of the silica (using ^{29}Si MAS NMR) [161, 169–171]. This could be attributed to low natural abundance of the ^{17}O isotope thus requiring enrichment to perform solid state NMR measurements. Using a combination of NMR, TEM and DFT calculations this work will focus on monitoring incorporation of Ca and Zn in the Stöber particles before and after the calcination step in the synthesis.

Table 5.1: Summary of the Stöber particles produced with different cation ratios.

Sample	Ratio of Ca/Zn : Si	Ion incorporation
Undoped	0:1	Undoped
10 % Ca	1.3:1	10.0 mol% Ca
10 % Zn	1:1	10.0 mol% Zn
20 % Zn	3:1	20.0 mol% Zn

5.2 Experimental

5.2.1 Particle Synthesis

To obtain uniform 100 *nm* Stöber particles, synthesis was carried out using a previously detailed method [161]. For the ^{17}O MAS NMR measurements isotropically enriched water (Cortecnet, 40 mol%) was substituted into the initial particle synthesis. All other reagents were purchased from Sigma-Aldrich. To create the non-calcined particles ethanol (ethyl alcohol, 200 proof, $\geq$99.5%), $H_2{}^{17}O$, and ammonium hydroxide (ACS reagent, 28.0-30.0 % NH_3 basis) were mixed in a ultrasonic bath at room temperature. After 10 minutes TEOS (tetraethyl orthosilicate, reagent grade, 98%) was added to the solution and the solution was left until the particles reached the desired size of 100 nm (determined by dynamic light scattering, DLS).

The solution was then centrifuged to obtain a solid pellet of particles, which was dried overnight at 60 °C. For the particles containing 10 mol% calcium, particles were first redispersed in distilled water and calcium nitrate tetrahydrate (ACS reagent, 99%) was then added to the solution. After 20 min, the particles were centrifuged again, the supernatant was removed and the pellet was dried at 60 °C overnight, as before. For the 10 and 20 mol% zinc particles zinc nitrate hexahydrate (Reagent grade, 98%) substituted the calcium precursor. The ratios of Ca and Zn added to the silica particles are given in Table 5.1.

Particles were then heated in an argon atmosphere at 680 °C for 3 hours, at a heating rate of 3 °C min^{-1}. The 680 °C temperature was chosen for the removal of nitrate and incorporation of the Ca and Zn cations, without any crystallisation processes taking place. Particles were then washed 3 times in ethanol to remove any excess cations not incorporated into the network. This is what you would consider to be the final stage of preparing Stöber particles and will be referred to as post-calcined henceforth.

5.2.2 HRTEM

Nanoparticles were dispersed in ethanol by applying sonication (30 s). A 5 µL ethanol suspension of nanoparticles were then drop-cast on a 300 mesh holey carbon TEM grid (TAAB), and dried under vacuum for transmission electron microscopy analysis. High resolution TEM (HRTEM) imaging was carried out using a FEI Titan 80-300 scanning/transmission electron microscope (S/TEM) operating at 80 kV, and fitted with a Cs (image) corrector.

5.2.3 Solid State NMR

All ^{29}Si single pulse MAS NMR measurements were performed at 7.0 T using a Varian/Chemagnetics InfinityPlus spectrometer operating at a Larmor frequency of 69.62 MHz. These experiments were performed using a Bruker 7 mm HX probe which enabled a MAS frequency of 5 kHz to be implemented. Flip angle calibration was performed on kaolinite from which a $\pi/2$ pulse time of 5.5 μs was measured. All measurements were undertaken with a $\pi/2$ tip angle along with a delay between subsequent pulses of 240 s. For CPMAS measurements for the ^{1}H pulse a Larmor frequency of 300.1 MHz was used. A $\pi/2$ pulse of 2.5 µs was used with a polarisation from a ramp between 75% and 100% on the ^{1}H channel for a contact time of 4 ms. This enabled a delay between subsequent pulses of 4 s. For both single pulsed and CPMAS experiment heteronuclear decoupling was applied on ^{1}H during collection of the FID, where the decoupling frequency was equal to 100 kHz. All ^{29}Si centre of gravity (apparent) shifts were reported against the IUPAC recommended primary reference of Me_4Si (1% in $CDCl_3$, $\delta_{iso} = 0.0$ ppm) [137], via a kaolinite secondary in which the resonance is a known shift of -91.5 ppm [172].

All ^{17}O MAS NMR measurements were performed at 11.7 T using a Bruker Avance III spectrometer operating at a Larmor frequency of 67.80 MHz. The ^{17}O experiments were performed using a Bruker 3.2 mm HX probe which enabled a MAS frequency of 20 kHz to be implemented. All ^{17}O spectra were acquired with a rotor synchronised echo ($\pi/2$–τ–π) sequence, using a selective (solid) $\pi/2$ pulse time of 2 μs along with a recycle delay of 5 s. The 2D ^{17}O 3QMAS experiments were measured using a three pulse z-filtered pulse sequence. Typical pulse widths for the excitation, conversion and soft z-filter pulses were 4, 1.25 and 20 µs, respectively. Shearing of the MQMAS experiments was performed within the Bruker software using the standard conventions [42]. For the static experiments a Hahn echo sequence ($\pi/2$–τ–π) was employed with a τ delay of 5 µs. For the non-selective static experiments a $\pi/2$ pulse time of 5 µs was employed with a recycle delay of 1 ms. For the selective

static experiments a $\pi/2$ pulse time of 1.67 µs was employed with a recycle delay of 1 s. All ^{17}O centre of gravity (apparent) shifts were reported against the IUPAC recommended primary reference of D_2O (Neat, $\delta_{iso} = 0.0$ ppm) [137].

5.2.4 Density-functional theory calculations

To gain insight into the crystalline structure of the nanoparticles, density-functional theory (DFT) calculations were performed for various proposed crystallite structures. The DFT calculations utilised the CASTEP code which employs a combination of plane waves and pseudopotentials [173]. The calculations employed the PBE functional, a k-point spacing of 0.05, and energy cut off of 900 eV were used throughout. These values were chosen due to convergence of the final energy for single point calculations, and therefore would be sufficient for further geometry optimisation and NMR calculations. During geometry optimisation atomic coordinates and lattice parameters were varied until the structure was suitably relaxed. To obtain NMR shielding tensors, shifts and electric field tensor values, the MagRes task was employed from within the CASTEP code [174–176]. To make comparisons with experimental data, the calculated isotropic chemical shift $\delta(r)$ is defined as:

$$\delta(r) = -[\sigma(r) - \sigma^{ref}] \tag{5.1}$$

Where $\sigma(r)$ is the isotropic shielding determined from the CASTEP calculations and σ^{ref} is determined from the isotropic shielding of the same nucleus in a reference system. In this case we used a value of 250.4 ppm for ^{17}O which was determined by running a series of similar reference compounds with the same calculation parameters.

5.3 Results and Discussion

5.3.1 The Stöber Process (Non-Calcined)

To study incorporation of beneficial Ca^{2+} and Zn^{2+} cations into the Stöber nanoparticle, this investigation is primarily focused on 4 main samples. First, a sample with no doped cations added to the Stöber nanoparticle to act as a reference, called undoped. In addition, three nanoparticle samples with 10 mol% Ca, 10 mol% Zn and 20 mol% Zn were to be investigated. The 10% mol Ca nanoparticles were chosen as previous work [161], has noted that this is the maximum amount of Ca possible to incorporate using this method. However, Zn does not have such a low incorporation potential, thus enabling synthesis of a 20 mol% Zn Stöber nanoparticle. Knowing

Table 5.2: The Q species content, δ_{iso} shifts and network connectivity (NC) of the non-calcined and calcined Stöber particles determined by ^{29}Si MAS NMR

	Q^1		Q^2		Q^3		Q^4		
Samples	δ_{iso} [ppm]	I [%]	δ_{iso} [ppm]	I [%]	δ_{iso} [ppm]	I [%]	δ_{iso} [ppm]	I [%]	(NC)
Error	±0.1	±0.2	±0.1	±0.2	±0.1	±0.2	±0.1	±0.2	±0.02
Non-Calcined									
Undoped	-	-	-94.1	2.7	-103.3	26.0	-113.0	71.2	3.68
10 mol% Ca	-	-	-93.9	1.7	-102.3	26.4	-112.4	72.0	3.70
10 mol% Zn	-	-	-94.4	3.9	-102.9	26.5	-112.8	69.6	3.66
20 mol% Zn	-	-	-94.3	4.1	-103.2	31.1	-113.0	71.2	3.61
Calcined									
Undoped	-	-	-92.0	2.8	-99.8	10.6	-109.9	86.7	3.84
10 mol% Ca	-78.2	0.9	-87.8	4.8	-98.9	17.6	-109.8	76.7	3.70
10 mol% Zn	-79.1	0.8	-92.0	9.7	-101.0	21.6	-110.3	67.9	3.57
20 mol% Zn	-77.2	8.8	-87.8	7.4	-97.9	23.0	-110.0	60.8	3.36

this, a choice was made to investigate both a 10 mol% and a 20 mol% Zn sample to probe any possible differences in the structure and thus reasons for this extra incorporation.

From the analysis of the non-calcined Stöber particles, using ^{29}Si MAS NMR, the Si speciation can be determined. This gives information on the relative amounts, of the Q^m speciation in the particles, where m is determined as the number of bridging oxygens (BO) to the corresponding Si atom. Through this method we can determine how the addition of Ca or Zn into this stage of the synthesis affects the nanoparticle. At this early stage no differences between samples should be observed, as pre-calcination introduced cations should be on the surface of the nanoparticles and will not have penetrated the silica moieties.

As seen in the non-calcined ^{29}Si spectra (Figure 5.1), the nanoparticles are primarily dominated by a large amount of Q^4 units with a small amounts of Q^3 and Q^2 present. The ratios between different the Q^m sites (Table 5.2), show that the Stöber particle with no Ca or Zn added is composed of 71.2 % Q^4 units. The remaining 29 % is primarily made up of Q^3 units and a small amount of Q^2 units. By determining the network connectivity (NC) the average silicon oxygen bonds per sample can be quickly compared.

$$NC = \frac{(Q^1 + 2Q^2 + 3Q^3 + 4Q^4)}{100} \tag{5.2}$$

This NC formula calculates the average amount connectivity per sample,

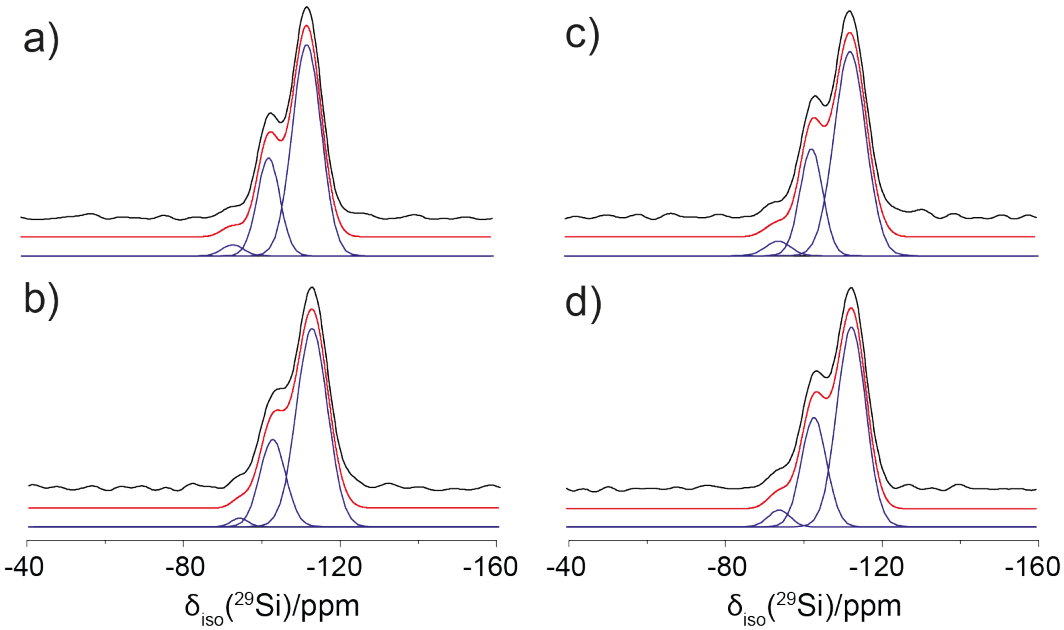

Figure 5.1: The ^{29}Si MAS NMR spectra of non-Calcined Stöber particles for (a) undoped, (b) 10 mol% Ca, (c) 10 mol% Zn and (d) 20 mol% Zn. The individual deconvolutions are shown in blue and the sum of these are marked in red.

where a NC of 4 is considered highly connected, and a NC of 1 is extremely unconnected. Utilising this determined value comparisons between the samples can then readily be made. For these non-calcined samples, little variation exists upon the addition of Ca or Zn. This indicates that in the non-calcined Stöber particles, the silicon network is not modified to any significant degree upon the addition of Ca or Zn thus the cations are just sitting on the surface. While there are slight changes in the Q^2 resonances of the 10 mol% Ca, overall the network connectivity is still within error of the pure silicon samples, indicating no overall structural change has taken place on cation doping.

This lack of change in the silicate framework is mirrored in the ^{17}O MQMAS data (Figure 5.2), with no significant differences observed in lineshape or quadrupolar broadening with the addition of any cation species. Only the presence of the characteristic BO resonance is observed in the ^{17}O spectra of all non-calcined samples. This is confirmed by the fact that the spectra show little or no chemical shift dispersion or quadrupolar induced broadening. This is reminiscent of other studies that have shown silicon bridging oxygens [168, 177]. As both the ^{29}Si and the ^{17}O MAS NMR show no significant disruption in the undoped samples, it can be inferred that no cation incorporation into the Stöber network occurs before calcination.

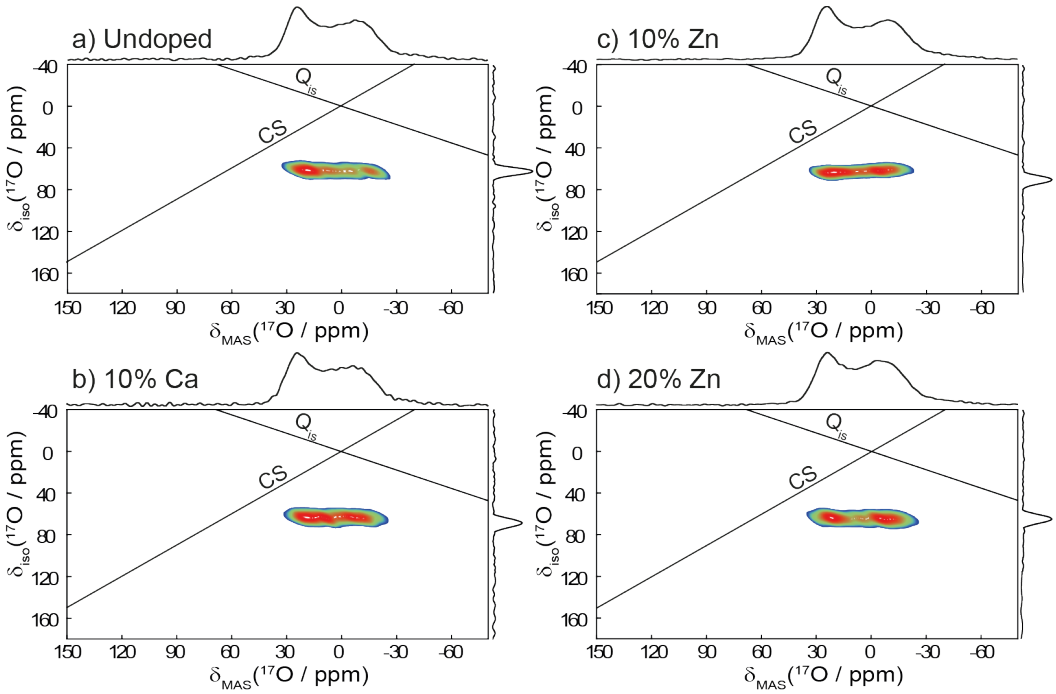

Figure 5.2: The ^{17}O MQMAS spectra of non-calcined Stöber particles for (a) Si particle, (b) 10 mol% Ca, (c) 10 mol% Zn and (d) 20 mol% Zn

5.3.2 The Stöber Process (Post-Calcination)

Upon calcination, Ca^{2+} and Zn^{2+} cations are incorporated into the Stöber nanoparticles. Previously, it has been demonstrated that incorporating Ca^{2+} with this method produces spherical nanoparticles [161]. Investigations into the structure of the silicon matrix look at how this incorporation has affected the silicon structure. Firstly, as seen in Table 5.2, the NC of the undoped Stöber particle has increased from 3.68 in the non-calcined samples to 3.84 in the calcined samples. This indicates that during calcination some hydroxyls were removed from the structure forming a more connected network. For the undoped particle, the ^{17}O Echo and MQMAS measurements (Figure 5.5(a)) resembles a BO resonance, as shown in the undoped non-calcined spectra (Figure 5.2(a)), further indicating a well connected network.

The ^{29}Si spectra of the doped samples shows that upon 10 mol% Ca addition, an identical network connectivity as the un-calcined version (Table 5.2) is maintained. However, the network connectivity is still lower than the calcined undoped sample, indicating that although hydroxyls are removed from the network during calcination, as Ca enters the Stöber network, it acts as a network modifier and decreases the NC. Further evidence can be concluded from the observation of

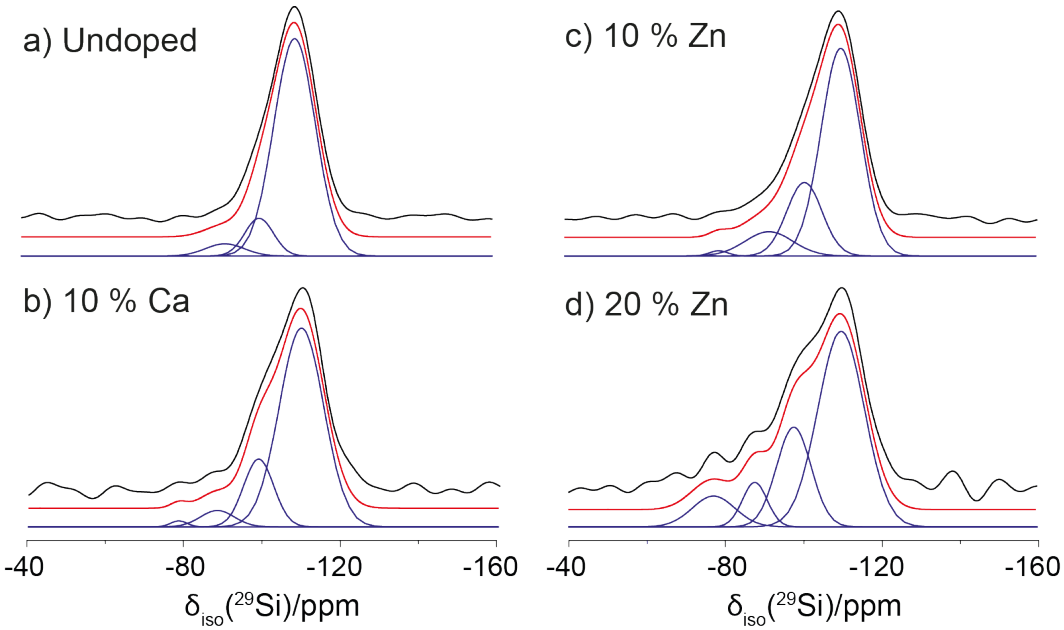

Figure 5.3: The ^{29}Si MAS NMR spectra of calcined Stöber particles for (a) undoped, (b) 10 mol% Ca, (c) 10 mol% Zn and (d) 20 mol% Zn. The individual deconvolutions are shown in blue and the sum of these are marked in red.

a Q^1 Si site. The identification of this Q^1 site was made with the use of cross polarisation (CP) NMR, from ^{1}H, to enhance the resonance (Appendix: Figure B.1). Further evidence of Ca incorporation is detected, in the ^{17}O MAS NMR measurements, with the observation of a small Ca non-bridging resonance (NBO) appearing at 100 ppm (Figure 5.5). While the proportion of the NBO site is small compared to the BO resonance (20 ppm), this is to be expected with such little Ca incorporation. These characteristic resonances are mirrored in the MQMAS data where the 10 mol% Ca sample for the NBO exhibits little CS or Q_{is} broadening. This is characteristic of a Ca BO observed previously in the literature [168].

Similarly to the 10 mol% Ca sample, doping the Stöber nanoparticle with 10 mol% Zn results in a lower NC than the undoped sample. However, this effect is significantly larger in the 10 mol% Zn sample, with a significant increase in Q^2 and Q^3 structural units observed, resulting in a more significant NC decrease than that of the 10 mol% Ca nanoparticles. From this we can infer that the Zn nanoparticle is having a larger disruptive effect on the Stöber nanoparticle than the introduction of Ca. This network disruption continues in the 20 mol% Zn sample, where a further reduction of the Q^4 site is observed resulting in a NC of 3.36. This drop in NC is comparatively similar in scale to the reduction seen from the undoped to the 10

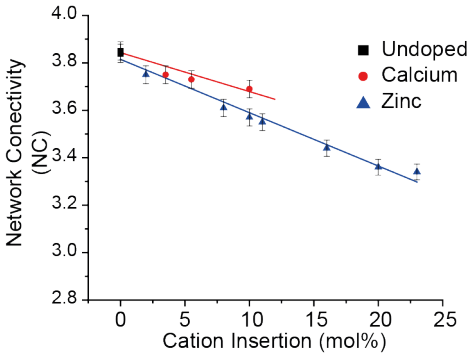

Figure 5.4: The network connectivity (NC) determined by ^{29}Si MAS NMR for the Ca and Zn Stöber particles plotted against there respective cation (mol%) insertion.

mol% Zn sample. Upon measuring a range of Ca and Zn samples and plotting the NC against cation content (Figure 5.4), this effect becomes more apparent. Both the Ca and Zn series observe a linear relationship of NC when the cation dopant concentration is increased, although significantly more disruption is observed for Zn.

The ^{17}O MQMAS data for the 10 and 20 mol% Zn samples (Figure 5.5) highlights a second resonance, at δ_{iso} = 20 ppm, hidden underneath the bridging oxygen resonance. Upon overlaying the 1D ^{17}O spectra (Figure 5.6(a)) this becomes even more apparent. At first glance this would appear to be a non-bridging oxygen resonance, however, shifted due to the similar ^{17}O NMR shifts of ZnO and SiO_2 [176, 178].

Further investigation using the method developed by Eck, Smith and Kohn to observe hydroxyls, a peculiarity becomes apparent [177]. Through the use of fast recycle delays and liquid (non-selective) pulses we can suppress the BO, while observing the hydroxyls in the nanoparticles. As shown in Figure 5.7, by employing a selective excitation scheme we see the characteristic static lineshape of the Si BO's in the undoped sample [177]. However, when the 'non-selective' scheme is applied to the undoped nano particle, the static BO resonance is observed in an anti-phase position while observing a sharp resonance, previously assigned as a hydroxyl group, is selectively excited [177]. This resonance is also clearly observed in the 10 mol% Ca nanoparticles. However, upon applying this technique to the Zn systems, this hydroxyl resonance is not observed. While, the 10 mol% Zn Stöber nanoparticle appears to only contain a BO resonance, for 20 mol% Zn a second anti-phase site is apparent in both the selective and non-selective static ^{17}O spectra. This likely results from the Zn NBO resonance observed in the MQMAS data (Figure 5.5).

In the HRTEM images of the 10 mol% Zn Stöber nanoparticles (Figure 5.8(a) & (b)), evidence for crystalline areas is observed. These are not apparent in the

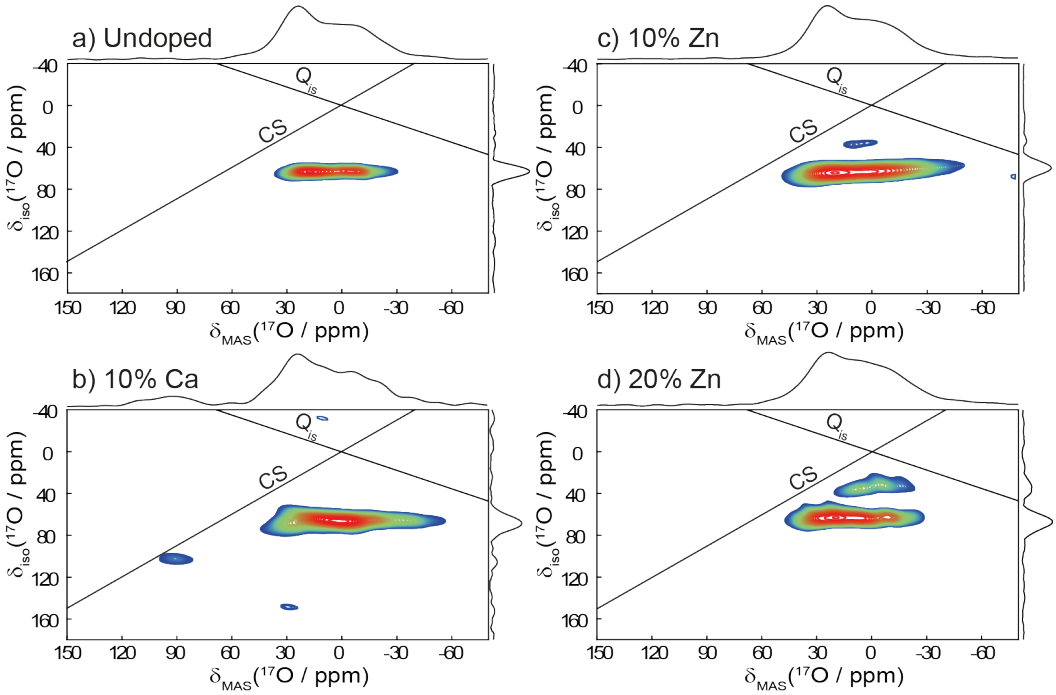

Figure 5.5: The ^{17}O MQMAS spectra of calcined Stöber particles with Hahn-echo projections for (a) undoped, (b) 10 mol% Ca, (c) 10 mol% Zn and (d) 20 mol% Zn

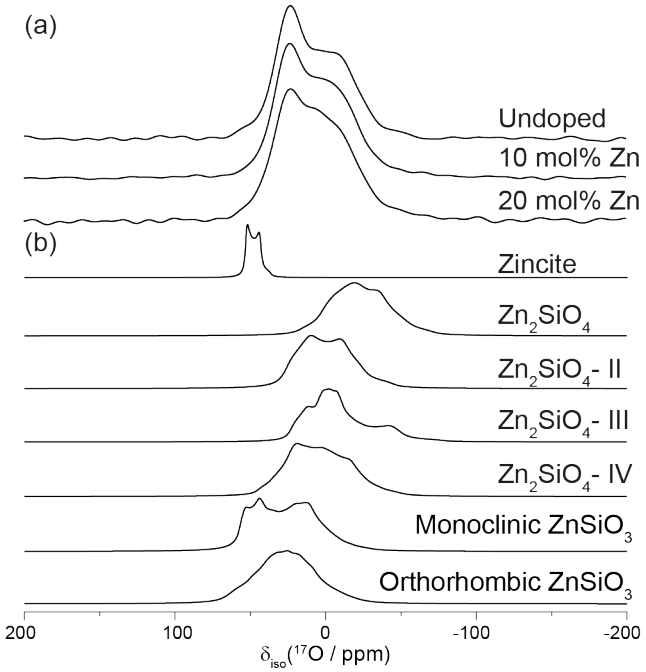

Figure 5.6: Overlay of ^{17}O Hahn-echo data of the (a) calcined Stöber nanoparticles and (b) calculated ^{17}O CASTEP data.

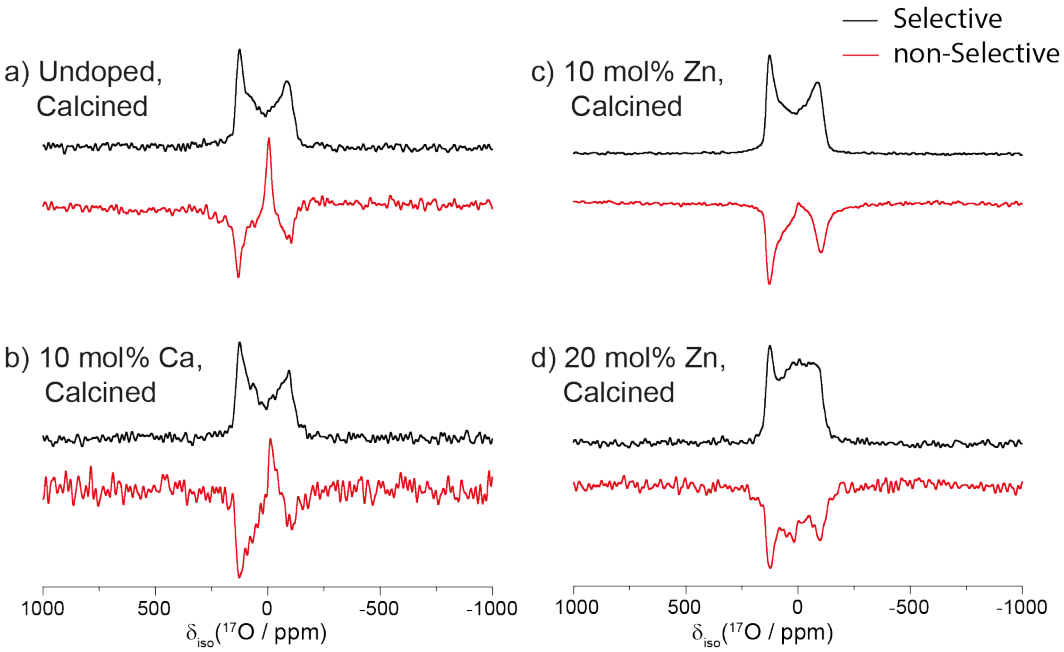

Figure 5.7: Selective and non-selective ^{17}O static echo NMR of the calcined Stöber particles (a) undoped, (b) 10 mol% Ca, (c) 10 mol% Zn, and (d) 20 mol% Zn.

Stöber particles featured in the previous work by Greasley et al. [161], where Ca was fully incorporated into the nanoparticle network. These areas mean, that unlike Ca, Zn does not incorporate into the glass network, but forms a separate phase. As this is only observed in the Zn samples, we can conclude that it is a Zn containing crystallite. This has been previously seen by investigations into similar materials, which suggest that Zn disrupts the amorphous nature of the silicon glasses forming zinc tetrahedra [179]. Through measurements of the atomic spacing from the HRTEM results (Figure 5.8(c) & (d)), determination of the lattice constant of this crystallite phase can be achieved giving d-spacings of 2.70 and 2.82 Å. Various zinc silicate [180–183] and zinc oxide [184] minerals were compared to these values, and a comparable d-spacing was found in the Zn_2SiO_4–II phase. A list of the most prominent d-spacing's for these minerals are included in the Appendices (Table B.1).

To confirm this, CASTEP has been used to calculate the theoretical ^{17}O NMR shifts for these minerals which can be compared with experimental data. The calculated lineshapes resulting of the various Zinc silicates [180–183] and Zinc Oxides [184], are shown below the measured ^{17}O NMR data (Figure 5.6(b)). The calculated ^{17}O parameters for the minerals shown in Figure 5.6(b) are included in the appendix in Table B.2. From these calculated values, we can see that the II and IV forms of Zn_2SiO_4 both agree with the experimentally measured shifts.

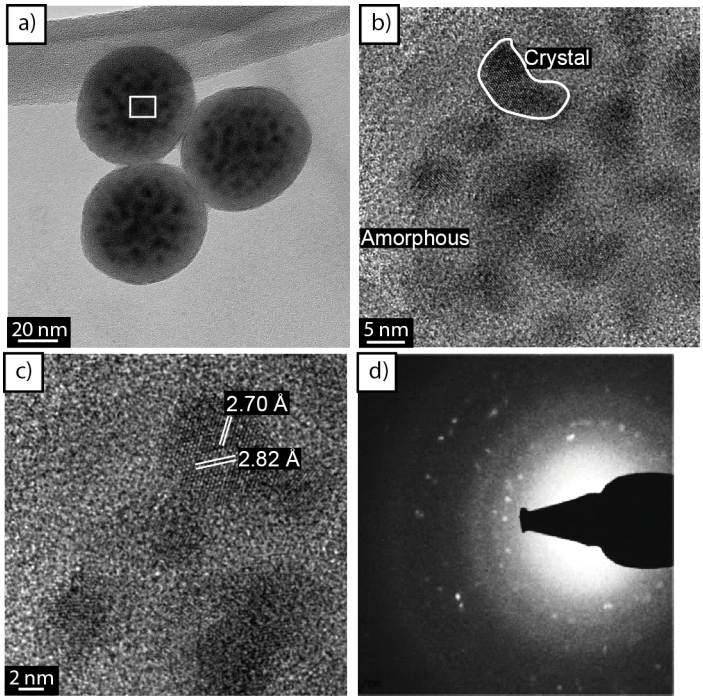

Figure 5.8: The HRTEM images of calcined 10 mol% Zn Stöber particles at (a) showing the distribution throughout the entire particle, (b) high resolution of the boxed area showing amorphous and crystalline areas, (c) high resolution of the crystalline area indicating the obtained d-spacings, (d) diffraction pattern of crystalline area within nanoparticle.

However, Zn_2SiO_4–IV is made up of multiple ^{17}O environments (Appendix B.2) and no evidence for this is observed for in the MQMAS results (Figure 5.5). It can be concluded that crystallite observed in the 10 and 20 mol% Stöber particles are likely to be a Zn_2SiO_4-II phase.

5.4 Conclusions

The structure of Stöber nanoparticles has been successfully probed through a combination of solid state NMR, CASTEP and HRTEM. Using $H_2{}^{17}O$ to label the Stöber particles it has been possible to follow the synthesis steps. From this we can observe the characteristic BO resonance in the Ca containing Stöber particle suggesting that the addition of Ca acts as a network modifier. This agrees with the obtained ^{29}Si MAS NMR which indicates a reduced NC from undoped Stöber particles.

In the Zn containing Stöber particles we can observe the evidence of crystalline regions forming inside the nanoparticle. These crystalline regions have been attributed to the formation of Zn_2SiO_4–II phases inside the particle. This crystallisation might also explain why there is a decrease in network connectivity for Zn with respect to Ca nanoparticles. Since the crystalline Zn is surrounded by the silica network we are likely to see a greater amount of low Q units due to the increased surface area. Further work will be needed to explore methods of integrating Zn into the Stöber network without crystallisation.

Chapter 6

Quadrupolar Solid State NMR Investigation into the Curing Process of Alkali-Activated C-(N)-(A)-S-H Geopolymers

6.1 Introduction

6.1.1 Background of Geopolymers

A geopolymer was originally defined as a synthetic alkali-aluminosilicate material, which since been expanded to include all inorganic polymer [185]. Whilst this covers a broad range of materials, this definition excludes many hybrid inorganic-organic geopolymers that have been developed to enhance existing material's properties such as; mechanical strength, toughness, and electrical conductivity [186–189]. Therefore, while the focus of this investigation will be on an inorganic geopolymer system, some organic containing geopolymers will be discussed, and the term geopolymer be used to describe both sets of materials.

The studied aluminosilicate network of geopolymers contains a series of AlO_4 and SiO_4 edge sharing tetrahedra which are charge balanced by positive ions (Na^+, K^+, Li^+, Ca^{2+}, Ba^{2+}, $NH_4{}^+$, H_3O^+) [190]. The resulting polysilate chain has the empirical formula:

$$M_n\{-(SiO_2)_z-AlO_2\}_n \cdot wH_2O \tag{6.1}$$

where M is a positively charged cation (listed above), n is the degree of polycondensation, and z modifies the Al to Si ratio, which is generally 1, 2 or 3 [190]. As a

result a highly cross linked, disordered pseudo-zeolitic network is formed [191].

With modification of this composition, it has been shown that it is possible to tune the properties of the geopolymers to give; high compressive strength, low shrinkage, non-combustibility, heat-resistance, low temperature formation, fast or slow setting, and fire/acid resistance [185, 192, 193]. These properties and the wide range of possible compositions has made the use of geopolymers attractive for many applications including; cements, organic dye removal, turbine/engine parts, medical applications, and for nuclear waste immobilisation [194–198].

6.1.2 Geopolymer Based Cements

Ordinary Portland cement (OPC) has for a long time been the dominant hydraulic cement in use worldwide [199]. The use of cement is mainly as a binder of inert mineral aggregates to produce concrete. However, the energy required for production, and the calcination of $CaCO_3$ to produce the needed CaO (driving off CO_2 in the process), generates an average carbon emission of 0.81 kg of CO_2 per kg of concrete manufactured [200]. With an estimated 907 kg of cement used per year per person, this results in approximately 5 % of the global carbon emissions originating from the manufacture of cement [200–203]. To reduce this high carbon footprint of OPC in the construction sector, environmentally friendly alternatives need to be developed.

Geopolymers have been touted as one such potential replacement for OPC, due to their potential to reduce carbon emissions by up to 80 % [193]. However, some more conservative estimates indicate only a 25 % reduction of CO_2 emissions is possible [203]. This low carbon footprint is driven by alkali activation of industrial waste materials such as fly ash or blast furnace slag, which contain high amounts of aluminosilicate bi-products, to form geopolymer cements [193]. As geopolymer cements have been shown to have comparable or greater compressive strengths to OPC, this makes them an attractive replacement material [204–206].

While fly ash and blast furnace slag are viable precursors to synthesise geopolymers, the composition can vary greatly making it difficult for consistent final products to be produced [194, 207]. Although this uncertainty in precursor composition can be accurately measured, it is important to fully understand the structural variation and performance arising from these differences [207]. Through the use of a synthetic calcium (alkali) aluminosilicate hydrate gel (C-(N)-(A)-S-H), modification of the Ca:Na:Al:Si ratios can be readily achieved. This synthetic C-(N)-(A)-S-H gel can be generated by the addition of a sodium metasilicate solution to a synthetically produced fly ash [208]. This activating solution polymerises the synthetic fly ash resulting in the cured C-(N)-(A)-S-H geopolymer. Solid state NMR

investigations into the precursor and activated materials can then be undertaken to provide structural insight on the resulting calcium aluminosilicate network.

6.1.3 Solid State NMR of Geopolymers

As geopolymers contain a high amount of NMR active nuclei (^{23}Na, ^{27}Al, ^{29}Si), solid state NMR has been key for elucidating structural information of these materials. While other common analytical techniques such as X-ray powder diffraction, Fourier transform infra-red (FTIR) spectroscopy and pair distribution (PDF) have been essential for characterisation of geopolymers, the inherent dynamics and disorder present in the system lends itself to solid state NMR investigations.

The high SiO_2 content has prompted many ^{29}Si MAS NMR investigations into the structure of geopolymers, despite the inherent low sensitivity and long T_1 relaxation times of the silicon nucleus [194, 197, 208–216]. Additionally probes into the quadrupolar nuclei present in geopolymers has provided powerful structural information on the local interactions of ^{27}Al and ^{23}Na in the aluminosilicate network [194, 197, 208, 210, 212, 214–217]. This multi-nuclear NMR approach has enabled insights into the coordination state of ^{27}Al, the connectivity of ^{29}Si, and the role of ^{23}Na cations [197, 208–218].

The use of multiple quantum magic angle spinning (MQMAS) experiments, has been demonstrated as an important probe of structural information of quadrupolar nuclei in the geopolymer system [211, 219, 220]. This technique was used to identify multiple ^{23}Na sites in the metakaolinite geopolymer system, aiding refinement of the proposed structural models [211]. While other quadrupolar techniques, such as nuclear quadrupole resonance (NQR), have occasionally been used to investigate incorporation of additives into the geopolymer matrix, this has primarily been used to observe the presence of Cu_2O in the systems and will not be relevant here [195, 221]. However, so far this multi-nuclear approach has not been applied to the C-(N)-(A)-S-H system, where investigating the curing process here will provide information on the impact of Na^+ on the local aluminosilicate structure.

Solid state NMR of ^{17}O has been shown by many researchers to be a powerful probe for similar aluminosilicate structures including zeolites, silicate glasses, and aluminosilicate glasses [222–226]. While a large amount of solid state NMR investigations have successfully probed the geopolymer structure, relatively few have investigated the role that ^{17}O plays in the aluminosilicate network [220, 227]. This is due to the low natural abundance (0.037 %) of ^{17}O, resulting in a low inherent sensitivity (0.029 relative to carbon) making investigations difficult. Fortunately, though the introduction of ^{17}O through the use of enriched materials, such as $H_2{}^{17}O$, the

role that oxygen has to play in the system can be probed.

Investigations using ^{17}O so far have been limited to non Ca containing geopolymers [220, 227]. As many classifications of fly ash contain high levels of Ca present in the structure, the previous ^{17}O investigations are not fully representative of geopolymers produced with these compositions. Therefore, in the Ca containing synthetic C-(N)-(A)-S-H system investigated here, the introduction of $H_2{}^{17}O$ during the curing step is hoped to provide an insight into the local structure of Ca geopolymer cements. In addition the use of a multi nuclear NMR approach (^{17}O, ^{23}Na, ^{27}Al, ^{29}Si), along with modification of the Ca/(Al+Si) and Al/Si ratio, will probe the change in structure with variation of the composition.

6.2 Experimental

6.2.1 Synthesis

To produce the synthetic calcium-aluminosilicate powders used as precursors in this study an organic steric entrapment solution-polymerisation method previously detailed in literature was used [208]. These synthetic powders were chosen to investigate the Ca content for varying Al/Si ratios (0.05 and 0.15). These are represented by series A and B given in the ternary plot (Figure 6.1). The molar ratio and compositions of these synthetic calcium-aluminosilicate powders are outlined in Table 6.1. These synthetic precursor powders were then activated by a solution of sodium metasilicate (Na_2SiO_3, 37.5 wt%) and distilled water. The stoichiometry was designed to keep a final 2:1 Al to Na molar ratio. The activating solution was subsequently mixed with the precursor powder to form a homogeneous paste, which was then cast until fully cured. To produce the ^{17}O labelled samples, distilled water in the activating solution was replaced with $H_2{}^{17}O$ (Cortecnet, 40 mol%).

6.2.2 Solid State NMR

All ^{17}O MAS NMR measurements were performed at 14.10 T using a Bruker Avance II+ spectrometer operating at a Larmor frequency of 81.26 MHz. These experiments were performed using a Bruker 3.2 mm HX probe which enabled a MAS frequency of 20 kHz to be implemented. The pulse length calibration was performed on D_2O, from which a non selective (liquid) $\pi/2$ pulse of 4.5 µs was measured. All ^{17}O spectra were acquired with a rotor synchronised echo ($\theta - \tau - 2\theta$) sequence, using a selective (solid) $\pi/2$ pulse time of 1.5 µs along with a measured recycle delay of 1 s. The 2D ^{17}O 3QMAS experiments were completed using a three pulse z-filter sequence. The

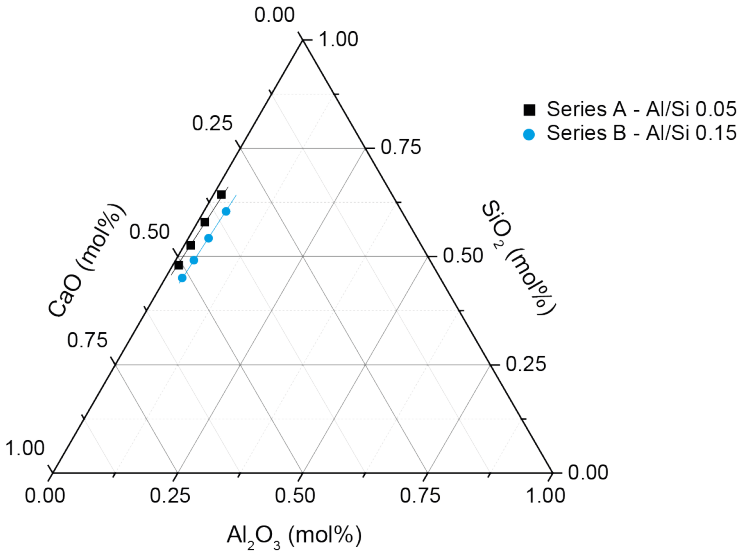

Figure 6.1: A tertiary plot of the C-(N)-(A)-S-H precursors materials showing where the 0.05 (Series A) and 0.15 (Series B) Al/Si ratio series are located.

Table 6.1: The molar ratios and composition of the C-(N)-(A)-S-H geopolymer series

Sample		Molar ratios (mol%)			Composition (mol%)			
Precursor	Activated	Ca/(Al+Si)	Al/Si	Na/Al	CaO	SiO_2	Al_2O_3	Na_2O
A0.5P	A0.5A	0.51	0.05	0.5	33.82	63.78	1.59	0.80
A0.7P	A0.7A	0.67	0.05	0.5	40.30	57.53	1.45	0.72
A0.8P	A0.8A	0.84	0.05	0.5	45.80	52.24	1.31	0.65
A1.0P	A1.0A	1.00	0.05	0.5	50.50	47.70	1.20	0.60
B0.5P	B0.5A	0.51	0.15	0.5	34.30	59.06	4.43	2.21
B0.7P	B0.7A	0.67	0.15	0.5	40.90	53.12	3.99	1.99
B0.8P	B0.8A	0.84	0.15	0.5	46.33	48.24	3.62	1.81
B1.0P	B1.0A	1.00	0.15	0.5	50.74	44.28	3.32	1.66

pulse widths for the excitation, conversion and soft z-filter pulses were 6.5, 1.75, and 15 µs, respectively. The shearing of the MQMAS experiments was performed within the Bruker software using the standard conventions [42]. All ^{17}O centre of gravity (apparent) shifts were reported against the IUPAC recommended primary reference of $D_2O_{(l)}$ (Liquid neat, $\delta_{iso} = 0.0$ ppm) [137].

All ^{23}Na MAS NMR measurements were performed at 14.10 T using a Bruker Avance II+ spectrometer operating at a Larmor frequency of 158.55 MHz. These experiments were performed using a Bruker 3.2 mm HX probe which enabled a MAS frequency of 20 kHz to be implemented. The pulse length calibration was performed on $NaCl_{(s)}$ from which a selective (solid) $\pi/2$ pulse of 5 µs was measured. All ^{23}Na spectra were acquired with a selective (solid) $\pi/6$ pulse time of 1.5 µs along with a measured recycle delay of 1 s. The 2D ^{23}Na 3QMAS experiments were measured using a three pulse z-filter pulse sequence, with pulse widths for the excitation, conversion and soft z-filter pulses determined to be 3.5, 1.5 and 17 µs, respectively. The shearing process of the MQMAS experiments was performed within the Bruker software using the standard conventions [42]. All ^{23}Na centre of gravity (apparent) shifts were reported against the IUPAC recommended primary reference of $NaCl_{(aq)}$ (0.1 mol in D_2O, $\delta_{iso} = 0.0$ ppm), via a $NaCl_{(s)}$ secondary in which the resonance has a known shift of 7.0 ppm [137].

All ^{27}Al MAS NMR measurements were performed at 14.10 T using a Bruker Avance II+ spectrometer operating at a Larmor frequency of 156.19 MHz. These experiments were performed using a Bruker 3.2 mm HX probe which enabled a MAS frequency of 20 kHz to be implemented. The pulse length calibration was performed on the AlO_6 site of yttrium aluminium garnet (YAG, $Y_3Al_5O_{12(s)}$), from which a quantitative sold pulse length ($\pi/12$) of 1.5 µs was measured. This quantitative pulse length was determined by ensuring a 1:1 ratio between the AlO_4 and AlO_6 sites in YAG. [20] All ^{27}Al spectra were acquired with this quantitative pulse time of 1.5 µs along with a determined recycle delay of 1 s. The 2D ^{27}Al 3QMAS experiments were measured using a three pulse z-filter pulse sequence. The pulse widths for the excitation, conversion and soft z-filter pulses were 3.5, 1.5 and 17 µs, respectively. Whilst the shearing of the MQMAS experiments was performed within the Bruker software using the standard conventions [42]. All ^{27}Al centre of gravity (apparent) shifts were reported against the IUPAC recommended primary reference of $Al(NO_3)_{3(aq)}$ (1.1 mol in D_2O, $\delta_{iso} = 0.0$ ppm), via the secondary reference of the AlO_6 site in YAG, which has a known shift of 0.7 ppm [137].

All ^{29}Si single pulse MAS NMR measurements were performed at 7.05 T Varian/Chemagnetics InfinityPlus spectrometer operating at a Larmor frequency

of 69.62 MHz. These experiments were performed using a Bruker 7 mm HX probe which enabled a MAS frequency of 5 kHz to be implemented. The pulse length calibration was performed on kaolinite$_{(s)}$ ($Al_2Si_2O_5(OH)_4$) from which a $\pi/2$ pulse time of 5.5 µs was measured. All measurements were undertaken with a $\pi/2$ tip angle along with a delay between subsequent pulses of 240 s. For CPMAS measurements for the ^{1}H pulse a Larmor frequency of 300.1 MHz was used. A $\pi/2$ pulse of 2.5 µs was used with a polarisation from a ramp between 75% and 100% on the ^{1}H channel for a contact time of 12.5 ms. This enabled a delay between subsequent pulses of 4 s. For both single pulsed and CPMAS experiment hetronuclear decoupling was applied on ^{1}H during collection of the FID, where the decoupling frequency was equal to 100 kHz. All ^{29}Si centre of gravity (apparent) shifts were reported against the IUPAC recommended primary reference of $(CH_3)_4Si_{(l)}$ (1% in $CDCl_3$, $\delta_{iso} = 0.0$ ppm), via a kaolinite$_{(s)}$ secondary standard which has a known shift of -91.5 ppm [172].

Due to the inherent amorphous nature present in the structure, simulations of the disorder in the quadrupolar resonances was achieved through the use of the in-house QuadFit program [228].

6.3 Results and Discussion

6.3.1 ^{27}Al MAS NMR

The ^{27}Al single pulse MAS, and triple quantum magic angle spinning (3QMAS) NMR data, for both the precursor powders and the activated powders of series A, are presented and deconvoluted in Figure 6.2, with Table 6.2 containing the simulated parameters acquired. Whilst similar precursor powders and activated materials have been previously investigated, through the use of the QuadFit program to simulate the disorder in the parameters, a more accurate picture of the system is provided [208, 228].

As described in Kemp *et al.* [228], QuadFit uses a Gaussian distribution to represent disorder where the centre and width of the C_Q distribution is represented. Where, the C_Q centre represents the average value, and width is an indication of the deviation from this value. The simulations of the resonances are displayed in Table 6.2. For these simulations the asymmetry parameter (η_Q), while varied during fitting, has not significantly deviated from zero.

For both the precursor and activated samples the primary resonance observed is large and featureless, it is assigned to an $AlO_4(Q^4)$ site. Due to the low content of Al relative to Si, and the Loewenstein avoidance principle, it can safely be assumed that no Al–O–Al bonds exist in the AlO_4 aluminosilicate network.

Therefore, all ^{27}Al present in the $AlO_4(Q^4)$ network exists as Al−O−Si bonds [229]. In the 3QMAS (Figure 6.2) the resonance primarily exists parallel to the CS axis, indicating significant chemical shift disorder, giving an ambiguous δ_{iso}. Likewise, significant broadening is also observed along the Q_{is} dimension, indicating disorder in C_Q parameters of the site. This is typical for an $AlO_4(Q^4)$ resonance, as observed in similar aluminosilicate materials [219].

In the precursor samples (series A), as Ca is increased, trends are observed in the simulated parameters for the $AlO_4(Q^4)$ site. A higher concentration of Ca results in an increase in δ_{iso} observed, relating to increased shielding observed around the ^{27}Al nucleus. Additionally, a reduction in the centre and width values of the C_Q is observed, indicating an increase in order of the $AlO_4(Q^4)$ resonances. Both of these factors provide evidence that the series A precursors are incorporating Ca partially, indicating Ca is supporting the $AlO_4(Q^4)$ site. This could be evidence that some cross linking may be occurring before activation of the samples.

Post activation, A0.5A, A0.7A, and A0.8A, reductions in both centre and width values of C_Q for the $AlO_4(Q^4)$ resonance are seen. This is evidence for the rearrangement of the structure into a more ordered network, post curing, as expected [230]. Unusually, the final sample in series A (A1.0A), does not exhibit this same expected reduction in disorder. Instead, the curing process has the opposite effect on the AlO_4 site and an increase in the centre and width of the C_Q parameters are observed (Table 6.2). Additionally, the trend in the precursor samples, where greater Ca concentration exhibits an increase in δ_{iso} and C_Q, is not mirrored in the activated samples. However, both of these differences could be due to the multiple Si phases as indicated by the silicon NMR (*vide infra*). Furthermore, introduction of significant proportions of AlO_6 resonances in the sample may be contributing towards this disorder.

For the majority of series A, only the single $AlO_4(Q^4)$ resonance is observed, however A0.8P, A0.8A, and A1.0A contain additional resonances observed in the AlO_6 region. The resonance observed at $\delta_{iso} = \sim 9.2$ ppm, in A0.8A and A1.0A, can be attributed to a hydroxy AFm phase (C_4AH_{13}, $Ca_4Al(OH)_{14} \cdot 6\,H_2O$) as previously observed in similar C-(N)-A-S-H/N-A-S-H gel blends and in Portland cements [230, 231]. The formation of this phase is attributed to increased availability of Ca in these samples.

The shift associated with the smaller AlO_6 resonance observed in A0.8A, is attributed to the formation of a 'third aluminium hydrate' (TAH) phase. This amorphous aluminate hydrate is typically found with high concentrations of available Ca and Al [230, 232]. Interestingly the highest Ca containing sample in series

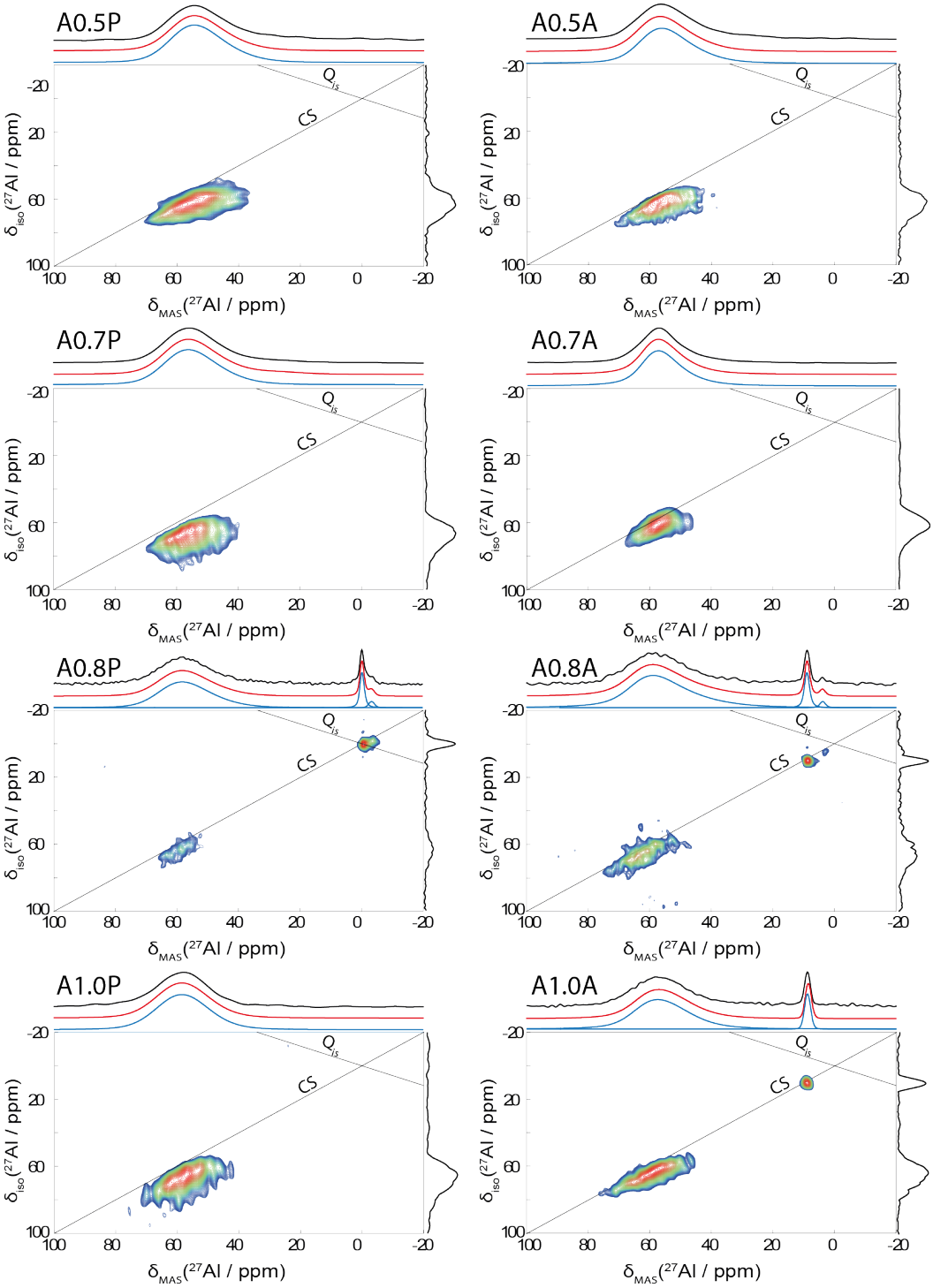

Figure 6.2: The 1D deconvoluted MAS and 3QMAS ^{27}Al spectra of the 0.05 Si/Al Geopolymers. The deconvolutions of the 1D MAS NMR are shown as projections in the MAS dimension. The individual sites are shown in blue and the sum of these are marked in red.

A (A1.0A) does not exhibit formation of this phase, however possible explanations for this are given in the ^{29}Si MAS NMR (*vide infra*).

Only one of the precursor materials in series A (A0.8P) contains evidence of AlO_6 phases. Both phases are observed in similar proportions to the hydroxy AFm and TAH phases in the activated sample (A0.8A), however, the δ_{iso} of both phases are significantly lower (9.3 to 0.0 ppm for hydroxy AFm, 4.2 to -3.3 ppm for TAH). The drastic difference in shift results in the AlO_6 resonances observed in A0.8P not being the hydroxy AFm or TAH phases produced after activation. However, the similar proportions of each resonance indicates they are related precursors of these phases.

The ^{27}Al MAS and 3QMAS NMR spectra of series B (0.15 Al/Si) is observed in Figure 6.3, with the simulated parameters shown in Table 6.2. Similarly to series A, the primary resonance observed in the precursor samples is $AlO_4(Q^4)$ contained within the silica network. However, in the precursor samples, the reduction in disorder at higher Ca concentrations observed in series A is not mirrored. Although, this disruption is caused by the increase in non $AlO_4(Q^4)$ phases prevalent for the high Ca containing precursors of series B, as only one sample (B0.5P) purely contains an $AlO_4(Q^4)$ resonance.

An increased number of resonances occurs in the spectra of all but the lowest Ca content of the 0.15 Al/Si precursors. This is initially manifested by the appearance of an AlO_6 resonance at $\sim$12 ppm in the B0.7P, B0.8P, and B1.0P precursors. This AlO_6 site is observed in small quantities for all three samples, with an intensity of 2$\pm$0.5 % (Table 6.2), making it difficult to observe in the 1D projection and is only visible in the 3QMAS spectra of B0.8P (Figure 6.3). This AlO_6 resonance at $\sim$12 ppm has been observed in other synthetic precursors as the formation of a silicon free garnet phase ($Ca_3Al_2(OH)_{12}$, C_3A) [208, 214]. While the C_Q of C_3A in the literature is narrower than that observed here (Table 6.2), the increases, can be attributed to a more disordered phase [215]. As the C_3A phase is not observed in the series A, which contains a third of the Al content, or in the B0.5P which contains the least Ca in series B, then formation of this phase is be attributed to high amounts of available Ca and Al during the precursor synthesis [208].

In addition to this C3A resonance, in both B0.8P and B1.0P, additional resonances are observed at 80 and 90 ppm respectively. The high isotropic shifts indicate additional AlO_4 environments, which are not integrated into the silicon network [20, 218]. Due to the large differences in shift, C_Q, and disorder between these sites (Table 6.2) we conclude, that these two different phases are discrete. The additional AlO_4 environments are only observed in the MQMAS spectrum of B0.8P,

Table 6.2: The ^{27}Al parameters from the deconvoluted 1D MAS spectra acquired for both precursor and activated samples in series A & B. For all samples, η_Q is fixed during iterations to be 0.

Sample	Site	Area (%)	δ_{iso} (ppm)	C_Q Centre (MHz)	C_Q Width (MHz)	Assignment
Precursor 0.05 Al/Si						
A0.5P	Al^{IV}	100.0	60.6	6.38	6.20	$AlO_4(Q^4)$
A0.7P	Al^{IV}	100.0	62.8	6.19	4.82	$AlO_4(Q^4)$
A0.8P	Al^{IV}	86.1	64.1	5.44	2.76	$AlO_4(Q^4)$
	Al^{VI}	12.0	0.0	1.40	1.30	
	Al^{VI}	1.9	−3.3	1.10	1.00	
A1.0P	Al^{IV}	100.0	64.2	4.95	2.07	$AlO_4(Q^4)$
Activated 0.05 Al/Si						
A0.5A	Al^{IV}	100.0	62.0	6.15	6.06	$AlO_4(Q^4)$
A0.7A	Al^{IV}	100.0	61.9	4.70	3.50	$AlO_4(Q^4)$
A0.8A	Al^{IV}	89.0	64.9	5.33	2.01	$AlO_4(Q^4)$
	Al^{VI}	9.2	9.3	1.41	1.32	Hydrated AFm
	Al^{VI}	1.8	4.2	1.10	1.00	TAH
A1.0A	Al^{IV}	88.8	64.3	6.33	4.35	$AlO_4(Q^4)$
	Al^{VI}	11.2	9.1	1.10	1.00	AFm
Precursor 0.15 Al/Si						
B0.5P	Al^{IV}	100.0	65.1	6.87	5.35	$AlO_4(Q^4)$
B0.7P	Al^{IV}	98.0	63.8	5.56	4.33	$AlO_4(Q^4)$
	Al^{VI}	2.0	12.2	3.28	1.50	$Ca_3Al_2(OH)_{12}$ (C_3A)
B0.8P	Al^{IV}	10.4	85.0	8.81	1.13	$Ca_{12}Al_{14}O_{33}$
	Al^{IV}	4.2	82.2	3.42	1.2	$Ca_{12}Al_{14}O_{33}$
	Al^{IV}	83.3	62.7	6.4	6.20	$AlO_4(Q^4)$
	Al^{VI}	1.6	11.8	3.28	1.50	$Ca_3Al_2(OH)_{12}$ (C_3A)
B1.0P	Al^{IV}	3.4	92.2	6.15	0.14	
	Al^{IV}	94.1	69.2	6.70	2.22	$AlO_4(Q^4)$
	Al^{VI}	2.5	11.7	3.28	1.50	$Ca_3Al_2(OH)_{12}$ (C_3A)
Activated 0.15 Al/Si						
B0.5A	Al^{IV}	36.4	78.8	6.69	2.07	$AlO_4\,Q^3$ (3Si), $AlO_4(AlO_6)$
	Al^{IV}	57.6	63.1	7.14	4.46	$AlO_4(Q^4)$
	Al^{VI}	6.1	9.5	1.07	1.00	AFm
B0.7A	Al^{IV}	3.8	76.2	4.75	0.63	$AlO_4(AlO_6)$
	Al^{IV}	70.1	64.5	6.55	5.91	$AlO_4(Q^4)$
	Al^{VI}	26.1	9.5	1.10	1.00	AFm
B0.8A	Al^{IV}	1.8	74.7	2.85	2.50	$AlO_4(AlO_6)$
	Al^{IV}	51.5	62.8	6.12	5.50	$AlO_4(Q^4)$
	Al^{VI}	46.7	9.3	1.10	1.00	AFm
B1.0A	Al^{IV}	61.9	65.6	6.45	4.70	$AlO_4(Q^4)$
	Al^{VI}	36.6	9.3	1.07	1.00	AFm

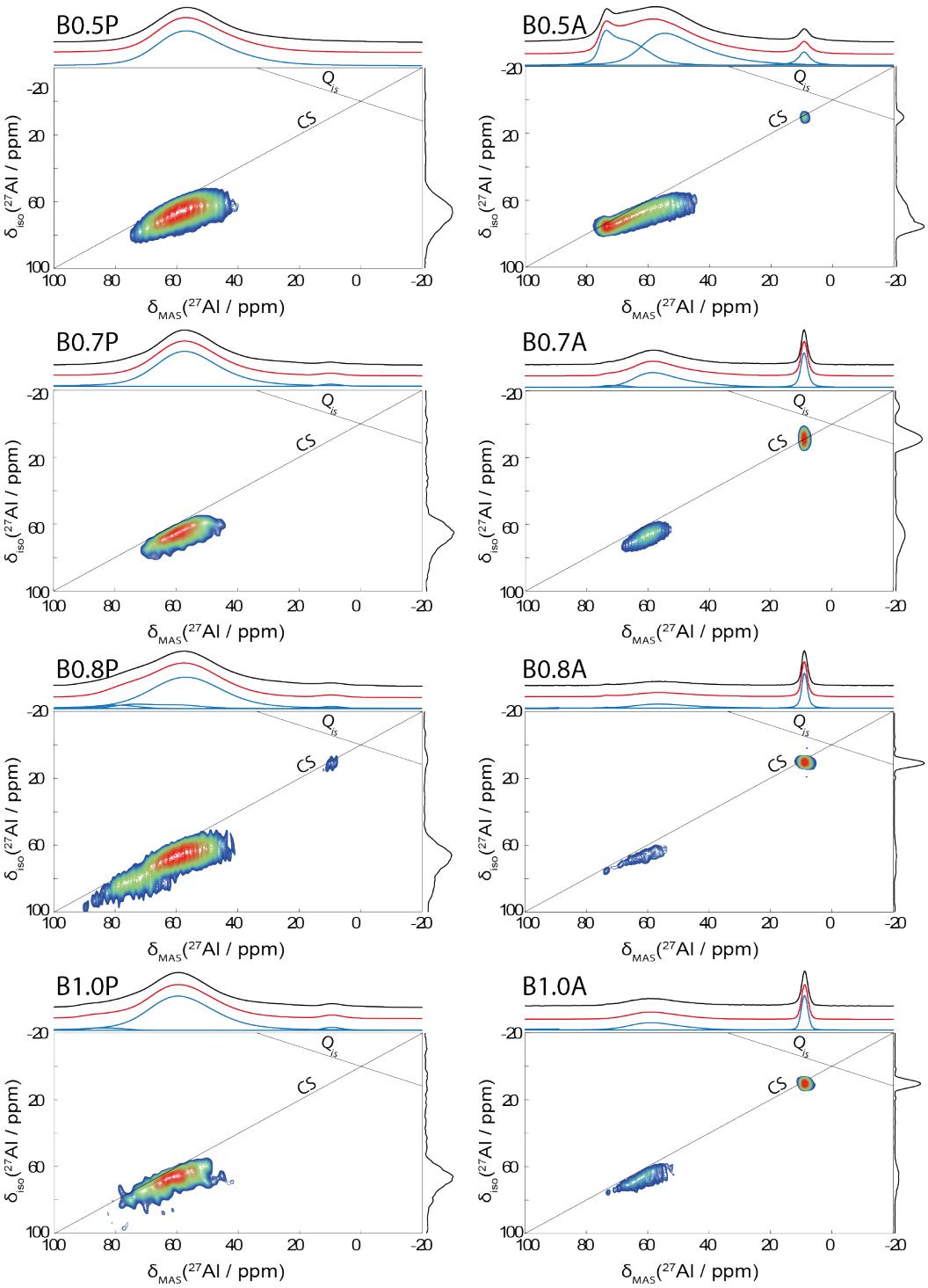

Figure 6.3: The 1D deconvoluted MAS and MQMAS ^{27}Al spectra of the 0.15 Si/Al geopolymers. Deconvolutions of the 1D MAS NMR are shown as projections in the MAS dimension. The individual sites are shown in blue and the sum of these are marked in red.

where the distribution of this resonance would suggest it is a single site with disorder in both the CS and Q_{is} axes (Figure 6.3). However, no single fit was sufficient to simulate this site in the 1D projection. As calcium aluminates have been known to show up in this region, many of which have 2 or more ^{27}Al sites, simulations were based on these previous studies. From the resulting fit for B0.8P, the AlO_6 resonances were determined to be the two ^{27}Al sites of $Ca_{12}Al_{14}O_{33}$ [215].

For B1.0P, while a single site fit, was possible to simulate the disorder present, the high shift and C_Q do not match up with known calcium aluminates. When multiple sites were fitted with parameters given in the literature, in a similar manner to B0.8P, no suitable fit could be achieved. This suggests the formation of a new calcium aluminate phase, previously not observed in the literature. Although, the high δ_{iso} of this site puts the resonance in the AlO_xN_{x-1} range, indicating some remaining aluminium nitrate from synthesis of the synthetic precursors has formed this phase [20].

Upon curing, the precursors from series B undergo large structural differences from their Al counterparts in series A. It is immediately apparent that curing of the 0.15 Si/Al precursors the geopolymers now contain hydroxy-AFm (Figure 6.3), whereas this was not seen until the high concentration Ca geopolymers in series A. This increase in Al results in some of the samples, such as B0.8A, containing as much as 46.7 % AlO_6. It is apparent that the increased Al in this series cannot be supported in the silica network upon activation, resulting in the formation of a calcium aluminium hydrate phase.

In addition to $AlO_4(Q^4)$ and hydroxy-AFm phases formed in every sample, for B0.5A another prominent resonance is observed. While this resonance is most prominent in B0.5A, it can also be observed in smaller amounts in B0.7A and B0.8A. The δ_{iso} (78.8 ppm) obtained from simulation of the resonance for B0.5A indicates either at the lower end of the AlO_4 shift region or at the upper ranges of tetrahedral Al surrounded by three SiO_4 units ($AlO_4(Q^3)$) or AlO_4 groups which surround chains of AlO_6 ($AlO_4(AlO_6)$) [20, 218]. Due to the decreased shielding effect that Ca has on towards the ^{27}Al nucleus it is unlikely that AlO_4 is being observed. Indicating the resonance is determined to be either $AlO_4(Q^3)$ or $AlO_4(AlO_6)$ instead.

6.3.2 ^{29}Si MAS NMR

The ^{29}Si MAS NMR spectra and deconvolutions of the precursor materials for both series A & B are presented in Figure 6.4. When, compared to other Ca^{2+} containing silica networks (Chapter 5), the addition of Al^{3+} enhances the complexity of the ^{29}Si environments in the geopolymer network resulting in a greater number of

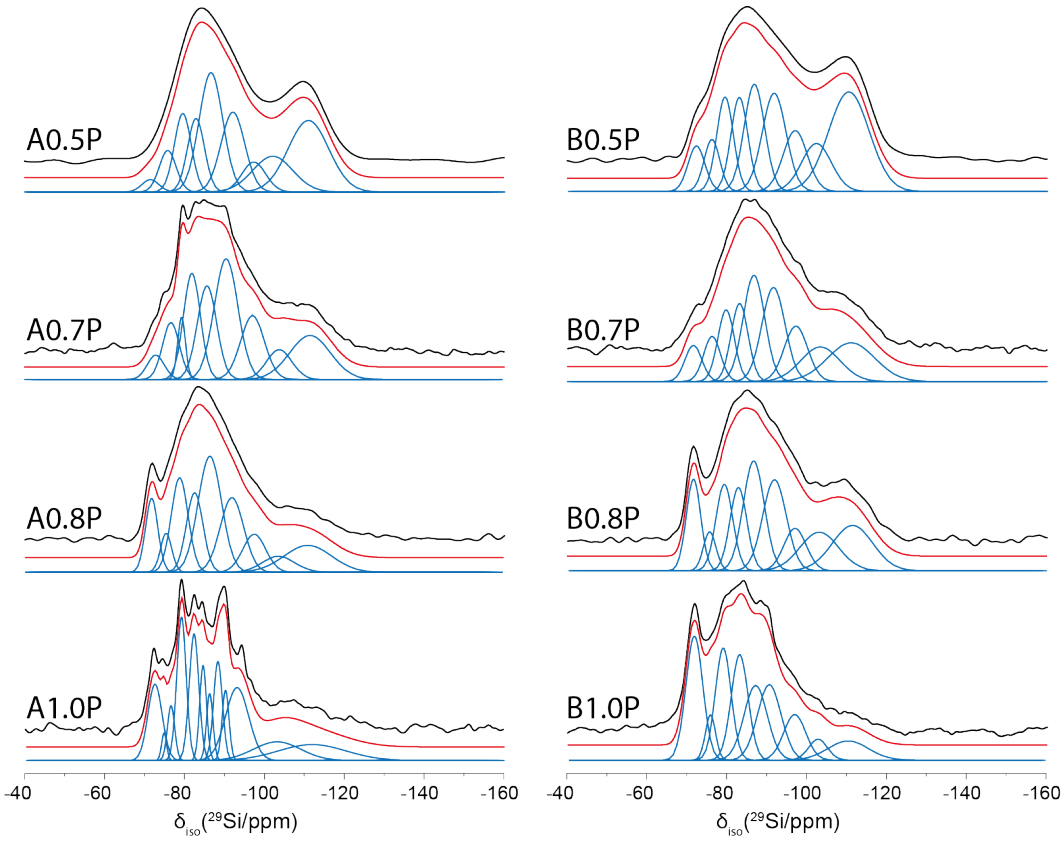

Figure 6.4: The deconvoluted ^{29}Si MAS NMR (5 kHz) spectra of the precursor 0.05 & 0.15 Si/Al geopolymers. The individual sites are shown in blue and the sum of these are displayed in red.

resonances observed. These differences arise from their respective interactions with the network, as either a network modifier or a network former. Network formers, include small, high charge ions (Si^{4+}, Al^{3+}, B^{3+}, P^{5+}), which tend to form three or fourfold coordinated bridging oxygen's (BO). Large ions such as Ca^{2+} and Na^{+} then modify this existing network, disrupting the BO bonds.

For these networks, the number of bridging oxygens bonded to a ^{29}Si environment can be described as Q^m, where m gives the number of BO bonds around the observed nucleus $(0-4)$. However, in aluminosilicates, this does not accurately describe how the ^{29}Si shifts are affected by Si-O-Al bonds. To describe this a Q^m_n term can be used, where n refers to the amount of Si-O-Al bonds. The contributions that Al^{3+} and Ca^{2+} have on the ^{29}Si shifts in geopolymers, and there precursors, is well documented and has allowed accurate determination of the observed resonances [208, 216, 218]. The assignment of the spectra, and relative amounts of the deconvolution are displayed in the appendices (Table C.1). While care has been

Table 6.3: The summed Q^m species content, and network connectivity (NC) determined by ^{29}Si MAS NMR, for both the precursor and activated samples of series A & B.

Sample	Q^0	Q^1	Q^2	Q^3	Q^4	NC
Series A						
A0.5P	1.6	15.3	30.7	19.6	32.7	2.67
A0.7P	3.4	12.0	40.5	25.3	18.8	2.44
A0.8P	8.0	17.9	35.4	23.0	15.8	2.21
A1.0P	10.6	18.2	22.3	21.2	19.2	2.03
A0.5A	1.9	13.7	29.4	25.7	29.3	2.67
A0.7A	1.8	14.6	31.3	32.8	19.6	2.54
A0.8A	4.2	21.2	32.6	27.9	14.1	2.27
A1.0A	1.9	17.0	20.7	26.7	27.5	2.48
Series B						
B0.5P	4.7	14.7	23.3	23.4	33.8	2.67
B0.7P	4.8	15.2	28.0	27.1	24.9	2.52
B0.8P	9.8	14.6	27.7	23.1	24.8	2.39
B1.0P	17.8	18.9	29.8	23.7	9.9	1.89
B0.5A	1.9	12.1	30.9	24.4	30.7	2.70
B0.7A	2.2	10.6	32.9	30.8	23.5	2.63
B0.8A	1.7	20.1	27.1	31.3	19.8	2.47
B1.0A	4.3	26.1	31.0	30.9	7.7	2.12

taken to not over fit the spectra, due to the overlapping nature of the ^{29}Si resonances, the spectral simulations in this case should not be considered definitive, but as approximations of the observed sites.

As both Al and Si act as network formers, the equation to derive the network connectivity (Equation 5.2) can be re-purposed for these aluminosilicates. Modification of this equation for the observed sites, with summation of the differing n provides a new equation:

$$NC = \frac{\sum\limits_{0 \leq n < 4} \left(0Q_n^0 + Q_n^1 + 2Q_n^2 + 3Q_n^3 + 4Q_n^4\right)}{100} \tag{6.2}$$

The summation of each Q^m level, and the NC, for series A & B is displayed in Table 6.3.

The ^{29}Si MAS NMR data for both series A and B of the precursor C-(N)-(A)-S-H gels, are displayed in Figure 6.6. For the three lowest values of Ca dopant (0.5, 0.6, and 0.8) the ^{29}Si lineshape has no significant differences between the two series. Although, this trend is negated by the A1.0P and B1.0P precursors, where a significant increase in the number of ^{29}Si resonances is observed for the

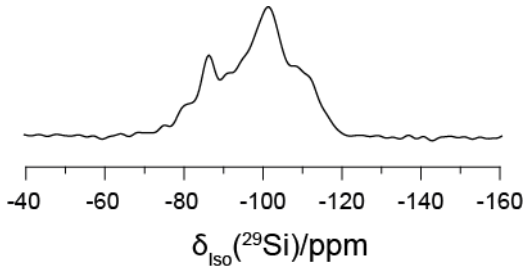

Figure 6.5: The ^{29}Si CPMAS (5 kHz, 100 kHz decoupling) of A1.0A showing the amorphous resonances.

series A precursor. The additional resonances, in A1.0P, are also mirrored in its corresponding activated sample (A1.0A, Figure 6.6), although the resonances are more resolved in this case. In the activated sample the majority of the resonances appear too narrow for amorphous ^{29}Si, indicating a semi-crystalline structure is present. This is due to a large concentration of Ca, in A1.0P and A1.0A, supporting the Al bridging bonds in the Si network resulting in a highly ordered network. The CPMAS data for A1.0A (Figure 6.5) indicate an amorphous phase in this sample. While this amorphous phase should also be observed in the one pulse data, for a large part of the spectra the resonances are obscured by the observation of the semi-crystalline phase in A1.0A.

Whilst B1.0P also contains the same Ca/(Si+Al) ratio, too much relative Al is present to be supported in the Si phase in this manner, thus promoting the formation the calcium aluminate and calcium aluminium hydroxide phases observed in the ^{27}Al MAS NMR (Figures 6.2 & 6.3). Observation of this highly ordered structure results in A1.0P and A1.0A not fitting with the observed trends in the rest of the precursor samples, and therefore will be excluded from the discussion.

A key feature of increasing the Ca content of both series A and B is corresponding changes in overall Q^m speciation. For the precursors of both series A & B, greater Ca content corresponds to an increase in the amount of Q^0_0 observed (Table 6.3), giving rise to an increase in dissociated silica. This is mirrored by a subsequent decrease in the fully connected silica units (Q_4) and NC values upon increasing Ca. While no obvious trends are observed for Q^1-Q^3 units, the overall reduction in NC indicates that Ca is reducing the silicon network connectivity within the geopolymer network.

Several observations made from the ^{27}Al MAS NMR of the precursors (Section 6.3.1) are corroborated in the ^{29}Si data. For A0.8P and its activated product the observation of non (AlO4)(Q^4) units results in a reduction of Q_n ^{29}Si species

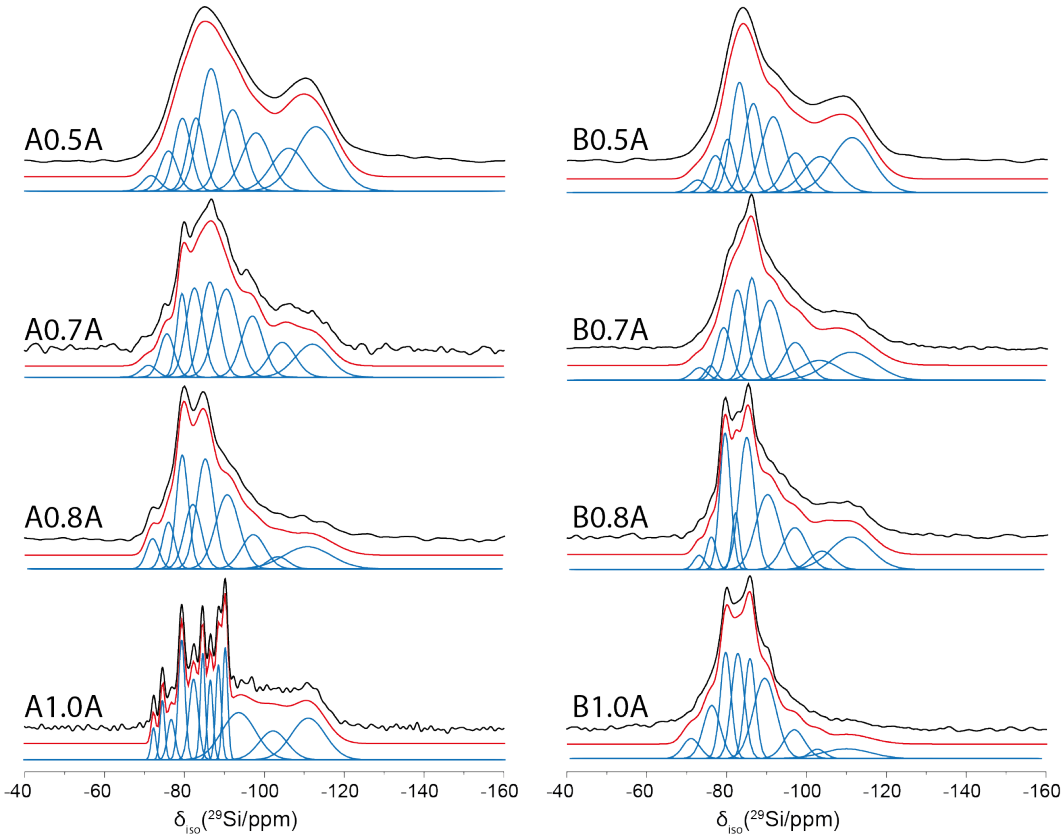

Figure 6.6: Deconvoluted ^{29}Si spectra of the activated 0.05 & 0.15 Si/Al geopolymers. The individual sites are shown in blue and the sum of these are marked in red.

observed (Table C.1). Changing the Al/Si ratio from 0.05 in series A to 0.15 in series B you might expect a corresponding increase in Q_n. However, no significant change in Q_n speciation is observed upon increasing the Al/Si ratio to 0.15. This suggests that the increased Al in series B is not fully integrated into the Si network. This is observed in the ^{27}Al MAS NMR of the series B precursors, where a greater amount of non $AlO_4(Q^4)$ units are observed. Additionally, the increased disorder seen observed in the ^{27}Al MAS NMR results of series B, could indicate some Al not fully integrated into the precursor network.

Upon activation several changes in the ratios of the ^{29}Si speciation are hypothesised. The addition of Na_2SiO_3 is expected to encourage cross linking in the synthetic precursors. In general, for all activated samples a decrease in the Q^0 structures is observed, which corresponds to an increase in NC upon activation. This corresponds to a reduction in the total proportion of Q^4 species and an increase in the ratio of Q^3 units.

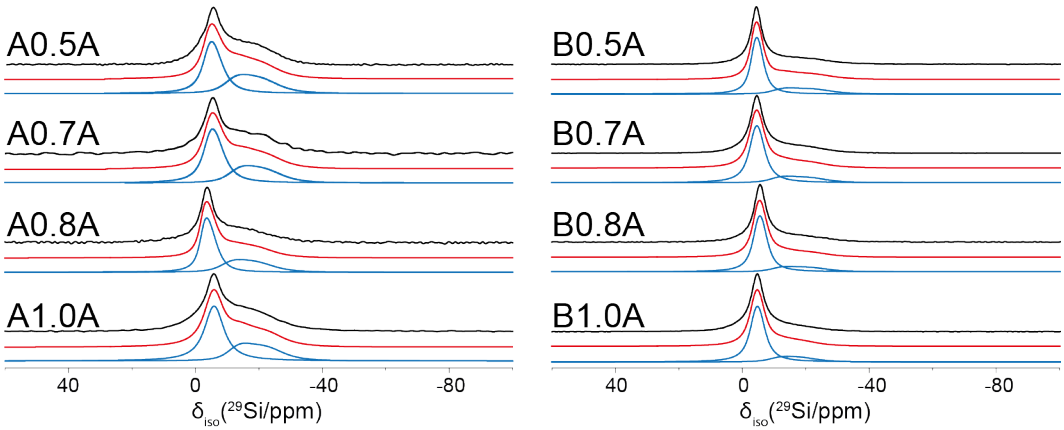

Figure 6.7: The deconvoluted ^{23}Na MAS NMR spectra of the 0.05 & 0.15 Si/Al Geopolymers. The individual sites are shown in blue and the sum of these are marked in red.

For most activated samples a significant change in the ^{29}Si lineshape is observed from their corresponding synthetic precursors. In many of the samples this presents in a narrowing of the resonances for the activated samples, suggesting a more ordered structure. Unusually activation of A0.5P does not have a significant impact on the ^{29}Si line shape. The only significant changes in Q_n^m speciation is observed in the Q_0^3 and Q_0^4 speciation, with the result giving no change to the NC. This is an indication that the majority of the silica added during the activated samples is not promoting cross linking. This is mirrored in the ^{27}Al MAS NMR (Figure 6.2) where no significant differences is observed in the Al environment. However, the amount of sodium silicate added during curing of series B is proportional to the added Al resulting in similar proportion of Q_n species formed.

6.3.3 ^{23}Na MAS NMR

The ^{23}Na MAS NMR (Figure 6.7) and 3QMAS (Appendix C, Figure C.1) are used to investigate the activation process of the C-(N)-(A)-S-H geopolymers. Deconvolutions of the two ^{23}Na spectra are shown in Figure 6.7, with the simulated parameters in Table 6.4. A clear initial observation is the ratio between the two resonances significantly differs between the series A & B, with the narrower resonance (Na1) having a higher proportion in series B. The narrower ^{23}Na resonance (Na1) is centred at approximately -3 ppm. This is the only observable resonance in the MQMAS data featured in the appendix (Figure C.1), with roughly equal distributions along both the Q_{is} and CS axes. In numerous investigations of C-N-A-S-H and N-A-S-H gels, Na1 has been attributed to Na^+ cations charge balancing the bridging aluminium

Table 6.4: The ^{23}Na parameters from the deconvoluted 1D MAS spectra acquired for the activated samples from series A & B. For all samples η_Q is set to 0.

Samples	Na1				Na2			
	Area (%)	δ_{iso} (ppm)	C_Q Centre (MHz)	C_Q Width (MHz)	Area (%)	δ_{iso} (ppm)	C_Q Centre (MHz)	C_Q Width (MHz)
A0.5A	57.3	−2.9	1.59	0.65	42.7	−8.1	3.09	0.65
A0.7A	61.5	−3.2	1.59	0.65	38.5	−9.3	3.09	0.65
A0.8A	62.5	−1.5	1.59	0.65	37.5	−6.8	3.09	0.65
A1.0A	63.1	−4.2	1.29	0.05	36.9	−8.7	3.20	0.62
B0.5A	73.1	−2.9	1.29	0.28	26.9	−7.4	3.37	0.65
B0.7A	77.5	−2.9	1.29	0.28	22.5	−6.9	3.27	0.62
B0.8A	78.8	−3.9	1.29	0.28	21.2	−7.4	3.27	0.62
B1.0A	81.5	−3.0	1.29	0.16	18.5	−7.6	2.91	0.62

tetrahedra within the geopolymer framework [217, 230, 233–235].

The broad featureless resonance (Na2, Table 6.4) is not featured in the 3QMAS spectra (Figure C.1). The δ_{iso} of Na2 is centred between 7-9 ppm and fitting required a large amount of Gaussian broadening, indicating a large disorder in chemical shift. The large distribution in δ_{iso} suggests why Na2 is not observed in the 3QMAS data. However, most of this disorder is not featured at the quadrupolar site, where despite a high centre value of C_Q, the width of the distribution from the simulations was small. The broadness of the resonance suggests that this is attributed to hydrated Na^+ bound to pore water within the geopolymer.

The increase in the proportion of Na1, for the 0.15 Al/Si series, suggests a larger amount of Na supported Al bridging tetrahedra between the frameworks. However, as observed in the activated ^{27}Al MAS NMR of series B (Figure 6.3), a large amount of calcium aluminium hydride phases. This can be attributed to the larger amount of Na present, increasing the amount of Ca free to form these Al^{VI} phases.

Additionally in both series, materials with greater Ca result in a corresponding increase in the Na1 environment. As at higher Ca concentrations the amount of activating sodium silicate added is reduced, and the amount of this resonance is unchanged, we are just observing a reduction in the Na2 resonance.

6.3.4 ^{17}O MAS NMR

Due to the associated cost of ^{17}O isotropic enrichment, the use of $H_2{}^{17}O$ during the activation process of the C-(N)-(A)-S-H gel was limited to 4 samples; A0.7A,

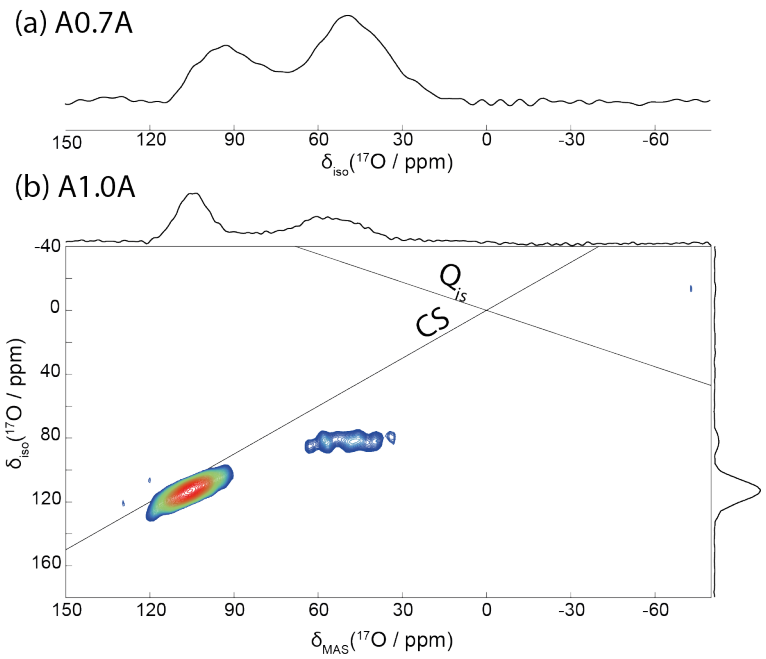

Figure 6.8: The ^{17}O MAS NMR of the activated 0.05 Al/Si geopolymers. (a) The 1D spectra of A0.7A. (b) The overlaid 1D and 3QMAS spectra of A1.0A.

A1.0A, B0.7A, and B1.0A. For series A, the ^{17}O MAS NMR is given in Figure 6.8. The 3QMAS spectra is only displayed for A1.0A as isotropic enrichment, was not sufficient enough in A0.7A for acquisition of a high quality spectra, fortunately a 1D MAS NMR measurement was still able to be obtained. Both A0.7A and A1.0A contain two observable resonances, centred at 100 & 50 ppm. The resonance at 100 ppm is assigned as a Si NBO resonance, this is similar to the NBO observed in Chapter 5, and seen in the literature for aluminosilicate glasses [236]. The observation of this resonance is typical for high Ca containing silicate systems, and as is evident between the A0.7A and A1.0A geopolymers, the proportion of this resonance increases with a greater Ca content.

The resonance centred at $\delta_{iso} = 50$ ppm is attributed to Si-O-Al bridging bonds formed during the activation process. Whilst it is possible that this resonance could be attributed to Si-O-Si BO's, the observed shift would indicate that this is not the case [168].

While similarities are observed in the ^{17}O 1D and 3QMAS data for B0.7A and B1.0A (Figure 6.9), some significant differences are apparent when they are compared to lower the Al/Si content samples (Figure 6.8). Both B0.7A and B1.0A are primarily dominated by the Si NBO peak centred at 100 ppm and contain evidence of the Si-O-Al BO resonance in the 3QMAS. However, for both B0.7A and

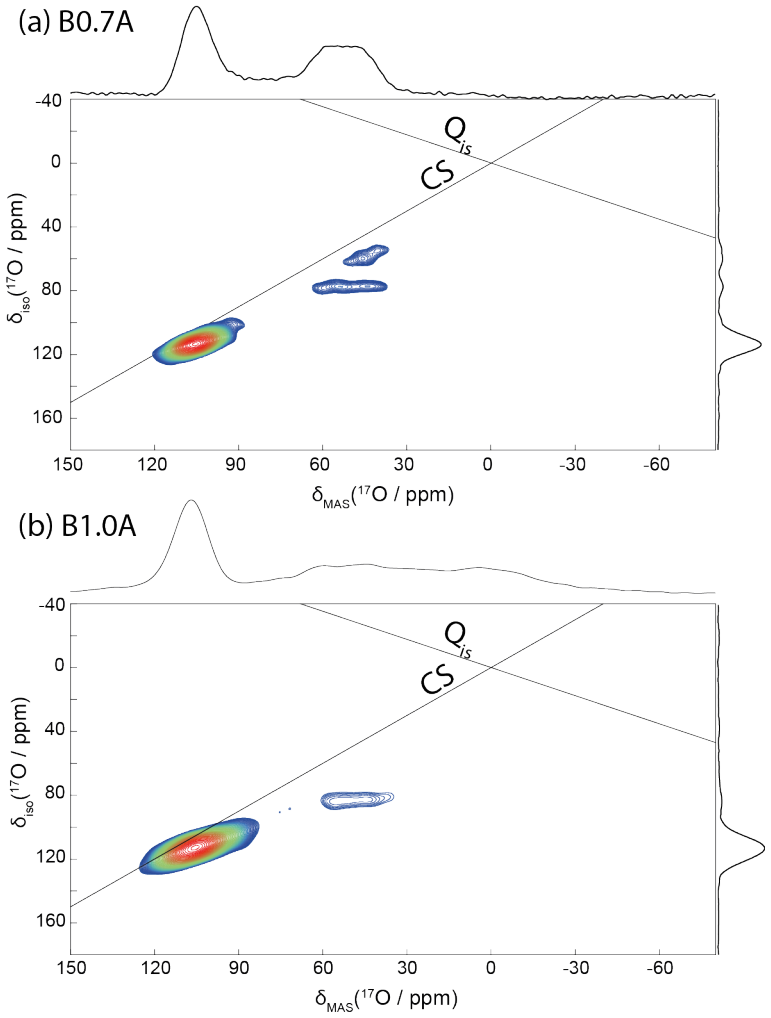

Figure 6.9: The ^{17}O 3QMAS for the activated 0.15 Al/Si geopolymers for (a) B0.7A. (b) B1.0A.

B1.0A (Figure 6.9), additional resonances are observed.

In B0.7A the additional resonance is clearly observed in the MQMAS (Figure 6.9), with distribution parallel to the CS axis. This resonance has a δ_{iso} similar to the Si-O-Al BO resonance causing an overlap in the 1D spectrum. This has been identified as an Al-O-Al resonance previously observed in low silica Ca containing aluminosilicate glasses [236]. This is an indication of the $AlO_4(AlO_6)$ phase formed in the ^{27}Al MAS NMR (Figure 6.3) upon activation.

In B1.0A the NBO and BO resonances are observed in the 3QMAS spectrum, a large additional resonance is observed in the 1D spectrum. This resonance spans the region where the Si-O-Si BO is observed [168, 224]. The lack of observation of this unit in the 3QMAS is due to the relatively small amount of this site contained in the system, to the NBO peak observed.

From the ^{17}O results it has been deduced that during the activation process, introduced ^{17}O is acting as either Si NBO's or as Si-O-Al BO. This observation of a Si-O-Al BO is confirmation that during the activation process these bonds are being formed. While the ^{29}Si shows no direct increase of these bridging bonds, a relative decrease in Q_0^0 and Q_0^4 suggest that the Q_n sites are increasing.

For A0.7A, the only ^{17}O sample investigated with no AFm phase observed in the ^{27}Al MAS NMR, the Si NBO resonance is broader and at a slightly lower ppm than in the other samples. This lower shift and increased disorder could indicate the presence of Si NBO resonances, which is not fully offset by Ca. While we might expect to observe differences between the Si NBO resonance in B0.7A and B1.0A due to the change in Ca, both have similar shifts to A1.0A.

Additionally, the Al BO resonance, for A0.7A, is observed in a larger proportion when compared to the Si-O-Al BO resonance, indicating that activation of A0.7A has an increase in the proportion of cross-linking Al. This reinforces the large reduction in disorder observed for the ^{27}Al MAS NMR upon curing. This resonance is observed in smaller quantities in all other investigated samples due to the large proportion of hydrated AFm produced.

6.4 Conclusions

The modification of the Ca/(Al+Si) and Al/Si ratios of calcium aluminosilicate precursors and there activated analogues were investigated. Fundamentally, the bulk structure of the precursor, is primarily made up of a silicon network with aluminium dispersed throughout the matrix. An increase in the Ca proportion promotes greater ordering in the aluminium structure of the 0.05 Al/Si precursor material. This is

shown through reduction in the measured disorder of the Al resonances. However, this reduction in Al comes at a trade off in the bulk Si structures, as increased Ca results in greater proportion of Q^0 units and a reduction in the proportion of the total Q^4 sites. This is also observed as a drop in total NC of the precursor system.

Increasing the Al/Si ratio from 0.05 to 0.15 results in the lowest Ca sample (B0.5P) containing only $AlO_4(Q^4)$ units. Further increases to the Ca ratio results in formation of C_3A and calcium aluminate phases. Additionally, a greater proportion of the ^{29}Si is observed as Q^0 units indicating greater disruption to the network.

Activation further highlights greater differences observed between series A and B. The increased Al in series B results in the activated samples containing at most 70 % of $AlO_4(Q^4)$ units, as observed by ^{27}Al MAS NMR. In contrast, the lower aluminium ratio of series A promotes more Al integrating into the Si network, as for A0.5A and A0.7A all Al is observed as $AlO_4(Q^4)$ units and A0.8A and A1.0A contain $\sim$90 % AlO_4 units. This increase in proportion of Al not contained in the Si network is not observed in the ^{29}Si MAS NMR, where no significant change in Q_n units is present.

Upon activation, evidence of cross linking is observed through the formation of Si-O-Al BO by ^{17}O MAS NMR. However, due to the greater proportion of Al in B0.7A, Al-O-Al bonds are also observed, reinforcing the $AlO_4(AlO_6)$ resonance in ^{27}Al MAS NMR. This is not observed in B1.0A, which does not contain the $AlO_4(AlO_6)$ resonance in ^{27}Al MAS NMR, instead evidence of Si-O-Si is observed. However, the ^{29}Si results for B1.0A do not show extra Q^4 units post activation, compared to the other enriched samples. In fact the Q^4 units experience a significant drop when compared to the rest of the series. However, significant increase in both the Q^1 and Q^3 units this is representation of these sites forming.

The findings suggest how subtle changes in the reaction mixture can result in significant changes in micro structure of C-(N)-(A)-S-H gels. This highlights the significance of carefully controlling the precursor mixtures so a desired product can be obtained upon curing.

Chapter 7

Summary and Outlook

7.1 Low Field and Fast MAS Studies on Paramagnetic Cathode Battery Materials

Through the use of a low magnetic field and fast MAS to paramagnetic cathode materials, it has been demonstrated that high resolution MAS NMR is possible. This has allowed the determination of slight differences in the observed ^{7}Li resonance in LFP. It has been shown that this shift is not dependent on factors including crystallite size, carbon coating, mass magnetic susceptibility or magnetic particles present. It has been determined this is likely due to changes in unit cell volume of the olivine phase. This is a result of less Li^{+} in the unit cell thus facilitating the reduction of some Fe^{2+} to Fe^{3+}. The position that ^{7}Li occupies in the LFP channels. These differences in the ^{7}Li δ_{iso} that occur between synthesis methods were also observed in the Mn substituted series. The bulk of these differences are attributed to greater Mn^{2+} substitution of the Fe^{2+} site corresponding to an increase in the magnetic susceptibility at the transition metal site. However, significant differences were still observed between the BM and FSP series, which are attributed to the change in the unit cell of LFP.

The use of ^{31}P MAS NMR did not indicate significant differences between the BM, FSP and ST techniques. However, due to the resolution of the ^{31}P in the $LiFe_xMn_{1-x}PO_4$ series, discrepancies in the ratio of sites were observed, resulting in an indication that synthesis produced a clustering of sites in the higher Mn FSP materials. Furthermore, MPMS measurements confirmed magnetic particles were also present in these high Mn FSP samples indicating that the synthesis did not proceed correctly. These magnetic particles were also observed in the BM samples, however it is likely an inherent property of the synthesis procedure and did not appear to af-

fect the ^{31}P site distribution. While one of the most common contaminates from the carbon coating process Fe_2P, was not able to be observed through ^{31}P MAS NMR, it was clearly observed in the SQUID magnetic measurements, further highlighting the need for a multi technique approach for analysis of these systems.

The doping of V into LFP has shown to be heavily dependent on the amount of Li precursor added. Both ^{31}P and ^{7}Li MAS NMR were able to clearly observe impurity resonances mirrored in the XRD reflections. There was no significant variation in the ^{7}Li δ_{iso} for the 3 and 5% amounts of doped V. However, the spectrum of the 1% doped sample did have a greater δ_{iso}, due to the small amount of V dopant added, likely resulting as a reduction in the magnetic susceptibility around the ^{7}Li site. This could be confirmed with the generation of a series with much greater V doping than investigated here.

It would be prudent in the future to correlate the isotropic shift data with electrochemical results of the different manufacturing methods. If factors like charge capacity or cycle stability could be correlated to the isotropic shift and unit cell volume it may hint to any further discrepancies observed between the BM, FSP and ST samples. It would also be interesting to see if changing the BM precursor or if any subtle tweaks to the method could produce LFP with no magnetic particles. For the V doped series in the future it would be interesting to investigate the materials by ^{51}V MAS NMR. This might give clues on the oxidation state of V and the environment that it is occupying in the LFP structure.

7.2 Using ^{17}O NMR to Monitor the Incorporation of Ca^{2+} and Zn^{2+} in Stöber Nanoparticles

Through the use of ^{17}O and ^{29}Si MAS NMR the integration of beneficial cations, such as Ca and Zn, into the Stöber network was probed. It was shown that before calcination, addition of beneficial cations had no real impact on the silicon structure, as shown by both the ^{29}Si network connectivity, and the ^{17}O structure. This is an indication that the cations are located primarily on the surface of the Stöber nanoparticles.

However, post calcination significant differences were observed indicating the incorporation of these cations into the Stöber network. The ^{29}Si results show that upon calcination Ca^{2+} and Zn^{2+} are incorporated into the Stöber network and disrupt the silicon Q^4 network. The network connectivity suggests that the incorporation of Zn disrupts the Stöber network more than Ca. This difference in NC was shown to be due to Zn forming a large amount of crystalline Zn_2SiO_4–II phases

instead of forming Zn BO or NBO resonances. Formation of Zn_2SiO_4 –II was supported by evidence obtained from HRTEM, DFT calculations, and ^{17}O MAS NMR.

Future work should likely involve different Zn precursors to investigate if crystallisation can be avoided. Additionally, the interesting structure of mesoporous Si nanoparticles could be another avenue for investigation with this technique. However, as the production of the mesoporous nanoparticles typically require large volumes of water, a different method for isotropic enrichment of ^{17}O would need to be found.

7.3 Quadrupolar Solid State NMR Investigation into the Curing Process of Alkali-Activated C-(N)-(A)-S-H Geopolymers

Solid state NMR was successful at probing the structural differences arising from changing the C-(N)-(A)-S-H geopolymer composition. Using Quadfit to simulate disorder inherent in the structure of the ^{27}Al and ^{23}Na nuclei, it was possible to gain a picture of how changing the Ca/(Si+Al) and Al/Si ratios affects the curing process.

For the lower Al/Si ratio it was seen that for the precursor materials, an increase in Ca/(Si+Al) generally reduced the disorder present in the $AlO_4(Q^4)$ site. However, this is not true when Al/Si = 0.15, where excess Al and Ca results in the formation of non $AlO_4(Q^4)$ phases. Furthermore, for both 0.05 & 0.15 Al/Si, additional Ca decreased the NC of the silicon network. Primarily caused through the reduction Q^4 units, and corresponding to an increase in free silica in the form of Q^0 resonances.

Upon the addition of Na_2SiO_3 and thus activation of the C-(N)-(A)-S-H Geopolymers, ^{29}Si MAS NMR proved that the silica network became more connected. This corresponded to the formation of a cross linked network between the particles forming as a result of the activation. It is also observed that when both the Ca/(Si+Al) and Al/Si ratios are high, that a greater proportion of crystalline phases are present. These mostly take the form of hydroxy AFm phases, and is attributed the high availability of Ca and Al. This high crystallinity could be an indication of why the NC is lower in the 0.15 Al/Si activated series.

In the future it would be interesting what effect common contaminants (such as: Fe_2O_3, MgO, SO_3, or K_2O) that have been observed in fly ash have on both the precursors and the activated materials. It would also be interesting to investigate

the highly semi crystalline nature of A1.0A. Dipolar coupling based experiments, such as a HMQC, could be used to investigate which ^{29}Si resonances are coupled to the ^{27}Al in the structure. However, this may not be feasible due to the low ^{27}Al content in the materials and also the likelihood that this would require expensive isotropic enrichment of the ^{29}Si nucleus.

Bibliography

[1] E. R. Andrew and E. Szczesniak. A historical account of NMR in the solid state. *Progress in Nuclear Magnetic Resonance Spectroscopy*, 28(1):11–36, 1995.

[2] C. Boesch. Nobel Prizes for nuclear magnetic resonance: 2003 and historical perspectives. *Journal of magnetic resonance imaging : JMRI*, 20(2):177–179, 2004.

[3] E. D. Becker. A brief history of nuclear magnetic resonance. *Analytical Chemistry*, 65(6):295–302, 1993.

[4] E. M. Purcell, H. C. Torrey, and R. V. Pound. Resonance absorption by nuclear magnetic moments in a solid. *Physical review*, pages 37–38, 1946.

[5] F. Bloch, W. W. Hansen, and M. Packard. Nuclear Induction. *Physical Review*, 70(7-8):474–485, 1946.

[6] W. D. Knight. Nuclear Magnetic Resonance Shift in Metals. *Physical Review*, 76(8):1259–1260, oct 1949.

[7] W. G. Proctor and F. C. Yu. The Dependence of a Nuclear Magnetic Resonance Frequency upon Chemical Compound*. *Physical Review*, 77(5):717, 1950.

[8] E. L. Hahn. Spin Echoes. *Physical Review*, 80(4):580–594, 1950.

[9] E. R. Andrew, A. Bradbury, and R. G. Eades. Nuclear Magnetic Resonance Spectra from a Crystal rotated at High Speed, 1958.

[10] K. T. Mueller, B. Q. Sun, G. C. Chingas, J. W. Zwanziger, T. Terao, and A. Pines. Dynamic-Angle Spinning of Quadrupolar Nuclei. *Journal of Magnetic Resonance (1969)*, 86(3):470–487, 1990.

[11] A. Samoson, E. Lippmaa, and A. Pines. High resolution solid-state N.M.R. Averaging of second-order effects by means of a double-rotor. *Molecular Physics*, 65(4):1013–1018, 1988.

[12] M. P. Klein and G. W. Barton. Enhancement of Signal To Noise Ratio By Continuous Averaging: Application To Magnetic Resonance. *The Review of Scientific Instruments*, 754, 1963.

[13] R. R. Ernst and W. A. Anderson. Application of Fourier Transform Spectroscopy to Magnetic Resonance. *Rev.Sci.Instrum.*, 37(1966):93–102, 1966.

[14] R. R. Ernst. Ernst, Richard R.: The Success Story of Fourier Transformation in NMR. *Encyclopedia of Magnetic Resonance*, 2007.

[15] W. P. Aue, E. Bartholdi, and R. R. Ernst. Two-dimensional spectroscopy. Application to nuclear magnetic resonance. *J. Chem. Phys.*, 64(1976):2229–2246, 1976.

[16] R. R. Ernst, G. Bodenhausen, and A. Wokaun. *Principles of Nuclear Magnetic Resonance in One and Two Dimensions*. International series of monographs on chemistry. Clarendon Press, 1990.

[17] A. Medek, J. S. Harwood, and L. Frydman. Multiple-Quantum Magic-Angle Spinning NMR: A New Method for the Study of Quadrupolar Nuclei in Solids. *Journal of the American Chemical Society*, 117(51):12779–12787, 1995.

[18] J. V. Hanna and M. E. Smith. Recent technique developments and applications of solid state NMR in characterising inorganic materials. *Solid State Nuclear Magnetic Resonance*, 38(1):1–18, 2010.

[19] M. H. Levitt. *Spin Dynamics: Basics of Nuclear Magnetic Resonance*. Wiley, 2013.

[20] K. J. D. MacKenzie and M. E. Smith. *Multinuclear Solid-state NMR of Inorganic Materials*. Pergamon materials series. Elsevier Science Limited, 2002.

[21] M. J. Duer. *Introduction to Solid-State NMR Spectroscopy*. Wiley, 2005.

[22] R. E. Wasylishen, S. E. Ashbrook, and S. Wimperis. *NMR of Quadrupolar Nuclei in Solid Materials*. eMagRes Books. Wiley, 2012.

[23] S. Blundell. *Magnetism in Condensed Matter*. Oxford Master Series in Condensed Matter Physics. OUP Oxford, 2001.

[24] M Bertmer. Paramagnetic solid-state NMR of materials. *Solid State Nuclear Magnetic Resonance*, 81(November 2016):1–7, 2016.

[25] I. Bertini, C. Luchinat, and G. Parigi. Magnetic susceptibility in paramagnetic NMR. *Progress in Nuclear Magnetic Resonance Spectroscopy*, 40(3):249–273, apr 2002.

[26] C. P. Grey and N. Dupré. NMR studies of cathode materials for lithium-ion rechargeable batteries. *Chemical reviews*, 104(10):4493–512, oct 2004.

[27] G. Pintacuda and G. Kervern. Paramagnetic solid-state magic-angle spinning NMR spectroscopy. *Modern NMR Methodology*, 335:157–200, 2013.

[28] I. Bertini, C. Luchinat, G. Parigi, and E. Ravera. *NMR of Paramagnetic Molecules: Applications to Metallobiomolecules and Models*. Current Methods in Inorganic Chemistry. Elsevier Science, 2016.

[29] M. Edén. Computer Simulations in Solid-State NMR. I. Spin Dynamics Theory. *Concepts in Magnetic Resonance Part A*, 17A(1):117–154, 2003.

[30] W. C. Dickinson. Dependence of the F^{19} nuclear resonance position on chemical compound*. *Physical Review*, 77(5):736–737, 1950.

[31] E. Lenz. Ueber die Bestimmung der Richtung der durch elektodynamische Vertheilung erregten galvanischen Ströme. *Annalen der Physik und Chemie*, 107:483–494, 1834.

[32] P. P. Man. Quadrupolar Interactions. *Encyclopedia of Magnetic Resonance*, 9:165–196, 2011.

[33] I. Bertini, C. Luchinat, G. Parigi, and E. Ravera. Introduction. In *Solution NMR of Paramagnetic Molecules*, pages 1–24. Elsevier, 2017.

[34] E. R. Andrew, A. Bradbury, and R. G. Eades. Removal of Dipolar Broadening of Nuclear Magnetic Resonance Spectra of Solids by Specimen Rotation. *Nature*, 183(4678):1802–1803, 1959.

[35] H. Y. Carr and E. M. Purcell. Effects of Diffusion on Free Precession in Nuclear Magnetic Resonance Experiments. *Physical Review*, 94(3):630–638, 1954.

[36] R. M. Pearson and C. Job. Instrumentation for the Home Builder. *eMagRes*, 1062, 2007.

[37] G. N. Chmurny and D. I. Hoult. The Ancient and Honourable Art of Shimming. *Concepts in Magnetic Resonance*, 2(3):131–149, 1990.

[38] V. I. Bakhmutov. Strategies for solid-state NMR studies of materials: From diamagnetic to paramagnetic porous solids. *Chemical Reviews*, 111(2):530–562, 2011.

[39] B. M. Fung, A. K. Khitrin, and K. Ermolaev. An Improved Broadband Decoupling Sequence for Liquid Crystals and Solids. *Journal of Magnetic Resonance*, 101:97–101, 2000.

[40] A. E Bennett, C. M. Rienstra, M. Auger, K. V. Lakshmi, R. G. Griffin, A. E. Bennett, C. M. Rienstra, and R. G. Griffin. Heteronuclear decoupling in rotating solids Heteronuclear decoupling in rotating solids. *The Journal of Chemical Physics*, 103(1995):6951–6958, 1995.

[41] L. Frydman and J. S. Harwood. Isotropic Spectra of Half-Integer Quadrupolar Spins from Bidimensional Magic-Angle Spinning NMR. *Journal of the American Chemical Society*, 117(19):5367–5368, 1995.

[42] J. P. Amoureux and C. Fernandez. Triple, quintuple and higher order multiple quantum MAS NMR of quadrupolar nuclei. *Solid state nuclear magnetic resonance*, 10:211–223, 1998.

[43] M. McElfresh. Fundamentals of magnetism and magnetic measurements.

[44] A. K. Padhi, K. S. Nanjundaswamy, and Goodenough J. B. Phospho-olivines as Positive-Electrode Materials for Rechargeable Lithium Batteries. *Journal of The Electrochemical Society*, 144(4):1188, 1997.

[45] A. S. Andersson, J. O. Thomas, B. Kalska, and L. Häggström. Thermal Stability of $LiFePO_4$-Based Cathodes. *Electrochemical and Solid-State Letters*, 3(2):66–68, 2000.

[46] J. B. Goodenough and Y. Kim. Challenges for rechargeable Li batteries. *Chemistry of Materials*, 22(3):587–603, 2010.

[47] E. J. Shin, S. Kim, J. K. Noh, D. Byun, K. Y. Chung, H. S. Kim, and B. W. Cho. A green recycling process designed for $LiFePO_4$ cathode materials for Li-ion batteries. *Journal of Materials Chemistry A*, 3(21):11493–11502, 2015.

[48] S. Wang, H. Yang, L. Feng, S. Sun, J. Guo, Y. Yang, and H. Wei. A simple and inexpensive synthesis route for $LiFePO_4$/C nanoparticles by co-precipitation. *Journal of Power Sources*, 233:43–46, 2013.

[49] D. Bian, Y. Sun, S. Li, Y. Tian, Z. Yang, X. Fan, and W. Zhang. A novel process to recycle spent $LiFePO_4$ for synthesizing $LiFePO_4$/C hierarchical microflowers. *Electrochimica Acta*, 190:134–140, 2016.

[50] Research In China: Beijing; China. Global and China Lithium Iron Phosphate ($LiFePO_4$) and Battery Industry Report, 2016-2020. Technical report, Research In China: Beijing, China, 2016.

[51] D. Morgan, A. Van der Ven, and G. Ceder. Li Conductivity in Li_xMPO_4 (M = Mn, Fe, Co, Ni) Olivine Materials. *Electrochemical and Solid-State Letters*, 7:A30, 2004.

[52] A. Jena and B. R. K. Nanda. Unconventional Magnetism and Band Gap Formation in $LiFePO_4$: Consequence of Polyanion Induced. *Nature Publishing Group*, (December 2015):1–11, 2016.

[53] M. S. Whittingham. Lithium batteries and cathode materials. *Chemical reviews*, 104(10):4271–301, oct 2004.

[54] S. Yang, Y. Song, P. Y. Zavalij, and M. S. Whittingham. Reactivity, stability and electrochemical behavior of lithium iron phosphates. *Electrochemistry Communications*, 4:239–244, 2002.

[55] L. X. Yuan, Z. H. Wang, W. X. Zhang, X. L. Hu, J. T. Chen, Y. H. Huang, and J. B. Goodenough. Development and challenges of $LiFePO_4$ cathode material for lithium-ion batteries. *Energy Environ. Sci.*, 4(2):269–284, 2011.

[56] K. Dokko, S. Koizumi, H. Nakano, and K. Kanamura. Particle morphology, crystal orientation, and electrochemical reactivity of $LiFePO_4$ synthesized by the hydrothermal method at 443 K. *Journal of Materials Chemistry*, 17:4803–4810, 2007.

[57] X. Qin, X. Wang, H. Xiang, J. Xie, J. Li, and Y. Zhou. Mechanism for Hydrothermal Synthesis of $LiFePO_4$ Platelets as Cathode Material for Lithium-Ion Batteries. *Platelets*, 114:16806–16812, 2010.

[58] Y. Yiu, M. D. Le, R. Toft-Petersen, G. Ehlers, R. J. McQueeney, and D. Vaknin. Hybrid excitations due to crystal field , spin-orbit coupling , and spin waves in $LiFePO_4$. 104409:1–7, 2017.

[59] S. Shi, C. Ouyang, Z. Xiong, L. Liu, Z. Wang, H. Li, D. Wang, L. Chen, and X. Huang. First-principles investigation of the structural, magnetic, and electronic properties of olivine $LiFePO_4$, url = https://link.aps.org/doi/10.1103/PhysRevB.71.144404, volume = 71, year = 2005. *Physical Review B*, (14):144404.

[60] A. Burrows, J. Holman, A. Parsons, G. Pilling, and G. Price. *Chemistry^3: Introducing Inorganic, Organic and Physical Chemistry*. OUP Oxford, 2013.

[61] B. Goßner and H. Strunz. Über strukturelle Beziehungen zwischen Phosphaten (Triphylin) und Silikaten (Olivin) und über die chemische Zusammensetzung von Ardennit. *Zeitschrift für Kristallographie - Crystalline Materials*, 83(1-6):415–421, 1932.

[62] G. Kucinskis, G. Bajars, and J. Kleperis. Graphene in lithium ion battery cathode materials: A review. *Journal of Power Sources*, 240:66–79, 2013.

[63] M. Takahashi, S. Tobishima, K. Takei, and Y. Sakurai. Characterization of $LiFePO_4$ as the cathode material for rechargeable lithium batteries. *Journal of Power Sources*, 97-98:508–511, 2001.

[64] F. Croce, A. D' Epifanio, J. Hassoun, A. Deptula, T. Olczac, and B. Scrosati. A Novel Concept for the Synthesis of an Improved $LiFePO_4$ Lithium Battery Cathode. *Electrochemical and Solid-State Letters*, 5:A47, 2002.

[65] N. Ravet, J. B. Goodenough, S. Besner, M. Simoneau, P. Hovington, and M. Armand. In Precedings of the 196 ECS meeting. In *In Precedings of the 196 ECS meeting*, page 172, 1999.

[66] N. Ravet, Y. Chouinard, J.F. Magnan, S. Besner, M. Gauthier, and M. Armand. Electroactivity of natural and synthetic triphylite. *Journal of Power Sources*, 97-98:503–507, jul 2001.

[67] M. M. Doeff, Y. Hu, F. McLarnon, and R. Kostecki. Effect of Surface Carbon Structure on the Electrochemical Performance of $LiFePO_4$. *Electrochemical and Solid-State Letters*, 6:A207, 2003.

[68] Z. Chen and J. R. Dahn. Reducing Carbon in $LiFePO_4$/C Composite Electrodes to Maximize Specific Energy, Volumetric Energy, and Tap Density. *Journal of The Electrochemical Society*, 149:A1184, 2002.

[69] R. Dominko, M. Gaberscček, J. Drofenik, M. Bele, and S. Pejovnik. A Novel Coating Technology for Preparation of Cathodes in Li-Ion Batteries. *Electrochemical and Solid-State Letters*, 4:A187, 2001.

[70] M. Islam, S. C. Ur, and M. S. Yoon. Improved performance of porous $LiFePO_4$/C as lithium battery cathode processed by high energy milling comparison with conventional ball milling. *Current Applied Physics*, 15(4):541–546, 2015.

[71] C. Delacourt, P. Poizot, S. Levasseur, and C. Masquelier. Size Effects on Carbon-Free $LiFePO_4$ Powders. *Electrochemical and Solid-State Letters*, 9(7):A352, 2006.

[72] H. Yang, X. Wu, M. Cao, and Y. Guo. Solvothermal Synthesis of $LiFePO_4$ Hierarchically Dumbbell-Like Microstructures by Nanoplate Self-Assembly and Their Application as a Cathode Material in Lithium-Ion Batteries. *Society*, pages 3345–3351, 2009.

[73] D. S. Jung, Y. N. Ko, Y. C. Kang, and S. B. Park. Recent progress in electrode materials produced by spray pyrolysis for next-generation lithium ion batteries. *Advanced Powder Technology*, 25(1):18–31, 2014.

[74] I. D. Johnson, M. Lübke, O. Y. Wu, N. M. Makwana, G. J. Smales, H. U. Islam, R. Y. Dedigama, R. I. Gruar, C. J. Tighe, D. O. Scanlon, F. Corá, D. J. L. Brett, P. R. Shearing, and J. A. Darr. Pilot-scale continuous synthesis of a vanadium-doped $LiFePO_4$/C nanocomposite high-rate cathodes for lithium-ion batteries. *Journal of Power Sources*, 302:410–418, 2016.

[75] A. Yamada, S. C. Chung, and K. Hinokuma. Optimized $LiFePO_4$ for Lithium Battery Cathodes. *Journal of The Electrochemical Society*, 148(3):A224, 2001.

[76] C. H. Mi, X. B. Zhao, G. S. Cao, and J. P. Tu. In Situ Synthesis and Properties of Carbon-Coated $LiFePO_4$ as Li-Ion Battery Cathodes. *Journal of The Electrochemical Society*, 152:A483, 2005.

[77] N. Kosova and E. Devyatkina. On mechanochemical preparation of materials with enhanced characteristics for lithium batteries. *Solid State Ionics*, 172(1-4 SPEC. ISS.):181–184, 2004.

[78] G. T. K. Fey, Y. G. Chen, and H. M. Kao. Electrochemical properties of $LiFePO_4$ prepared via ball-milling. *Journal of Power Sources*, 189(1):169–178, 2009.

[79] S. J. Kwon, C. W. Kim, W. T. Jeong, and K. S. Lee. Synthesis and electrochemical properties of olivine $LiFePO_4$ as a cathode material prepared by mechanical alloying. *Journal of Power Sources*, 137(1):93–99, 2004.

[80] S. Franger, F. Le Cras, C. Bourbon, and H. Rouault. Comparison between different $LiFePO_4$ synthesis routes and their influence on its physico-chemical properties. *Journal of Power Sources*, 119-121:252–257, 2003.

[81] C. M. Julien, A. Mauger, A. Ait-Salah, M. Massot, F. Gendron, and K. Zaghib. Nanoscopic scale studies of $LiFePO_4$ as cathode material in lithium-ion batteries for HEV application. *Ionics*, 13:395–411, 2007.

[82] M. Armand, M. Gauthier, JF Magnan, and N Ravet. 2009 Method for synthesis of carbon-coated redox materials with controlled size WO 02/27823 A1, 2001.

[83] A. Ait-Salah, A. Mauger, C. M. Julien, and F. Gendron. Nano-sized impurity phases in relation to the mode of preparation of $LiFePO_4$. *Materials Science and Engineering B: Solid-State Materials for Advanced Technology*, 129(1-3):232–244, 2006.

[84] P. Subramanya Herle, B. Ellis, N. Coombs, and L. F. Nazar. Nano-network electronic conduction in iron and nickel olivine phosphates. *Nature Materials*, 3(3):147–152, 2004.

[85] J. Barker, M. Y. Saidi, and J. L. Swoyer. A Carbothermal Reduction Method for the Preparation of Electroactive Materials for Lithium Ion Applications. *Journal of The Electrochemical Society*, 150(6):A684, 2003.

[86] A. Ait-Salah, K. Zaghib, A. Mauger, F. Gendron, and C. M. Julien. Magnetic studies of the carbothermal effect on $LiFePO_4$. *Physica Status Solidi (A) Applications and Materials Science*, 203(1):2–4, 2006.

[87] G. Demazeau. Solvothermal processes: Definition, key factors governing the involved chemical reactions and new trends. *Zeitschrift fur Naturforschung - Section B Journal of Chemical Sciences*, 65(8):999–1006, 2010.

[88] S. Yang, P. Y. Zavalij, and M. S. Whittingham. Hydrothermal synthesis of lithium iron phosphate cathodes. *Electrochemistry Communications*, 3(May):505–508, 2001.

[89] Z. Xu, L. Xu, Q. Lai, and X. Ji. A PEG assisted sol-gel synthesis of $LiFePO_4$ as cathodic material for lithium ion cells. *Materials Research Bulletin*, 42(5):883–891, 2007.

[90] L. N. Wang, Z. G. Zhang, and K. L. Zhang. A simple, cheap soft synthesis routine for $LiFePO_4$ using iron(III) raw material. *Journal of Power Sources*, 167(1):200–205, 2007.

[91] G. T. K. Fey, K. P. Huang, H. M. Kao, and W. H. Li. A polyethylene glycol-assisted carbothermal reduction method to synthesize $LiFePO_4$ using industrial raw materials. *Journal of Power Sources*, 196(5):2810–2818, 2011.

[92] S. Yang, X. Zhou, J. Zhang, and Z. Liu. Morphology-controlled solvothermal synthesis of $LiFePO_4$ as a cathode material for lithium-ion batteries. *Journal of Materials Chemistry*, 20(37):8086, 2010.

[93] T. Muraliganth, K. R. Stroukoff, and A. Manthiram. Microwave-solvothermal synthesis of nanostructured Li_2MSiO_4/C (M = Mn and Fe) cathodes for lithium-ion batteries. *Chemistry of Materials*, 22(20):5754–5761, 2010.

[94] J. S. Lim, D. H. Kim, V. Mathew, D. C. Ahn, and J. K. Kim. Synthesis of $LiFePO_4$ nanoparticles by solvothermal process using various polyol media and their electrochemical properties. *Journal of nanoscience and nanotechnology*, 11(2):1451–1454, 2011.

[95] B. Wang, T. Liu, A. Liu, G. Liu, L. Wang, T. Gao, D. Wang, and X. S. Zhao. A Hierarchical Porous C@$LiFePO_4$/Carbon Nanotubes Microsphere Composite for High-Rate Lithium-Ion Batteries: Combined Experimental and Theoretical Study. *Advanced Energy Materials*, 6(16):1600426, 2016.

[96] M. Cuisinier, N. Dupré, P. Moreau, and D. Guyomard. NMR monitoring of electrode / electrolyte interphase in the case of air-exposed and carbon coated $LiFePO_4$. *Journal of Power Sources*, 243:682–690, 2013.

[97] D. H. Kim and J. Kim. Synthesis of $LiFePO_4$ Nanoparticles in Polyol Medium and Their Electrochemical Properties. *Electrochemical and Solid-State Letters*, 9(9):A439, 2006.

[98] K. Vediappan, A. Guerfi, V. Gariépy, G. P. Demopoulos, P. Hovington, J. Trottier, A. Mauger, C. M. Julien, K. Zaghib, V. Gariépy, G. P. Demopoulos,

P. Hovington, J. Trottier, A. Mauger, C. M. Julien, and K. Zaghib. Stirring effect in hydrothermal synthesis of nano C-$LiFePO_4$. *Journal of Power Sources*, 266:99–106, 2014.

[99] Y. Zhang, W. Wang, P. Li, Y. Fu, and X. Ma. A simple solvothermal route to synthesize graphene-modified $LiFePO_4$ cathode for high power lithium ion batteries. *Journal of Power Sources*, 210:47–53, 2012.

[100] C. Su, X. Bu, L. Xu, J. Liu, and C. Zhang. A novel $LiFePO_4$/graphene/carbon composite as a performance-improved cathode material for lithium-ion batteries. *Electrochimica Acta*, 64:190–195, 2012.

[101] M. Wu, Z. H. Wang, L. X. Yuan, W. X. Zhang, X. L. Hu, and Y. H. Huang. Morphology-controllable solvothermal synthesis of nanoscale $LiFePO_4$ in a binary solvent. *Chinese Science Bulletin*, 57(32):4170–4175, 2012.

[102] O. Waser, R. Büchel, A. Hintennach, P. Novák, and S. E. Pratsinis. Continuous flame aerosol synthesis of carbon-coated nano-$LiFePO_4$ for Li-ion batteries. *Journal of Aerosol Science*, 42:657–667, 2011.

[103] N. A. Hamid, S. Wennig, S. Hardt, A. Heinzel, C. Schulz, and H. Wiggers. High-capacity cathodes for lithium-ion batteries from nanostructured $LiFePO_4$ synthesized by highly-flexible and scalable flame spray pyrolysis. *Journal of Power Sources*, 216:76–83, 2012.

[104] R. Strobel, A. Baiker, and S. E. Pratsinis. Aerosol flame synthesis of catalysts. *Advanced Powder Technology*, 17(5):457–480, 2006.

[105] S. Y. Chung, J. T. Bloking, and Y. M. Chiang. Electronically conductive phospho-olivines as lithium storage electrodes. *Nature Materials*, 1(2):123–128, 2002.

[106] Y. Wen, L. Zeng, Z. Tong, L. Nong, and W. Wei. Structure and properties of $LiFe_{0.9}V_{0.1}PO_4$. *Journal of Alloys and Compounds*, 416(1-2):206–208, 2006.

[107] M. S. Chen, S. H. Wu, and W. K. Pang. Effects of vanadium substitution on the cycling performance of olivine cathode materials. *Journal of Power Sources*, 241:690–695, 2013.

[108] J. Hong, C. S. Wang, X. Chen, S. Upreti, and M. S. Whittingham. Vanadium Modified $LiFePO_4$ Cathode for Li-Ion Batteries. *Electrochemical and Solid-State Letters*, 12(2):A33, 2009.

[109] F. Omenya, N. A. Chernova, Q. Wang, R. Zhang, and M. S. Whittingham. The Structural and Electrochemical Impact of Li and Fe Site Substitution in $LiFePO_4$. *Chemistry of Materials*, 25(13):2691–2699, 2013.

[110] F. Omenya, N. A. Chernova, S. Upreti, P. Y. Zavalij, K. W. Nam, X. Q. Yang, and M. S. Whittingham. Can vanadium be substituted into $LiFePO_4$? *Chemistry of Materials*, 23(21):4733–4740, 2011.

[111] J. Ma, B. H. Li, and F. Y. Kang. Improved electrochemical performances of nanocrystalline $LiFePO_4$/C composite cathode via V-doping and VO_2(B) coating. *Journal of Physics and Chemistry of Solids*, 73(12):1463–1468, 2012.

[112] F. Zhou, M. Cococcioni, K. Kang, and G. Ceder. The Li intercalation potential of $LiMPO_4$ and $LiMSiO_4$ olivines with M = Fe, Mn, Co, Ni. *Electrochemistry Communications*, 6(11):1144–1148, 2004.

[113] K. Amine, H. Yasuda, and M. Yamachi. Olivine $LiCoPO_4$ as 4.8 V Electrode Material for Lithium Batteries. *Electrochemical and Solid-State Letters*, 3(4):178, 1999.

[114] M. Zhao, Y. Fu, N. Xu, G. Li, M. Wu, and X. Gao. High performance $LiMnPO_4$/C prepared by a crystallite size control method. *Journal of Materials Chemistry A*, 2(36):15070, 2014.

[115] Y. Ishii, N. P. Wickramasinghe, and S. Chimon. A New Approach in 1D and 2D ^{13}C High-Resolution Solid-State NMR Spectroscopy of Paramagnetic Organometallic Complexes by Very Fast Magic-Angle Spinning. *J. Am. Chem. Soc*, 125:3438–3439, 2003.

[116] N. P. Wickramasinghe, M. Shaibat, and Y. Ishii. Enhanced Sensitivity and Resolution in ^1H Solid-State NMR Spectroscopy of Paramagnetic Complexes under Very Fast Magic Angle Spinning. *Journal of the American Chemical Society*, 127(16):5796–5797, 2005.

[117] C. P. Grey and Y. J. Lee. Lithium MAS NMR studies of cathode materials for lithium-ion batteries. *Solid State Sciences*, 5(6):883–894, jun 2003.

[118] R. J. Clément, A. J. Pell, D. S. Middlemiss, F. C. Strobridge, J. K. Miller, M. S. Whittingham, L. Emsley, C. P. Grey, and G. Pintacuda. Spin-Transfer Pathways in Paramagnetic Lithium Transition-Metal Phosphates from Combined Broadband Isotropic Solid-State MAS NMR Spectroscopy and DFT

Calculations. *Journal of the American Chemical Society*, 134(41):17178–85, oct 2012.

[119] D. S. Middlemiss, A. J. Ilott, R. J. Clément, F. C. Strobridge, and C. P. Grey. Density Functional Theory-Based Bond Pathway Decompositions of Hyperfine Shifts: Equipping Solid-State NMR to Characterize Atomic Environments in Paramagnetic Materials. *Chemistry of Materials*, 25(9):1723–1734, 2013.

[120] F. C. Strobridge, D. S. Middlemiss, A. J. Pell, M. Leskes, R. J. Clément, F. Pourpoint, Z. Lu, J. V. Hanna, G. Pintacuda, L. Emsley, A. Samoson, and C. P. Grey. Characterising local environments in high energy density Li-ion battery cathodes: a combined NMR and first principles study of $LiFe_xCo_{1-x}PO_4$. *J. Mater. Chem. A*, 2(30):11948–11957, 2014.

[121] V. Luca, C. S. Griffith, M. G. Blackford, and J. V. Hanna. Structural and ion exchange properties of nanocrystalline Si-doped antimony pyrochlore. *Journal of Materials Chemistry*, 15(5):564–572, 2005.

[122] H. Lührs, A. Senyshyn, S. P. King, J. V. Hanna, H. Schneider, and R. X. Fischer. Neutron diffraction and ^{11}B solid state NMR studies of the crystal structure of B-doped mullite. *Zeitschrift für Kristallographie - Crystalline Materials*, 228:130521045435006, 2013.

[123] J. M. Porras-Vazquez, T. F. Kemp, J. V. Hanna, and P. R. Slater. Synthesis and characterisation of oxyanion-doped manganites for potential application as SOFC cathodes. *Journal of Materials Chemistry*, 22(17):8287, 2012.

[124] S. Wiemers-Meyer, M. Winter, and S. Nowak. A battery cell for *in situ* NMR measurements of liquid electrolytes. *Phys. Chem. Chem. Phys.*, 19(7):4962–4966, aug 2017.

[125] F. Blanc, M. Leskes, and C. P. Grey. In Situ Solid-State NMR Spectroscopy of Electrochemical Cells: Batteries, Supercapacitors, and Fuel Cells. *Accounts of chemical research*, 46(9), 2013.

[126] L. Zhou, M. Leskes, A. J. Ilott, N. M. Trease, and C. P. Grey. Paramagnetic electrodes and bulk magnetic susceptibility effects in the in situ NMR studies of batteries: application to $Li_{1.08}Mn_{1.92}O_4$ spinels. *Journal of magnetic resonance (San Diego, Calif. : 1997)*, 234:44–57, sep 2013.

[127] P. P. R. M. L. Harks, F. M. Mulder, and P. H. L. Notten. *In situ* methods for Li-ion battery research: A review of recent developments. *Journal of Power Sources*, 288(August):92–105, 2015.

[128] F. Chevallier, M. Letellier, M. Morcrette, J. M. Tarascon, E. Frackowiak, J. N. Rouzaud, and F. Be'guin. *In Situ* ^{7}Li-Nuclear Magnetic Resonance Observation of Reversible Lithium Insertion into Disordered Carbons. *Electrochemical and Solid-State Letters*, 6(11):A225, 2003.

[129] R. Bhattacharyya, B. Key, H. Chen, A. S. Best, A. F. Hollenkamp, and C. P. Grey. In situ NMR observation of the formation of metallic lithium microstructures in lithium batteries. *Nature Materials*, 9(6):504–510, 2010.

[130] M. Kaus, I. Issac, R. Heinzmann, S. Doyle, S. Mangold, H. Hahn, V. S. K. Chakravadhanula, C. Kübel, H. Ehrenberg, and S. Indris. Electrochemical delithiation/relithiation of $LiCoPO_4$: A two-step reaction mechanism investigated by in situ X-ray diffraction, in situ X-ray absorption spectroscopy, and ex situ ^{7}Li/31 P NMR spectroscopy. *Journal of Physical Chemistry C*, 118(31):17279–17290, 2014.

[131] B. Key, M. Morcrette, J. M. Tarascon, and C. P. Grey. Pair Distribution Function Analysis and Solid State NMR Studies of Silicon Electrodes for Lithium Ion Batteries : Understanding the (De)lithiation Mechanisms. *American Chemical Society*, 133:503–512, 2010.

[132] I. Bezza, M. Kaus, R. Heinzmann, M. Yavuz, M. Knapp, S. Mangold, S. Doyle, C. P. Grey, H. Ehrenberg, S. Indris, and I. Saadoune. Mechanism of the Delithiation/Lithiation Process in $LiFe_{0.4}Mn_{0.6}PO_4$: In Situ and ex Situ Investigations on Long-Range and Local Structures. *Journal of Physical Chemistry C*, 119(17):9016–9024, 2015.

[133] G. Kobayashi, S. I. Nishimura, M. S. Park, R. Kanno, M. Yashima, T. Ida, and A. Yamada. Isolation of solid solution phases in size-controlled Li_xFePO_4 at room temperature. *Advanced Functional Materials*, 19(3):395–403, 2009.

[134] Y. Wang, B. Zhu, Y. Wang, and F. Wang. Solvothermal synthesis of $LiFePO_4$ nanorods as high-performance cathode materials for lithium ion batteries. *Ceramics International*, 42(8):10297–10303, 2016.

[135] F. Krumeich, O. Waser, and S. E. Pratsinis. Thermal annealing dynamics of carbon-coated LiFePO4nanoparticles studied by in-situ analysis. *Journal of Solid State Chemistry*, 242:96–102, 2016.

[136] J. S. O. Evans. Advanced input files & parametric quantitative analysis using topas. *Materials Science Forum*, 651:1–9, 9 2010.

[137] R. K. Harris, E. D. Becker, S. M. Cabral de Menezes, R. Goodfellow, and P. Granger. NMR nomenclature: nuclear spin properties and conventions for chemical shifts. IUPAC Recommendations 2001. International Union of Pure and Applied Chemistry. Physical Chemistry Division. Commission on Molecular Structure and Spectroscopy. *Magnetic Resonance in Chemistry*, 40(7):489–505, jul 2002.

[138] H. T. Edzes. Determination of the Resonance Frequency Ratio of the ^{31}P and ^{1}H NMR resonance shift standards 85% orthophosphoric acid and tetramethylsilane. *Magnetic Resonance in Chemistry*, 30(9):850–854, sep 1992.

[139] T. F. Kemp, G. Balakrishnan, K. J. Pike, M. E. Smith, and R. Dupree. Thermometers for low temperature Magic Angle Spinning NMR. *Journal of magnetic resonance (San Diego, Calif. : 1997)*, 204(1):169–72, may 2010.

[140] L. J. M. Davis, I. Heinmaa, B. L. Ellis, L. F. Nazar, and G. R. Goward. Influence of particle size on solid solution formation and phase interfaces in $Li_{0.5}FePO_4$ revealed by ^{31}P and ^{7}Li solid state NMR spectroscopy. *Physical chemistry chemical physics : PCCP*, 13(11):5171–7, 2011.

[141] D. Arčon, A. Zorko, R. Dominko, and Z. Jagličič. A comparative study of magnetic properties of $LiFePO_4$ and $LiMnPO_4$. *Journal of Physics: Condensed Matter*, 16(30):5531–5548, 2004.

[142] J. Yao, S. Bewlay, K. Konstantionv, V. A. Drozd, R. S. Liu, X. L. Wang, H. K. Liu, and G. X. Wang. Characterisation of olivine-type LiMnxFe1-xPO4 cathode materials. *Journal of Alloys and Compounds*, 425(1-2):362–366, 2006.

[143] L. Lundgren, G. Tarmohamed, O. Beckman, B. Carlsson, and S. Rundqvist. First Order Magnetic Phase Transition in Fe_2P. *Physica Scripta*, 17(1):39, 1978.

[144] N. Wizent, G. Behr, F. Lipps, I. Hellmann, R. Klingeler, V. Kataev, W. Löser, N. Sato, and B. Büchner. Single-crystal growth of $LiMnPO_4$ by the floating-zone method. *Journal of Crystal Growth*, 311(5):1273–1277, 2009.

[145] J. Xiao, N. A. Chernova, S. Upreti, X. Chen, Z. Li, Z. Deng, D. Choi, W. Xu, Z. Nie, G. L. Graff, J. Liu, M. S. Whittingham, and J. G. Zhang. Electrochemical performances of $LiMnPO_4$ synthesized from non-stoichiometric

Li/Mn ratio. *Physical chemistry chemical physics : PCCP*, 13(40):18099–106, 2011.

[146] A. Yamada, Y. Takei, H. Koizumi, N. Sonoyama, R. Kanno, K. Itoh, M. Yonemura, and T. Kamiyama. Electrochemical, Magnetic, and Structural Investigation of the $Li_x(Mn_yFe_{1-y})PO_4$ Olivine Phases. *Chemistry of Materials*, 18(3):804–813, 2006.

[147] G. Hu, Z. Xiao, Z. Peng, K. Du, and X. Deng. Preparation of $LiFePO_4$ for lithium ion battery using $Fe_2P_2O_7$ as precursor. *Journal of Central South University of Technology*, 15(4):531–534, aug 2008.

[148] K. L. Harrison, C. A. Bridges, M. P. Paranthaman, C. U. Segre, J. Katsoudas, V. A. Maroni, J. C. Idrobo, J. B. Goodenough, and A. Manthiram. Temperature dependence of aliovalent-vanadium doping in $LiFePO_4$ cathodes. *Chemistry of Materials*, 25(5):768–781, 2013.

[149] L. S. Cahill, C. W. Kirby, and G. R. Goward. $^{6}Li\{^{31}P\}$ rotational-echo, double-resonance studies of lithium ion site dynamics in $Li_3V_2(PO_4)_3$. *Journal of Physical Chemistry C*, 112(6):2215–2221, 2008.

[150] L. S. Cahill, R. P. Chapman, J. F. Britten, and G. R. Goward. ^{7}Li NMR and two-dimensional exchange study of lithium dynamics in monoclinic $Li_3V_2(PO_4)_3$. *Journal of Physical Chemistry B*, 110(14):7171–7177, 2006.

[151] O. Tsigkou, S. Labbaf, M. M. Stevens, A. E. Porter, and J. R. Jones. Monodispersed bioactive glass submicron particles and their effect on bone marrow and adipose tissue-derived stem cells. *Advanced Healthcare Materials*, 3(1):115–125, 2014.

[152] A. Hoppe, N. S. Güldal, and A. R. Boccaccini. A review of the biological response to ionic dissolution products from bioactive glasses and glass-ceramics. *Biomaterials*, 32(11):2757–2774, 2011.

[153] J. R Jones. Review of bioactive glass: From Hench to hybrids. *Acta Biomaterialia*, 9(1):4457–4486, 2013.

[154] M. Bellantone, N. J. Coleman, and L. L. Hench. Bacteriostatic action of a novel four-component bioactive glass. *Journal of Biomedical Materials Research*, 51(3):484–490, sep 2000.

[155] S. Lin, C. Ionescu, K. J. Pike, M. E. Smith, and J. R. Jones. Nanostructure evolution and calcium distribution in sol-gel derived bioactive glass. *Journal of Materials Chemistry*, 19(9):1276–1282, 2009.

[156] R. A. Martin, S. Yue, J. V. Hanna, P. D. Lee, R. J. Newport, M. E. Smith, and J. R. Jones. Characterizing the hierarchical structures of bioactive sol-gel silicate glass and hybrid scaffolds for bone regeneration. *Philosophical Transactions of the Royal Society A: Mathematical, Physical and Engineering Sciences*, 370(1963):1422–1443, 2012.

[157] L. L. Hench. The story of Bioglass®. *Journal of Materials Science: Materials in Medicine*, 17(11):967–978, 2006.

[158] L. L. Hench, R. J. Splinter, W. C. Allen, and T. K. Greenlee. Bonding Mechanisms at the Interface of Ceramic Prosthetic Materials. *Journal of Biomedical Materials Research*, 5(6):117–141, 1971.

[159] P. Sepulveda, J. R. Jones, and L. L. Hench. Characterization of melt-derived 45S5 and sol-gel-derived 58S bioactive glasses. *Journal of Biomedical Materials Research*, 58(6):734–740, 2001.

[160] B. Lei, X. Chen, Y. Wang, N. Zhao, C. Du, and L. Fang. Surface nanoscale patterning of bioactive glass to support cellular growth and differentiation. *Journal of Biomedical Materials Research - Part A*, 94(4):1091–1099, 2010.

[161] S. L. Greasley, S. J. Page, S. Sirovica, S. Chen, R. A. Martin, A. Riveiro, J. V. Hanna, A. E. Porter, and J. R. Jones. Controlling particle size in the Stöber process and incorporation of calcium. *Journal of Colloid and Interface Science*, 469:213–223, 2016.

[162] W. Stöber, A. Fink, and E. Bohn. Controlled growth of monodisperse silica spheres in the micron size range. *Journal of Colloid and Interface Science*, 26(1):62–69, 1968.

[163] G. M. Luz and J. F. Mano. Preparation and characterization of bioactive glass nanoparticles prepared by sol–gel for biomedical applications. *Nanotechnology*, 22(49):494014, 2011.

[164] W. Xia and J. Chang. Preparation and characterization of nano-bioactive-glasses (NBG) by a quick alkali-mediated sol-gel method. *Materials Letters*, 61(14-15):3251–3253, 2007.

[165] M. W. G. Lockyer, D. Holland, and R. Dupree. NMR investigation of the structure of some bioactive and related glasses. *Journal of Non-Crystalline Solids*, 188(3):207–219, 1995.

[166] E. Lippmaa, M. Mägi, A. Samoson, G. Engelhardt, and A. R. Grimmer. Structural studies of silicates by solid-state high-resolution ^{29}Si NMR. *Journal of the American Chemical Society*, 102(15):4889–4893, 1980.

[167] D. L. Green, S. Jayasundara, Y. F. Lam, and M. T. Harris. Chemical reaction kinetics leading to the first Stober silica nanoparticles - NMR and SAXS investigation. *Journal of Non-Crystalline Solids*, 315(1-2):166–179, 2003.

[168] Z. Lin, J. R. Jones, J. V. Hanna, and M. E. Smith. A multinuclear solid state NMR spectroscopic study of the structural evolution of disordered calcium silicate sol–gel biomaterials. *Phys. Chem. Chem. Phys.*, 17(4):2540–2549, 2015.

[169] T. I. Suratwala, M. L. Hanna, E. L. Miller, P. K. Whitman, I. M. Thomas, P. R. Ehrmann, R. S. Maxwell, and A. K. Burnham. Surface chemistry and trimethylsilyl functionalization of Stöber silica sols. *Journal of Non-Crystalline Solids*, 316(2-3):349–363, 2003.

[170] R. Joseph, S. M. Zhang, and W. T. Ford. Structure and Dynamics of a Colloidal Silica-Poly(methyl methacrylate) Composite by ^{13}C and ^{29}Si MAS NMR spectroscopy. *Macromolecules*, 29(4):1305–1312, 1996.

[171] K. Lee and A. McCormick. Effect of pH on the final connectivity distribution of the silicon atoms in the Stöber particles. *Journal of Sol-Gel Science and Technology*, 33(3):255–260, 2005.

[172] T. Watanabe, H. Shimizu, K. Nagasawa, H. Saito, and A. Masuda. 298I- and 27Al-Mas/Nmr Study of the Thermal Transformations of Kaolinite. *Clay Minerals*, 22:37–48, 1987.

[173] S. J. Clark, M. D. Segall, C. J. Pickard, P. J. Hasnip, M. I. J. Probert, K. Refson, and M. C. Payne. First principles methods using CASTEP. *Zeitschrift für Kristallographie*, 220(5-6-2005):567–570, 2005.

[174] J. R. Yates, C. J. Pickard, and F. Mauri. Calculation of NMR chemical shifts for extended systems using ultrasoft pseudopotentials. *Physical Review B - Condensed Matter and Materials Physics*, 76(2):1–11, 2007.

[175] C. J. Pickard and F. Mauri. All-electron magnetic response with pseudopotentials: NMR chemical shifts. *Physical Review B*, 63:1–13, 2001.

[176] M. Profeta, F. Mauri, and C. J. Pickard. Accurate First Principles Prediction of ^{17}O NMR Parameters in SiO_2 : Assignment of the Zeolite Ferrierite Spectrum. *Journal of the American Chemical Society*, 125(2):541–548, 2003.

[177] E. R. H. Van Eck, M. E. Smith, and S. C. Kohn. Observation of hydroxyl groups by ^{17}O solid-state multiple quantum MAS NMR in sol-gel-produced silica. *Solid State Nuclear Magnetic Resonance*, 15(3):181–188, 1999.

[178] Y. Champouret, Y. Coppel, and M. L. Kahn. Evidence for Core Oxygen Dynamics and Exchange in Metal Oxide Nanocrystals from In Situ ^{17}O MAS NMR. *Journal of the American Chemical Society*, 138(50):16322–16328, dec 2016.

[179] A. B. Rosenthal and S. H. Garofalini. Structural Role of Zinc Oxide in Silica and Soda-Silica Glasses. *Journal of the American Ceramic Society*, 70(11):821–826, 1987.

[180] F. Marumo and Y. Syono. The crystal structure of Zn_2SiO_4-II, a high-pressure phase of willemite. *Acta Crystallographica Section B Structural Crystallography and Crystal Chemistry*, 27:1868–1870, 1971.

[181] K. H. Klaska, J. C. Eck, and D. Pohl. New Investigation of Willemite. *Acta Crystallographica Section B Structural Crystallography and Crystal Chemistry*, 34(11):3324–3325, 1978.

[182] X. Liu, M. Kanzaki, and X. Xue. Crystal structures of Zn_2SiO_4 III and IV synthesized at 6.5-8 GPa and 1,273 K. *Physics and Chemistry of Minerals*, 40(6):467–478, 2013.

[183] N. Morimoto, Y. Nakajima, S. Syono, S. Akimoto, and Y. Matsui. Crystal structure of pyroxene-type $ZnSiO_3$ and $ZnMgSi_2O_6$. *Acta Crystallographica Section B Structural Crystallography and Crystal Chemistry*, 31(4):1041–1049, apr 1975.

[184] K. Kihara and G. Donnay. Anharmonic thermal vibrations in ZnO. *Canadian Mineralogist*, 23(CAN 104:92268):647–654, 1985.

[185] P. Duxson, A. Fernández-Jiménez, J. L. Provis, G. C. Lukey, A. Palomo, and J. S. J. Van Deventer. Geopolymer technology: The current state of the art. *Journal of Materials Science*, 42(9):2917–2933, 2007.

[186] C. Ferone, G. Roviello, F. Colangelo, R. Cioffi, and O. Tarallo. Novel hybrid organic-geopolymer materials. *Applied Clay Science*, 73(1):42–50, 2013.

[187] D. Kim, H. T. Lai, G. V. Chilingar, and T. F. Yen. Geopolymer formation and its unique properties. *Environmental Geology*, 51(1):103–111, 2006.

[188] K. A. Komnitsas. Potential of geopolymer technology towards green buildings and sustainable cities. *Procedia Engineering*, 21:1023–1032, 2011.

[189] S. Vaidya and E. N. Allouche. Strain sensing of carbon fiber reinforced geopolymer concrete. *Materials and Structures*, 44(8):1467–1475, 2011.

[190] J. Davidovits. Geopolymers Inorganic polymeric new materials. *Journal of Thermal Analysis*, 37(8):1633–1656, 1991.

[191] J. L. Provis, A. Palomo, and C. Shi. Advances in understanding alkali-activated materials. *Cement and Concrete Research*, 78:110–125, 2015.

[192] T. W. Cheng and J. P. Chiu. Fire-resistant geopolymer produce by granulated blast furnace slag. *Minerals Engineering*, 16(3):205–210, 2003.

[193] P. Duxson, J. L. Provis, G. C. Lukey, and J. S. J. van Deventer. The role of inorganic polymer technology in the development of 'green concrete'. *Cement and Concrete Research*, 37(12):1590–1597, 2007.

[194] B. Walkley, R. San Nicolas, M. A. Sani, S. A. Bernal, J. S. J. van Deventer, and J. L. Provis. Structural evolution of synthetic alkali-activated CaO-MgO-Na_2O-Al_2O_3-SiO_2 materials is influenced by Mg content. *Cement and Concrete Research*, 99(May):155–171, 2017.

[195] M. Falah, K. J. D MacKenzie, R. Knibbe, S. J. Page, and J. V. Hanna. New composites of nanoparticle Cu (I) oxide and titania in a novel inorganic polymer (geopolymer) matrix for destruction of dyes and hazardous organic pollutants. *Journal of Hazardous Materials*, 2:772–782, 2016.

[196] B. G. Nair, Q. Zhao, and R. F. Cooper. Geopolymer matrices with improved hydrothermal corrosion resistance for high-temperature applications. *Journal of Materials Science*, 42(9):3083–3091, 2007.

[197] Y. L. Tsai, J. V. Hanna, Y. L. Lee, M. E. Smith, and J. C. C. Chan. Solid-state NMR study of geopolymer prepared by sol-gel chemistry. *Journal of Solid State Chemistry*, 183(12):3017–3022, 2010.

[198] T. Hanzlicek, M. Steinerova, and P. Straka. Radioactive metal isotopes stabilized in a geopolymer matrix: Determination of a leaching extract by a radio-

tracer method. *Journal of the American Ceramic Society*, 89(11):3541–3543, 2006.

[199] J. L. Provis. *Cement*, pages 1–3. Springer International Publishing, Cham, 2017.

[200] C. A. Hendriks, E. Worrell, D. de Jager, and P. Riemer. Emission Eeduction of Greenhouse Gases from the Cement Industry. *Energy Agency (IEA*, pages 1–11, 2002.

[201] B. Lippiatt and S. Ahmad. Measuring the life-cycle environmental and economic performance of concrete: the BEES approach. In *In: International workshop on sustainable development and concrete technology*, pages 20–21, Beijing, 2004.

[202] D. N. Huntzinger and T. D. Eatmon. A life-cycle assessment of Portland cement manufacturing: comparing the traditional process with alternative technologies. *Journal of Cleaner Production*, 17(7):668–675, 2009.

[203] B. C. McLellan, R. P. Williams, J. Lay, A. van Riessen, and G. D. Corder. Costs and carbon emissions for geopolymer pastes in comparison to ordinary portland cement. *Journal of Cleaner Production*, 19(9-10):1080–1090, 2011.

[204] M. Abd elaty. Compressive strength prediction of Portland cement concrete with age using a new model. *HBRC Journal*, 10(2):145–155, 2014.

[205] X. Guo, H. Shi, and W. A. Dick. Compressive strength and microstructural characteristics of class C fly ash geopolymer. *Cement and Concrete Composites*, 32(2):142–147, 2010.

[206] P. Chindaprasirt, T. Chareerat, and V. Sirivivatnanon. Workability and strength of coarse high calcium fly ash geopolymer. *Cement and Concrete Composites*, 29(3):224–229, 2007.

[207] B. G. Kutchko and A. G. Kim. Fly ash characterization by SEM-EDS. *Fuel*, 85(17-18):2537–2544, 2006.

[208] B. Walkley, R. San Nicolas, M. A. Sani, J. D. Gehman, J. S. J. van Deventer, and J. L. Provis. Synthesis of stoichiometrically controlled reactive aluminosilicate and calcium-aluminosilicate powders. *Powder Technology*, 297:17–33, 2016.

[209] M. Criado, A. Fernández-Jiménez, A. Palomo, I. Sobrados, and J. Sanz. Effect of the SiO_2/Na_2O ratio on the alkali activation of fly ash. Part II: ^{29}Si MAS-NMR Survey. *Microporous and Mesoporous Materials*, 109(1-3):525–534, 2008.

[210] V. F. F. Barbosa, K. J. D. MacKenzie, and C. Thaumaturgo. Synthesis and characterisation of materials based on inorganic polymers of alumina and silica: Sodium polysialate polymers. *International Journal of Inorganic Materials*, 2(4):309–317, 2000.

[211] M. R. Rowles, J. V. Hanna, K. J. Pike, M. E. Smith, and B. H. O'Connor. ^{29}Si, ^{27}Al, ^{1}H and ^{23}Na MAS NMR study of the bonding character in aluminosilicate inorganic polymers. *Applied Magnetic Resonance*, 32(4):663–689, 2007.

[212] A. Fernández-Jiménez, A. Palomo, I. Sobrados, and J. Sanz. The role played by the reactive alumina content in the alkaline activation of fly ashes. *Microporous and Mesoporous Materials*, 91(1-3):111–119, 2006.

[213] P. Duxson, J. L. Provis, G. C. Lukey, F. Separovic, and J. S. J. Van Deventer. ^{29}Si NMR study of structural ordering in aluminosilicate geopolymer gels. *Langmuir*, 21(7):3028–3036, 2005.

[214] S. A. Bernal, J. L. Provis, B. Walkley, R. San Nicolas, J. D. Gehman, D. G. Brice, A. R. Kilcullen, P. Duxson, and J. S.J. van Deventer. Gel nanostructure in alkali-activated binders based on slag and fly ash, and effects of accelerated carbonation. *Cement and Concrete Research*, 53:127–144, 2013.

[215] P. Pena, J. M. Rivas Mercury, A. H. de Aza, X. Turrillas, I. Sobrados, and J. Sanz. Solid-state ^{27}Al and ^{29}Si NMR characterization of hydrates formed in calcium aluminate-silica fume mixtures. *Journal of Solid State Chemistry*, 181(8):1744–1752, 2008.

[216] P. S. Singh, M. Trigg, I. Burgar, and T. Bastow. Geopolymer formation processes at room temperature studied by ^{29}Si and ^{27}Al MAS-NMR. *Materials Science and Engineering A*, 396(1-2):392–402, 2005.

[217] P. Duxson, G. C. Lukey, F. Separovic, and J. S. J. Van Deventer. Effect of alkali cations on aluminum incorporation in geopolymeric gels. *Industrial and Engineering Chemistry Research*, 44(4):832–839, 2005.

[218] J. Brus, S. Abbrent, L. Kobera, M. Urbanova, and P. Cuba. Advances in ^{27}Al MAS NMR Studies of Geopolymers. In *Annual reports on NMR Spectroscopy*, pages 79–147. Elsevier, 2016.

[219] J. Brus, L. Kobera, M. Urbanová, D. Koloušek, and J. Kotek. Insights into the structural transformations of aluminosilicate inorganic polymers: A comprehensive solid-state NMR study. *Journal of Physical Chemistry C*, 116(27):14627–14637, 2012.

[220] J. D. Gehman and J. L. Provis. Generalized biaxial shearing of MQMAS NMR spectra. *Journal of Magnetic Resonance*, 200(1):167–172, 2009.

[221] M. Fallah, K. J. D. MacKenzie, J. V. Hanna, and S. J. Page. Novel photoactive inorganic polymer composites of inorganic polymers with copper(I) oxide nanoparticles. *Journal of Materials Science*, 50(22):7374–7383, 2015.

[222] S. K. Lee and J. F. Stebbins. Nature of cation mixing and ordering in Na-Ca silicate glasses and melts. *Journal of Physical Chemistry B*, 107(14):3141–3148, 2003.

[223] P. J. Dirken, S. C. Kohn, M. E. Smith, and E. R. H. Van Eck. Complete resolution of Si-O-Si and Si-O-Al fragments in an aluminosilicate glass by ^{17}O multiple quantum magic angle spinning NMR spectroscopy. *Chemical Physics Letters*, 266(March):568–574, 1997.

[224] A. Jaworski, B. Stevensson, and M. Edén. The Bearings from Rare-Earth (RE = La, Lu, Sc, Y) Cations on the Oxygen Environments in Aluminosilicate Glasses: A Study by Solid-State ^{17}O NMR, Molecular Dynamics Simulations, and DFT Calculations. *Journal of Physical Chemistry C*, 120(24):13181–13198, 2016.

[225] K. Kanehashi. Structural roles of calcium in alkaline and alkaline-earth aluminosilicate glasses by solid-state ^{43}Ca, ^{17}O and ^{27}Al NMR. *Solid State Nuclear Magnetic Resonance*, 84(January):158–163, 2016.

[226] H. I. Kim, J. C. Sur, and S. K. Lee. Effect of iron content on the structure and disorder of iron-bearing sodium silicate glasses: A high-resolution ^{29}Si and ^{17}O solid-state NMR study. *Geochimica et Cosmochimica Acta*, 173:160–180, 2016.

[227] P. Duxson. *The structure and thermal evolution of metakaolin geopolymers.* Doctor of philosophy, University of Melbourne, 2006.

[228] T. F. Kemp and M. E. Smith. QuadFit-A new cross-platform computer program for simulation of NMR line shapes from solids with distributions of interaction parameters. *Solid State Nuclear Magnetic Resonance*, 35(4):243–252, 2009.

[229] W. Loewenstein. The distribution of aluminum in the tetrahedra of silicates and aluminates. *American Mineralogist*, 39:92–96, 1954.

[230] B. Walkley, R. San Nicolas, M. A. Sani, G. J. Rees, J. V. Hanna, J. S. J. van Deventer, and J. L. Provis. Phase evolution of C-(N)-A-S-H/N-A-S-H gel blends investigated via alkali-activation of synthetic calcium aluminosilicate precursors. *Cement and Concrete Research*, 89:120–135, 2016.

[231] M. Zajac, A. Rossberg, G. Le Saout, and B. Lothenbach. Influence of limestone and anhydrite on the hydration of Portland cements. *Cement and Concrete Composites*, 46:99–108, 2014.

[232] S. D. Wang and K. L. Scrivener. ^{29}Si and ^{27}Al NMR study of alkali-activated slag. *Cement and Concrete Research*, 33(5):769–774, 2003.

[233] H. Viallis, P. Faucon, J. C. Petit, and A. Nonat. Interaction between Salts (NaCl, CsCl) and Calcium Silicate Hydrates (C-S-H). *Journal of Physical Chemistry B*, 103:5212–5219, 1999.

[234] F. Bonk, J. Schneider, M. A. Cincotto, and H. Panepucci. Characterization by Multinuclear High-Resolution NMR of Hydration Products in Activated Blast-Furnace Slag Pastes. *Journal of the American Ceramic Society*, 19(10):1712–1719, 2003.

[235] B. Walkley, R. San Nicolas, M. A. Sani, J. D. Gehman, Jannie S. J. van Deventer, and J. L. Provis. Phase evolution of Na_2O–Al_2O_3–SiO_2–H_2O gels in synthetic aluminosilicate binders. *Dalton Trans.*, 45(13):5521–5535, 2016.

[236] J. Allwardt, S. K. Lee, and J. F. Stebbins. Bonding preferences of non- bridging oxygens in calcium aluminosilicate glass: evidence from ^{17}O MAS and 3QMAS NMR on calcium aluminate glass. *American Mineralogist*, 88:949–954, 2003.

Appendix A

Low Field and Fast MAS Studies on Paramagnetic Cathode Battery Materials

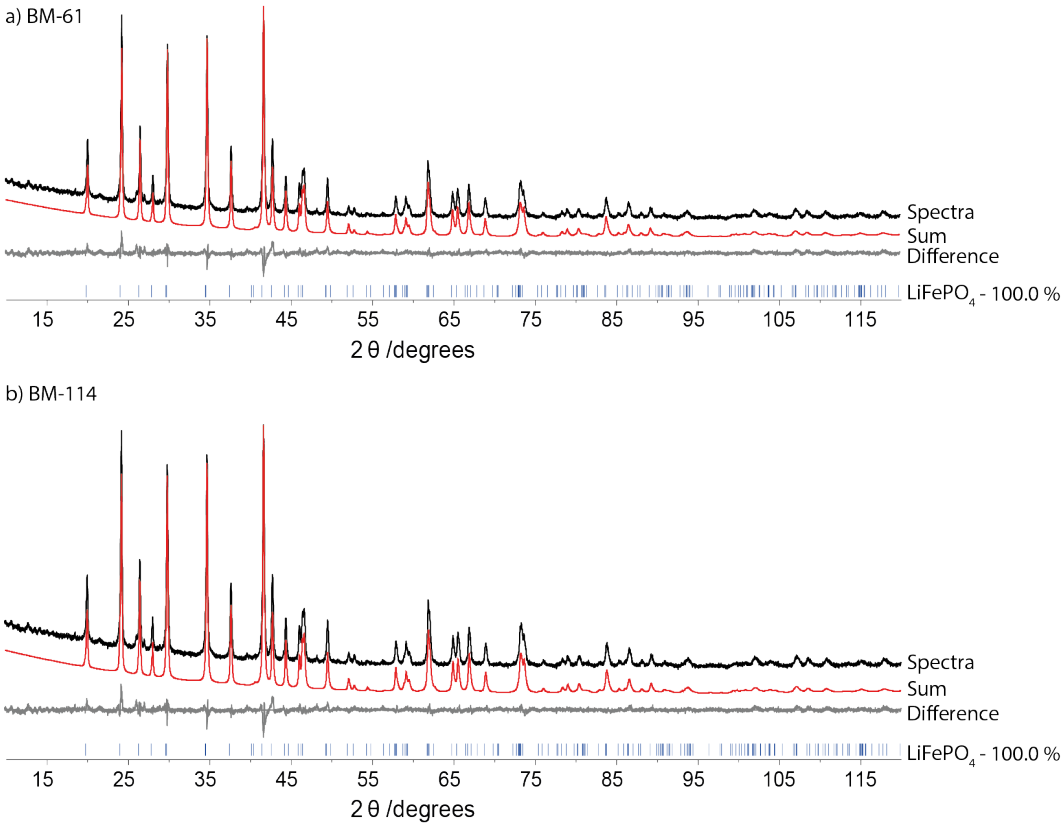

Figure A.1: The XRD patterns for (a)BM-61, (b)BM-114.

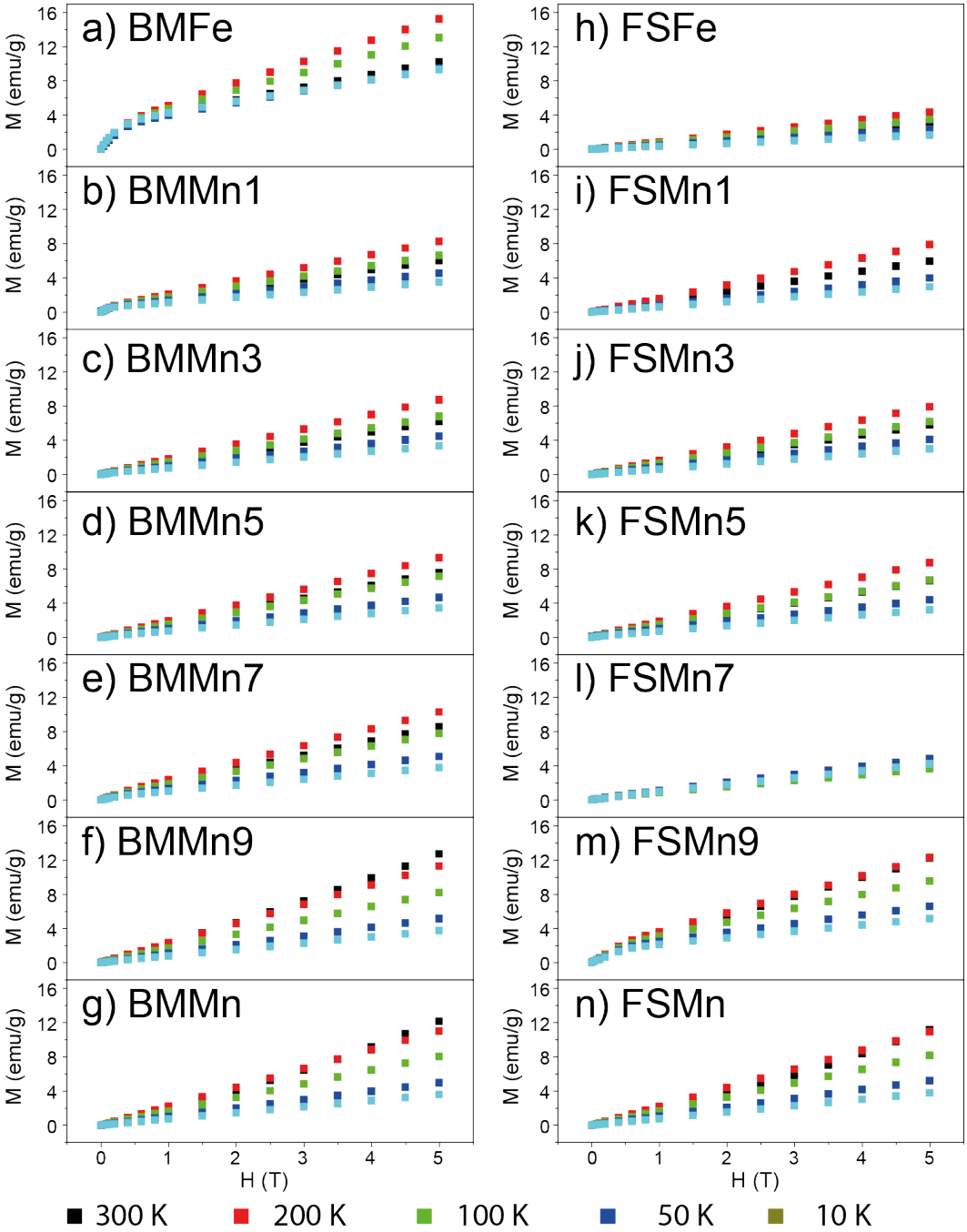

Figure A.2: The M(H) data for increasing Mn content where (a)-(g) is the ball milled series and (h)-(f) is the flame spray pyrolysis series.

Appendix B

Using ^{17}O NMR to Monitor the Incorporation of Ca^{2+} and Zn^{2+} in Stöber Nanoparticles

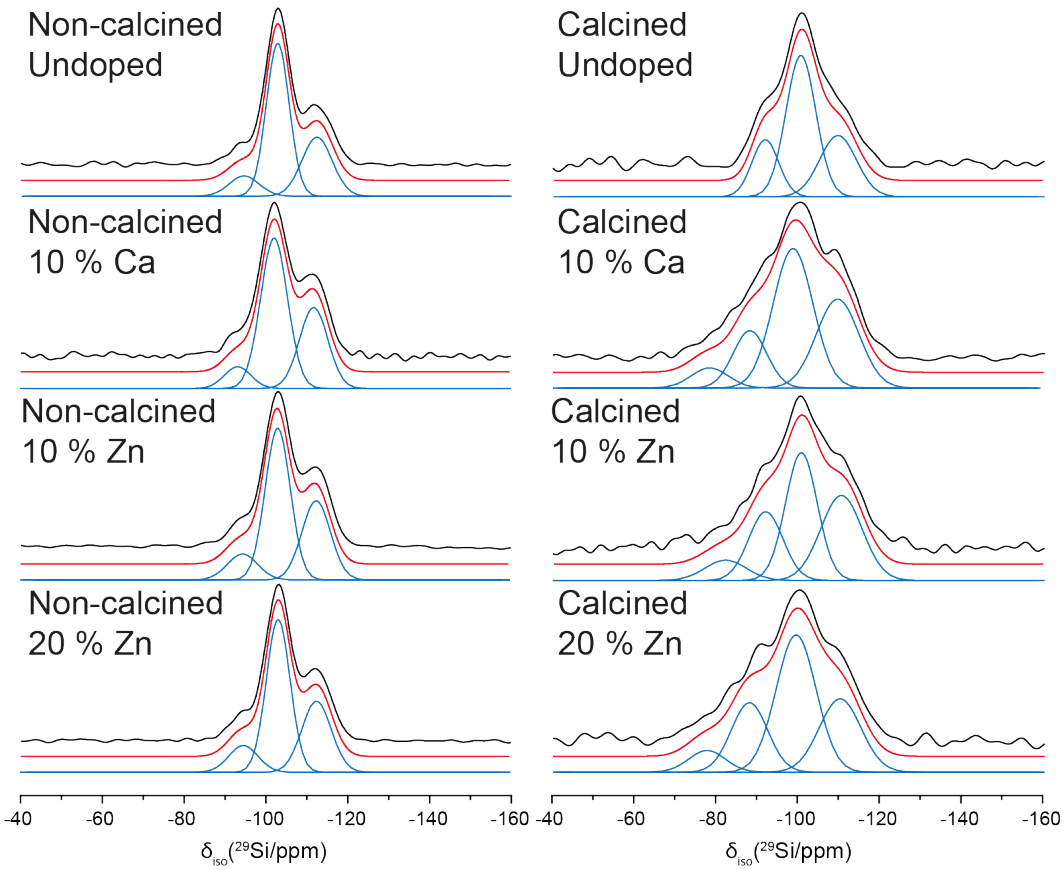

Figure B.1: The ^{29}Si CPMAS NMR spectra of non-calcined and calcined Stöber particles. The individual deconvolutions are shown in blue and the sum of these are marked in red.

Table B.1: Millar indices, d-spacing's and intensities for the prominent crystallographic plains of the investigated structures.

	ref	h	k	l	d (Å)	I
Zincite	[184]	0	1	1	2.4753	100.0
		0	1	0	2.8141	51.5
Willemite	[181]	1	-5	0	2.6359	100.0
		1	1	3	2.8366	89.7
		2	2	0	3.4870	74.4
Zn_2SiO_4-II	[180]	1	1	2	2.7069	90.3
		1	2	1	2.8197	100.0
Zn_2SiO_4-III	[182]	2	2	1	2.4502	81.7
		2	0	1	3.6109	100.0
Zn_2SiO_4-IV	[182]	0	3	0	2.7762	84.8
		2	1	2	2.8180	100.0
Monoclinic $ZnSiO_3$	[183]	-1	3	1	2.6337	100.0
		3	1	0	2.8827	74.4
		-2	2	1	3.0939	86.3
Orthorhombic $ZnSiO_3$	[183]	2	3	5	0.7703	100.0
		2	3	1	2.6002	84.0
		4	1	0	2.8778	80.6
		1	0	0	4.5510	76.2
		0	1	0	6.4308	77.0

Table B.2: Theoretical ^{17}O parameters determined by CASTEP. The relative intensity (I) of each peak, $\sigma(r)$ is the calculated isotropic shielding parameter, $\delta(r)$ is the calculated isotropic chemical shift, C_q is the quadrupolar coupling and η is the asymmetry parameter.

	ref	I	$\sigma(r)$	$\delta(r)$	C_q (MHz)	η_Q
Zincite	[184]	1	195.05	55.34	2.403	0.00
Willemite	[181]	1	242.72	7.67	4.837	0.39
		1	231.80	18.59	4.721	0.54
		1	245.72	4.67	4.757	0.50
		1	246.11	4.28	4.642	0.49
Zn_2SiO_4-II	[180]	1	220.32	30.06	4.715	0.38
Zn_2SiO_4-III	[182]	0.5	242.93	7.46	4.806	0.18
		0.5	245.27	5.12	5.014	0.15
		1	224.98	25.41	3.871	0.38
Zn2SiO4-IV	[182]	1	231.77	18.62	4.379	0.62
		1	205.75	44.64	3.666	0.89
		1	211.51	38.88	4.475	0.41
		1	218.81	31.58	5.013	0.24
Monoclinic $ZnSiO_3$	[183]	1	191.28	59.11	−2.832	0.24
		1	186.99	63.40	−5.289	0.29
		1	207.24	43.15	4.177	0.67
Orthorhombic $ZnSiO_3$	[183]	1	188.59	61.80	−2.814	0.15
		1	185.80	64.59	−4.971	0.24
		1	209.57	40.82	4.181	0.70
		1	182.03	68.36	−5.311	0.54
		1	199.07	51.32	3.766	0.70
		1	192.37	58.02	−2.757	0.20

Appendix C

Quadrupolar Solid State NMR Investigation into the Curing Process of Alkali-Activated C-(N)-(A)-S-H Geopolymers

Table C.1: The Q_n^m species content and δ_{iso} shifts of the precursor and activated C-(N)-(A)-S-H geopolymers

Part A

	Q_0^0				Q_1^1		Q_0^1		Q_1^2			
Sample	δ_{iso}	%	δ_{iso}	%	δ_{iso}	%	δ_{iso}	%	δ_{iso}	%	δ_{iso}	%
Series A												
A0.5P	−71.3	1.6			−75.7	5.3	−79.4	10.0	−82.8	9.4		
A0.7P	−72.7	3.4			−76.6	7.8	−79.2	4.1	−81.8	14.4		
A0.8P	−71.8	8.0			−75.4	3.9	−78.8	14.0	−82.6	11.5		
A1.0P	−72.5	10.6	−74.8	1.3	−76.5	3.9	−79.2	13.0	−82.3	11.8		
A0.5A	−71.5	1.9			−75.9	4.9	−79.4	8.8	−82.8	8.9		
A0.7A	−71.0	1.8			−75.6	6.0	−79.4	8.5	−82.5	14.6		
A0.8A	−72.1	4.2			−76.1	6.2	−79.5	15.0	−82.2	11.8		
A1.0A	−72.3	1.9	−74.5	3.5	−76.7	3.7	−79.4	9.8	−82.3	9.0	−84.6	6.4
Series B												
B0.5P	−72.3	4.7			−76.1	5.1	−79.4	9.7	−83.0	9.8		
B0.7P	−71.4	4.8			−76.1	5.9	−79.6	9.2	−83.0	10.3		
B0.8P	−71.5	9.8			−75.6	3.7	−79.2	10.9	−82.8	10.5		
B1.0P	−71.6	17.8			−75.7	3.9	−78.9	15.0	−83.0	15.1		
B0.5A	−72.5	1.9			−77.0	5.6	−80.0	6.6	−83.0	16.6		
B0.7A	−73.0	2.2			−75.8	1.7	−79.1	8.9	−82.5	16.7		
B0.8A	−73.0	1.7			−76.2	3.5	−79.5	16.6	−82.1	4.6		
B1.0A	−71.1	4.3			−76.2	11.4	−79.8	14.7	−82.8	17.1		

Part B

	Q_0^2				Q_1^3		Q_0^3		Q_1^4		Q_0^4	
Sample	δ_{iso}	%	δ_{iso}	%	δ_{iso}	%	δ_{iso}	%	δ_{iso}	%	δ_{iso}	%
Series A												
A0.5P	−86.5	21.4			−92.0	14.3	−97.2	5.4	−102.0	10.8	−110.9	21.9
A0.7P	−85.6	14.6			−90.4	23.1	−97.0	12.2	−103.7	6.0	−111.4	14.5
A0.8P	−86.4	23.8			−91.9	15.4	−97.6	7.6	−103.6	4.6	−111.0	11.2
A1.0P	−86.2	4.2	−88.3	8.5	−90.2	4.7	−93.1	16.5	−103.2	8.6	−112.0	10.5
A0.5A	−86.6	20.5			−92.0	13.9	−97.8	11.9	−106.0	10.4	−112.8	18.8
A0.7A	−86.4	16.7			−90.5	19.8	−97.0	12.9	−104.5	8.8	−112.0	10.9
A0.8A	−85.3	20.8			−90.9	19.1	−97.4	8.8	−103.5	2.7	−111.0	11.4
A1.0A	−86.5	5.2	−88.6	6.4	−90.3	6.9	−93.6	19.7	−102.3	9.9	−111.1	17.5
Series B												
B0.5P	−86.8	13.5			−91.7	14.4	−97.0	9.1	−102.3	8.8	−110.4	25.0
B0.7P	−86.6	17.8			−91.5	17.0	−97.1	10.1	−103.3	10.6	−111.0	14.3
B0.8P	−86.6	17.2			−91.8	16.1	−97.0	7.0	−103.1	11.1	−111.5	13.7
B1.0P	−87.0	14.7			−90.4	15.1	−96.7	8.5	−102.6	3.3	−110.2	6.6
B0.5A	−86.5	14.3			−91.4	16.0	−97.1	8.5	−103.2	10.8	−111.2	19.8
B0.7A	−86.1	16.7			−90.6	20.9	−97.0	20.9	−103.0	8.9	−111.0	14.7
B0.8A	−84.9	22.5			−90.2	20.1	−97.0	11.2	−103.8	4.8	−111.0	15.0
B1.0A	−85.8	13.9			−89.5	23.2	−96.9	7.7	−102.7	1.8	−110.0	5.9

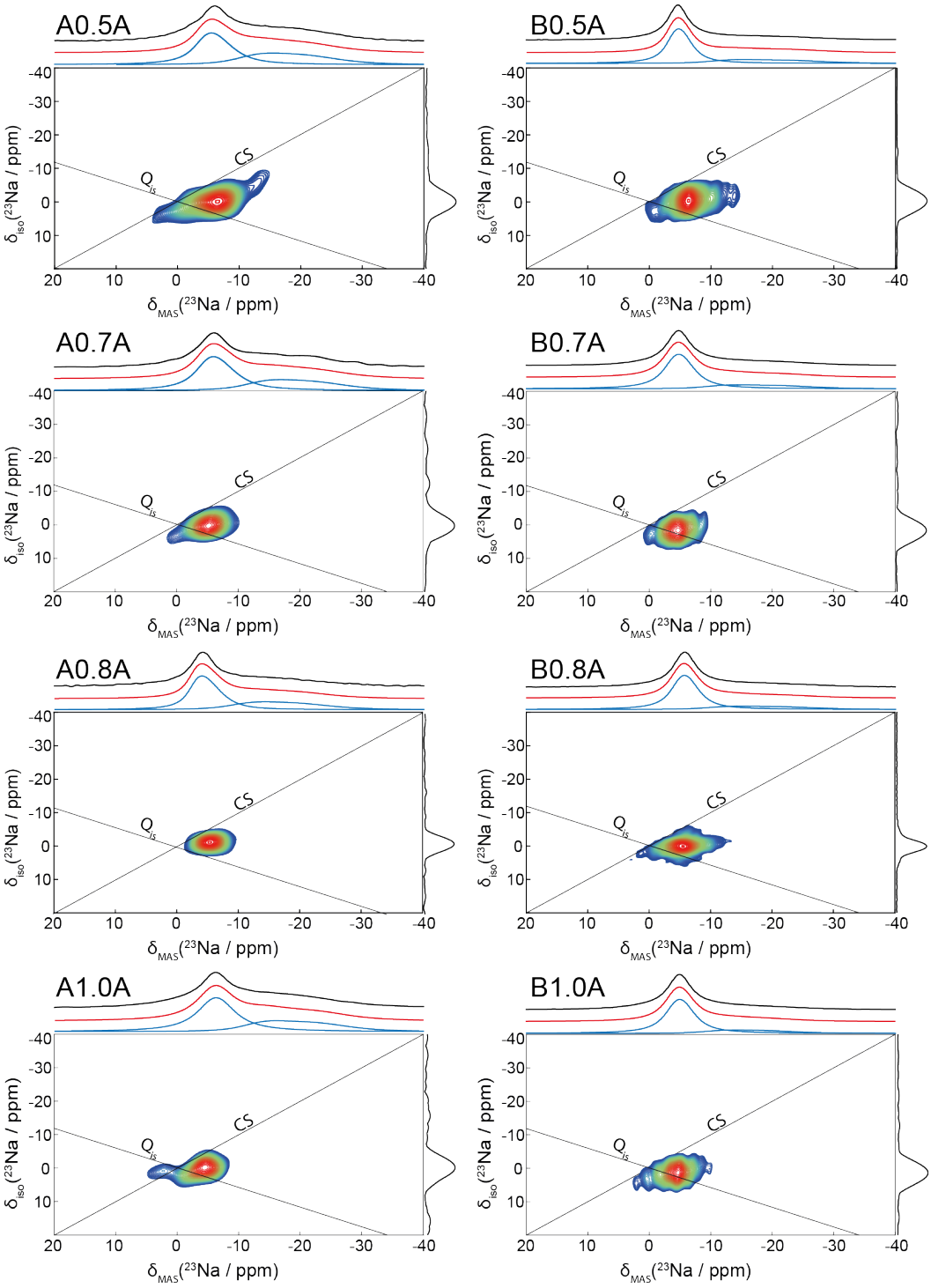

Figure C.1: The deconvoluted 1D MAS and MQMAS ^{23}Na spectra of the 0.05 & 0.15 Si/Al geopolymers. The deconvolutions of the 1D MAS NMR are shown as projections in the MAS dimension. The individual sites are shown in blue and the sum of these are marked in red.